

Department of Physics and Astronomy
Remote Sensing and Satellite Research Group

**Uncertainty in Hyperspectral Remote Sensing: Analysis of the
Potential and Limitation of Shallow Water Bathymetry and Benthic
Classification**

Rodrigo Alejandro Garcia

**This thesis is presented for the Degree of
Doctor of Philosophy
of
Curtin University**

October 2015

DECLARATION

To the best of my knowledge and belief this thesis contains no material previously published by any other person except where due acknowledgement has been made. This thesis contains no material which has been accepted for the award of any other degree or diploma in any university

Signature:



Date:

19 October 2015

In loving memory of
Maria-Dolores Garcia (1929-2013)
Forever in our hearts, our thoughts and in our actions

ABSTRACT

Hyperspectral remote sensing data of shallow water environments can be processed to provide bathymetry and benthic habitat maps through physics-based inversion models. However there is uncertainty inherent in the remote sensing reflectance that propagates to the derived products, and which limits the number and type of benthic classes that can be optically resolved. Notwithstanding the natural spectral variability that occurs in substrate reflectance and in absorption and backscattering coefficients of inherent optical properties; uncertainty also arises from sensor and environmental noise, the latter of which is introduced from imperfect atmospheric, sunglint and air-to-water interface corrections imposed on the at-sensor radiance. Estimating the confidence intervals or reliability of shallow water mapped products from image based uncertainty, can provide an understanding of the limitations of remote sensing for environmental monitoring. This research focuses on propagating uncertainty through a physics-based inversion model to assign confidence intervals to the bathymetry and benthic classification products derived from surface reflectance measurements. Subsequent processing techniques utilising these confidence intervals are also developed that aid in ecological interpretations and in understanding the potential of remote sensing for shallow water classification.

The accuracy and precision of products generated from shallow water inversion models is dependent in part on the optimisation algorithm used. Global optimisation algorithms that converge on the solution with the global minimum in parameter space have increasingly been used in ocean colour inversions. However they are hampered by longer computational processing time when compared to local optimisation algorithms such the Levenberg Marquardt (LM) algorithm. In this work, the Update-Repeat LM (UR-LM) and Latin Hypercube Sampling LM (LHS-LM) routines are presented. These solution methods test the parameter space for the best 'local' if not global minimum. The two methods are computationally faster than global optimisation algorithms, such as Simulated Annealing, particularly when propagating uncertainty through the inversion model. Our analysis showed that the LHS-LM and UR-LM methods improved the accuracy and precision of geophysical parameters derived from inversion models when compared to the standard LM.

Detecting trend and seasonal variability of key environmental parameters is of core interest for resource managers. Previous studies have tended to neglect any

consideration of the uncertainty of remotely sensed products and whether detected temporal changes are indeed significant above the uncertainty inherent in the system. A temporal analysis processing scheme is presented for bathymetry images and exemplified using nine HICO images of Shark Bay, Western Australia, captured between November 2011 and August 2012. Here uncertainty was propagated through a shallow water inversion model using the UR-LM optimisation algorithm to generate HICO-derived images of bathymetry and its associated uncertainty. An image-based tide correction procedure was additionally developed to correct the bathymetric data for variations in depth due to tide. The resultant dataset was subsequently analysed for depth changes due to bottom sediment resuspension and deposition using a per-pixel *t*-test analysis. Analysis revealed that temporal changes in depth to as low as 0.4 m can be detected and considered significant at a 95% confidence interval.

The limits of benthic classification from remotely sensed imagery was also analysed in this research through the ability to spectrally distinguish different benthic species above the inherent uncertainty. Here the uncertainty combined image-based sensor and environmental noise with the benthic species' taxonomic spectral variability. Knowing the number and type of benthic classes that can be optically distinguished *a priori* can aid in the analysis of the potential of optical remote sensing for benthic classification – particularly matching deliverables with expectations. We present a new hierarchical clustering using linear discriminant coordinates, termed the HDC, which when combined with a semi-analytical shallow water model, quantitates the number and type of benthic classes that can be distinguished at any given water column optical property and depth. The HDC is novel in that it incorporates the total system noise into the clustering procedure, and terminates when all benthic classes have an inter-class spectral overlap above a user-defined threshold. The HDC procedure is demonstrated by assessing the conditions (clustering accuracy, sensor spectral resolution, water column optical properties and depth) that enable the spectral distinction of the seagrass *Amphibolis antarctica* from benthic algae. Such an analysis can provide *a priori* insights into what sensor, classification accuracy, water turbidity and depth enable the spectral distinction between ecologically important classes such as live versus dead coral, or coral versus algae.

ACKNOWLEDGEMENTS

This body of work has evolved into something I'm proud of thanks to the support and knowledge of my supervisor Dr. Peter Fearn whose clarity of thought and ability to see the big picture got me out of several micro-chasms. I would also like to thank you for introducing me to the wonderful world of shallow water remote sensing back in 2008 when I was still an undergraduate; and for allowing me to explore and expand on interesting, but slightly off topic research ideas. To my co-supervisor, Dr. John Hedley, I'm ever grateful for your assistance, guidance and knowledge that you have imparted in me during this research, and I will always remember the time I visited Exeter and Tiverton with a smile. I'm always in awe of your scientific research. I would also like to thank Dr. Lachlan McKinna – my unofficial third supervisor – who helped me through the majority of my PhD and who also provided me with valuable advice on both my research and field work. To Dan Marrable (and Lachlan) for teaching me the intricate ways of the DALEC, may it never ever break down again! I'm also grateful to Dr. Mark Broomhall of the RSSRG for giving me a helping hand when I needed it. To Emeritus Prof. Merv Lynch for your valuable advice on my future career path – I wouldn't be where I am now if I didn't listen to you. In addition to all the staff of the Physics Department at Curtin University, a big thank you!

To my parents Maria-Marta Garcia and Harry Pickett, your strength, love and support have driven me to become the inquisitive person I am today. Do you still remember the little Einstein performing on stage all those years ago? And finally, to my beautiful partner Zoe Richards, who I love fiercely and intensely, you have brought so much happiness into my life since we met in the magical Kimberley. Your support and love have kept me going through countless sleepless nights. Remember, our adventure is far from over. To Myka and Amber who each day give me a warm smile and a big hug, thank you. My dear girls, I love you.

LIST OF PUBLICATIONS & REPORTS

DURING PHD CANDIDATURE

Publications Presented as part of this Thesis

Chapter 3

Garcia, R. A., Fearn, P. R. C. S., and McKinna, L. I. W. (2014). Detecting trend and seasonal changes in bathymetry derived from HICO imagery: A case study of Shark Bay, Western Australia. *Remote Sensing of Environment*, 147, 186-205.

Chapter 4

Garcia, R. A., McKinna, L. I. W., Hedley, D., and Fearn, P. R. C. S. (2014). Improving the Optimisation Solution for a Semi-analytical Shallow Water Inversion Model in the presence of Spectrally Correlated Noise. *Limnology and Oceanography: Methods*, 12, 651-669.

Chapter 5

Garcia, R. A., Hedley, J. D., Hoang, T. C., & Fearn, P. R. C. S. (2015). A method to analyze the potential of optical remote sensing for benthic habitat mapping. *Remote Sensing*, 7(10), 13157-13189.

The Statements of Contributions of the co-authors for each published manuscript as well as the journals copyright statement are provided in the Appendices.

Technical Reports written during PhD Candidature

Garcia, R. A., Fearn, P., and McKinna, L. (2014). Examining the potential of detecting change in HICO-derived bathymetry: a case study of Shark Bay, Western Australia, *HICO User's Annual Report II*, Report to the HICO Project Office, Oregon State University

McKinna, L., Fearn, P., and **Garcia, R. A.** (2013). Shallow water products for the Hyperspectral Imager for the Coastal Ocean, in the Western Australian Satellite Technology and Applications Consortium (WASTAC) 2012 Annual Report, pp. 38, WASTAC, Wembley, Western Australia.

McKinna, L., **Garcia, R. A.**, and Fearn, P. (2012). Determining inherent optical properties, bathymetry and benthic types using HICO imagery within northeast and western Australia, *HICO User's Annual Report I*, Report to the HICO Project Office, Oregon State University

STATEMENT OF CONTRIBUTION OF OTHERS

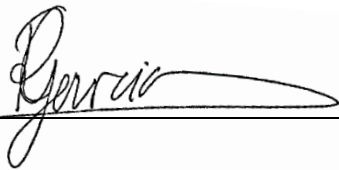
Rodrigo Garcia's input to this study and the associated papers included the execution of all experimental work as well as the dominant contribution to the intellectual input involved in the project. Other scientists made some contributions to the current work, as is almost always the case in the physical sciences. These contributions were significant enough to warrant co-authorship on the resulting journal articles. These are specified below:

Dr. Peter Fearn provided project supervision and manuscript editing.

Dr. John Hedley provided project co-supervision and manuscript editing

Dr. Lachlan McKinna performed atmospheric correction of satellite image data and manuscript editing

Mr. Tin C. Hoang provided fieldwork support and benthic species identification for Chapter 5



Rodrigo Garcia



Dr. Peter Fearn

LIST OF COMMON SYMBOLS

Symbol	Units	Definition
λ	nm	Wavelength
θ_v	degrees or radians	Subsurface sensor-viewing zenith angle
θ_w	degrees or radians	Subsurface solar zenith angle
φ_r	degrees or radians	Relative azimuth angle between the sun and sensor
$a(\lambda)$	m^{-1}	Total spectral absorption coefficient of the water column
$a_{phy}(\lambda)$	m^{-1}	Spectral absorption coefficients of phytoplankton
$a_{dg}(\lambda)$	m^{-1}	Spectral absorption coefficients of dissolved and detritus matter
$a_w(\lambda)$	m^{-1}	Spectral absorption coefficient of pure water
$b_b(\lambda)$	m^{-1}	Total spectral backscattering coefficient of the water column
$b_{bw}(\lambda)$	m^{-1}	Spectral backscattering coefficient of pure water
$b_p(\lambda)$	m^{-1}	Spectral backscattering coefficient of suspended particulate matter
G	m^{-1}	Absorption coefficient of dissolved and detrital matter at 440 nm
H	m	Geometric depth of the water column
$\kappa(\lambda)$	m^{-1}	Spectral attenuation coefficient, $\kappa = a + b_b$
k	dimensionless	Number of benthic classes
K_d	m^{-1}	Downwelling diffuse attenuation coefficient
n	dimensionless	Number of wavebands
ρ_b	dimensionless	Benthic irradiance reflectance
$\rho^*_i(\lambda)$	dimensionless	Normalised irradiance reflectance of benthic class i
B_i	dimensionless	Bottom albedo at 550 nm of benthic class i

P	m^{-1}	Absorption coefficient of phytoplankton at 440 nm
R_{rs}	sr^{-1}	Above-water surface remote sensing reflectance
r_{rs}	sr^{-1}	Subsurface remote sensing reflectance
r_{rs}^M	sr^{-1}	Forward modelled subsurface remote sensing reflectance
s	dimensionless	Number of LD eigenvectors
τ_m	dimensionless	Proportion of misclassified Linear Discriminant Functions between a pair of classes
u	dimensionless	Single scattering albedo of the water column defined by the ratio of backscattering coefficients to the attenuation coefficient, $b_b/(a + b_b)$
X	m^{-1}	Backscattering coefficient of suspended particles at a reference wavelength
Z_{SD}	m	Secchi Depth

LIST OF ABBREVIATIONS

Acronym	Definition
ALLUT	Adaptive Linearised Look-up Trees
AOP	Apparent Optical Property
AOT	Aerosol optical thickness
<i>BA</i>	Brown algae
BRUCE	Bottom Reflectance Un-mixing Computation of the Environment algorithm
C_{SE}	Spectral covariance matrix pertaining to $NE\Delta r_{rs}$
CDOM	Colour dissolved organic and detrital matter
CLMVAP	Vertical column of water vapour (cm)
CRISTAL	Comprehensive Reflectance Inversion based on Spectrum matching and Table Look-up
CZCS	Coastal Zone Color Scanner
DII	Depth invariant indices computed by the Lyzenga (1985) method
<i>GA</i>	Green algae
GLTs	Geographic Look up Tables
HDC	Hierarchical clustering using linear Discriminant Coordinates
HICO	Hyperspectral Imager for the Coastal Ocean
HOPE	Hyperspectral Optimisation Process Exemplar model
IOPs	Inherent Optical Properties

IR	Infrared
LAT	Lowest astronomical tide
LDA	Linear Discriminant Analysis
LHS	Latin Hypercube Sampling
LM	Levenberg-Marquardt optimisation algorithm
LUT	Look up table
MHM	Marine benthic Habitat Maps
MLC	Maximum Likelihood Classifier
MODIS	MODerate resolution Imaging Spectroradiometer
$NEAr_{rs}$	Sensor-environmental noise equivalent perturbation of r_{rs}
NIR	Near infrared
RMSE	Root mean square error
<i>RA</i>	Red algae
RTE	Radiative Transfer Equation
SA	Semianalytical shallow water forward model
<i>SD</i>	Sediment
SeaDAS	SeaWiFS Data Analysis System
SeaWiFS	Sea-viewing Wide Field-of-view Sensor
<i>SG</i>	Seagrass

SAMBUCA	Semi-Analytical Model for Bathymetry, Un-mixing and Concentration Assessment
SNR	Signal-to-Noise Ratio
SRF	Spectral response function
SLM	Standard Levenberg-Marquardt approach
SWIR	Shortwave infrared
Tafkaa-6S	Second Simulation of the Satellite Signal in the Solar Spectrum (6S) implementation of Tafkaa atmospheric correction algorithm
TOA	Top of atmosphere
UR-LM	Update-Repeat Levenberg-Marquardt approach
WV2	WorldView-2

TABLE OF CONTENTS

DECLARATION	i
ABSTRACT	v
ACKNOWLEDGEMENTS	vii
LIST OF PUBLICATIONS & REPORTS	viii
STATEMENT OF CONTRIBUTION OF OTHERS	x
LIST OF COMMON SYMBOLS	xi
LIST OF ABBREVIATIONS	xiii
TABLE OF CONTENTS	xvi
LIST OF FIGURES	xx
LIST OF TABLES	xxviii
CHAPTER 1	1
1.1 OVERVIEW	1
1.2 BACKGROUND	1
1.3 PASSIVE REMOTE SENSING	3
1.4 RESEARCH OBJECTIVES AND SIGNIFICANCE	6
1.5 THESIS OUTLINE	7
CHAPTER 2	10
2.1 OVERVIEW	10
2.2 THEORETICAL CONSIDERATIONS	10
2.2.1 Propagation of light through optically shallow waters	11
2.2.2 Assumptions	14
2.2.3 Relating AOPs to IOPs	14
2.2.4 Inherent Optical Properties	15
2.3 EMPIRICALLY DERIVING BATHYMETRY	17
2.3.1 Spectral Transformations	17
2.3.2 Artificial Neural Networks	20

2.3.3	Limitations	22
2.4	BENTHIC CLASSIFICATION	22
2.5	RADIATIVE TRANSFER BASED ALGORITHMS	29
2.5.1	Physics Based Inversion Models	30
2.5.2	Look up tables (LUT) methods	37
2.5.3	Inter comparison	42
2.6	UNCERTAINTY ESTIMATION AND FUTURE DIRECTIONS	44
2.7	SUMMARY	50
CHAPTER 3		52
3.1	ABSTRACT	52
3.2	INTRODUCTION	53
3.3	METHODOLOGY	56
3.3.1	Study area and HICO imagery	56
3.3.2	Atmospheric Correction	58
3.3.3	Retrieval of bathymetry using the BRUCE model	61
3.3.4	Smoothing techniques	64
3.3.5	Tide height correction of bathymetric products	65
3.3.6	Geo-registration	67
3.4	RESULTS AND DISCUSSION	68
3.4.1	Evaluation of Tafkaa-6S atmospheric correction	68
3.4.2	Bathymetry retrievals and smoothing techniques	70
3.4.3	Tide corrections	77
3.4.4	Geo-registration	83
3.4.5	Change detection	86
3.5	CONCLUSION	94
CHAPTER 4		97
4.1	ABSTRACT	97
4.2	INTRODUCTION	98
4.3	METHODS AND DATA	101
4.3.1	Shallow water model	101

4.3.2	Hyperspectral data	102
4.3.3	Optimisation and uncertainty propagation	106
4.3.4	Optimising initial guess	107
4.4	RESULTS AND DISCUSSION	110
4.4.1	Inverting measured hyperspectral data	110
4.4.2	Inverting simulated hyperspectral data	118
4.5	CONCLUSION	129
4.6	RECOMMENDATIONS	134
CHAPTER 5		135
5.1	ABSTRACT	135
5.2	INTRODUCTION	136
5.3	METHODOLOGY	138
5.3.1	Benthic reflectance library	139
5.3.2	Clustering	141
5.4	RESULTS AND DISCUSSION	147
5.4.1	Hierarchical clustering of benthic irradiance reflectance spectra	147
5.4.2	Water-column specific benthic spectral libraries	154
5.4.3	Resolving seagrass species from algae	161
5.4.4	Implications to shallow water habitat mapping	164
5.5	CONCLUSIONS AND FUTURE WORK	170
CHAPTER 6		173
6.1	CONCLUSIONS	173
6.2	FUTURE WORK AND RECOMMENDATIONS	176
APPENDIX A		180
APPENDIX B		191
APPENDIX C		201
APPENDIX D		213
APPENDIX E		222

APPENDIX F	230
REFERENCES	233

LIST OF FIGURES

- Figure 3.1: Shark Bay, Western Australia, with the Faure Sill located between the two curved black dotted lines. The solid black and dot-dot-dashed grey rectangles show the different approximate orientations of the HICO swaths. The dashed black rectangle illustrates the translational drift in the HICO swath position. 57
- Figure 3.2: pseudo true colour composites of the HICO-derived remote sensing reflectance imagery over Shark Bay, WA, on: (a) 19-Nov-2011; (b) 14-Dec-11; (c) 21-Jan-2012; (d) 07-Feb-12; (e) 27-Feb-12; (f) 02-Apr-12; (g) 01-Jun-12; (h) 04-Jun-12, and; (i) 08-Aug-12. The apparent illumination variation between these images is due to the different scaling used to generate the pseudo true colour composites. 58
- Figure 3.3: The 13 common ground control points used in the geo-registering of HICO imagery of Shark Bay, Western Australia, and the four test locations for geospatial consistency. The HICO image (19 Nov 2011) displayed has been geo-referenced with the geographic lookup table. 68
- Figure 3.4: The remote sensing reflectance of a quasi-deep water pixel (a), (25.718 °S/113.978 °E), and a shallow water pixel with a sandy bottom (c), (25.907 °S/113.934 °E), through time. (b) and (d) show the sun-glint corrected R_{rs} spectra of (a) and (c) respectively. Note that the wavelengths past 750-nm are not used in the inversion procedure and are not displayed in (b) and (d). 70
- Figure 3.5: Illustration of the three stage smoothing technique applied to HICO derived depth product of Shark Bay on 19 November 2011. Cross-sectional profiles at row number 1604 (top two panels) and at 1686 (bottom two panels). (a) and (c) contain: the raw depth (black dot-dash); impulse pixels (red triangles); depth product after impulse noise pixel removal (solid blue curve), and; the subsequent smoothed depth product. (b) and (d) are the uncertainty profiles of (a) and (c) respectively, and contain: the initial uncertainty (black dot-dash); pixels identified as outliers (red triangles), and; the final modified uncertainty product (pink). 72
- Figure 3.6: Relative uncertainty of the retrieved depth vs. pseudo SNR at 550 nm, obtained from HICO images of Shark Bay on (a) 14-Dec-11; (b) 02-Apr-12; (c) 04-Jun-12, and; (d) 08-Aug-12. Note: (1) vertical axes are displayed in logarithmic form; (2) 35 000 random data points, with depth > 0.3 m, were presented for each panel, and; (3) the summed spectral

variance, taken from the deep water region of the given HICO $r_{rs}^{deglinted}$ image are also presented. 74

Figure 3.7: Smoothed bathymetry images (before geo-referencing) derived from HICO imagery of the Shark Bay region, from 19-Nov-11 to 08-Aug-12. Note: for simplicity the bathymetry image of 02-Apr-12 is not displayed; black water pixels (e.g. 12-Jan-12 and 27-Feb-12) had $R_{rs}(750) > R_{rs}(400)$ and were not processed, and; blue and white represent shallow and deeper areas respectively. 76

Figure 3.8: Harmonic tidal analysis for a 3 day interval centred on the HICO overpass of 14 December 2011: (a) Time adjusted Carnarvon tide height data for Monkey Mia (+2:02 hrs - Black dots) and Hamelin Pool (-0:32 hrs - Grey dots) overlaid with the respective modelled tide curves using equation (3.8); (b) Modelled tide curves for Monkey Mia (Black line) and Hamelin Pool (Grey line). The triangles in (b) display the modelled water level height at the time of the HICO overpass at Monkey Mia and Hamelin Pool. 78

Figure 3.9: Predicted tide heights at Monkey Mia against the median depth of the shallow water pixels surrounding the northern section of Faure Island. The predicted tide heights were taken from Table 3.2, whilst the median shallow water depths were taken from HICO derived bathymetry prior to tide correction. The nine data points represent the nine HICO scenes. 80

Figure 3.10: (a) illustration of the empirical tide correction technique applied to the HICO dataset of Shark Bay. The horizontal black line represents the reference depth. Histograms of the depth of shallow water pixels (less than 3 m depth) before (b) and after tide correction (c). 83

Figure 3.11: Geo-spatial consistency of each HICO image of Shark Bay, relative to 19 November 2011, after (a) Geo-referencing using the provided GLT files, and (b) subsequent Geo-registration using the ground control points. NW-SE and SW-NE refers to the HICO swath orientation. 85

Figure 3.12: Cross-sectional depth profiles of the Faure Sill, at row 1686, taken from geo-registered HICO derived bathymetry images. The solid black line and grey envelope surrounding it represents the retrieved depth and its uncertainty respectively. Highlighted are two sets of deep water channels, A and B, located at column positions 950-1050 and 1280-1380 respectively. The depth of these channels show high temporal variability, the cause of which is discussed in the text. 88

Figure 3.13: Change detection analysis of HICO-derived, tide corrected bathymetry of the Faure Sill between the dates of: (a) 14-

Dec-2011 and 21-Jan-2012; (b) 21-Jan- and 27-Feb-2012; (c) 27-Feb- and 04-Jun-2012 and; (d) 04-Jun- and 08-Aug-2012. Deep-water and land are presented as dark and black pixels respectively. The blue and green circles in (b) and (c) highlight regions of change discussed in the text. Separate image-based tide corrections were performed for the dashed magenta presented in (a). 91

Figure 3.14: HICO derived pseudo true colour images of: the shallow water region parallel to the coast, north of the Wooramel River (top panels), and; the Faure Sill (bottom panels). The top panels show sediment flowing north from the Wooramel River, and through the seagrass channels orientated perpendicular to the coast, indicated by the red circle. The red square on 27-Feb-2012 highlights a plume of turbid water on the southern Faure Sill (bottom panel). 94

Figure 4.1: Map of Shark Bay, Western Australia, Australia, with HICO-derived R_{rs} pseudo true colour imagery captured on 14 December 2011. 104

Figure 4.2: Flow chart of the Latin Hypercube Sampling (left panel) and Update-Repeat LM optimisation (right panel) techniques. 108

Figure 4.3: (a) Tafkaa-6S atmospherically corrected and deglinted, noise-perturbed r_{rs} of pixels *A* (row 1082, col 317), *B* (row 1083, col 212), *C* (row 1031, col 210) and *D* (row 1200, col 445). Note that 3000 noise-perturbed r_{rs} spectra were generated and shown for each of these four HICO pixels. (b) The ‘noise-free’ simulated HICO r_{rs} dataset. 110

Figure 4.4: Retrieved BRUCE model parameters vs. retrieved depth for the 3000 noise perturbed r_{rs} spectra of HICO pixel *A* (row 1082, col 317) using SLM optimisation. The seed guess parameters were arbitrarily set. The red dot points are those retrievals whose inversion obtained a Euclidean distance $< 1.0 \times 10^{-4}$. 115

Figure 4.5: Retrieved BRUCE model parameters vs. retrieved depth for the 3000 noise perturbed r_{rs} spectra of the HICO pixel *A* (row 1082, col 317). The optimised guess values used to seed the LM optimisation were dynamically chosen using the UR-LM method shown as grey diamonds. 116

Figure 4.6: Retrieved BRUCE model parameters vs. retrieved depth for the 3000 noise perturbed r_{rs} spectra of the HICO pixel *A* (row 1082, col 317). The optimised guess values were dynamically chosen using the LHS method, shown as grey diamonds. 117

Figure 4.7: Inter-comparison between the SLM (left-hand panels), UR-LM (central panels) and LHS (right-hand panels)

optimisation of the noise-added simulated r_{rs} spectra using the BRUCE model. These graphs show the retrieved vs. actual model parameters for P , and G . Note: (1) the uncertainty in each retrieval (grey diamonds) are represented as error bars; (2) the dashed line in each graph represents the ideal 1:1 ratio between retrieved and actual. 125

Figure 4.8: Inter-comparison between the SLM, UR-LM and LHS optimisation of the noise-added simulated r_{rs} spectra using the BRUCE model. These graphs show the retrieved vs. actual model parameters for X , and H . 126

Figure 4.9: Inter-comparison between the SLM, UR-LM and LHS optimisation of the noise-added, simulated r_{rs} spectra using the BRUCE model. These graphs show the retrieved vs. actual model parameters for B_{sand} (top), $B_{seagrass}$ (middle), and B_{algae} (bottom). 127

Figure 4.10: Density plots of (a) $K_d(490\text{ nm})$ bias vs. depth bias; (b) B_{sand} bias vs. depth bias; (c) $B_{seagrass}$ vs. depth bias, and; (d) B_{algae} bias vs. depth bias. Each pixel in the density plot has a frequency of occurrence, represented by its colour. The left- and right-hand panels show the bias obtained using the SLM and LHS optimisation methods respectively. 128

Figure 4.11: Non-uniqueness – retrieved BRUCE model parameters vs. retrieved depth, for the 3000 noise perturbed r_{rs} spectra of quasi-deep HICO pixel at row 1107, column 226, Shark Bay 14-December-2011. The optimised guess values were dynamically chosen using the LHS method and are shown as grey diamonds. The red data points (Group 2) have negative B_{sand} and $B_{seagrass}$ that are not physically possible. 133

Figure 5.1: The average irradiance reflectance spectra of the benthos collected, convolved to the spectral resolutions of (a) HICO (b) HyMap and (c) WV2. 144

Figure 5.2: The LDHC algorithm using the basic bottom reflectances (flowchart A) and coupled with a shallow water forward model to include a water column (flowchart B). 146

Figure 5.3a: HDC dendrogram of ρ_b spectra using HICO's spectral bands. The iterative selection of eigenvectors chose the first six that produced 18 classes. 150

Figure 5.4: HDC dendrogram of ρ_b spectra using HyMap spectral bands. The iterative selection of eigenvectors chose the first seven that produced 18 classes. 152

- Figure 5.5: HDC dendrogram of ρ_b spectra using WV2's spectral bands. The iterative selection of eigenvectors chose the first four that produced 14 classes. 153
- Figure 5.6: Dendrogram from the LDHC of modelled r_{rs} spectra using HICO's spectral bands. The water column was modelled with depth 15 m and $P=0.05$, $G=0.1$ and $X=0.010 \text{ m}^{-1}$. Here the iterative selection of eigenvectors chose only one eigenvector. 156
- Figure 5.7: Number of optically separable classes vs. depth using the spectral bands and resolutions for (a) HICO; (b) HyMap, and; (c) WV2. Four water-columns were modelled with varying water turbidity representing very clear to turbid waters. The exponential curves were derived through a least squares fit. 157
- Figure 5.8: The estimated modelled depth (m) at which *A. antarctica* can no longer be distinguished from green algae at various clustering accuracies for (a) HICO; (b) HyMap, and; (c) WV2 wavebands. Clear (water type 1) to turbid (water type 4) water clarities were modelled. The depths given here are estimates as the clustering at every 0.25 m depth increment were analysed. 162
- Figure 5.9: Number of optically separable classes vs. depth at three different clustering accuracies using the spectral bands and resolutions for HICO. The water column was modelled with $P=0.05$, $G=0.1$ and $X=0.010 \text{ m}^{-1}$. 165
- Figure 5.10: LD coordinates of the four brown algae species using HICO wavebands. The HDC-derived dendrogram is shown on the top left corner. Here one eigenvector (z_1) allowed the optimal distinction of the following three clusters: (1) *S. linearifolium*/*S. spinuligerum*; (2) *E. radiata*, and (3) *C. sinuosa*. 168
- Figure A.1: Retrieved BRUCE model parameters vs. retrieved depth for the 3000 noise perturbed r_{rs} spectra of HICO pixel B (row 1083, col 212) using SLM optimization. The fixed guess model parameters were arbitrarily set. The red dot points are the retrieved values that converged onto the group with the lowest Euclidean distance. 181
- Figure A.2: Retrieved BRUCE model parameters vs. retrieved depth, for the 3000 noise perturbed r_{rs} spectra of the HICO pixel B (row 1083, col 212). The optimized guess values were dynamically chosen using the UR-LM method and are shown as grey diamonds. 182

- Figure A.3: Retrieved BRUCE model parameters vs. retrieved depth, for the 3000 noise perturbed r_{rs} spectra of the HICO pixel *B* (row 1083, col 212). The optimized guess values were dynamically chosen using the LHS method and are shown as grey diamonds. 183
- Figure A.4: Retrieved BRUCE model parameters vs. retrieved depth for the 3000 noise perturbed r_{rs} spectra of HICO pixel *C* (row 1031, col 210) using SLM optimization. The fixed guess model parameters were arbitrarily set. The red dot points are the retrieved values that converged onto the group with the lowest Euclidean distance. 184
- Figure A.5: Retrieved BRUCE model parameters vs. retrieved depth, for the 3000 noise perturbed r_{rs} spectra of the HICO pixel *C* (row 1031, col 210). The optimized guess values were dynamically chosen using the UR-LM method and are shown as grey diamonds. 185
- Figure A.6: Retrieved BRUCE model parameters vs. retrieved depth, for the 3000 noise perturbed r_{rs} spectra of the HICO pixel *C* (row 1031, col 210). The optimized guess values were dynamically chosen using the LHS method and are shown as grey diamonds. 186
- Figure A.7: Retrieved BRUCE model parameters vs. retrieved depth for the 3000 noise perturbed r_{rs} spectra of HICO pixel *D* (row 1200, col 445) using SLM optimization. The fixed guess model parameters were arbitrarily set. The red dot points are the retrieved values that converged onto the group with the lowest Euclidean distance. 187
- Figure A.8: Retrieved BRUCE model parameters vs. retrieved depth, for the 3000 noise perturbed r_{rs} spectra of the HICO pixel *D* (row 1200, col 445). The optimized guess values were dynamically chosen using the UR-LM method and are shown as grey diamonds. 188
- Figure A.9: Retrieved BRUCE model parameters vs. retrieved depth, for the 3000 noise perturbed r_{rs} spectra of the HICO pixel *D* (row 1200, col 445). The optimized guess values were dynamically chosen using the LHS method and are shown as grey diamonds. 189
- Figure A.10: The uncertainties of the BRUCE model parameters vs. number of noise-perturbed r_{rs} spectra for seven pixels selected from the HICO image of Shark Bay, 14 December 2011. Here the LHS implementation of the BRUCE model was used 190

- Figure B.1: Inter-comparison between the SLM (left-hand panels), UR-LM (central panels) and LHS (right-hand panels) optimization of the noise-added, simulated r_{rs} spectra using the BRUCE forward model. These graphs show the retrieved vs. actual model parameters for P and G . Here the lower bounds for the constrained LM optimization were set to zero. 196
- Figure B.2: Inter-comparison between the SLM, UR-LM and LHS optimization of the noise-added, simulated r_{rs} spectra using the BRUCE forward model. These graphs show the retrieved vs. actual model parameters for X and H . Here the lower bounds for the constrained LM optimization were set to zero. 197
- Figure B.3: Inter-comparison between the SLM, UR-LM and LHS optimization of the noise-added, simulated r_{rs} spectra using the BRUCE forward model. These graphs show the retrieved vs. actual model parameters for B_{sand} , $B_{seagrass}$, and B_{algae} . Here the lower bounds for the constrained LM optimization were set to zero. 198
- Figure B.4: Retrieved BRUCE model parameters vs. retrieved depth, for the 3000 noise perturbed r_{rs} spectra. Here the UR-LM method was used and the lower bounds for each model parameter were set to zero. 199
- Figure B.5: Retrieved BRUCE model parameters vs. retrieved depth, for the 3000 noise perturbed r_{rs} spectra. Here the UR-LM method was used and the lower bounds set to negative values. 200
- Figure C.1: (a) The measured benthic irradiance reflectance spectrum of *Possidonia* sp. convolved to HyMap wavelengths; (b) After the addition of sensor and environmental noise to each spectrum in (a). 201
- Figure C.2: An example of a LD plot generated from the HyMap ρ_b spectral library. Here each point represents an individual spectrum, where each class (a total of 22) has 2000 points. The colours of the LD points represent their genera, such that yellow, red, grey, light green and dark green represent sediment, red algae, brown algae, seagrass and green algae respectively. 203
- Figure C.3: The number of classes output from the LDHC vs. the cumulative proportional contribution of successive eigenvectors for different depths for a modelled water column. Here the IOPs were set to $P = 0.01 \text{ m}^{-1}$, $G = 0.01 \text{ m}^{-1}$ and $X = 0.001 \text{ m}^{-1}$. 205

Figure C.4: An example of two optically indistinguishable green algae classes, *C. germinata* (green dots) and *C. flexis* (green triangles) using LD coordinates. Here, the blue circle highlights the misclassified *C. germinata* point, and the larger green circle and triangle represent the position of the two class means. 207

Figure C.5: HDC Dendrogram of the ρ_b spectra using HyMap's spectral bands. The iterative selection of eigenvectors chose the first seven, and consequently produced 18 classes 208

Figure C.6: Effect of non-normality and unequal variance-covariance on the merging of red alga *A. anceps* (squares) and *H. ramentacea* (+) in LD space with WV2 bands. The group means are shown in bold along with the separating plane. (a) ρ_b spectra with no modelled water column, $\tau_m = 11.7\%$; (b) ρ_b with a modelled water column at 3 m depth and IOP type 1 ($P=0.01$, $G=0.01$, $X=0.001$), $\tau_m = 5.2\%$. The circle in (a) highlights the misclassified *A. anceps* spectra. 211

LIST OF TABLES

Table 1.1: Brief summaries of thesis chapters	9
Table 2.1: Benthic substrate classification methodology, number of classes and overall accuracy from a variety of imaging sensors in the literature. Note that in the Classification Method column, DII stands for Depth Invariant Indices from the method of Lyzenga (1981); MLC for Maximum Likelihood Classifier; SAM for Spectral Angle Mapper; UC for Unsupervised Classification; CE for Contextual Editing; DN for digital numbers.	25
Table 2.2: Comparison of pre-processing steps, parameterisations of shallow water models, optimisation cost functions for the HOPE, BRUCE, SAMBUCA inversion models and the ALLUT forward models as described in Dekker et al. (2011).	40
Table 2.3: A comparison between bathymetry retrievals and benthic classification accuracy of the different algorithms tested by Dekker et al. (2011). The RMSE in bathymetry between actual and derived are presented for Lee Stocking Island (LSI) and Moreton Bay (MN) respectively. The classification accuracy was only assessed in MB between 0-3 m.....	42
Table 3.1: MODIS-derived vertical column of water vapour (CLMVAP), aerosol optical thickness at 550 nm (AOT) and ozone concentration, with the solar-viewing geometries for each HICO overpass of Shark Bay, WA. The time presented is Australian Western Standard Time (WST; UTC +8 hours). Here θ_w , θ_v and ϕ_r are the solar zenith, viewing zenith and relative azimuth angles respectively.	60
Table 3.2: Modelled tide heights (cm), above LAT, during each HICO overpass time for Monkey Mia, Hamelin Pool and the Faure Sill. Also present are the: standard deviation and range of these tide heights, and , correlation coefficients of the tide height curves used to extract the M_2 , S_2 , K_1 , and O_1 tide constituent phases from the time adjusted Carnarvon data. .	79
Table 3.3: The mean depth of the shallow water pixels, $\langle H(t) \rangle$, for each HICO derived bathymetry image. The standard error in the means (SEM) of the uncorrected, image based and harmonic tide correction techniques are also present.....	81
Table 4.1: The set of input model parameters used to generate the 4375 simulated HICO r_{rs} spectra via forward modelling. A view angle of 6.3° from nadir and a solar zenith angle of 45° were used.....	105

Table 4.2: A comparison between the mean and relative standard deviations of the retrieved model parameters, average Euclidean distance and total number of iterations obtained from the SLM, UR-LM and LHS implementation of the BRUCE model. Presented are the retrieved model parameters from the four pixels in the HICO image of Shark Bay, 14 th December 2011.	114
Table 4.3: An inter-comparison of the RMSE (scatter), percent accuracy, average relative uncertainty and average retrieved value for each BRUCE model parameter between the three optimisation approaches. Recall that 100% accuracy is ideal as all the retrievals would be with 1% of the input model parameter.	120
Table 5.1: List of the benthic species collected from the Point Peron study site.	140
Table 5.2: The classes from the HICO spectral libraries at depths 3-6 m using water column optical properties of $P = 0.01 \text{ m}^{-1}$, $G = 0.01 \text{ m}^{-1}$, and $X = 0.001 \text{ m}^{-1}$. The superscripts represent the number of species that form that cluster, for example mixed brown algae ⁴ means that four brown algae species were merged to form one mixed brown algae class. The spectral libraries at 5 and 6 m depth are identical.	158
Table 5.3: The classes from the HyMap spectral libraries at depths 3-6 m using water column optical properties of $P = 0.01 \text{ m}^{-1}$, $G = 0.01 \text{ m}^{-1}$, and $X = 0.001 \text{ m}^{-1}$	159
Table B.1: An inter-comparison of the RMSE (scatter), percent accuracy and average relative uncertainty for each BRUCE model parameter between the three optimization approaches. Here, the lower bounds of each model parameter were set to zero.	193
Table B.2: Comparison between the inversions (using the UR-LM optimization) that had the lower bounds set to zero and negative values. Here, inversions that had a retrieved value equal to the lower bound were not included in the calculation of the average retrieved value and standard error (uncertainty).	195

CHAPTER 1

GENERAL INTRODUCTION

1.1 Overview

This thesis examines the inherent uncertainty present in the remotely sensed products of bathymetry and benthic classification derived from hyperspectral imagery of shallow water environments. The main aim is to utilise knowledge of the uncertainty to ascertain the potential and limitations of bathymetry and benthic classification, that is, what is possible and what is not, for environmental monitoring. Outcomes as a result of this research may lead to an improved understanding of what optical remote sensing can offer with regard to these two important products and may help assess whether other methods are needed to meet the outcomes of the user. This chapter provides a general overview of the importance of bathymetry and benthic classification to environmental monitoring and remote sensing techniques that can aid in the monitoring. The thesis aims, significance and outline are also presented.

1.2 Background

Coastal and coral reef ecosystems exert a major influence on a nation's social well-being and economy through recreational activities and by providing important commercial valuables (Costanza et al., 1997; Moberg & Folke, 1999). However, the ever increasing human-induced impact of over-fishing, spread of marine diseases, coastal development and influx of pollution from land-based activities can alter and even destroy these fragile and rapidly declining ecosystems (Fabricius, 2005; Aronson & Pretch, 2006; Halpern et al., 2008). Due to their sensitivity to disturbances and importance to human activities, conservation and sustainable resource development has being identified as a key outcome for improved management plans (Obura & Grimsditch, 2009). In this context conservation arises first through an inventory of the resources present and subsequent monitoring of changes (Nichols & Williams, 2006). Accurate monitoring, or at least an understanding of the accuracy of monitoring, is therefore crucial for the development of effective management plans that provide

trade-offs between human uses, protection of these ecosystems and the services that they provide (Halpern et al., 2008).

Marine benthic Habitat Maps (MHMs) are spatial distribution datasets describing the habitat conditions that include bathymetry, water currents, sea bed morphology and substratum and benthic biota of a local or regional ecosystem. MHMs are utilised in research and managerial fields such as in habitat diversity assessments (Conroy & Noon, 1996; Gray, 1997; Barbera et al., 2012) and ecosystem-based management (Cendrero, 1989; Diaz, Solan, & Valente, 2004; Cogan, Todd, Lawton, & Noji, 2009). Temporal monitoring using MHMs allows ecosystem managers to determine the natural seasonal variation in structure and composition of a given ecosystem (Cogan et al., 2009). This can delineate changes caused by natural and human disturbances and can aid in the selection of appropriate recommendations and actions by managers (Cogan et al., 2009). Alternatively, MHMs can be used as a tool to provide advice on the sustainable management of these ecosystems (Bax & Williams, 2001), or the development of Marine Protected Areas (Ward, Vanderkleft, Nicholls, & Kenchington, 1999; Roff & Taylor, 2000; Roff, Taylor, & Laughren, 2003; Dalleau et al., 2010). As such, the need for accurate and precise MHMs of coastal and coral reef environments, or at least an understanding of their accuracy and precision, is paramount for their management, conservation and sustainable use.

Traditionally, aerial photography and diver surveys were methods used to derive MHMs. Diver surveys, although very accurate, can only provide information either at very specific locations (point data) or at most, transect data. Aerial photography on the other hand can be used to produce maps of much larger areas but requires trained interpreters to identify features such as vegetation beds or reef systems which are classified according to human interpretation of their edge smoothness, size and colour (e.g. Larkum & West, 1990; Remillard and Welch, 1992; Sotheran, Foster-Smith, & Davis, 1997). The latter method is limited by: (a) the experience of the observer, and as such is subjective; (b) the excessive amount of time it takes an observer to classify an image "by eye", and; (c) the qualitative nature of the maps. In the last 30 years, these mapping techniques have evolved to utilise digitised aerial photographs and satellite imagery coupled with a type of computerised classification that includes supervised and unsupervised classification (e.g. Sotheran et al., 1997; Pasqualini, Pergent-Martini, Clabaut, & Pergent, 1998; Pasqualini et al., 2005; Fornes

et al., 2006), advanced image segmentation techniques (e.g. Kendrick et al., 2002), and; others such as neural networks (e.g. Calvo, Ciraolo, & Loggia, 2003). The limiting factors of these modern photography techniques are: (1) the need of a training dataset, which usually comprises some type of *in situ* data; (2) the subjective nature of class definition in unsupervised classification, and; (3) the in-ability to estimate the proportion of cover of each benthic substratum - particularly important, for instance, if a mixture of benthic vegetation and sand are present.

1.3 Passive Remote Sensing

Passive remote sensing is the act of measuring the radiant flux reflected or emitted by an object over a selected set of wavelengths. For remote sensing of the coastal ocean, spectral bands are typically in the visible to near-infrared (NIR) portion of the electromagnetic spectrum (Sathyendranath et al., 2000) and reflectance is the primary mechanism giving rise to the photons collected by the instrument. In the context of shallow water environments the “colour” of spectral radiance leaving the water’s surface is directly affected by the absorptive and scattering properties of the water column, the depth and the bottom substrate (Mobley, 1994) which modulate the incident solar irradiance into the “colour” observed. Hence measuring the spectral radiance using passive space-borne or airborne imaging sensors can offer a quantitative and efficient approach for mapping water column optical properties and bottom substrate properties. The development of remote sensing tools for ocean colour and that of bathymetry and benthic classification has followed different research objectives. Many of the differences in these approaches relate to the treatment of the water column effects; which for benthic classification are considered an impeding factor and research into their removal from the signal measured by a sensor has been extensive (Zoffoli, Frouin, & Kampel, 2014); for bathymetry the complex interactions between the water depth and water optical properties have resulted in mainly empirical algorithms; for ocean colour, the signal from the water column conveys information on the abundances of the major optically active constituents (the primary objective). These differences in objectives have thus resulted in the development of different empirical algorithms that may rely on different bio-optical assumptions.

Ocean colour remote sensing has traditionally assumed that in the open ocean the spatial variability of the measured spectral radiance arises from variations in

phytoplankton pigment (mostly by Chlorophyll *a*) concentration, i.e. case 1 waters (Morel & Prieur, 1977; Morel, 1988). In addition the concentrations of other optically active in-water constituents such as coloured dissolved organic matter (CDOM) and suspended particulate matter (SPM) are assumed to be negligible or correlated with this pigment concentration (Morel, 1988; Sathyendranath et al., 2000). As a consequence of this simplified view, open ocean bio-optical algorithms typically used empirically tuned radiance ratios to compute the Chlorophyll *a* concentrations and diffuse attenuation coefficients (O'Reilly et al., 2000; Mueller, 2000). Under these bio-optical assumptions (applicable to limited oceanic conditions) the number of spectral bands utilised by passive satellite sensors such as the Coastal Zone Color Scanner (CZCS), Sea-viewing Wide Field-of-view Sensor (SeaWiFS) and the MODerate Resolution Imaging Spectroradiometer (MODIS) were adequate to retrieve chlorophyll-*a*, CDOM and SPM (McClain, Hooker, Feldman, & Bontempi, 2006).

In contrast, the shallow water marine environment is perhaps the most complex of ecosystems with regards to the physical processes that influence the propagation of light from the target to sensor. Here the depth, bottom substrate and the concentrations of phytoplankton pigments, CDOM and SPM influence the water leaving radiance (Maritorena, Morel, & Gentili, 1994; Lee et al., 1994; Lee, Carder, Mobley, Steward, & Patch, 1998). In addition, the concentrations of the optically active in-water constituents are not necessarily correlated (Sathyendranath et al., 2000; Siegel, Maritorena, Nelson, Behrenfeld, & McClain, 2005) and where CDOM, SPM and the bottom reflectance can greatly influence the water leaving radiance (Carder et al., 1991). As such the simplified bio-optic assumptions used for open ocean, case 1 waters are typically not transferable to coastal shallow waters (Carder et al., 1991), where more spectral information is needed to separate the different constituents (McClain et al., 2006).

A hyperspectral sensor measures the radiant flux across a large number of spectral bands each having narrow bandwidths (typically less than 10 nm). Given a high enough signal-to-noise ratio (SNR) a hyperspectral sensor is able to detect subtle changes in the radiant flux due to changes in the water column optical properties, depth and bottom type (Philpot et al., 2003). Lee et al. (1998) developed a semi-analytical model specifically for coastal shallow waters that delineates the impact each component has on the water leaving radiance. Further, by making assumptions on the

spectral shape of each component (excluding the depth) and by reducing the number of unknowns to solve; Lee, Carder, Mobley, Steward, and Patch (1999) were able to simultaneously retrieve the absorption by phytoplankton and by CDOM; backscattering by SPM, the depth and albedo from a single substrate solely from the reflectance derived by a hyperspectral sensor. This method of inverting the reflectance has led to the development of other physics-based inversion models that incorporate mixtures of bottom substrates (Klonowski, Fearn, & Lynch, 2007; Hedley, Roelfsema, & Phinn, 2009) and additional in-water constituents (Brando et al., 2009).

The advantage of these shallow water inversion models is the potential of mapping the abundances of phytoplankton, CDOM, SPM, depth and benthic classification from airborne and satellite hyperspectral imagery (Lee, Carder, Chen, & Peacock, 2001; Lee et al., 2007; Klonowski et al., 2007; Brando et al., 2009; Hedley et al., 2009). As such, remote sensing techniques can offer the potential to monitor water quality, changes in bathymetry and bottom substrate through time and space. Empirical models can be used to relate the water column properties to meaningful geophysical parameters. For instance the chlorophyll concentration can be computed from the absorption of phytoplankton (Prieur & Sathyendranath, 1981), while the backscattering of suspended matter can be used to calculate SPM (Babin, Morel, Fournier-Sicre, Fell, & Stramski, 2003a; Volpe, Silvestri, & Marani, 2010). Inversion models however are typically applied to hyperspectral image data as they require the number of spectral bands to exceed the number of model parameters. Despite extensive research into new inversion models and their applicability (see Dekker et al., 2011) there has been very little analysis of the uncertainty of the results (with exceptions see Hedley, Roelfsema, & Phinn, 2010; Hedley, Roelfsema, Koetz, & Phinn, 2012a).

Physics-based inversion models rely on the apparent optical property (AOP) of subsurface remote sensing reflectance, r_{rs} . Satellite and airborne sensors however measure the at-sensor radiance. Several radiometric corrections are therefore needed to convert at-sensor radiance to r_{rs} , the process of which can introduce varying magnitudes of uncertainty and spectral artefacts. In addition to inherent sensor noise, the combined radiometric uncertainty (termed sensor and environmental noise) can negatively impact the accuracy of outputs from physics-based inversion models, potentially limiting their use for subsequent ecological interpretations or temporal analysis. For example high uncertainties in benthic classification are unsuitable to establish baseline data and subsequent temporal monitoring to delineate changes from

natural and human induced changes – particularly as management decisions are based on statistical significance (Fairweather, 1991; Kirkman, 1996). As such, quantifying the uncertainty of these geophysical products can aid in quantifying the limitations and potential of shallow water remote sensing tools.

1.4 Research Objectives and Significance

The inherent uncertainty present in remote sensing derived inversion products such as bathymetry and benthic classification affects their confidence for any subsequent ecological interpretations. The overall theme of this thesis is to quantify the uncertainty and use it to explore the potential and limitation of bathymetry and benthic classification from a physics based optical reflectance model. The three general aims that are explored within individual self-contained chapters are to:

1. Propagate uncertainty through an inversion model and to analyse the uncertainty associated with bathymetry derived from spaceborne hyperspectral data in an effort to detect statistical significant temporal changes in depth;
2. Test the accuracy and precision of inversion model parameters from the standard implementation of the Levenberg-Marquardt (LM) optimisation algorithm, and to develop new approaches that provide improved results for bathymetry and benthic classification;
3. To quantify the number and type of optically distinguishable benthic species above the total system noise and attenuating properties of a variable water column in an effort to quantify the potential of benthic classification from optical remote sensing.

Modelling based sensitivity analysis to assess the impact the water column IOPs, depth and the sensor's SNR on benthic class separability have been performed to understand the effectiveness of optical remote sensing for mapping coastal and coral reef ecosystems (e.g. Lubin, Dustan, Mazel, & Stammes, 2001; Hochberg, Atkinson, & Andrefouet, 2003; Vahtmae, Kutser, Martin, & Kotta, 2006; Kutser, Vahtmae, & Martin, 2006; Hedley, Roelfsema, Phinn, & Mumby, 2012b). However, with the exception of Hedley et al. (2010) and Hedley et al. (2012a) the impact of sensor and environmental noise on parameters derived from physics-based inversion models (that include benthic classification) has not been explored in great detail and has not been

extended to assess and quantify the potential of these products for ecological interpretations. This research presents new tools that aid such an assessment for bathymetry and benthic classification derived from physics-based inversion models. Furthermore new optimisation algorithms that give improved accuracies and precision of inversion model parameters are presented to maximise the potential of optical remote sensing. The following lists the outcomes and significance of this research:

1. The development of a per-pixel statistical procedure to assess temporal changes in depth. This procedure can be extended to other parameters, such as water column optical properties, to highlight regions where temporal changes can or cannot be inferred.
2. The development of an image-based tide normalisation procedure that can be used to remove the tidal influences from a time series of remotely sensed bathymetry. The advantage of this technique is that tide normalisation can be performed in the absence of reliable tide data. Such a methodology can be used to determine changes in depth (above uncertainty) that are due to bottom sediment resuspension, transportation and deposition;
3. The development of two LM based optimisation algorithms that maximise the accuracy, precision and computational efficiency of parameters when sensor and environmental noise is propagated through the inversion model. Such optimisation techniques can be extended to operational ocean colour inversion models, and;
4. The development of a clustering algorithm that models the number and type of benthic classes that can be optically distinguished *a priori*. This clustering methodology can aid in analysing the potential of optical remote sensing to benthic classification – particularly when considering the matching of deliverables with expectations. Such an analysis can determine if alternative benthic classification methods should be investigated.

1.5 Thesis Outline

This thesis comprises six chapters; a summary of each chapter is displayed in Table 1.1. Chapters 3, 4 and 5 are published manuscripts in peer-reviewed journals –

as described in Table 1.1. Firstly, Chapter 2 presents a literature critique of the theory and practice relevant to this research, with focus on remote sensing inversion algorithms and alternative image-based methods of bathymetry and benthic classification. Chapter 3 presents an analysis of the propagation of sensor and environmental noise through a physics-based inversion model to derive bathymetric imagery and its uncertainty from nine HICO images of Shark Bay, Western Australia, spanning 10 months. The aim was to determine if the bathymetry retrievals were precise enough to detect seasonal variability unrelated to tidal variations. With the aid of the uncertainty, a per-pixel statistical procedure was developed to explore the optical conditions that allowed or prohibited temporal changes in depth to be made.

The accuracy and precision of bathymetry and benthic classification derived from physics-based inversion models are in-part affected by the optimisation algorithm used. Chapter 4 illustrates the effect the standard implementation of the LM algorithm has on the accuracy and precision of the retrievals and the overall computational efficiency when propagating sensor and environmental noise. In this chapter, two new optimisation algorithms based on the LM are proposed and are shown to improve accuracy, precision and efficiency. Chapter 5 explores the effect total system noise – which includes sensor and environmental noise and the spectral variability within benthic substrates – and the attenuating properties of a water column have on the optical separability of a set of benthic spectral endmembers. A new clustering procedure is proposed that predicts the number and type of benthic classes that are optically separable for a given set of water column optical properties, depth and the total system noise. An analysis is also performed to explore the conditions (sensor spectral resolution, clustering accuracy, depth, water column optical properties) that enable the optical distinction between seagrass and benthic algae. Finally, the research conclusions, implications and future avenues of investigation are presented in Chapter 6.

Table 1.1: Brief summaries of thesis chapters

Chapter	Title	Summary
1	Introduction	General introduction to this research and its potential application for coastal and coral reef ecosystem monitoring.
2	Literature Review	A comprehensive literature review and critique of shallow water remote sensing and uncertainty propagation.
3	Challenges in detecting trend and seasonal changes in bathymetry derived from HICO imagery: A case study of Shark Bay, Western Australia	Explores the effect sensor and environmental noise has on bathymetry products and whether it is precise enough for temporal analysis. <i>Published in: Remote Sensing of Environment, 2014, Vol. 147, p. 186-205.</i>
4	Improving the optimisation solution for a semi-analytical shallow water inversion model in the presence of spectral noise	Explores the effect the optimisation algorithm has on the accuracy and precision of the retrieved products, and proposes two new optimisation algorithms. <i>Published in: Limnology and Oceanography: Methods, 2014, Vol. 12, p. 651-669.</i>
5	A method to analyse the potential of optical remote sensing for benthic habitat mapping	A new clustering method is proposed that determines the number and type of benthic classes that are optically distinct above total system noise for any given water column. <i>Published in: Remote Sensing, 2015, Vol. 7, Issue 10, pp. 13157-13189.</i>
6	Conclusion and Future work	A concise discussion on the important findings, and recommendations for future research

CHAPTER 2

LITERATURE REVIEW

2.1 Overview

This chapter begins with an overview of the key principles of passive remote sensing and the propagation of light in optically shallow water. This is followed by a literature critique of algorithms available to derive bathymetry and benthic classification from remote sensing. For bathymetry these include empirical algorithms trained by *in situ* depth, while for benthic classification, thematic mapping techniques are discussed. Physics based inversion models and look up table methods that are capable of the simultaneous retrieval of water column optical properties, bathymetry and benthic classification from hyperspectral imagery are also reviewed. Finally, methods of estimating the uncertainty from remotely sensed products and how it can be used to understand their limitations are presented.

2.2 Theoretical considerations

This section derives the equation for surface upwelling irradiance using the single scattering approximation. Here the propagation of light through an optically shallow water column with a substrate having an albedo is also described. The upwelling and downwelling hemispherical cosine irradiance, E_u and E_d respectively, are used extensively here and are defined as the radiant flux incident on a surface per unit area (W m^{-2}). The irradiance reflectance (unit-less) is defined as,

$$R = \frac{E_u}{E_d} \quad (2.1)$$

The water-leaving radiance ($\text{W m}^{-2} \text{sr}^{-1}$), L_u , defined as the upwelling radiance just above the water's surface is used to obtain the remote sensing reflectance, R_{rs} ,

$$R_{rs} = \frac{L_u}{E_d}, \text{ per steradian (sr}^{-1}\text{)} \quad (2.2)$$

R_{rs} essentially describes the irradiance reflectance just above the sea surface per unit solid angle. The subsurface remote sensing reflectance, r_{rs} , is the irradiance reflectance just beneath the water's surface per unit solid angle.

$$r_{rs} = \frac{L_u(0-)}{E_d(0-)}, \text{ per steradian (sr}^{-1}\text{)} \quad (2.3)$$

2.2.1 Propagation of light through optically shallow waters

The interaction of radiation with matter as it propagates through the water column in optically shallow waters is described. We limit this description to radiation in the visible portion of the electromagnetic spectrum (400-750 nm) and in situations where radiation reflected from the sea bottom (referred to as substrate) is detectable by a sensor. Under these conditions the downwelling and upwelling irradiance in the water column is scattered and absorbed by water molecules, suspended algal and non-algal particulates and coloured dissolved organic matter CDOM (Gordon, Smith, & Zaneveld, 1980). Molecular fluorescence (inelastic scattering of light) caused by algal pigments or from CDOM is not considered here. For optically shallow waters, according to the single scattering assumption, the total upwelling irradiance just below the water surface (at depth 0- meters) is the sum of the irradiance backscattered by the water column, E_u^C , and the irradiance from the bottom substrate, E_u^B ,

$$E_u(0-) = E_u^C(0-) + E_u^B(0-) \quad (2.4)$$

We begin with the derivation of E_u^C . At a given wavelength and solar angle, the downwelling irradiance incident on an infinitesimally thin water column layer dz at depth z is given by (Gordon, 1989; Zaneveld, 1989),

$$E_d(z) = E_d(0-) \exp\left\{-\int_0^z K_d(z) dz\right\} \quad (2.5a)$$

$$E_d(z) \approx E_d(0-) \exp\{-\overline{K_d}z\} \quad (2.5b)$$

$E_d(0-)$ and $E_d(z)$ are the downwelling solar irradiances just below the water's surface and at depth z respectively. $\overline{K_d}$ is the averaged downwelling diffuse attenuation coefficient describing the average rate of decay of $E_d(0-)$ per unit length between the water's surface and z . K_d is an apparent optical property (AOP) whose values vary with the solar geometry (Gordon, 1989) and is also depth dependent even in vertically homogeneous water columns (Zaneveld, 1989). At the dz layer a portion of $E_d(z)$ is scattered back towards the water surface. This portion is governed by the diffuse

backscattering coefficient of downwelling light, b_{bd} (Philpot, 1987; Kirk, 1989; Maritorena et al., 1994),

$$dE_u^C(z) = b_{bd}E_d(z)dz \quad (2.6)$$

where $dE_u^C(z)$ is the upwelling irradiance created by the dz layer, which is then attenuated as it propagates towards the water surface,

$$dE_u^C(0-) = dE_u^C(z) \exp\{-\overline{K_u^C}z\} \quad (2.7)$$

$\overline{K_u^C}$ is the averaged upwelling diffuse attenuation coefficient from depth z to 0 m. Substitution of 2.5b and 2.6 into 2.7 yields the contribution of $dE_u^C(0-)$ to the total $E_u^C(0-)$ from the dz layer at depth z (Kirk, 1989),

$$dE_u^C(0-) \approx b_{bd}E_d(0-) \exp\{-(\overline{K_u^C} + \overline{K_d})z\} dz \quad (2.8)$$

Integrating over all infinitesimally small layers from depth z to just beneath the water surface gives (Philpot, 1987; Maritorena et al., 1994),

$$dE_u^C(0-, z) \approx \frac{b_{bd}}{\overline{K_u^C} + \overline{K_d}} E_d(0-) \{1 - \exp[-(\overline{K_u^C} + \overline{K_d})z]\} \quad (2.9)$$

To simplify this equation further, the irradiance reflectance of an infinitely deep water column – derived by integrating equation 2.8 from 0 m depth to infinity – is defined as (Philpot, 1987; Kirk, 1989),

$$R^{dp} = \frac{b_{bd}}{\overline{K_u^C} + \overline{K_d}} \quad (2.10)$$

and thus the first term in equation 2.9 can be substituted as R^{dp} to give,

$$E_u^C(0-, z) \approx R^{dp} E_d(0-) \{1 - \exp[-(\overline{K_u^C} + \overline{K_d})z]\} \quad (2.11)$$

Deriving the bottom contribution of the upwelling radiant flux, $E_u^B(0-)$, first begins by assuming that the bottom substrate is a Lambertian reflector with a wavelength dependent albedo of ρ , located at depth z . The reflected flux transmitted through the water column to a depth of 0 m is given by (Maritorena et al., 1994),

$$E_u^B(0-) \approx \rho E_d(0-) \exp\{-(\overline{K_d} + \overline{K_u^B})z\} \quad (2.12)$$

where $\overline{K_u^B}$ is the average upwelling diffuse attenuation for bottom reflected light. Summing equations 2.11 with 2.12 yields the total upwelling irradiance of optically shallow water columns,

$$E_u(0-, z) \approx R^{dp} E_d(0-) \{1 - \exp[-(\overline{K_d} + \overline{K_u^C})z]\} + \rho E_d(0-) \exp\{-(\overline{K_d} + \overline{K_u^B})z\} \quad (2.13)$$

A more useful AOP that a remote sensing radiometer can derive is irradiance reflectance, which is obtained by dividing equation 2.13 by $E_d(0-)$ (Maritorena et al., 1994) to give,

$$R(0-) \approx R^{\text{dp}}\{1 - \exp[-(\overline{K_d} + \overline{K_u^C})z]\} + \rho \exp\{-(\overline{K_d} + \overline{K_u^B})z\} \quad (2.14)$$

or alternatively subsurface remote sensing reflectance which is obtained by dividing equation 2.14 by π steradians – assuming a Lambertian upwelling radiance distribution.

$$r_{\text{rs}} \approx r_{\text{rs}}^{\text{dp}}\{1 - \exp[-(\overline{K_d} + \overline{K_u^C})z]\} + \frac{\rho}{\pi} \exp\{-(\overline{K_d} + \overline{K_u^B})z\} \quad (2.15)$$

Division by $E_d(0-)$ also serves to partially normalise any variations in solar illumination conditions caused from varying sky and atmospheric conditions. For above water radiometers $R(0-)$ will need to be propagated through the air-water interface. This can be performed by accounting for the transmission and internal reflection of light at the water-to-air interface (Lee et al., 1998; 1999),

$$R_{\text{rs}}(\lambda) = \frac{\xi r_{\text{rs}}}{1 - \Gamma r_{\text{rs}}} \quad (2.16)$$

here ξ is a coefficient that accounts for the transmittance of both upwelling (water-to-air) and downwelling (air-to-water) light, whilst the proportion of upwelling light that undergoes internal reflection at the water-to-air interface is taken into consideration by the denominator, $1 - \Gamma r_{\text{rs}}$. Both ξ and Γ vary with sensor view angles, however at nadir they can be approximated to values of 0.5 and 1.5 respectively (Lee et al., 1999).

It should be noted that $\overline{K_u^C} > \overline{K_d}$ primarily because of the angular distribution of E_u^C where it is biased towards small angles from the horizontal – a property caused by the angular dependent phase function of water and suspended particles (Kirk, 1987). Due to these shallow angles, backscattered photons travel further along the horizontal axis than the vertical before they are absorbed, and as such undergo higher attenuation with respect to the vertical axis than downwelling photons (Kirk, 1987). The isotropic angular distribution of bottom reflected light also governs its rate of attenuation, where $\overline{K_u^C} > \overline{K_u^B} > \overline{K_d}$, a consequence of assuming the substrate as a lambertian reflector. $\overline{K_u^C} > \overline{K_u^B}$ arises from the fact that the angular distribution of bottom reflected light does not have horizontal biases and are less attenuated vertically than the backscattered flux (Maritorena et al., 1994).

2.2.2 Assumptions

The derivation of equation 2.15 uses depth averaged diffuse attenuation coefficients. For Case 1 waters Gordon (1989) showed that using $\overline{K_d}$ satisfied the Beer-Lambert law to within 5-10% for wavelengths between 440-550 nm. These accuracies can be transferred to case-2 waters, however the Beer-Lambert law will fail in situations when: (1) the angular distribution of the under-water light field is independent of the diffuse attenuation coefficient; (2) the water column is dominated by non-absorbing particles (that cause high scatter) that do not simultaneously occur with high concentrations of other light absorbing matter such as CDOM, and; (3) the phase functions of suspended matter in the water column are not significantly different from pure seawater (Gordon 1989).

Equation 2.15 was also derived with a single scattering assumption where only one scattering term (b_{bd}) is included. Here, it is assumed that downwelling photons are absorbed as they traverse downwards until a single scattering event occurs at a given depth that produces $dE_u^C(z)$. Absorption is now assumed the only physical process affecting the attenuation of the backscattered light as it travels upwards (Philpot, 1987). Thus, forward scattering of downwelling and upwelling light is not considered nor is the backscattering of upwelling light. However as equation 2.15 was derived using irradiances (as opposed to radiances), according to Philpot (1987) “multiple scattering events are included implicitly” and would reduce errors associated with this assumption.

The bottom substrate is very rarely Lambertian and typically has a bi-directional distribution function (BRDF) where the reflected upwelling radiance is dependent on the view and solar angular geometry. Mobley, Zhang and Voss (2003) showed that deviations of at most 10% occur for upwelling radiance when assuming isotropic reflectance rather than a BRDF for solar and view angles most widely encountered in remote sensing. Indeed the BRDF of seagrasses for instance can be relatively uniform away from the solar hotspot (Hedley & Enriquez, 2010).

2.2.3 Relating AOPs to IOPs

Up to this point equation 2.15 relates the AOP of reflectance to the AOPs of upwelling and downwelling diffuse attenuation coefficients. As the inherent optical properties (IOPs) of the water column are important to a fundamental understanding of the biogeophysical processes it is essential to relate $K_u^{C,B}$ and K_d to the IOPs of

absorption, a , and backscattering, b_b . For quasi-single scattering theory, the attenuation coefficient, κ , is given by,

$$\kappa(z) = a(z) + b_b(z) \quad (2.17)$$

$\kappa(z)$ is solely dependent on depth and not on the angular distribution of the incident radiant flux. Intuitively it may seem that there is a direct, proportional relationship between κ and $K_u^{C,B}$ and K_d in which the angular distribution of the incident light field is taken into account. For quasi-single scattering theory, the vertical diffuse attenuation coefficient can be related to κ by (Gordon et al., 1980, p.41),

$$K_x = D_x \kappa \quad (2.18)$$

where D_x is known as the distribution function and is defined as the ratio between the scalar irradiance to the cosine irradiance and hence is the reciprocal of the average cosine of the zenith of the radiant flux (Preisendorfer, 1976). In other words D_x describes the average path length of photons propagating through a water layer dz at a given angle (Philpot, 1987). Equation 2.18 can be applied to the three diffuse attenuation coefficients given in equation 2.15 to give (Lee et al., 1998),

$$r_{rs} \approx r_{rs}^{dp} \{1 - \exp[-(D_d + D_u^C)\kappa z]\} + \frac{\rho}{\pi} \exp\{-(D_d + D_u^B)\kappa z\} \quad (2.19)$$

Equation 2.19 can therefore be used to model r_{rs} for a given a and b_b , or alternatively to invert the modelled r_{rs} to solve for the absorption and backscattering coefficients of the water column. Inversion methods are discussed later in section 2.5.1.

2.2.4 Inherent Optical Properties

2.2.4.1 Modelling the absorption

The spectral absorption coefficient of light in seawater is the fraction of the radiant flux absorbed per unit distance traversed in the medium (Gordon et al., 1980), and is the cumulative sum of the different absorptive constituents in the water column. These being the water molecules, CDOM and suspended algal and non-algal particulates, including phytoplankton pigments, and detritus and inorganic particulates (Prieur & Sathyendranath, 1981),

$$a(\lambda) = a_w(\lambda) + a_{phy}(\lambda) + a_{CDOM}(\lambda) + a_{NAP}(\lambda) \quad (2.20)$$

the subscripts w, phy and NAP stand for water, phytoplankton pigments and non-algal particulates respectively. The magnitude of absorption of each component, a_x , is determined by its concentration, C_x , and the specific absorption coefficient, a_x' , such that $a_x = C_x a_x'$. Here, a_x' has units of per metre per unit concentration (Morel &

Bricaud, 1981). Alternatively the absorption can be modelled by the absorption coefficient at a specific wavelength multiplied by its normalised spectral absorption coefficient (Prieur & Sathyendranath, 1981). We follow the latter parameterisation, such that, $a_x(\lambda) = a_x(440\text{nm}) \times a_x^*(\lambda)$, where a_x^* is the absorption coefficients normalised to a value of 1.0 at 440 nm (Prieur & Sathyendranath, 1981).

The absorption of CDOM can be modelled using a decaying exponential curve of the form (Bricaud, Morel, & Prieur, 1981),

$$a_{\text{CDOM}}(\lambda) = a_{\text{CDOM}}(440) \exp\{-S_{\text{CDOM}}(\lambda - 440)\} \quad (2.21)$$

The spectral slope, S_{CDOM} , has been shown to typically vary between 0.010 – 0.020 (Bricaud et al., 1981). The absorption of NAP, comprising detritus and inorganic particles, has also been shown to follow the same mathematical expression as equation 2.21 (Carder, Steward, Harvey, & Ortner, 1989; Bowers, Harker, & Stepham, 1996; Babin et al., 2003b). Based on the spectral slopes of NAP obtained from Roesler, Perry, and Carder (1989), and the fact that they are similar in value, Carder et al. (1989) assume that they are spectrally inseparable and can thus be represented by a single absorption parameter corresponding to detritus and gelbstoff (dissolved organic) matter, a_{dg} ,

$$a_{\text{dg}}(\lambda) = a_{\text{CDOM}}(\lambda) + a_{\text{NAP}}(\lambda) \quad (2.22)$$

The spectral absorption of phytoplankton can be modelled using either the averaged specific or normalised spectral absorption coefficients (Morel, 1980, Roesler & Perry, 1995). Both methods allow the calculation of a_{phy} by the multiplication of the concentration or the absorption coefficient at a specific wavelength respectively. A limitation of these approaches is that the spectral shape of phytoplankton remains constant, which typically does not occur spatially or temporally. Lee et al. (1999), based on field data, modelled the absorption of phytoplankton as,

$$a_{\text{phy}}(\lambda) = a_{\text{phy}}(440) \left[a_0(\lambda) + a_1(\lambda) \times \ln(a_{\text{phy}}(440)) \right] \quad (2.23)$$

where a_0 and a_1 are empirical spectral coefficients. This formulation allows the spectral shape of phytoplankton to change with its magnitude.

2.2.4.2 Modelling the backscattering

In an analogous manner to absorption, the total backscattering of seawater is the summation of the backscattering by pure seawater, b_{bw} , phytoplankton, b_{bphy} and non-algal particulates, b_{bNAP} (Sathyendranath, Prieur, & Morel, 1989),

$$b_b(\lambda) = b_{bw}(\lambda) + b_{bphy}(\lambda) + b_{bNAP}(\lambda) \quad (2.24)$$

The scattering of light by pure water is hypothesised to be caused by the random motion of the water molecules that in a small voxel causes fluctuations in density (Morel, 1974). The dissolved electrolytes in pure seawater cause it to scatter light approximately 1.30 times that of pure water (Morel, 1974). The main contribution to backscattered light in the coastal ocean is that caused from suspended particulate matter which in turn is dependent on its particle size distribution and the bulk refractive index (Twardowski et al., 2001). The backscattering coefficients of phytoplankton and NAP are generally combined into one spectral coefficient, b_{bp} (Roesler & Perry, 1995; Morel & Maritorena, 2001). In oceanic waters where the phytoplankton dominates the scattering of light, b_{bp} has typically been modelled with a strong dependency on the concentration of phytoplankton (Morel & Maritorena, 2001). However such an assumption may be not suitable for coastal ocean waters that typically have greater influx of terrigenous particles. In such cases b_{bp} has typically been modelled with a power law (Smith & Baker, 1981; Babin et al., 2003a),

$$b_{bp}(\lambda) = b_{bp}(\lambda_0) \left(\frac{\lambda_0}{\lambda} \right)^Y \quad (2.25)$$

where λ_0 is the reference wavelength. Lee et al. (1994; 1999) used $\lambda_0 = 400$ nm; Klonowski et al. (2007) used $\lambda_0 = 550$ nm, whilst; Lee, Carder, and Arnone (2002) used $\lambda_0 = 555$ nm. The parameterisation given by equation (2.25) assumes a non-absorbing medium (Babin et al., 2003a).

2.3 Empirically Deriving Bathymetry

This section describes the many bathymetric empirical algorithms that have been developed since 1970. As one of the aims of this research is the limitations and potential of bathymetry derived from hyperspectral imagery using physics based inversion models, this brief section is included for completeness.

2.3.1 Spectral Transformations

A common approach to deriving bathymetry is through an index that is sensitive to changes in depth above changes due to varying bottom albedos and water clarities. Such indices typically constitute a ratio between two spectral bands, which form the independent variable of an empirically derived algorithm to calculate the water depth. One of the earliest spectral ratio transformations was proposed by

Polcyn, Brown, and Sattinger (1970) to derive water depth from airborne multispectral imagery. Polcyn et al. (1970), like other researchers, first assumed that the reflectance solely by the water column at any given pixel could be estimated and removed by subtracting the average reflectance over an imaged deep water region (R^{dp}). The variability in the resultant imagery (i.e. $R(\lambda_i) - R^{\text{dp}}(\lambda_i)$) was thus assumed to be due to changes in depth, bottom albedo (ρ) and water column attenuation (κ). Taking the ratio between two bands gives,

$$\frac{R(\lambda_i) - R^{\text{dp}}(\lambda_i)}{R(\lambda_j) - R^{\text{dp}}(\lambda_j)} = \frac{\rho(\lambda_i)}{\rho(\lambda_j)} e^{-[\kappa(\lambda_i) - \kappa(\lambda_j)](\sec\theta_v + \sec\theta_w)z} \quad (2.26)$$

θ_v and θ_w are the viewing and solar zeniths. Next a pair of wavelengths were found, typically in the blue and green portion of the visible domain, where $\kappa(\lambda_i) - \kappa(\lambda_j)$ and $R_b(\lambda_i)/R_b(\lambda_j)$ are constant for varying water types and bottom albedos respectively. In other words $\kappa(\lambda_i) - \kappa(\lambda_j)$ and $R_b(\lambda_i)/R_b(\lambda_j)$ are values derived from *in situ* measurements and allow equation (2.26) to be inverted to calculate the depth.

Lyzenga (1978) noted that the pair of wavelengths that satisfy constant water attenuation may not satisfy constant bottom albedo ratio particularly if a scene has a wide range of water clarities and bottom substrates. Furthermore Polcyn et al. (1970) used an over simplified equation for estimating the radiance emanating from the water column, where according to equation 2.14, subtraction of R^{dp} would not cause its full removal from the right hand side,

$$R - R^{\text{dp}} = (\rho - R^{\text{dp}}) \exp[-(D_d + D_u^c)\kappa z] \quad (2.27)$$

Lyzenga (1978; 1985) proposed a linearised multiband bathymetry algorithm that reduces the effect of varying bottom albedo,

$$X_i = \ln[R(\lambda_i) - R^{\text{dp}}(\lambda_i)] = -2Kz \cdot \ln[\rho(\lambda_i) - R^{\text{dp}}(\lambda_i)] \quad (2.28)$$

and

$$z = a_0 + a_1X_1 + a_2X_2 \quad (2.29)$$

where a_i are coefficients determined from a regression analysis using *in situ* water depths. In a comparison, Clark, Fay, and Walker (1987) showed that the linearised method by Lyzenga (1985) achieved improved bathymetric retrievals compared to the ratio algorithm of Polcyn et al. (1970).

A major limitation to the linear method proposed by Lyzenga (1985) is the deep ocean reflectance subtraction in equation (2.28) which can result in negative values over dark seagrass or submerged vegetation pixels (Philpot, 1989; Stumpf,

Holderied, & Sinclair, 2003). This poses a problem as negative reflectance values are non-physical and the natural logarithm of negative values are undefined. In addition image segmentation would need to be performed when this technique is applied to a scene with regions of distinct water clarity (Philpot, 1989). To overcome these issues Stumpf et al. (2003) developed the linearised log ratio to derive depth,

$$\text{depth (m)} = m_0 \frac{\ln\{G \times R_w(\text{Green})\}}{\ln\{G \times R_w(\text{Blue})\}} - m_1 \quad (2.30)$$

the coefficients m_0 and m_1 were tuned with depth soundings from a nautical chart. G is a scaling factor that is held fixed to a user defined value, and R_w is the total above water reflectance as sunglint correction was not performed. With a comparison to Lidar measurements, Stumpf et al. (2003) showed that the ratio algorithm (equation 2.30), generally retrieved depths to 25 metres (for very clear waters), and had a 5 to 10 m greater dynamic range than the linear method of Lyzenga (1985). However for both methods, the normalised RMSE between the predicted and measured depth increased with depth and would typically exceed 20% for depths greater than 10 m – though the ratio method typically achieved lower RMSE than the linear (Lyzenga) method. Both methods show a plateau forming for plots of the estimated against measured depths and represent situations where the attenuation properties of the water column preclude any bottom reflected signal reaching the water's surface, a limitation of optical remote sensing. Ma et al. (2014) used a variant of equation 2.30 and obtained a RMSE between actual and predicted depths of less than 2 m for water depths less than 30 m.

In a similar fashion Dierssen, Zimmerman, Leathers, Downes, and Davis (2003) and Mishra, Narumalani, Rundquist, Lawson, and Perk (2007) used a log ratio between two reflectance bands and applied that to a second order polynomial whose coefficients (m_i) were optimised from *in situ* depth measurements.

$$\begin{aligned} \log(\text{Depth}) &= m_0 + m_1x + m_2x^2 \\ x &= \ln\left(\frac{R_{rs}(\lambda_1)}{R_{rs}(\lambda_2)}\right) \end{aligned} \quad (2.31)$$

Dierssen et al. (2003) used $\lambda_1 = 555$ nm and $\lambda_2 = 670$ nm, whilst Mishra et al. (2007) used $\lambda_1 = 481$ nm and $\lambda_2 = 553$ nm. The algorithms given by Stumpf et al. (2003), Dierssen et al. (2003) and Mishra et al. (2007) all utilise the reflectance of the green band due its ability to penetrate further into the water column in coastal waters, and as such can be very sensitive to changes in depth. Inclusion of a second reflectance band serves to minimise the influence of different substrates, where the varying

albedos affect the reflectances of these two bands in a similar fashion. The 670 nm band used by Dierssen et al. (2003) corresponds to the chlorophyll-*a* absorption peak from phytoplankton (Bricaud, Babin, Morel, & Claustre, 1995) and combined with the high absorption of the water molecules at this wavelength could cause R_{rs} to be less sensitive to both depth and bottom albedo than bands below 500 nm. Despite this, 50% of the calibration depth measurements were within 3.3 cm from the predicted depth for both Dierssen et al. (2003) and Mishra et al. (2007), however an accuracy assessment was not performed.

Principal Components Analysis on log transformed reflectance values from a single band have also been attempted to estimate water depth. The premise being that the variance in the water leaving radiance of an image is largely due to water depth and as such would be wholly contained in the first eigenvector of the PCA transform, whilst the second eigenvector contains variations due to bottom types (Khan, Fadlallah, & Al-Hinai, 1992; Liceaga-Correa, & Euan-Avila, 2002; Gholamalifard, Kutser, Esmaili-Sari, Abkar, & Naimi, 2013). Note that here the PCA eigenvectors are uncorrelated, orthogonal and correspond to transformed image bands. The first PCA eigenvector would then form the independent variable of a linear equation for depth, where the coefficients (gradient and intercept) are determined from regression analysis with *in situ* depth data. This approach however does not perform adequately for scenes with varying water clarities and bottom albedos (Ceyhun & Yalcin, 2010) and based on the results of Liceaga-Correa and Euan-Avila (2002) is less accurate than the linear model proposed by Lyzenga (1985).

2.3.2 Artificial Neural Networks

Artificial Neural Networks (ANNs) is a type of supervised learning that has been used successfully in making predictions from input variables that are contained in non-linear functions (Basheer & Hajmeer, 2000). Part of that success is the ability of ANNs to generalise complex numerical problems based solely on the input and expected output data. For the case of estimating bathymetry it is crucial for *in situ* water depths to be collected over a wide range of bottom substrates, water optical properties and solar/view angles so that the corresponding variability in the reflectance dataset trains the ANN (Sandidge & Holyer, 1998). The structure of an ANN contains several layers of nodes, where the nodes at one layer interconnect to all the nodes of the next layer. These connections allow information to be transferred forward (and

back) from one layer to the next (Basheer & Hajmeer, 2000). Each receiving node in a given layer individually weights the inputs from the previous layer. The weighted inputs are then passed through a non-linear function to form the output from that node. This process is continued until the output layer is reached. An iterative optimisation approach is needed to determine the weights of each node in each layer such that the RMSE between the predicted and actual outputs are minimised.

For depth estimations using remote sensing reflectance the output layer consists of one node representing the desired depth whilst the input reflectance spectrum (either the entire spectral range or a subset) consists of the input layer with the number of nodes equalling the number of bands (Sandidge & Holyer, 1998; Ceyhun & Yalcin 2010; Liu, Gao, Zheng, & Li, 2015). The number of layers and inner nodes are user defined and are selected based on the combination that provides the best results (Freeman & Skapura, 1991); Sandidge and Holyer (1998) used one inner layer with 21 nodes, with the input layer containing 41 nodes; Ceyhun and Yalcin (2010) used two inner layers each with four nodes; Liu et al. (2015) similarly used two inner layers having nine and three nodes; Gholamalifard et al. (2013) used one inner layer with six nodes. Sandidge and Holyer (1998) showed that the accuracy of the generalised ANN varied for the two AVIRIS scenes analysed, achieving an RMSE (between actual and predicted depth) of 0.83 m and 0.39 m for depths between 0-6 m. It should be noted that the plots of estimated versus actual depths described a non-linear response (rather than a linear 1:1 line), and that the ANN substantially over-estimated the depths (up to 3 m) for depths less than 2 m. The RMSE values reported by Sandidge and Holyer (1998) are similar to those produced by Corucci, Masini, and Cococcioni (2011) and Liu et al. (2015). Larger variability of the ANN estimated depth from the actual was observed by Ceyhun and Yalcin (2010), where the ANN consistently over-estimated the depth (refer to Fig.5 by Ceyhun and Yalcin, 2010). An independent analysis of the predicted and actual depths given in Table 1 by Gholamalifard et al. (2013) showed that for depths less than 10 m, the RMSE was 0.45 m in line with Sandidge and Holyer (1998). In addition, biases of greater than 2 metres were observed, for example there were three instances where the actual depth was 5 m, yet the ANN predicted 5.91-, 8.07- and 8.51-m.

2.3.3 Limitations

The linear and ratio spectral transformations mentioned in sections 2.3.1 rely on finding a pair of spectral bands within a given scene where: (a) the ratio of the bottom albedos in these two bands are the same for all bottom types, and; (b) the difference between the water column attenuation coefficients at these bands is constant. Selecting a pair of bands that satisfy these criteria is difficult, troublesome and is a potential source of error in depth predictions when they are not met. Furthermore, spectral ratio transformation algorithms do not take into account the complete spectral shape of the water leaving reflectance, and using two bands is subject to non-uniqueness issues. Here non-uniqueness arises when different sets of IOPs, depth and substrate generate the same reflectance value at a given wavelength. Thus in the case of Dierssen et al. (2003), equation 2.31, deep sand can be confused with shallow seagrass solely using a ratio between 555 and 670 nm leading to inaccurate retrievals of bathymetry (Mobley, 2012). PCA has been shown to perform adequately for scenes with varying water clarities and bottom albedos but in some situations it is less accurate than the linear model proposed by Lyzenga (1985). Methods that utilise non-linear relationships such as ANNs and Manifold Coordinate Representations (Bachmann et al., 2009) have the potential to retrieve more accurate bathymetry. However, they (like the linear, ratio and PCA transformations) require *in situ* depth measurements as a means of tuning these algorithms, and as such limits their applicability temporally and to other regions.

2.4 Benthic classification

There has been a plethora of benthic habitat classification techniques published on mapping coastal and coral reef ecosystems. As one of the research outcomes of this thesis is a method to analyse the potential and limitations of benthic classification from hyperspectral imagery, a brief review of classification from multispectral sensors is given for completeness. Due to the limited number of spectral bands in the visible domain of moderate to high spatial resolution satellite imaging sensors such Landsat TM, SPOT, QuickBird and IKONOS; mapping typically has centred on supervised or unsupervised classification of image-derived spectra. Current classification techniques are, however, migrating towards object-based image analysis where the textual patterns of a group of pixels are used, in combination with the spectra

(i.e. colour), to classify pixels (e.g. Benfield, Guzman, Mair, & Young, 2007; Zhang et al., 2013; Roelfsema et al., 2014). Such approaches are not within the scope of this research and therefore excluded from this review.

The most commonly used supervised method is the maximum likelihood classifier (MLC), where an image pixel is assigned to a class based on the highest posterior probability – i.e. the probability of a pixel belonging to class k given its spectral response (Atkinson & Lewis, 2000). MLC requires a representative imaged-based training dataset for each class in order to estimate the spectral mean and variance-covariance. Vahtmae and Kutser (2013) illustrated that the resultant classification accuracy can be severely degraded if the representative training datasets are not selected with caution or some expert knowledge of the scene. Inappropriate selection of training regions can increase misclassification errors between classes. Unsupervised classification, in contrast, has similarities to clustering where image pixels are segmented into separate clusters based on the similarities of their spectral signatures (Richards & Jia, 2006). The advantage here is that selecting training regions *a priori* is not required. However, the number of clusters (i.e. classes) with which to terminate the classification must be known beforehand, and the resultant classes are arbitrary with regards to their habitat definition unless knowledge of the study site exists. Combinations of the two approaches have also been used employed. Maeder et al. (2002) used an unsupervised ISODATA classifier to produce 100 classes in an atmospherically corrected IKONOS image. Based on the spectra of these classes and that of a training dataset the supervised MLC was used to classify the image into nine classes. With a similar approach Pu, Bell, Meyer, Baggett, and Zhao (2012) used the unsupervised ISODATA classifier on depth invariant indices, and subsequent supervised MLC to reduce and classify the number of classes based on a training dataset. Table 2.1 lists the different classification techniques used in multispectral imagery of coral or coastal marine ecosystems, the number of classes mapped and the overall accuracy obtained.

The early approaches to benthic classification typically neglected the impact of the water column contribution where classification was performed using the sensor's digital numbers (Luczkovich, Wagner, Michalek, & Stoffle, 1993; Zainal, Dalby, & Robinson, 1993; Ferguson & Korfmacher, 1997) or atmospherically corrected reflectances (Mumby, Green, Clark, & Edwards, 1998b; Maeder et al., 2002; Andrefouet et al., 2003; Gullstrom et al., 2006). As a consequence the overall accuracy

of the resultant classification maps varied from approximately 20% to typically less than 70% (Table 2.1). It should be noted that classification accuracy is dependent on the number of classes mapped and the spatial and spectral resolution of the sensor. The general trend in these studies follows that the fewer the classes and the higher the spatial or spectral resolution of the sensor the higher the overall accuracy. Indeed Pu et al. (2012) analysed the classification accuracies obtained with three satellite sensors (Landsat TM, EO-1 ALI, and Hyperion) each having 30 m spatial resolution but different spectral resolutions. Landsat TM, EO-1 ALI and Hyperion had 3, 4 and 24 spectral bands in the visible domain and obtained classification accuracies of 92%, 95% and 96% respectively for a three class map. Here each class represented a proportion of seagrass cover of <25%, 25-74% and $\geq 75\%$. When the number of classes increased to five these accuracies reduced to 66%, 78% and 79% for Landsat, EO-1 and Hyperion respectively (Pu et al., 2012). This trend of decreasing spectral resolution with decreasing classification accuracy was also observed by Hochberg and Atkinson (2003) and Karpouzli, Malthus and Place (2004).

Unfortunately there has been no definitive or optimal number of classes (and the benthos that constitute them) that future users should use that would give a particular classification accuracy. Andrefouet et al. (2003) did plot the classification accuracy against the number of classes mapped using IKONOS and Landsat and, despite the different methodologies used, it followed a decreasing linear trend. However selecting the optimal number of classes to use is still a trial and error approach. This was demonstrated by Zapata-Ramirez, Blanchon, Oliosio, Hernandez-Nunez and Sobrino (2013) who initially mapped an IKONOS imaged coral reef scene with 12 classes based on field data. Using supervised classification the overall accuracy of the subsequent map was too low and thus Zapata-Ramirez et al. (2013) collapsed the number of classes into six relatively broad classes with an overall accuracy of 82%. This suggests the potential value of a technique that *a priori* describes the number and type of benthic classes that could be distinguished for the given scene and spectral resolution of the sensor.

Table 2.1: Benthic substrate classification methodology, number of classes and overall accuracy from a variety of imaging sensors in the literature. Note that in the Classification Method column, DII stands for Depth Invariant Indices from the method of Lyzenga (1981); MLC for Maximum Likelihood Classifier; SAM for Spectral Angle Mapper; UC for Unsupervised Classification; CE for Contextual Editing; DN for digital numbers.

Reference	Sensor	Number of Classes	Accuracy (%)	Classification Method
Gullstrom et al. (2006)	Landsat-TM	2	Not Assessed	Supervised MLC of at- atmosphere corrected spectra
Zainal et al. (1993)	Landsat-TM	8 ^{†, ‡}	Not Assessed	Supervised MLC of DN
Ferguson & Korfmacher (1997)	Landsat-TM	2	63.4-72.6	UC using DN and depth data
Purkis & Pasterkamp (2004)	Landsat-TM	7	76	Supervised MLC of derived bottom reflectances
Call, Hardy, and Wallin, (2003)	Landsat-TM	7 ^{*, †, ‡}	74	UC of DII
Mumby et al. (1998a)	Landsat-TM	4	~50	Supervised MLC of atmosphere corrected spectra
			~70	Supervised MLC of DII
			~75	Supervised MLC of DII followed by CE
		13	~20	Supervised MLC of atmosphere corrected spectra
			~28	Supervised MLC of DII
			~31	Supervised MLC of DII followed by CE
Mishra et al. (2006)	QuickBird	6 [*]	81.46	UC of derived bottom reflectances
Vahtmae et al. (2011)	QuickBird	7 [*]	68	Supervised MLC of atmosphere corrected spectra
Maeder et al. (2002)	IKONOS	5 [*]	89	UC of image spectra followed by supervised MLC

* Deep water is included as a substrate mapped;

† Includes classes of sand at different geomorphic zones, e.g. “sand at backreef”, “Sand at lagoon floor” or at different depths e.g. “Shallow Sand”, “Deep sand”

‡ Includes classes of seagrass, algae or coral at different depths, e.g. “Shallow seagrass on lagoon floor”, “Deep seagrass on lagoon floor”

Table 2.1: continued

Reference	Sensor	Number of Classes	Accuracy (%)	Classification Method
Andrefouet et al. (2003)	The following location and results were based on IKONOS imagery			
	Shiraho, Nth Japan	4	81	UC of image spectra
	Glovers	5	77	UC of DII followed by CE
	Boca Paila	7 [†]	74	Supervised MLC of DII
	Addu	8 [†]	66	Supervised MLC
	Dubai	8 ^{‡, †}	71	Supervised MLC
	Biscayne Bay	8 [‡]	84	Supervised MLC
	Andros Island	8 [†]	74	Supervised MLC of DII
	Heron Island	13	42	Supervised MLC of DII
Mayotte	14 [†]	61	Supervised MLC of image spectra	
Purkis (2005)	IKONOS	8	69	Supervised MLC of derived bottom reflectances
Zapata-Ramirez et al. (2013)	IKONOS	6	82	Supervised MLC of atmosphere & sunglint corrected spectra
Vahtmae & Kutser (2013)	WV2	5 [*]	61.6	Supervised SAM of atmosphere & sunglint corrected spectra
	CASI	5 [*]	77.5	
Mumby et al. (1998b)	CASI	9	~64	Supervised MLC of atmosphere corrected spectra
			~65	Supervised MLC followed by CE
			~77	Supervised MLC of DII
			~81	Supervised MLC of DII followed by CE

* Deep water is included as a substrate mapped;

[†] Includes classes of sand at different geomorphic zones, e.g. “sand at backreef”, “Sand at lagoon floor” or at different depths e.g. “Shallow Sand”, “Deep sand”

[‡] Includes classes of seagrass, algae or coral at different depths, e.g. “Shallow seagrass on lagoon floor”, “Deep seagrass on lagoon floor”

Not accounting for the attenuating effects of a variable water depth causes a higher level of misclassification between different classes at different depths, for example between seagrass and deep sand or seagrass and deep corals (Zainal, Dalby, & Robinson, 1993). As the water depth increases the difference in spectra (digital numbers or above water reflectance) between certain habitats at different depths become less than the variance within each class and the supervised or unsupervised classifier cannot separate them. Furthermore, supervised classification works best when the reflectance spectra of the classes have well defined variance-covariance. This poses issues for shallow water mapping as a class such as sand for example will exist at different depths with slightly varying water optical properties. This consequently increases the intra-class variability for the sand class thereby increasing spectral confusion between classes. Water column correction has therefore demonstrated improved benthic classification accuracies by increasing the spectral differences between classes to allow greater separation (Mumby, Clark, Green, & Edwards, 1998a). Note that the exponential nature of light attenuation by depth means that a small spectral difference in the above water reflectances would constitute a larger difference in the spectra at the depth of the substrate. There will of course be a depth limit where water column correction no longer spectrally separates classes sufficiently. This limit would vary from scene to scene as it is dependent on the water column optical properties (Kutser, Dekker, & Skirving, 2003; Hedley, et al., 2012b). O'Neill and Costa (2013) estimated the depth limit *a priori* in order to mask out optically deep water pixels. This depth limit was optimised for eelgrass (the classification objective) and was defined when the above water reflectance of eelgrass could no longer be distinguished from that of deep water. Here the optical properties of the water column were based on field measurements.

To date, analysis of spectral confusion is briefly analysed after classification, where for instance it has been noted that confusion between seagrass and different types of algae exist (Mumby, Green, Edwards, & Clark, 1997; Gullstrom et al., 2006; O'Neill & Costa, 2013) or between dense coral habitat and algae in deeper waters (Purkis, 2005; Zapata-Rameriez et al., 2013). A method that is able to describe which classes are spectrally distinguishable given the optical properties of a water column and the range of depths expected in a scene will aid in understanding the potential of spectral classification methodology to the particular scene and sensor *a priori*.

For multispectral sensors, the two most common approaches to removing the influence of the water column are the method by Lyzenga (1981) or by estimating the water column optical properties and water depth, and then using a bio-optical model to remove the influence of the water column from the image. Lyzenga (1981) illustrated that the image pixels of a single substrate at a variety of depths fall on a linear line on a bi-plot of two log transformed visible bands. Similarly, image pixels of different substrates would fall onto other parallel lines. The gradient is the ratio of the effective diffuse attenuation coefficient of the water column at these two bands and the y-intercept the depth invariant index – where pixels belonging to that substrate share the same value irrespective of their depth. Thus two spectral bands generate one depth invariant index (DII). Although this is a simple yet useful tool that does not require any *in situ* measurements, it does have several drawbacks. The first of which, as stated by Andrefouet et al. (2003), is that the spectral shape of the DII cannot be related to *in situ* substrate reflectances and thus (supervised or unsupervised) classification must still be performed with the aid of ground-truthed image pixels whose habitats are known. The second are errors arising from spatially heterogeneous water column optical properties (Tassan, 1996), and the third deals with the applicability of this method when benthos only occupy a limited depth range. The latter drawback is the reason why Andrefouet et al. (2003) could not use the Lyzenga method for all images analysed in an inter-comparison study into the standardising of methodologies. Zhang et al. (2013) also experienced this limitation over the shallow areas of Florida Keys where the key substrates only occurred in a narrow depth range. Despite these limitations classification using DII has shown improvements in accuracy, where Mumby et al. (1998a) showed on average a 16%, 11% and 7% accuracy improvement for classification maps with four, nine and 13 classes respectively.

Correcting the water column radiance signal using a bio-optical model, to retrieve the bottom substrate reflectance does potentially alleviate all the drawbacks encountered by the Lyzenga (1981) method. However, knowledge of the water column optical properties for each pixel in the image is needed, which is not possible from field measurements. As such researchers have assumed that the water column optical attenuation across the imaged area is spatially homogeneous and represented by an effective diffuse attenuation coefficient (Mumby et al., 2004; Purkis & Pasterkamp, 2004; Purkis, 2005; O'Neill & Costa, 2013). In these studies the depth across the scene

was estimated either by linear interpolation of discrete *in situ* depth measurements or boat-based bathymetry surveys using acoustics. Other researchers have attempted to estimate the depth and optical properties for each pixel using empirical relationships that utilise reflectance ratios (Mishra, Narumalani, Rundquist, & Lawson, 2006). Supervised or unsupervised classification of the retrieved substrate reflectances would then be performed. The resultant classification accuracies varied from 69% to 81.46% (Table 2.1), however given that the researchers did not perform a comparison without using water column correction, it can only be assumed that improved accuracy is afforded. Note that supervised classification in this context compares an image pixel to a library of benthic endmembers (Purkis, 2005). This represents a shift from the initial mapping of habitats that represented an assemblage of benthos (e.g. Mumby et al., 1998a; 1998b; Andrefouet et al., 2003) to mapping individual benthos. These studies did not take spectral mixing of the benthic components into account (e.g. Hedley & Mumby, 2003) and may have potentially reduced the classification accuracy for pixels that have a high level of benthic heterogeneity. Unmixing the substrate reflectance to the fractional coverage of benthic endmembers however does require more bands in the visible domain to achieve and is typically limited to hyperspectral remote sensing.

2.5 Radiative Transfer Based Algorithms

Methods that simultaneously solve for the optical properties of the water column, depth and bottom substrate from the water leaving reflectance are desirable for bathymetry and benthic classification. Such methods can be categorised into two groups: semianalytical (SA) inversion models that utilise spectral optimisation and look-up-table (LUT) routines, both of which circumvent the need for *in situ* data calibration. The SA models reviewed are an approximation to the Radiative Transfer Equation (RTE) as they utilise single-scattering theory, assume a homogeneous water column with vertically constant IOPs, a Lambertian bottom reflectance, and fixed spectral shapes to the IOPs. LUT methods in contrast utilise exact Radiative transfer numerical models, such as Hydrolight (Mobley & Sundman, 2000) or PlanarRad (Hedley, 2008), to generate a lookup table of reflectance spectra pertaining to different IOPs, depth and bottom substrate types. Thus SA models are approximations whilst LUT methods are exact but do not continuously sample the parameter space. Both have

advantages and disadvantages, as will be discussed in this section. SA and LUT methods have been primarily developed for hyperspectral sensors where the number of bands in the visible domain (with high enough SNR) can detect subtle spectral differences due to changes in depth, bottom substrate or magnitudes of in-water optically active constituents (Philpot et al., 2003).

2.5.1 Physics Based Inversion Models

2.5.1.1 Hyperspectral Optimisation Process Exemplar model (HOPE)

The semi-analytical shallow water model developed by Lee et al. (1999) forms the basis of the other more complex physics-based inversion models such as BRUCE (Klonowski et al., 2007) and SAMBUCA (Brando et al., 2009). As such its parameterisation and spectral optimisation are discussed here in detail. The subsurface remote sensing reflectance model used by all semi analytical inversion techniques is given by (Lee et al., 1999),

$$r_{rs} \approx r_{rs}^{dp} \{1 - \exp[-(D_d + D_u^C)\kappa H]\} + \frac{\rho}{\pi} \exp\{-(D_d + D_u^B)\kappa H\} \quad (2.32)$$

where H is the depth. Section 2.2 outlines the derivation of this equation. Through Hydrolight (Mobley & Sundman, 2000) simulations, and using a Petzold phase function for the angular distribution of scattering of light by suspended particles, Lee et al. (1999) derived semi-analytical approximations for r_{rs}^{dp} , D_u^C and D_u^B ,

$$r_{rs}^{dp} \approx [0.084 + 0.170u(\lambda)]u(\lambda) \quad (2.33a)$$

$$D_u^C \approx \frac{1.03\sqrt{[1.0 + 2.4u(\lambda)]}}{\cos \theta_v} \quad (2.33b)$$

$$D_u^B \approx \frac{1.04\sqrt{[1.0 + 5.4u(\lambda)]}}{\cos \theta_v} \quad (2.33c)$$

$$D_d \approx \frac{1}{\cos \theta_w} \quad (2.33d)$$

and,

$$u(\lambda) = \frac{b_b(\lambda)}{a(\lambda) + b_b(\lambda)} \quad (2.34)$$

Note that from equations 2.33b and 2.33c, $D_u^C < D_u^B$ which would mean that $\overline{K_u^C} < \overline{K_u^B}$. This contradicts the results given by Kirk (1987) who states that $\overline{K_u^C} > \overline{K_u^B}$, as discussed in section 2.2.1. According to Lee et al. (1998) this contradiction is a

consequence of using the quasi-single scattering theory. By not including multiple scattering events in equation 2.32, which would require a more complicated expression, the best-fit values to the Hydrolight dataset for D_u^C and D_u^B are such that $D_u^C < D_u^B$. Here, the modelled optically deep water subsurface remote sensing reflectance, r_{rs}^{dp} (equation 2.33a), is independent of the solar and viewing zenith angles. This same parameter derived from first principles by Kirk (1989) and Maritorena et al. (1994) is inversely proportional to $\overline{K_d}$ and $\overline{K_u^c}$, see equation 2.10, which are themselves functions of the subsurface solar and viewing zenith angles respectively (Kirk, 1983). Despite this, the R_{rs} computed by the SA model given by Lee et al. (1999) on average deviated by ~6.3% from Hydrolight generated R_{rs} .

Equation 2.32 states that if the absorption and backscattering coefficients of the water column are known along with the depth and bottom substrate reflectance, then the r_{rs} can be modelled. However, of interest is inverting r_{rs} to solve for a , b_b , H and ρ . Given that a and b_b can be decomposed into the summation of the various constituents as given by equations (2.20) and (2.24), the r_{rs} derived from an n band sensor can then be represented by the following set of equations (Lee et al., 2001),

$$\begin{aligned} r_{rs}(\lambda_1) &= f \left\{ \begin{array}{l} a_w(\lambda_1), a_{phy}(\lambda_1), a_{dg}(\lambda_1), \\ b_{bw}(\lambda_1), b_{bp}(\lambda_1), \rho(\lambda_1), H \end{array} \right\} \\ &\quad \vdots \\ r_{rs}(\lambda_n) &= f \left\{ \begin{array}{l} a_w(\lambda_n), a_{phy}(\lambda_n), a_{dg}(\lambda_n), \\ b_{bw}(\lambda_n), b_{bp}(\lambda_n), \rho(\lambda_n), H \end{array} \right\} \end{aligned} \quad (2.35)$$

Given that a_w and b_{bw} are known (see Morel, 1974; Smith & Baker, 1981) the number of equations needed to analytically solve for a_{phy} , a_{dg} , b_{bp} , ρ and z are $4n + 1$. Clearly this is not possible solely from the r_{rs} which only provides n known values. Lee et al. (1999) parameterised a_{phy} , a_{dg} , b_{bp} and ρ such that each can be represented by a scalar variable that governs the magnitude of absorption or backscattering,

$$\begin{aligned} a(\lambda) &= a_w(\lambda) + P[a_0(\lambda) + a_1(\lambda) \ln(P)] \\ &\quad + G \exp[-0.015(\lambda - 440)] \end{aligned} \quad (2.36a)$$

$$b_b(\lambda) = b_{bw}(\lambda) + X \left(\frac{400}{\lambda} \right)^Y \quad (2.36b)$$

$$Y \approx 3.44 \left[1 - 3.17 \exp \left(-2.01 \frac{R_{rs}(440)}{R_{rs}(490)} \right) \right] \quad (2.36c)$$

P and G are absorption coefficients at 440 nm, and are scalars designed to control the magnitude of the spectral shapes of a_{phy} and a_{dg} , respectively. X is the backscattering

coefficient of suspended particles (both algal and non-algal) at 400 nm and scales the magnitude of the spectral shape of b_{bp} . The spectral slope of b_{bp} is governed by the parameter Y which typically ranges from 0 to 2.5 (Lee et al., 1999). The bottom albedo is also parameterised such that,

$$\rho(\lambda) = B\rho_{sd}^*(\lambda) \quad (2.37)$$

where B is the albedo at 550 nm and ρ_{sd}^* is the spectral diffuse reflectance of sediment normalised to a value of 1.0 at 550 nm. Hence B scales ρ_{sd}^* in order to account for the various benthic substrates that would have different diffuse reflectance spectra. The rationale here is that the spectral shape of ρ for different substrates between 450 and 600 nm – the wavelength range that have the greatest transparency in water – are relatively minor and can be approximated by equation 2.37.

From the parameterisation of the bottom reflectance and absorption and backscattering coefficients, r_{rs} then becomes a function of P , G , X , B and H . In other words, this parameterisation now allows the measured remote sensing reflectance to be modelled by adjusting these five scalars. Finding the values of P , G , X , B and H that best matches the measured remote sensing reflectance forms the basis of the non-linear optimisation scheme proposed by Lee et al. (1999). This optimisation protocol is simply a predictor-corrector process in which initial guess values for P , G , X , B and H are inserted into the parameterised semi-analytical (SA) shallow water model to generate a modelled r_{rs} . This is then compared with the measured reflectance spectrum using a difference measure such as normalised Euclidean distance. The initial guess values are adjusted until the difference between the modelled and measured reflectance spectrum reaches a minimum. When this occurs the values of P , G , X , B and H are considered to be derived.

2.5.1.2 Bottom Reflectance Un-mixing Computation of the Environment model (BRUCE)

The HOPE model proposed by Lee et al. (1999) is suited for retrieving the water depth and water optical properties over homogeneous substrates. This is due to the parameterisation of the bottom reflectance allowing the retrieval of the bottom albedo of one benthic class. The default benthic class is sand (Lee et al., 1999), however in later research an additional class of seagrass was added (Lee et al., 2001; Dekker et al., 2011). Here, a simple reflectance spectrum criteria was used to select the benthic class (seagrass or sand) for the inversion process.

Assuming a homogeneous substrate is very limiting, unless the hyperspectral sensor images a scene with very high spatial resolution (< 1 m), and may not reflect the spatial heterogeneity of coastal or coral reef environments (Lim, Hedley, LeDrew, Mumby, & Roelfsema, 2009; Hedley, Roelfsema, Koetz, & Phinn, 2012a). Often multiple substrate classes populate a given pixel producing a benthic reflectance spectrum that is a mixture of the substrate classes present. This is known as sub-pixel spectral mixing, the mechanism of which has been assumed to be linear (Hedley & Mumby, 2003; Hedley, Mumby, Joyce, & Phinn, 2004; Goodman & Ustin, 2007; Klonowski et al., 2007; Brando et al., 2009). Incorporation of linear unmixing to the benthic reflectance has been directly implemented in BRUCE (Klonowski et al., 2007) and SAMBUCA (Brando et al., 2009).

The parameterisation of the SA shallow water model used in BRUCE follows that of HOPE (Lee et al., 1999) with the exception of the absorption of phytoplankton, backscattering of suspended particles and bottom reflectance,

$$a_{\text{phy}}(\lambda) = P a_{\text{phy}}^*(\lambda) \quad (2.38a)$$

$$b_{\text{bp}}(\lambda) = X \left(\frac{550}{\lambda} \right)^Y \quad (2.38b)$$

$$\rho(\lambda) = B_1 \rho_1^*(\lambda) + B_2 \rho_2^*(\lambda) + B_3 \rho_3^*(\lambda) \quad (2.38c)$$

where ρ_i and B_i are the diffuse reflectance spectrum normalised at 550 nm and the albedo of benthic class i , respectively. a_{phy}^* is the absorption coefficient for phytoplankton taken from Morel (1988) normalised to a value of 1.0 at 440 nm. Thus unlike in HOPE the spectral shape of phytoplankton is fixed. The spectral slope Y is set to a value of 1.0 to represent coastal waters. Babin et al. (2003a) showed that measured mineral particle backscattering coefficient was more properly modelled when $Y = 0.4$, and Lee et al. (2001) used a value of 0.5 to represent turbid waters.

The B_i values effectively represent the 'light' contribution of benthic class i to the reflectance. These values do not necessarily add up to one as they represent the albedo not fractional cover, although the higher the albedo the higher the likelihood that that benthic class will dominate the fractional cover (Klonowski et al., 2007; Fearn, Klonowski, Babcock, England, & Phillips, 2011). Converting these values to proportional cover was initially done through scaling, such that each B_i value was divided by their total sum for that pixel. This however may not be the most appropriate scaling method as illustrated in the following example. Figure 5j presented by Klonowski et al. (2007) showed the Hydrolight modelled benthic albedo values at 550

nm of a pixel equally mixed with sand, *Posidonia* sp. and *Sargassum* sp., that is ~33.3% coverage by each. The benthic albedo of these classes were 0.101, 0.017 and 0.013 equating to 77%, 13.4% and 9.6% using the scaling method proposed by Klonowski et al. (2007) for sand, *Posidonia* sp. and *Sargassum* sp. respectively. This scaling approach clearly does not take into consideration the intrinsic albedo of each class (and would only work if each class has the same intrinsic albedo). Note the intrinsic albedo of benthic class i refers to its albedo value when it completely covers a pixel, which for sand, *Posidonia* and *Sargassum* are 0.305, 0.052 and 0.040 respectively (see Table 2 in Klonowski et al. (2007)). Hence $0.101/0.305 = 0.331$; $0.017/0.052 = 0.327$, and; $0.013/0.040 = 0.325$, which approximately represents the 33% fractional coverage of each benthic substrate modelled. Thus the fractional cover of a given benthic class should therefore be calculated using,

$$\text{Fract. Cover of Class } i = \frac{B_i}{B_{in,i}} \quad (2.39)$$

where $B_{in,i}$ is the intrinsic albedo of benthic class i . Finally, although Klonowski et al. (2007) and Fearn et al. (2011) parameterised the bottom reflectance as a linear combination of sediment, seagrass and brown algae it is possible to use other substrate reflectances. For instance, coral, bleached coral and algae, and even to iterate through endmembers of a spectral library selecting those three that give the best fit.

2.5.1.3 Semi-Analytical Model for Bathymetry, Un-mixing, and Concentration Assessment (SAMBUCA)

Another variant of HOPE (Lee et al., 1999) is SAMBUCA (Brando et al., 2009). The main difference of this model compared to HOPE and BRUCE is the use of specific inherent optical properties and the way that the absorption and backscattering coefficients and bottom reflectances are parameterised. Specifically, the total absorption (a) and backscattering (b_b) coefficients are extended to include the spectral signatures of non-algal and phytoplankton particulates respectively,

$$\begin{aligned} a(\lambda) = & a_w(\lambda) + C_{\text{CHL}} a'_{\text{phy}}(\lambda) \\ & + C_{\text{CDOM}} a'_{\text{CDOM}}(440) \exp[-0.0157(\lambda - 440)] \\ & + C_{\text{NAP}} a'_{\text{NAP}}(440) \exp[-0.0106(\lambda - 440)] \end{aligned} \quad (2.40)$$

where C_{CHL} , C_{CDOM} and C_{NAP} are the concentrations of chlorophyll bearing particles, CDOM and NAP respectively. $a'_i(440)$ is the specific absorption coefficient of component i at 440 nm; for CDOM, a'_{CDOM} was set to 1.0. a'_{phy} is the specific

absorption coefficient that remains fixed when processing a hyperspectral image. The parameterisation of a_{NAP} follows that published by Babin et al. (2003b), and who showed that the relative contribution of the absorption of NAP to total absorption in coastal, case 2 waters typically varies from 11% to 28% on average at 443 nm. This small contribution is also conveyed by $a_{\text{NAP}}'(440) = 0.0048$, obtained from field measurements by Brandro et al. (2009). Absorption of phytoplankton and CDOM however typically dominate at 443 nm.

In Brandro et al. (2009), the backscattering term (b_b) is parameterised as,

$$b_{\text{bp}}(\lambda) = b_{\text{bw}}(\lambda) + C_{\text{CHL}} b'_{\text{bphy}} \left(\frac{548}{\lambda}\right)^{0.681} + C_{\text{NAP}} b'_{\text{bNAP}} \left(\frac{548}{\lambda}\right)^{0.681} \quad (2.41a)$$

$$b_{\text{bp}}(\lambda) = b_{\text{bw}}(\lambda) + [C_{\text{CHL}} b'_{\text{bphy}} + C_{\text{NAP}} b'_{\text{bNAP}}] \left(\frac{548}{\lambda}\right)^{0.681} \quad (2.41b)$$

b'_{bphy} is the specific backscattering coefficient of phytoplankton particles at 542 nm. This backscattering term is modelled as a power law according to Voss (1992). During the optimisation process the values of a_{NAP}' , b'_{bphy} and b'_{bNAP} are fixed but are also scene-specific. Note that Babin et al. (2003a) showed that measured $b_b(\lambda)$ of suspended algal particles is not modelled well using a λ^{-1} power law. In fact measured $b_b(\lambda)$ were spectrally flatter than the λ^{-1} relationship and contained troughs (or minima) at wavelengths where absorption of algal pigments are high, particularly the chlorophyll-*a* absorption band at 676 nm. The magnitude of these absorption troughs in $b_b(\lambda)$ was shown to be dependent on the concentration of phytoplankton, where in case 1 waters these troughs were more pronounced than in case 2 waters that were more mineral dominated. Thus, according to Babin et al. (2003a), the λ^{-1} law is only suitable when non-absorbing suspended particles populate the water column.

SAMBUCA assumes that the bottom reflectance is a linear combination of two substrata,

$$\rho(\lambda) = f_i \rho_i(\lambda) + (1 - f_i) \rho_j(\lambda) \quad (2.42)$$

here ρ_i and ρ_j are the substrate diffuse reflectances of substratum *i* and *j* respectively, and f_i represents the fractional cover of substratum *i*. To determine the type of substrate, SAMBUCA iterates through endmembers in a spectral library, keeping those two substrata and their fractional cover that give the best spectral fit. In this case the substrate reflectances are not normalised to 550 nm, as they are in HOPE and BRUCE, which allows SAMBUCA to solve for fractional coverage directly rather than retrieving the benthic albedo. In other words the albedos of the different substrate

reflectances are fixed. This has the advantage of readily interpretable results without the need of extra scaling as in BRUCE. Additionally, solving for the albedo is rather abstract since the albedo of a given substrates' diffuse reflectance should be constant for any given environmental conditions. For example, the albedo of a pixel solely composed of sand (or any other substrate for that matter) should not vary for varying depths or water clarity, and should only change if other substrate types populate the pixel.

2.5.1.4 Optimisation

In this section we describe the spectral optimisation used by HOPE, BRUCE and SAMBUCA, which are also different for these three inversion models. HOPE uses an error function that is analogous to a normalised Euclidean distance (or RMSE) of the modelled spectrum, \widehat{R}_{rs} , from that measured, R_{rs} (Dekker et al., 2011),

$$\Delta_{\text{HOPE}} = \frac{\left[\sum_{400}^{675} (R_{rs} - \widehat{R}_{rs})^2 + \sum_{750}^{800} (R_{rs} - \widehat{R}_{rs})^2 \right]^{0.5}}{\sum_{400}^{675} (R_{rs}) + \sum_{750}^{800} (R_{rs})} \quad (2.43)$$

Here the wavelengths relating to chlorophyll-*a* fluorescence (675-750 nm), which the SA shallow water models do not account for, are omitted from the determination of the error function. The goal here is to find the parameters that generates a \widehat{R}_{rs} spectrum such that $\Delta = 0$. The error function used by BRUCE is similar to equation 2.43 except that the denominator is equal to the number of spectral bands rather than the sum of the measured R_{rs} across all usable wavelengths (Klonowski et al., 2007). This effectively becomes the Euclidean distance between the modelled and measured R_{rs} , though as in equation 2.43, the lower the Δ the better the fit. Note that during spectral optimisation a set of parameters such that $\Delta=0$ is almost never found. There are three reasons for this: (1) the semi-empirical formulation of the SA models were developed from a wide range of Hydrolight simulations and as such there is an error attributed to the forward modelled R_{rs} ; (2) Atmospheric and sunglint corrections can be inaccurate or introduce spectral artefacts to the sensor-derived R_{rs} , or; (3) The spectral optimisation algorithm may converge to a solution that is a local minimum rather than a global minimum.

In SAMBUCA, the error function combines the spectral angle presented by Kruse et al. (1993) and the least squares minimisation from equation 2.43. The spectral angle, α , between the modelled and measured R_{rs} is given by,

$$\alpha = \cos^{-1} \frac{\sum_{400}^{800} (R_{rs} \times \widehat{R}_{rs})}{\left[\sum_{400}^{800} \widehat{R}_{rs}^2 \right]^{0.5} \cdot \left[\sum_{400}^{800} R_{rs}^2 \right]^{0.5}}, \quad (2.44)$$

$$0 < \alpha < \cos^{-1}(0)$$

and is effectively a measure of the difference in spectral shape between the measured and modelled R_{rs} , and in which the magnitudes are disregarded. Thus combining α with the least squares distance creates an error function that takes into account the spectral shape and magnitudes such that (Brando et al., 2009),

$$\Delta_{\text{SAMBUCA}} = \alpha \times \frac{\left[\sum_{400}^{800} (R_{rs} - \widehat{R}_{rs})^2 \right]^{0.5}}{\sum_{400}^{800} (R_{rs})} \quad (2.45)$$

2.5.2 Look up tables (LUT) methods

Look up table (LUT) and spectrum matching approaches to simultaneously retrieve the water depth, inherent optical properties and the benthic reflectance from input remote sensing reflectance was first proposed by Kutser and Jupp (2002) and later extended by Mobley et al. (2005). The LUT approach proposed by Mobley et al. (2005) was termed the Comprehensive Reflectance Inversion based on Spectrum matching And Table Lookup (CRISTAL). In these approaches a large database of modelled reflectance data (the LUT) are simulated using Hydrolight for varying water depths, IOPs and benthic endmembers. Spectral matching is then used to locate the simulated R_{rs} spectrum that best match the measured R_{rs} spectrum. The environmental conditions (i.e. depth, IOPs, and benthic substrata) of that simulated R_{rs} are then assumed to correspond to the conditions that formed the measured R_{rs} . Spectrally matching the measured R_{rs} for every pixel in a hyperspectral image is used to generate bathymetric, IOP and benthic habitat maps.

The LUT of simulated R_{rs} can contain in excess of 10,000 spectra owing to the fact that the simulated R_{rs} must be modelled for a range of different water depths, backscattering coefficients and benthic reflectance spectra. Indeed Lesser and Mobley (2007) varied the values of the absorption and backscattering coefficients to generate 28 IOP combinations, where for each IOP set the bottom reflectance was varied for 84 depths that ranged from 0.25- to 15.0-m. 118 bottom reflectance spectra were used which included the spectra for sand, seagrass, turf algae, pavement, coral-sargassum and extensive mixtures of these bottom types. From these combinations more than

277,000 simulated R_{rs} were modelled using HydroLight. Unlike the SA models of HOPE, BRUCE and SAMBUCA, which are approximations; the Radiative transfer model employed by HydroLight is numerically exact and in principle would generate more accurate retrievals in IOPs, depth and benthic substrate.

The LUT technique proposed by Mobley et al. (2005) has two limitations: (1) the accuracy of the retrieved depth, IOP and benthic type is dependent on how well these parameters were represented when the LUT was constructed. For example, using IOP parameters for the LUT construction that did not occur during the time of acquisition of the hyperspectral image would severely degrade the accuracy not only of the retrieved IOPs but also the depth and benthic substrate. In other words it becomes necessary to roughly know the range of depths, IOPs and benthos endemic to the region of interest at the time of acquisition. This also implies that a LUT, constructed for a particular site or condition (e.g. clear waters), cannot be re-used for another site or condition (e.g. flood events that increase water turbidity); (2) the discretisation of the input parameters (such as depth, IOPs and benthic reflectance) can generate errors due to under-sampling of regions where a small change has a significant effect on R_{rs} . For example, the R_{rs} at a given wavelength decreases exponentially with increasing depth (see equation 2.32). Thus discretising the depth parameter by regular intervals would cause over-sampling at larger depths, where a large change in depth causes miniscule changes in R_{rs} that are typically overshadowed by noise from a sensor, and under-sampling at shallower depths where a small change in depth causes a significant change in R_{rs} (Hedley et al., 2009).

Hedley et al. (2009) devised the Adaptive Look-Up-Tree (ALUT) technique where points¹ in the automated table construction are chosen based on spectral differences of R_{rs} between successive points, rather than simply separating the points by regular intervals as in the case of Mobley et al. (2005). In other words the ALUT seeks an evenly sampled spectral space rather than an evenly sampled parameter space. Spectral matching of an input R_{rs} to its corresponding R_{rs} in the table is performed with binary space partitioning trees and allows a more efficient search than by comparing each individual R_{rs} . The ALUT method was extended in Dekker et al. (2011) to include

¹ a point in the LUT represents a set of real value parameters (i.e. depth, absorption and backscattering coefficients, bottom reflectance)

the local linear gradient of each R_{rs} in the LUT (denoted Adaptive Linearised Look-Up-Tree, ALLUT). The premise behind this is that the input R_{rs} will not perfectly match any of the R_{rs} in the table due to residual discretisation errors. Therefore the corresponding local linear gradient will pin point exactly where the input R_{rs} will lie in parameter space within the corresponding voxel of the table. The ALUT method shows improved accuracies in depth, IOP and bottom substrate retrievals over conventional LUT methodology.

Table 2.2: Comparison of pre-processing steps, parameterisations of shallow water models, optimisation cost functions for the HOPE, BRUCE, SAMBUCA inversion models and the ALLUT forward models as described in Dekker et al. (2011).

	HOPE	BRUCE	SAMBUCA	ALLUT
Pre-processing	$R_{rs}^1(\lambda) = R_{rs}^{Raw}(\lambda) - R_{rs}^{Raw}(750)$ $R_{rs}^1(750) = 0.02R_{rs}^1(650) + 0.0001$ $R_{rs}^{corr}(\lambda) = R_{rs}^1(\lambda) + R_{rs}^1(750)$	$R_{rs}^1(NIR)$ $= \text{median}[R_{rs}^{raw}(650): R_{rs}^{raw}(800)]$ $R_{rs}^{corr}(\lambda) = R_{rs}^{raw}(\lambda) + R_{rs}^1(NIR)$	Substratum detectability index, $SDI = \max\left(\frac{ r_{rs}^{model} - r_{rs}^{dp} }{NE\Delta r_{rs}}\right)$	N/A
water-to-air interface	$R_{rs}^{corr}(\lambda) = \frac{0.5r_{rs}}{1 - 1.5r_{rs}}$	$R_{rs}^{corr}(\lambda) = \frac{0.5r_{rs}}{1 - 1.5r_{rs}}$	$R_{rs}(\lambda) = \frac{0.5r_{rs}}{1 - 1.5r_{rs}}$	$R_{rs}(\lambda) = \frac{0.55r_{rs}}{1 - 1.5r_{rs}}$
$r_{rs}^{dp}(\lambda) \approx$	$(0.084 + 0.170u)u$	$(0.084 + 0.170u)u$	$(0.084 + 0.170u)u$	$(0.084 + 0.170u)u$
$a(\lambda) =$	$a_w + Pa_{phy} + Ge^{-S_{CDOM}(\lambda-440)}$	$a_w + Pa_{phy} + Ge^{-S_{CDOM}(\lambda-440)}$	$a_w + C_{CHL}a'_{phy}$ $+ C_{CDOM}a'_{CDOM}(440)e^{-S_{CDOM}(\lambda-440)}$ $+ C_{NAP}a'_{NAP}(440)e^{-S_{NAP}(\lambda-440)}$	As in HOPE
$b_b(\lambda) =$	$b_{bw} + X\left(\frac{550}{\lambda}\right)^Y$	$b_{bw} + X\left(\frac{550}{\lambda}\right)^Y$	$b_{bw} + C_{CHL}b_{bphy}'\left(\frac{548}{\lambda}\right)^{Y_{phy}}$ $+ C_{NAP}b_{bNAP}'\left(\frac{548}{\lambda}\right)^{Y_{NAP}}$	$b_{bw} + X\left(\frac{440}{\lambda}\right)^Y$
$\rho(\lambda) =$	$\rho = B\rho_{sand}^*$ If $R_{rs}(550) > 0.01$ & $R_{rs}(710)/R_{rs}(670) > 1.2$ then $\rho = B\rho_{seagrass}^*$	$B_1\rho_1^* + B_2\rho_2^* + B_3\rho_3^*$	$f_i\rho_i + (1 - f_i)\rho_i$	$f_i\rho_i + (1 - f_i)\rho_i$

Table 2.2: continued

	HOPE	BRUCE	SAMBUCA	ALLUT
Cost functions	$\frac{\sqrt{\sum_{400}^{675} (R_{rs} - \hat{R}_{rs})^2 + \sum_{750}^{800} (R_{rs} - \hat{R}_{rs})^2}}{[\sum_{400}^{675} R_{rs}] + [\sum_{750}^{800} R_{rs}]}$	$\sqrt{\frac{\sum_{400}^{800} (R_{rs} - \hat{R}_{rs})^2}{N}}$	$\alpha = \cos^{-1} \frac{\sum_{400}^{800} (R_{rs} \times \hat{R}_{rs})}{[\sum_{400}^{800} (R_{rs})^2]^{0.5} [\sum_{400}^{800} (\hat{R}_{rs})^2]^{0.5}}$ $\Delta = \alpha \times \left[\frac{\sqrt{\sum_{400}^{800} (R_{rs} - \hat{R}_{rs})^2}}{\sum_{400}^{800} R_{rs}} \right]$	N/A
Optimisation scheme	Estimate P, G, X, B, H using a corrector-predictor optimisation procedure that minimises Δ	Estimate $P, G, X, B_1, B_2, B_3, H$ that minimises Δ using Levenberg-Marquardt optimisation	Estimate $C_{CHL}, C_{CDOM}, C_{NAP}, f_1,$ and H that minimises Δ using Downhill Simplex optimisation	N/A

2.5.3 Inter comparison

Dekker et al. (2011) compared the bathymetry and benthic habitat map products from the inversion and LUT routines outlined above. Table 2.2 compares the parameterisation of the HOPE, BRUCE, SAMBUCA and ALUT models, to illustrate the differences. The datasets on which these algorithms were applied were airborne hyperspectral imagery of Lee Stocking Island, Bahamas and Moreton Bay, Australia, captured using Ocean PHILLS and CASI-2 respectively. Results from Dekker et al. (2011) suggest that SA and LUT methods have comparatively high accuracies in bathymetry retrievals between 0 to 13 m depth with RMSE ranging from 0.86 m for BRUCE to 4.71 m using CRISTAL (Table 2.3). Here, the lower the RMSE the higher the bathymetry accuracy. Seagrass classification accuracy ranged from 59% using SAMBUCA to 84% with BRUCE. The overall benthic classification accuracy ranged from 52% using SAMBUCA to 79% using BRUCE (Table 2.3).

Table 2.3: A comparison between bathymetry retrievals and benthic classification accuracy of the different algorithms tested by Dekker et al. (2011). The RMSE in bathymetry between actual and derived are presented for Lee Stocking Island (LSI) and Moreton Bay (MN) respectively. The classification accuracy was only assessed in MB between 0-3 m.

Algorithm	Model type	Bathymetry	Classification accuracy (%)	
		RMSE (m) LSI, MB	Seagrass Reference = 89%	Overall Reference = 89%
BRUCE	SA	0.86, 2.11	84	79
SAMBUCA*	SA	1.30, 0.96	59	52
HOPE	SA	1.12, 3.17	N/A	N/A
CRISTAL	LUT	1.14, 4.71	83	65
ALLUT	LUT	2.24, 2.36	79	78
Lyzenga (1985)	Empirical	1.68, 3.12	N/A	N/A

*Substratum Detectability Index (SDI) used – see text.

The cause of the differences in bathymetry RMSE and benthic classifications accuracies (Table 2.3) are due to algorithm differences as well as the different pre-processing steps and optimisation algorithms employed by the SA models. For SA models the accuracy in bathymetry and benthic classification is dependent on how suitable their assumptions to the RTE are, where in addition the total absorption and backscattering coefficients are decomposed into a limited set of optically active constituents. In contrast, the accuracy of the LUT methods is dependent on whether

the finite IOP, depth and bottom substrate combinations are representative of the imaged area. It should be noted that both SA and LUT methods must define the benthic endmembers and spectral shapes of the IOPs beforehand.

The varying pre-processing steps performed by the inversion and LUT algorithms may have an impact on the accuracy of the retrievals. For instance the CRISTAL method did not correct for sunglint contamination, while HOPE and BRUCE did, but they used different correction algorithms (Table 2.2). It is unclear from Dekker et al. (2011) the sunglint correction algorithms (if any) performed by the SAMBUCA and ALUT methods. Also HOPE, BRUCE and SAMBUCA used different optimisation algorithms with different cost functions, which would likely create differences in the retrievals. Note that ALUT and CRISTAL are spectral matching techniques and as such do not perform spectral optimisation. Also included in SAMBUCA, and not used by other algorithms, is the substratum detectability index (SDI) to flag quasi-optically deep and optically deep pixels from the inversion process. Bathymetry retrievals from inversion and LUT methods are generally poor for such pixels as the proportion of bottom reflectance in the total reflectance signal is very small or non-existent. Hence quasi- to optically deep pixels typically act to increase the RMSE between retrieved and actual depths. Dekker et al. (2011) also showed that SA and LUT methods that accounted for the mixing of more than one benthic type retrieved more accurate water column corrected bottom reflectance – although lower classification accuracies were obtained in areas whose benthos were not represented in the spectral library.

There are several advantages of physics-based inversions and LUT approaches to hyperspectral imagery such as minimising the non-uniqueness issues plagued by band ratio approaches for bathymetry retrieval, and the avoidance of *in situ* data calibration. The hyperspectral algorithms presented in this section also can provide water column corrected bottom reflectances leading to potentially improved benthic classification and the ability to assign fractional coverage of different classes. Such spectral matching and unmixing approaches therefore lead away from the limitations of supervised and unsupervised thematic mapping described in section 2.4.

2.6 Uncertainty Estimation and Future Directions

As with all natural systems there is inherent undesired noise in the sensor-derived R_{rs} spectrum. In the case of shallow water SA algorithms, such noise leads to uncertainties in the retrieved depth, IOPs and bottom substrate albedos (Hedley et al., 2010). Uncertainty in R_{rs} can also lead to non-uniqueness issues. A noise-free R_{rs} corresponds to a unique combination of environmental parameters (Mobley et al., 2005), however when uncertainty is added, a variety of different combinations of environmental parameters can form that particular R_{rs} within the error bounds (Hedley et al., 2010), hence being non-unique. Quantifying the uncertainty is therefore crucial to understanding the precision of the geophysical parameters, the level of optical closure, non-uniqueness and whether the level of precision is suitable for any subsequent ecological interpretation. In this section we focus on uncertainty due to sensor and environmental noise, and not due to SA model approximations or uncertainty caused when the modelled spectral shapes of the IOPs are varied as done by Wang, Boss, and Roesler (2005). Other forms of uncertainty assessments not considered in this research includes uncertainty in the methodology of field based radiometric measurements (Antoine et al., 2008). In remote sensing, uncertainty in the R_{rs} derived by satellite or airborne sensors is introduced mainly by the sensor and the environment conditions that processing steps, such as atmospheric, sunglint and air-water interface corrections attempt to remove (Hedley et al., 2010).

Any given hyperspectral imager has noise and offsets attributed to it; offsets are generally corrected for by the appropriate calibration. Sensor noise, a consequence of photon noise, dark current noise and digitisation noise (Moses, Bowles, Lucke, & Corson, 2012), is random and its magnitude typically varies over the spectral bands. The previous section illustrated that both SA and LUT methods require R_{rs} or r_{rs} as input. Ignoring whitecaps, the radiance received by the sensor is a summation of the solar irradiance scattered by the atmosphere, sunglint, sky glint and water leaving radiances modulated by the absorptive and scattering properties of the atmosphere (Gordon & Wang, 1994); corrections need to be performed to extract the water leaving radiance from the at-sensor radiance. Physical based atmospheric correction algorithms such as Tafkaa (Gao, Montes, Ahmad, & Davis, 2000), FLAASH (Matthew et al., 2003) and HyCorr exist that are able to derive either the at-surface reflectance or sunglint-corrected R_{rs} . With the necessary spectral bands, these algorithms are able

to invert the at-sensor radiance to estimate the required atmospheric properties for atmospheric correction at each pixel in a hyperspectral image. The atmospheric inversion is typically performed from finite size lookup tables of atmospheric parameters for a set of solar and sensor angles. Interpolation is typically performed between the atmospheric parameters of the LUT to match the actual solar and sensor angles during image acquisition. Hence given the use of LUTs and interpolations, atmospheric correction approximates the atmospheric parameters encountered in the image.

Atmospheric correction typically provides at-surface reflectance. Subsequent sunglint correction must then be performed to remove any contamination from specular reflection from the water's surface. Sunglint algorithms such as those proposed by Hedley, Harborne, and Mumby (2005), Goodman, Lee, and Ustin (2008) and those in the pre-processing steps of HOPE and BRUCE (see Table 2.2) are image-based rather than physics-based corrections. The reason being that sunglint is dependent on the slope statistics of the individual wave facets, wind speed and direction and the sun-sensor angular geometry at the time of the image acquisition (Kay, Hedley, & Lavender, 2009). The spatial resolution of the sensor is typically greater than an individual wave facet, and thus the wave facet slope distribution is not estimated directly per pixel but instead the Near Infra Red (NIR) reflectance is used as a glint indicator, based on the assumption the subsurface reflectance is zero in the NIR (Kay et al., 2009).

Such approximations to these crucial radiometric corrections typically leave residual spatial noise in hyperspectral imagery as illustrated in Figure 1b in Hedley et al. (2005) and Figure 7 in Kay et al. (2009). Estimating the magnitude of such spatial noise arising from sensor and environmental noise is crucial in quantitating the uncertainty in the retrieved parameters from the SA models. Deriving the uncertainties of the various SA model parameters cannot be determined through analytical expressions as done in Lee, Arnone, Hu, Werdell and Lubac (2010). The reason for this is that the R_{rs} determined by a SA inversion algorithm never exactly matches the sensor-derived R_{rs} thus inhibiting a direct analytical expression of the uncertainty in R_{rs} to that of the derived parameters. Furthermore the R_{rs} computed is also dependent on whether a global or local minimum was converged to during the optimisation. Hedley et al. (2010) developed a simple numerical method for the propagation of uncertainty through the inversion process of a SA model. Here the combined sensor

and environmental noise is estimated from an imaged homogeneous deep water region where the assumption of constant IOPs is valid. The spectral covariance matrix of such a region is then used to compute a set of noise-perturbed R_{rs} spectra for any given pixel. Inverting these spectra allows the estimation of the range of IOPs, depth and bottom albedo that that pixel is likely to have due to sensor and environmental noise. This method is in line with Salama and Stein (2009) who determined the uncertainty in R_{rs} due to sensor noise and atmospheric correction variability due to fluctuations in the aerosol optical thickness. In Salama and Stein (2009) the probability distribution of the IOPs due to uncertainty in R_{rs} is determined solely from the upper and lower bounds of the variability of R_{rs} . Under the assumption that the IOPs follow a lognormal probability distribution a series of refinement steps and look up tables are used to determine the posterior probability from which the uncertainties in the IOPs are determined. The method by Hedley et al. (2010) follows a much simpler approach where the variability in R_{rs} is contained in the image spectral covariance matrix, and through a process of bootstrapping determines the uncertainty in the products.

Hedley et al. (2010) and Hedley et al. (2012a) showed that uncertainty in the retrieved depth and proportion of benthic type from hyperspectral airborne imagery is quite variable, with the most precise retrievals occurring over shallow sand substrates with low water turbidity. Under these conditions the retrieved depth was shown to be quite precise up to 10 m depth. As the water turbidity is increased the uncertainty in the depth is shown to increase, particularly for depths greater than 5 m. The precision of the retrieved depth decreases even further when different (usually darker than sand) substrates are included in the analysis. Sand substrates produce the most precise retrievals because of their high albedo which increases the SNR. Such an analysis indicates that bathymetric precision is dependent on the SNR and sensor and environmental noise. Clearly the need to quantitate the uncertainty is crucial as it would vary from pixel to pixel in an image depending on the depth, substrate albedo and water turbidity. This is especially important if subsequent analysis is performed on the bathymetry product. For instance analysing the underlying geophysical processes that cause temporal changes in bathymetry would require the selection of those pixels that achieved high enough precision for statistical significance. Such an extension and application of these SA models with uncertainty propagation is exemplified with a time series of satellite hyperspectral imagery in Chapter 3 (Garcia, Fearn, & McKinna, 2014).

Hedley et al. (2010; 2012a) showed that in some pixels the variation in the proportion of benthic cover can exceed 100% of the actual value. Indeed the uncertainty in substrate cover was shown to be dependent on the number of benthic endmembers in the spectral library, the depth and spectral resolution of the sensor. Increasing the number of benthic endmembers by including spectra of individual species rather than using the averaged spectra for each genus, reduced the precision in benthic cover. This was attributed to larger degrees of freedom during spectral optimisation when more benthic endmembers were used. Furthermore, a more complex spectral library would contain endmembers that have very similar spectra, and would increase the spectral confusion between endmembers when sensor and environmental noise is propagated. A simplified spectral library containing only average spectra of the representative genera thereby produces lower inter-class confusion and hence lower uncertainty as shown in Hedley et al. (2010; 2012a). Note that using a simplified spectral library may not maximise the potential of remote sensing. Karpouzli, Malthus and Place (2004) showed that for high spectral resolution, clustering pure endmembers based on their genus to give a simplified library of average coral, seagrass, macroalgae and sand reduced subsequent classification accuracy. In this case higher classification accuracy was obtained with a more complex spectral library. To date, a method that clusters the endmembers in a complex library to produce a more simplified library that optimises the uncertainty and accuracy in benthic classification has not been described in the literature. A method that can potentially resolve this issue is proposed in Chapter 5 (Garcia, Hedley, Hoang, & Fearn, 2015).

The SA models described in section 2.5.1 utilise a complex spectral library of endmembers as outlined in Dekker et al. (2011). Under such parameterisations, specific benthic classes would be obtained for a range of environmental conditions even in situations where it is unlikely that one benthic species can be distinguished from another. For instance at increased depth or decreased water clarities, certain benthic species may not be resolvable particularly when incorporating sensor and environmental noise – as illustrated by Hedley et al. (2012b). For remote sensing applications, being able to quantitate which benthic species are spectrally distinct for any environmental condition above sensor and environmental noise is key in assessing the potential and limitations in benthic classification. With the exception of Hedley et al. (2012b), research into the environmental conditions that enable the spectral

distinction of benthic substrates have been limited to a few different water types and mainly focused on the depth limits at which substrates are no longer detectable above the reflectance of deep water, as described below.

Lubin, et al. (2001) compared the top-of-atmosphere (TOA) radiances of sand, coralline algae, green macroalgae, algal turf and four coral species. Clear oceanic waters with a flat air-water interface and an atmosphere with maritime aerosols were considered for the modelling of TOA radiances. Under these idealised conditions, the modelling showed that the differences in radiance between sand, coralline algae, and the corals are large enough to enable their spectral distinction using remote sensing at a given depth up to 20 m. Hochberg et al. (2003) investigated the depth at which a coral substrate was no longer observable for three water types (pure water and clear and turbid reef water) at depths ranging from 0-30 m. With the depth limit, z_{lim} , set at where the coral substrate signal contributed 5% of the total R_{rs} , Hochberg et al. (2003) showed that z_{lim} was wavelength dependent and decreased with increasing water turbidity. An analysis of whether coral is distinguishable from other substrates was not performed at any of the modelled depths and water types. In an analogous manner, Kutser et al. (2006) used a bio-optical model coupled with in-air spectral reflectances of several benthic macroalgae to determine the maximum depths where spectral differentiation is still possible. The optical properties of the water column used in the modelling were based on that typically encountered in the CDOM-dominated Estonian Archipelago. The depth limit was inferred when the spectral difference between the modelled R_{rs} of a benthic substrate and of optically deep water was less than the SNR of the sensor.

Vahtmae et al. (2006) extended this analysis to include hyperspectral sensors and spectral distinction between algal species at different depths. Based on spectral differences above the SNR the following general trends were inferred: green macroalgae was detectable from sand to 10 m depth; red and brown macroalgae were distinguishable from sand to 11 m; brown and green macroalgae can be separated to 8 m; green and red macroalgae are distinct to 8 m, and; brown and red macroalgae are separable to 4 m. This type of analysis however did not consider which benthic substrates are distinguishable at a given depth. For instance although green and red macroalgae are separable to 8 m, brown and red macroalgae are not distinguishable beyond 4 m. Thus at 5 m, sand, green algae and mixed brown/red macroalgae would likely be distinguishable. After 8 m, green algae is no longer distinguishable from

brown or red macroalgae, and thus only sand would be separable from a green/brown/red macroalgae mixture. Beyond 11 m sand is no longer distinguishable from the mixed vegetation as the water column dominates the water leaving reflectance.

Hedley et al. (2012b) developed a generic method to assess at what scenarios the above-surface reflectance of different benthic substrates become inseparable. Here scenarios relate to a set of environmental conditions typically encountered in coral reef ecosystems. A total of 4680 scenarios were modelled that encompassed a variety of sun elevations, wind speeds, water column IOPs, depths, sensor SNR's and benthic substrates. Radiative transfer modelling was performed for each scenario to give a set of above-surface total reflectance, R_t , which incorporates specular reflection from the water's surface. To account for sensor noise, each R_t was perturbed by the SNR to generate 30 new noise-perturbed spectra. Hierarchical class significance diagrams were used to show how the different scenarios affect the mean separability between a given pair of benthic endmembers (live coral, bleached coral, dead coral and algal turf, macroalgae). This extensive sensitivity analysis indicated the effect of the different environmental conditions on benthic separability. Some general conclusions are: (a) depth is the most influential factor governing benthic class distinction and dampens the effect of IOP variability, sun elevation, wind speed and SNR; (b) the variation in IOPs considered had minor impact on benthic class separability for depths up to 5 m; (c) higher solar zenith angles improves benthic class separability; and; (d) the influence of SNR on benthic class distinction is more pronounced at low solar zenith angles.

These modelling results provide a generic outlook on optical remote sensing for mapping coastal and coral reef ecosystems with environmental parameters (i.e. water column IOPs, depth etc.) described in the literature. However, applying a per-pixel procedure to predict the benthic classes that are optically separable given the IOPs, depth and total system noise of a given image has yet to be developed and a method is presented in Chapter 5 (Garcia et al., 2015). Such knowledge will potentially aid in what can be distinguishable and help guide the benthic classification from physics-based inversion models.

2.7 Summary

There are many methods of deriving bathymetry from remote sensing imagery. Empirically based ratio transformations, though simple to implement, suffer either from coarse approximations such as the dark pixel subtraction in the Lyzenga (1981) method, or from non-uniqueness issues in the spectral ratio approaches (Dierrsen et al., 2003; Stumpf et al., 2003; Mishra et al., 2007). In this case non-uniqueness arises as the full spectral information is not used and where the ratio of two spectral bands can generate the same value from reflectance spectra pertaining to a bright deep substrate to that of a darker substrate at a shallow depth. However, the far more limiting factor of such approaches, including those that use PCAs and ANNs are the need for *in situ* depth data calibration that often is not available concurrently or historically, particularly for very remote regions.

Benthic classification historically started with the use of multispectral satellite imagery such as Landsat and SPOT and then extended to higher spatial resolution sensors including QuickBird, and IKONOS. The lack of sufficient visible spectral bands of these sensors resulted in the use of supervised and unsupervised image classification techniques to classify the benthos in an image. Initially the raw digital numbers or at-surface reflectances were used as the basis for the thematic mapping, where the number and type of classes selected were based on knowledge of the imaged area. For supervised classification, training regions are surveyed *a priori* to identify the type of benthos that they represent. In contrast, the classes produced from unsupervised classification are determined from local knowledge or subsequent field surveys. Furthermore, as spectral unmixing of benthic endmembers was never attempted (due to the low spectral resolution) the classes are generally comprised of benthic assemblages specific to the site under investigation. This makes comparison of benthic classification maps between regions difficult. Research showed that improved benthic classification accuracies are obtained when mapping water column corrected bottom reflectances. The Lyzenga (1985) method generates depth invariant indices; however the resultant images cannot be compared with actual benthic reflectance, prohibiting direct spectral matching. In addition, for the Lyzenga (1985) method to be effective the imaged benthos must occupy a wide range of depths, which may not always be the case as shown by Andrefouet et al. (2003) and thus limits its

application. Other research that performed water column correction did so using *in situ* optical measurements and mostly assumed spatially invariant water optical properties.

Semi-analytical shallow water inversion models and lookup table approaches offer the ability to simultaneously retrieve the inherent optical properties, water depth and benthic substrate type and fractional cover. Such approaches are designed for hyperspectral imagery with sufficient number of bands and high enough SNR to detect subtle changes in the R_{rs} due to changes in depth, bottom substrate composition and IOPs. Although these methods do require some level of site-specific bio-optical model calibration such as the spectral shapes of a_{dg} , b_{bp} and benthic endmembers, they are often assumed according to either expert knowledge of the region or from literature data. An additional advantage for benthic classification is that unmixing of the bottom substrate to derive the fractional cover of the various benthic classes can be performed. Hence only a spectral library of the representative benthic endmembers is needed, rather than knowledge of the benthic assemblages that the different training datasets represent.

The accuracy of the SA models is partly dependent on the adequacy of the approximations to the RTE. For LUT methods the accuracy is dependent on how representative the finite database is to the scene in question, and whether the finite parameter steps are suitable. The ALUT developed by Hedley et al. (2009) and extended in Dekker et al. (2011) minimises this discretisation error. The accuracy of both SA and LUT methods are also dependent on whether the spectral shapes of the IOPs and benthic endmembers in the spectral library are suitable for the scene. Despite these limitations, SA and LUT methods have achieved moderate to high benthic classification accuracies and high bathymetry accuracies below 10 m depths. Propagating uncertainty through SA inversion models has seldom been performed, and as a consequence the potential and limitations of bathymetry and benthic classification derived using SA models from hyperspectral imagery has not been explored. This thesis attempts to utilise uncertainty arising from sensor and environmental noise to: (a) determine the conditions that enable and prohibit the derived bathymetry in detecting temporal changes in depth, and; (b) quantify the number and type of optically distinguishable benthic species above the total system noise and attenuating properties of a variable water column in an effort to quantify the limitations and potential of benthic classification from optical remote sensing.

CHAPTER 3

CHALLENGES IN DETECTING TREND AND SEASONAL CHANGES IN BATHYMETRY DERIVED FROM HICO IMAGERY: A CASE STUDY OF SHARK BAY, WESTERN AUSTRALIA

This chapter has been published in the journal: Remote Sensing of Environment

Rodrigo A. Garcia, Peter R. C. S. Fearn, Lachlan I. W. McKinna. Detecting Trend and Seasonal Changes in Bathymetry derived from HICO imagery: A case study of Shark Bay, Western Australia. *Remote Sensing of Environment*, 147 (2014), pp. 186-205. DOI: <http://dx.doi.org/10.1016/j.rse.2014.03.010>. <http://www.sciencedirect.com/science/article/pii/S0034425714000819>.

3.1 Abstract

The Hyperspectral Imager for the Coastal Ocean (HICO) aboard the International Space Station has offered for the first time a dedicated space-borne hyperspectral sensor specifically designed for remote sensing of the coastal environment. However, several processing steps are required to convert calibrated top-of-atmosphere radiances to the desired geophysical parameter(s). These steps add various amounts of uncertainty that can cumulatively render the geophysical parameter imprecise and potentially unusable if the objective is to analyse trends and/or seasonal variability. This research presented here has focused on: (1) atmospheric correction of HICO imagery; (2) retrieval of bathymetry using an improved implementation of a shallow water inversion algorithm; (3) propagation of uncertainty due to environmental noise through the bathymetry retrieval process; (4) issues relating to consistent geo-location of HICO imagery necessary for time series analysis, and; (5) tide height corrections of the retrieved bathymetric dataset. The underlying question of whether a temporal change in depth is detectable above uncertainty is also addressed. To this end, nine HICO images spanning November 2011 to August 2012, over the Shark Bay World Heritage Area, Western Australia, were examined. The results presented indicate that precision of the bathymetric retrievals are dependent on the shallow water inversion algorithm used. Within this study, an average of 70% of

pixels for the entire HICO-derived bathymetry dataset achieved a relative uncertainty of less than $\pm 20\%$. A per-pixel t -test analysis between derived bathymetry images at successive timestamps revealed observable changes in depth to as low as 0.4 m. However, the present geolocation accuracy of HICO is relatively poor and needs further improvements before extensive time series analysis can be performed.

3.2 Introduction

Detecting change in the near-shore coastal marine environment is necessary for understanding mechanisms that drive change in these dynamic systems. One important challenge for coastal marine managers is detecting change in bathymetry over large areas in a timely manner. With such information, informed decisions can be made for efficient and effective management of these fragile ecosystems (Fabbri, 1998; Galparsoro et al., 2010). The bathymetry of the near-shore could change seasonally or in response to acute disturbances, such as storms and extreme weather events (Morton, 2002; Morton & Sallenger, 2003), or human induced disturbances such as dredging (Cooper et al., 2007). These changes can have flow-on impacts to the marine flora and fauna that resource managers are tasked to protect. As such, accurate bathymetric monitoring techniques that are time and cost effective are required to assess any residual geological and ecological impacts.

Accurate bathymetry maps can be achieved using active remote sensing such as an airborne LiDAR system (Irish & Lillycrop, 1999; Guenther, Cunningham, LaRocque, & Reid, 2000). However, frequent long-term monitoring of large coastal areas can be costly even with airborne systems. Satellite-based passive remote sensing offers an even more cost effective means of obtaining bathymetry maps as it can repeatedly sample large areas (hundreds to thousands of square kilometres) frequently (Green, Mumby, Edwards, & Clark, 1996). The temporal resolution and large spatial coverage makes satellite remote sensing ideal for monitoring changes in bathymetry over large areas.

One of the first quantitative methods of measuring bathymetry from multispectral imagery was proposed by Polcyn et al. (1970). This method manipulates the ratio of two spectral indices to generate a semi-empirical relationship for depth. This algorithm can remove the influence of varying water clarity and bottom

reflectance only in very specific conditions (see Polcyn et al., 1970) that are rarely encountered in the coastal ocean.

Lyzenga (1978) proposed a linearised multiband bathymetry algorithm that corrects for bottom type variation. This algorithm however requires a depth calibration from *in situ* depth data and, as such, the approach is scene-specific (Paredes & Spero, 1983; Lyzenga, 1985; Clark et al., 1987) though has been shown to give improved results over the band ratio algorithm of Polcyn et al. (1970) (Clark et al., 1987). Practical complications arise when a scene has varying water clarity and undefined depths when the water leaving reflectance of a shallow area is less than that over deep water (Philpot, 1989). Other algorithms that use *in situ* depth data for tuning empirical coefficients include Dierssen et al. (2003) and Stumpf et al. (2003), both of which use spectral band ratios.

Although the algorithms proposed by Lyzenga (1978), Dierssen et al. (2003) and Stumpf et al. (2003) can be accurate with imagery that fit their empirical constraints, they still require *in situ* depth data which often is not available, historically or con-currently. Thus for the purposes of transferability between sensors and scenes, it is crucial to have bathymetric algorithms that circumvent the need for *in situ* data.

Semi-analytical, physics-based shallow water inversion algorithms (HOPE in Lee et al., 1998; 1999; BRUCE in Klonowski et al., 2007; SAMBUCA in Wettle and Brando, 2006 and Brando et al., 2009) and Look-up-table (LUT) techniques (CRISTAL in Mobley et al., 2005; ALLUT in Hedley et al., 2009) designed for hyperspectral sensors, appear to be more suitable for retrieving bathymetry, water column inherent optical properties (IOPs) and for rudimentary benthic classification (Dekker et al., 2011). An advantage of semi-analytical algorithms is their non-reliance on possibly erroneous assumptions of uniform water IOPs or bottom reflectance, or crude corrections (e.g. the deep water radiance correction). Instead, semi-analytical algorithms are derived from radiative transfer theory making them more analytically exact with lower sources of model error. Consequently, they have been used to retrieve bathymetry with relatively high accuracy from airborne hyperspectral imagery captured over optically complex coastal marine environments (Mobley et al., 2005; Klonowski et al., 2007; Brando et al., 2009; Hedley et al., 2009; Dekker et al., 2011).

Shallow water semi-analytical inversion algorithms rely on spectral matching and/or optimisation routines which require image data with enough spectral bands in the visible domain (typically: 400 – 800 nm) to resolve subtle optical signatures.

Hyperspectral image data with a modest signal-to-noise ratio (SNR) can achieve this (Philpot et al., 2003). Moreover, the spectral information provided by hyperspectral imagery minimises non-uniqueness issues, resulting in lower confidence interval limits of the retrieved parameters (Defoin-Platel & Chami, 2007; Mobley et al., 2005). The lack of accessible hyperspectral satellite imagery has limited the applicability of the physics-based semi-analytical algorithms to airborne hyperspectral imagery. However, there have been a few examples in the literature, such as Lee et al. (2007), who used HOPE to retrieve the spatial distribution of water absorption, depth and bottom reflectance from Hyperion imagery of Looe Key, Florida, USA.

Although the Hyperion sensor has over 200 spectral bands between 430-2400 nm, it was designed primarily for land-use applications and as such has a relatively low SNR that ranges from 50-150 (Ungar, 2003). Over dark targets, such as water, a low SNR effectively creates a 'noisier' signal and subtle changes in the reflectance spectrum may not be differentiated above the noise inherent to the sensor (Hu et al., 2012). This confounds the remote sensing signal leading to non-uniqueness and hence higher uncertainty of the retrieved parameter(s). However, as stated by Lee et al. (2007), many shallow coastal areas are subject to high water turbidity resulting from suspended sediment run-off or where the water-leaving radiance signal has significant contribution from a bright bottom substrate, thus in such cases, Hyperion may have a high enough SNR to afford results with higher confidence. These represent a limited range of coastal environmental conditions suitable for Hyperion applications, as these waters may also be subject to highly absorbing waters (due to phytoplankton and/or coloured dissolved organic matter), dark bottom substrates (such as seagrass and algae), and large bathymetric ranges that requires higher SNR for more accurate assessments.

The Hyperspectral Imager for the Coastal Ocean (HICO) is the first prototype, low cost sensor onboard the International Space Station designed with the necessary specifications for remote sensing of a diverse range of coastal marine environments (Lucke et al., 2011). HICO has a spatial resolution of 96×96 m at nadir with 87 contiguous spectral bands between 400-900 nm. HICO's SNR varies spectrally but is generally greater than 200 between 400 and 600 nm, and ranges from 100-200 between 600 and 700 nm (Lucke et al., 2011). These sensor attributes make HICO suitable for analysing the spectral and spatial complexity encountered in many coastal marine environments throughout the globe.

To date, there has been limited work reported on the routine monitoring of bathymetry using standardised processing of satellite hyperspectral imagery. In this chapter, the semi-analytical Bottom Reflectance Un-mixing Computation of the Environment inversion algorithm (BRUCE: Klonowski et al., 2007) is used to retrieve bathymetry from multi-temporal HICO imagery of the Shark Bay World Heritage Area, Western Australia. Of conservational interest and the focal point of the temporal analysis is the Faure Sill, a shallow water region within Shark Bay noted for its unique seascape and ecological features. This Chapter's aims are: (1) to test whether a change in bathymetry is measurable above statistical uncertainty through time; (2) examine the robustness of the Tafkaa (Gao et al., 2000) atmospheric model when applied to HICO imagery whose spectral range does not extend beyond 900 nm; (3) to determine the precision of a HICO-derived bathymetric dataset using an improved implementation of the BRUCE model, specifically redesigned to allow uncertainty propagation; (4) compare tide correction techniques and; (5) to study the geolocation accuracy of HICO imagery and its implication to routine monitoring.

3.3 Methodology

3.3.1 Study area and HICO imagery

Shark Bay is a World Heritage Area located in the northwest of Western Australia (Figure 3.1), covering an area of ~14 000 km². This shallow coastal bay has two major sub-embayments orientated in a NW-SE direction; Freycinet Reach, located to the west of the Peron peninsula, and Hopeless Reach on the east. In this case study the analysis is limited to Hopeless Reach with focus on the Faure Sill; a shallow (1-2 m in depth) region ~30 km long and ~15 km wide, containing several narrow water channels (5-6 m in depth) extending into Hamelin Pool and which run parallel to the tidal currents (Burling, Pattriaratchi, & Ivey, 2003; Walker, Kendrick, & McComb, 1988). Shark Bay's seascape, ecology and corresponding hydrodynamics are inter-related and unique. Semi-enclosed by three islands, Shark Bay experiences limited oceanic exchange and mixing, and combined with low annual rainfall (low land runoff) results in calm waters (Department of Environment and Conservation, no date). These are favourable conditions for seagrasses which cover ~4200 km² of Shark Bay (Walker et al., 1988). These extensive seagrass meadows influence the sedimentation processes within Shark Bay and over time have created large sand banks (e.g. the Faure Sill) that

restrict water movement into Hamelin Pool, a unique hypersaline region inhabited by stromatolites (Logan & Cebulski, 1970).

A total of nine HICO images, each with a central image coordinate of $\sim 25.9^{\circ}\text{S}/113.9^{\circ}\text{E}$, were captured over Shark Bay, Western Australia, from 19 November 2011 to 8 August 2012. Pseudo true colour imagery of the HICO dataset are displayed in Figure 3.2. Two different swath orientations of HICO were observed: NW-SE and SW-NE, with the Faure Sill captured within successive swaths. Though each swath had the same coverage/footprint, they often appeared to have a slight translational drift (illustrated in Figure 3.1).

All HICO image data and geographic look-up-tables (GLTs) used in this study were accessed through the Oregon State University, College of Earth, Ocean, and Atmospheric Sciences, HICO web portal (hico.coas.oregonstate.edu). Note, the distributed HICO level-1B (L1B) calibrated radiance files had both spectral and radiometric vicarious calibrations (Gao et al., 2012) and, second order light effect corrections applied (Li, Lucke, Korwan, & Gao, 2012).

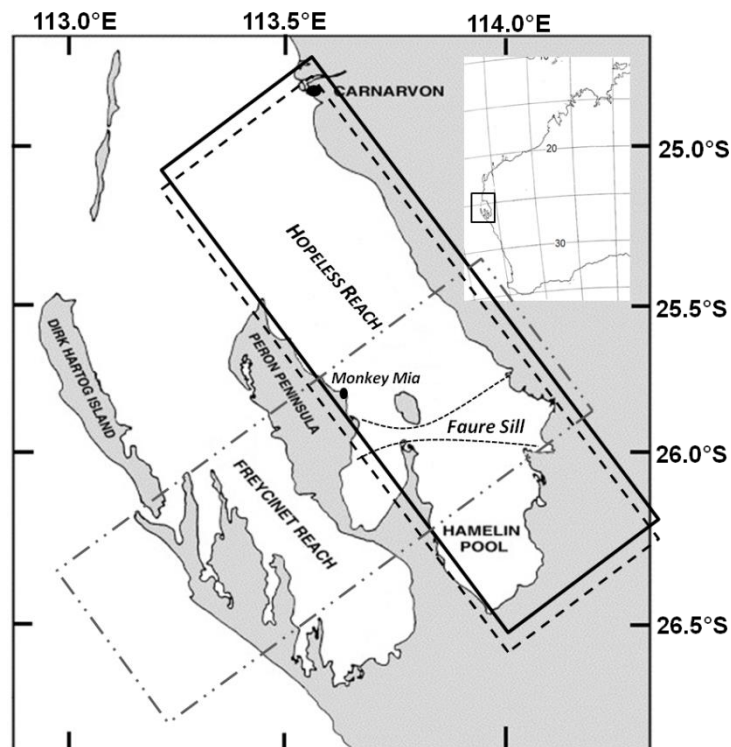


Figure 3.1: Shark Bay, Western Australia, with the Faure Sill located between the two curved black dotted lines. The solid black and dot-dot-dashed grey rectangles show the different approximate orientations of the HICO swaths. The dashed black rectangle illustrates the translational drift in the HICO swath position.

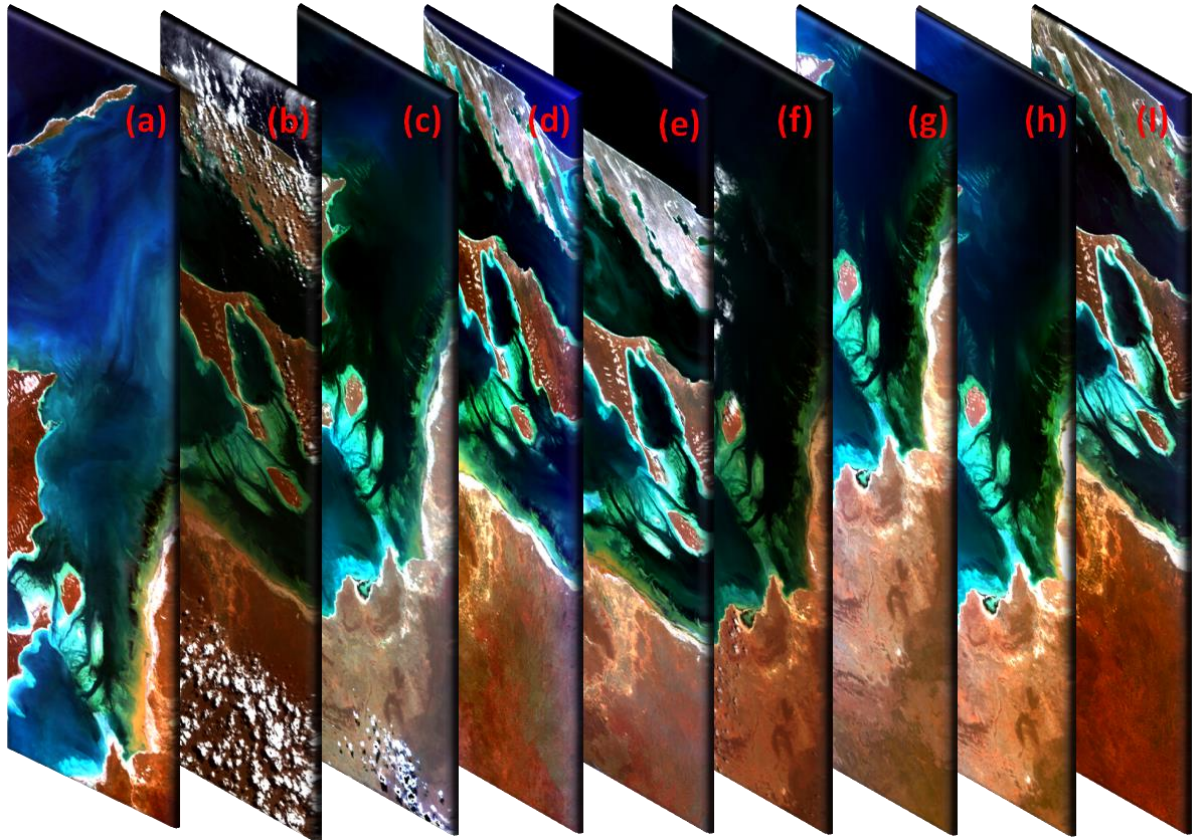


Figure 3.2: pseudo true colour composites of the HICO-derived remote sensing reflectance imagery over Shark Bay, WA, on: (a) 19-Nov-2011; (b) 14-Dec-11; (c) 21-Jan-2012; (d) 07-Feb-12; (e) 27-Feb-12; (f) 02-Apr-12; (g) 01-Jun-12; (h) 04-Jun-12, and; (i) 08-Aug-12. The apparent illumination variation between these images is due to the different scaling used to generate the pseudo true colour composites.

3.3.2 Atmospheric Correction

The Second Simulation of the Satellite Signal in the Solar Spectrum (6S) implementation of the Tafkaa algorithm (Gao et al., 2000) was used to atmospherically correct the level-1B, calibrated top-of-atmosphere radiance imagery. The standard Tafkaa 6S algorithm uses several bands greater than 900 nm to estimate key atmospheric parameters - namely, the aerosol model, the aerosol optical thickness, AOT, at 550 nm, the vertical column water vapour, ozone concentration and the atmospheric and aerosol models in a per-pixel basis (Gao et al., 2000). However, HICO lacks any SWIR and IR (> 900 nm) bands and thus limits the application of Tafkaa-6S. Previous research has highlighted the importance of selecting appropriate AOT values for Tafkaa when atmospherically correcting HICO scenes (Paterson & Lamela, 2011). Therefore, within this study, coincident MODerate resolution Imaging Spectroradiometer (MODIS) level-2 data of Shark Bay were used to estimate the AOT

at 550 nm, vertical column water vapour, CLMVAP, and ozone concentration which were then used to parameterise the Tafkaa 6S algorithm. The MODIS imagery of Shark Bay, were downloaded from the Ocean Biology Processing Group data browse website (<http://oceancolor.gsfc.nasa.gov/cgi/browse.pl?sen=am>) and processed from raw radiance counts (level 0) to calibrated TOA radiance (level-1B). The standard MODIS ocean colour atmospheric correction algorithm (Ahmad et al., 2010; Bailey, Franz, & Werdell, 2010) implemented in SeaDAS 6.4 was then used to obtain the three atmospheric properties.

Simplified at-nadir viewing geometry was assumed and the Tafkaa 6S aerosol and atmospheric model were fixed to “maritime” and “mid-latitude summer” respectively for all HICO scenes as these were deemed the most appropriate for Shark Bay. Hence Tafkaa 6S was not used to solve for any atmospheric properties using HICO’s NIR bands; rather it removed the atmospheric radiance signal based on predefined inputs. Note: (1) MODIS data were not used to select these Tafkaa 6S models, where the vertical pressure, temperature and relative humidity profiles are described; (2) given the atmospheric model and the atmospheric water vapour, Tafkaa 6S then determines the vertical structure of the water vapour (Montes, Gao, & Davis, 2004), and; (3) the aerosols in Tafkaa 6S all assume 70% relative humidity (Montes et al., 2004).

Table 3.1: MODIS-derived vertical column of water vapour (CLMVAP), aerosol optical thickness at 550 nm (AOT) and ozone concentration, with the solar-viewing geometries for each HICO overpass of Shark Bay, WA. The time presented is Australian Western Standard Time (WST; UTC +8 hours). Here θ_w , θ_v and ϕ_r are the solar zenith, viewing zenith and relative azimuth angles respectively.

HICO overpass	MODIS overpass	CLMVAP (cm)	AOT (550 nm)	Ozone (atm-cm)	θ_w (°)	θ_v (°)	ϕ_r (°)
19-Nov-11, 1632 hrs	19-Nov, 1435 hrs	1.8	0.08	0.28	60.02	21.4	-214.1
14-Dec-11, 1539 hrs	14-Dec, 1425 hrs	2.0	0.1	0.27	45.25	6.3	-128.6
21-Jan-12, 1538 hrs	21-Jan, 1350 hrs	2.7	0.15	0.26	42.45	23.2	-41.98
07-Feb-12, 1722 hrs	07-Feb, 1435 hrs	3.0	0.15	0.25	66.50	36.6	-128.96
27-Feb-12, 0940 hrs	27-Feb, 1410 hrs	3.0	0.35	0.25	45.47	13.4	58.35
02-Apr-12, 1035 hrs	02-Apr, 1440 hrs	2.3	0.055	0.26	41.06	20.8	1.12
01-Jun-12, 1038 hrs	01-Jun*, 0005 hrs	1.7	0.035	0.26	53.99	16.1	16.93
04-Jun-12, 0932 hrs	04-Jun, 1355 hrs	1.0	0.035	0.26	63.31	4.09	2.25
08-Aug-12, 1625 hrs	08-Aug, 1440 hrs	1.45	0.045	0.27	71.00	16.7	-165.56

* MODIS Terra

The lack of concurrent *in situ* above-water radiometry, photometry or AERONET data prevented a quantitative measure of the accuracy of the atmospheric correction. However, a cursory evaluation of the atmospheric correction was performed by examining the reflectance spectra for two locations representing: (i) bright shallow water (25.907 °S/113.934 °E), and (ii) quasi-deep water (25.718 °S/113.978 °E), through time. It should be noted that atmospheric correction removes approximately 90% of the signal that any satellite sensor records. Thus under- or over-corrections and spectral artefacts introduced to R_{rs} can be delineated from changes in the optical properties of the water column at these positions through time.

3.3.3 Retrieval of bathymetry using the BRUCE model

According to Lee et al. (1998, 1999), the hyperspectral sub-surface remote sensing reflectance signal, $r_{rs}(\lambda)$, of a shallow water pixel can be modelled as a function of the total in-water spectral absorption and backscattering coefficients, $a(\lambda)$ and $b_b(\lambda)$, the spectral benthic albedo, $\rho(\lambda)$, the geometric depth (i.e. bathymetry), H , the sub-surface solar zenith angle, θ_w , and the sub-surface viewing angle from nadir, θ_v .

$$r_{rs}(\lambda) = f(a(\lambda), b_b(\lambda), H, \rho(\lambda), \theta_v, \theta_w) \quad (3.1)$$

The view and solar geometries can be considered as fixed, or known. The total absorption coefficient is a function of the absorption of pure water, phytoplankton and colour dissolved organic and detrital matter (CDOM), and the total backscattering coefficient is function of the backscattering of pure water and suspended particulates, as given by,

$$\begin{aligned} a(\lambda) &= a_w(\lambda) + P a_{phy}(\lambda) + G e^{-0.015(\lambda-440)} \\ b_b(\lambda) &= b_{bw}(\lambda) + X \left(\frac{550}{\lambda} \right)^{1.0} \\ \rho(\lambda) &= \sum_{i=1}^{n=3} B_i \rho_i(\lambda) \end{aligned} \quad (3.2)$$

where a_w and b_{bw} are the spectral absorption and backscattering coefficients of pure water, respectively. a_{phy} is the spectral absorption coefficient of phytoplankton normalised at 440 nm; B_i is the bottom albedo coefficient at 550 nm and ρ_i is spectral irradiance reflectance normalised at 550 nm of benthic class i , respectively. The scalars P and G are the magnitudes of the absorption coefficients of phytoplankton and CDOM respectively, whilst X is the magnitude of the particulate backscattering coefficient. Thus, the shallow water forward model can be expressed as:

$$r_{rs}(\lambda) = f(P, G, X, H, B, \theta_v, \theta_w) \quad (3.3)$$

Though the spectral shapes and slopes of the optically active in-water constituents and benthic end-members were predefined and fixed, their magnitudes (P , G , X , B_i), including the depth, are solved using the Levenberg-Marquardt algorithm. This non-linear least-squares optimisation compares sensor-derived with modelled r_{rs} values, and once the solution converges, the best fit values of P , G , X , B_i and H are deemed to have been solved. Further comprehensive detail of physics-based semi-analytical shallow water inversion algorithms can be found in Dekker et al. (2011) and references therein.

In this study the BRUCE model, developed by Klonowski et al. (2007) is used to derive bathymetry. This semi-analytical shallow water model is a variant of the Hyperspectral Optimisation Process Exemplar model, HOPE, proposed by Lee et al. (1998; 1999). The difference arises in the parameterisation of the benthic albedo, $\rho(\lambda)$. Unlike HOPE, which considers the net benthic albedo is due to only a single benthic substrate, BRUCE assumes it to be a spectral mixture of three benthic end-members. In this case study, the bottom albedo is expressed as a linear mix of two benthic classes, sand and mixed seagrass (50% *Posidonia australis* and 50% *Amphibolis antarctica*). These two species of seagrass were previously recorded as the most dominant across Shark Bay (Walker et al., 1988). The irradiance reflectance spectra of sand, *P. australis* and *A. antarctica* were measured using a handheld hyperspectral radiometer during a field campaign to Shark Bay.

Tafkaa 6S outputs R_{rs} uncorrected for specular reflection of direct solar and sky radiance from the ocean surface (Montes et al., 2004). Thus before implementing the non-linear least squares optimisation, the R_{rs} spectra were corrected for sunglint contamination using a correction scheme based on Lee et al. (1999) and Goodman et al. (2008),

$$R_{rs}(\lambda) = R_{rs}^{raw}(\lambda) - \gamma + \Delta \quad (3.4a)$$

$$\Delta = 1.9 \times 10^{-5} + 0.1[R_{rs}^{raw}(640) - \gamma] \quad (3.4b)$$

$$\gamma = \min(R_{rs}^{raw}(640): R_{rs}^{raw}(750)) \quad (3.4c)$$

where γ is the lowest R_{rs}^{raw} value between 640 and 750 nm. Note that γ was included to avoid negative reflectances if R_{rs}^{raw} of a wavelength shorter than 750 nm was less than that at 750 nm. Whilst there are other sun-glint corrections in the literature (see Kay et al., 2009), Goodman et al. (2008), used a similar correction to equations (3.4) and obtained quite accurate depth retrievals for shallow waters of Kaneohe Bay, Hawaii. Sub-surface remote sensing reflectances were then computed using (Lee et al., 1999; IOCCG, 2006),

$$r_{rs}(\lambda) = \frac{R_{rs}}{(0.51 + 1.5R_{rs})} \quad (3.5)$$

A two-step inversion approach was used to retrieve depth that included: (1) a brief search of the parameter space for the optimal initial guess parameters used in the BRUCE model, and; (2) the uncertainty propagation scheme proposed by Hedley et al. (2010; 2012a).

As stated by Hedley et al. (2010), the uncertainty procedure begins with computing the spectral covariance matrix from a homogeneous deep water region of the image. The Cholesky decomposition matrix, L , is then calculated from the covariance matrix. The procedure then iterates through the r_{rs} image where, for each pixel, the L matrix is used to compute 20 noise-perturbed r_{rs} spectra, $r_{rs} + \delta r_{rs}$. Each spectrally correlated noise term, δr_{rs} , is generated by product multiplication of the L matrix by an n -band vector, whose values are normally distributed random numbers ($\mu = 0, \sigma = 1$). The BRUCE model, through non-linear least squares optimisation provided by the Levenberg-Marquardt (LM) algorithm, then retrieves the values of P, G, X, H, B_{sand} and $B_{seagrass}$ for each noise-perturbed r_{rs} spectrum. The mean and standard deviation are then computed for each parameter set, where the former is taken to be the actual retrieved parameter value and the latter its uncertainty.

In the standard implementation of BRUCE, the initial guess parameters used to initiate the LM optimisation routine are kept constant for all pixels in an image. However, analysis (see Chapter 4) has shown that different initial guess values lead to different local minima having different Euclidean distances. Here, the Euclidean distance is defined as,

$$Euclidian\ Distance = \sqrt{\sum_i^N (r_{rs,i} - \hat{r}_{rs,i})^2} \quad (3.6)$$

where $r_{rs,i}$ and $\hat{r}_{rs,i}$ are the sensor-derived and modelled subsurface remote sensing reflectance at waveband i , respectively. To assist the LM optimisation in locating the best local minimum, an update-repeat process was used. This procedure began by inverting the r_{rs} spectrum of a given pixel to solve for the in-water optical parameters, depth and bottom albedo coefficients. If this initial inversion achieved a Euclidean distance of $\leq 1.0 \times 10^{-4}$, the optimal set of model parameters were then used as initial guesses for inverting the set of noise perturbed spectra, $r_{rs} + \delta r_{rs}$. If, however, the Euclidean distance of the initial LM fit was greater than this threshold, the procedure entered a 'repeat' stage, where the initial optimal set of model parameters were randomly perturbed by 10% of their value and used as the initial guess for the subsequent inversion attempt. This process was repeated until either the Euclidean distance fell below this threshold, or if this repetition occurred more than four times. In the latter case, the set of optimised values that generated the lowest Euclidean distance was used as the initial guess for inverting the set of noise perturbed spectra.

A comparison between this improved method and the standard approach is presented in Chapter 4.

A simple pixel-by-pixel land masking procedure was also performed during the inversion process, whereby a pixel is identified as “land” if its $R_{rs}(750 \text{ nm}) > R_{rs}(400 \text{ nm})$.

3.3.4 Smoothing techniques

The most noticeable artefact in the retrieved bathymetry and bottom albedo images was the amount of impulse (i.e. salt-and-pepper speckling) noise present. Using a median filter would reduce this effect and replace the values of impulse noise pixels with a reasonable estimate; however it would also cause blurring of regions where impulse noise pixels are absent and thereby cause information loss. To limit the blurring of unaffected image regions, a three step smoothing approach was designed to eliminate impulse noise pixels, reduce the magnitude of random (systematic) noise as well as to preserve image sharpness. This smoothing approach is as follows: (1) An impulse noise detection algorithm was applied to the image, generating a binary, 'impulse' - 'not impulse', image; (2) an adaptive median filter on these 'impulse' pixels was applied, and; (3) a second order binomial average kernel was applied to all pixels in the image. Steps (1) and (2) could be replaced by a LUM (Hardie & Boncelet, 1993) or centre weighted median filters (Ko & Lee, 1991), however for the bathymetry image a more manual and flexible definition of a impulse noise is desired – which can be changed according to the user’s prior knowledge. Additionally, step (2) allows the median filter to change size according to the number of other unwanted pixels in the kernel.

For the impulse noise detection algorithm, a 3×3 square pixel region was created and centred on a given pixel of the raw image. The absolute differences between the value of the central pixel and the values of the eight surrounding pixels were then computed. The central pixel was then classified as ‘impulse noise’ if the differences are greater than a given threshold for more than four of its surrounding pixels. For bathymetry images, this threshold was set to a value of 2.0 m, whilst for the bottom albedos of sand and seagrass, thresholds of 0.1 and 0.01 were used respectively. Note that this kernel was not centred on pixels that were flagged such as land or clouds.

Typically, a 3×3 median filter kernel is used to replace impulse noise pixels, as it finds an estimate from the most immediate surrounds; however each raw image also contained unwanted land, cloud or other impulse noise pixels. Such undesired pixels can heavily contaminate a 3×3 pixel neighbourhood, thereby reducing the number of pixels from which the median value is calculated. Thus an adaptive approach was implemented whereby the kernel size of the median filter is increased if more than 50% of its pixels are undesired (i.e. cloud, land or other impulse noise pixels). In this approach, the maximum kernel size was set to 15×15, whereby the kernel cannot increase past this size and the median value calculation is forced even if the condition was not met.

The third step involved iterating a second order binomial smoother (Jahne, 2005) through all pixels of the image (except the edges) given by,

$$\text{Binomial Smoother} = \frac{1}{16} \begin{bmatrix} 1 & 2 & 1 \\ 2 & 4 & 2 \\ 1 & 2 & 1 \end{bmatrix} \quad (3.7)$$

Application of this kernel to a given pixel replaced its value with a centrally weighted average of its pixel neighbourhood. The uncertainty products (δH , δB_{sand} and $\delta B_{\text{seagrass}}$) were also modified during the adaptive median filtering and binomial smoothing stages. In the former, the uncertainty of a given impulse noise pixel was replaced by that of the selected pixel, whilst in the latter the kernel of equation (3.7) was convolved through the resultant uncertainty image.

3.3.5 Tide height correction of bathymetric products

Delineating the changes in depth caused by resuspension and sedimentation from changes in tide heights is an important task in detecting trends and seasonal changes in bathymetry. Ideally, the retrieved bathymetric data are corrected for tidal influences to a common tidal datum such as lowest astronomical tide, LAT. However, water level data measured by *in situ* gauges was not available for the Faure Sill. This prevented direct correction of tidal influences observed in the set of bathymetry images through time (henceforth referred to as bathymetry time series). Two approaches to tide correction were investigated, the first consisting of harmonic tidal analysis and the second based on image analysis.

3.3.5.1 Harmonic Tidal Analysis

Water height data, above LAT, at five minute intervals were obtained from the Carnarvon tide station (approximately 120 km NW of Faure Sill) from December 2011 to November 2012 – courtesy of the Western Australian Department of Transport. In the harmonic analysis, we followed Burling et al. (2003) and assumed that the tide height is the summation of the M_2 , S_2 , K_1 and O_1 tidal constituents,

$$height(t) = \bar{h} + \sum_{i=1}^N a_i \cos(\sigma_i t + g_i) \quad (3.8)$$

where \bar{h} is the mean sea height and a_i , σ_i and g_i are the amplitude (cm), frequency (radians/hour) and phase (radians) of tidal constituent i , respectively. The frequencies, σ , of each tidal constituent are known parameters and were obtained from Doodson and Warburg (1941). With \bar{h} set as the mean sea height of the Carnarvon data, equation (3.8) was used to estimate the water heights at Monkey Mia and Hamelin Pool using: (a) the modelled amplitudes presented by Burling (1998), and; (b) phases derived from harmonic analysis of Monkey Mia and Hamelin Pool tide times. 2 hours and 2 minutes were added (+02:02 hrs) to the tide times of the Carnarvon water height data to estimate the Monkey Mia tide times, as recommended by the Australian Bureau of Meteorology. Thirty-two minutes were subtracted (-0:32 hrs) from the tide times of the Carnarvon dataset to approximate the Hamelin Pool tide times. Harmonic analysis, in this case, simply involved fitting equation (3.8) to the approximated tide times using LM least squares minimisation, over multiple time series - each being a three day interval with the HICO overpass being the central point. Finally, the average water height between these two locations (Monkey Mia and Hamelin Pool) was then used to correct for the tide over the Faure Sill.

3.3.5.2 Image based empirical tidal corrections

In the image based approach, an offset was added to each bathymetry image that normalises the bathymetry time series to an arbitrary reference depth (tidal datum). This method began by locating those pixels, $P(i,j)$, in the bathymetry time series, $H(i,j,t)$, that consistently had a depth of less than three metres through time,

$$H(i,j) \in P(i,j) \text{ if } H(i,j,t) < 3 \text{ meters } \forall t = 0, \dots, N \quad (3.9)$$

where i and j represent the spatial coordinates, t the time and N is the number of bathymetry images in the time series. This constraint effectively excluded any deep

water pixel that may have been incorrectly assigned a depth less than three metres through the inversion process at one or more instances in time. Thus the pixels of the set $P(i, j)$ consisted of only shallow water pixels where the signal-to-noise ratio (SNR) was highest and where the retrieved depth was expected to be most accurate. Two medians were then computed: (1) $\widetilde{H}(t)$, the median depth of pixels $P(i, j)$ in each bathymetry image, and; (2) \widetilde{H}_{ref} , the median depth of pixels $P(i, j)$ taken across the entire bathymetry time series. This latter median was used as a reference depth to generate an offset value, $\Delta H(t)$,

$$\Delta H(t) = \widetilde{H}(t) - \widetilde{H}_{ref} \quad (3.10)$$

If $\Delta H(t) > \min[H(i, j)]$; then $\Delta H(t) = \min[H(i, j)]$

adding $\Delta H(t)$ to its respective bathymetry image normalised it with respect to \widetilde{H}_{ref} , and in doing so minimised the tidal influence across the dataset. In some instances the value of $\Delta H(t)$ was greater than the minimum depth in the bathymetry image, and to avoid over-correction issues $\Delta H(t)$ was set to this minimum.

3.3.6 Geo-registration

For the purpose of time series analysis in detecting changes in depth, each HICO swath was overlaid on the same raster grid to ensure geospatial consistency through time. This was performed by first geo-referencing each HICO image with the provided geographic lookup tables (GLTs) where an additional rotation was added to orientate north as “up”. This was followed by geo-registration where the geo-referenced image was warped by translation/scaling/rotation using at least thirteen ground control points selected from Google EarthTM imagery of Shark Bay. In the absence of accurately registered digital maps of the area, we have assumed the Google Earth imagery to be an accurate reference, noting that a relative, geospatial consistency through time was sought after, rather than absolute geolocation accuracy.

Due to the lack of man-made features in the Shark Bay region, distinct and spatially invariant land features were chosen as ground control points (GCPs). The central position of nine different birridas (see Figure 3.3) - salty depressions that are either circular, oval or irregularly shaped (Department of Environment and Conservation, n.d) – and four other landscape features formed the 13 common GCPs (Figure 3.3) used in the geo-registration. Additional GCPs that corresponded to roads, distinct sections of rivers, dry inland lakes and tips of islands were also used. Note that

these additional GCPs were different for each HICO swath due to cloud cover and the changing swath orientation and translational drift (see Figure 3.1).

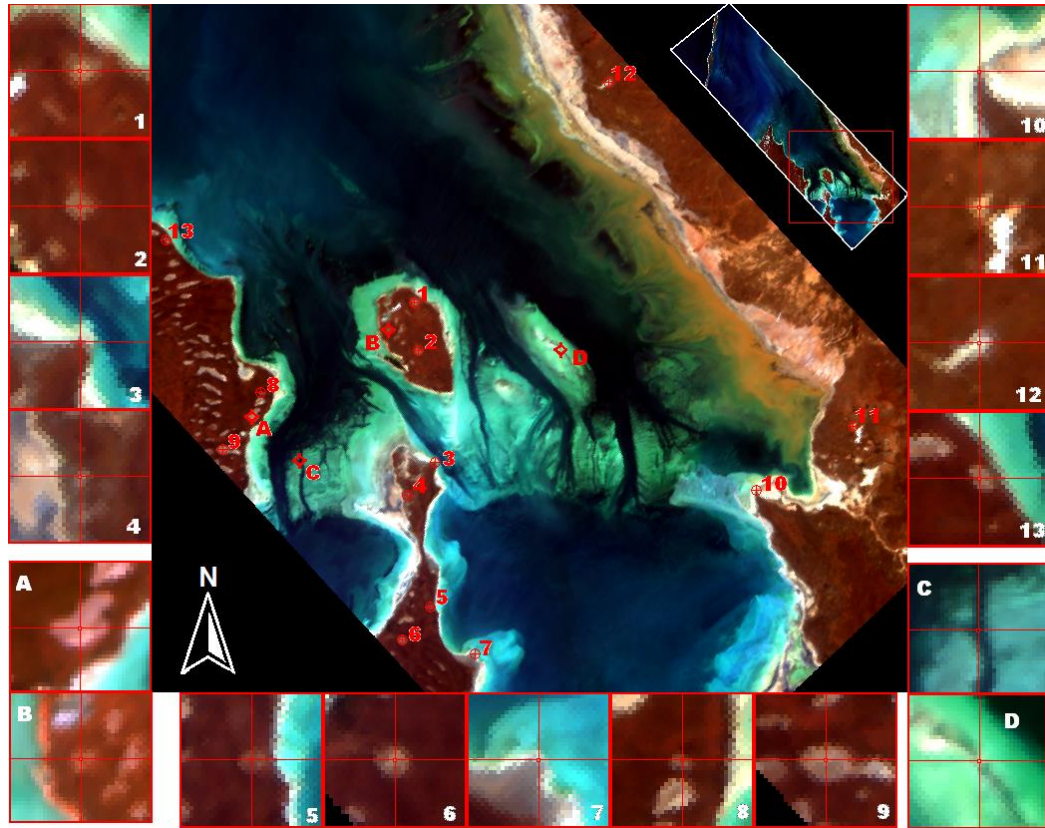


Figure 3.3: The 13 common ground control points used in the geo-registering of HICO imagery of Shark Bay, Western Australia, and the four test locations for geospatial consistency. The HICO image (19 Nov 2011) displayed has been geo-referenced with the geographic lookup table.

3.4 Results and Discussion

3.4.1 Evaluation of Tafkaa-6S atmospheric correction

Figure 3.4 shows the reflectance spectra of two separate pixels through time: a quasi-deep water and shallow submerged sand pixel. The left-hand panels (Figures 3.4a and 3.4c) and right-hand panels (Figures 3.4b and 3.4d) show the R_{rs} before and after sun-glint correction, respectively. The reflectance spectra of the shallow submerged sand pixel (Figure 3.4a) exhibits three spectral artefacts: (1) an upward spectral shift occurring from 400 – 450 nm (e.g. 27 February- and 02 April 2012); (2) negative reflectance values from 400 – 420 nm (e.g. 08 August- and 04 June-2012), and; (3) negative reflectance values beyond 600 nm (e.g. 21 January- and 27 February-2012).

The first spectral artefact, according to Goodman et al. (2008), can be "considered a function of uncorrected sunglint effects" and "attributed to artefact

suppression algorithms". The cause of the second spectral artefact is uncertain, however it could arise from an over-estimation of either the radiance of Rayleigh scattering or from the atmospheric aerosol model at the blue wavelength region. This particular artefact has been observed in R_{rs} of optically deep water pixels by other researchers (see Fig. 9c in Gao et al., 2000; and Fig. 6b and 7b in Goodman et al., 2003), and noted specifically for HICO-derived R_{rs} by Moses et al. (2014). The latter authors recommended a very low AOT when applying Tafkaa 6S to circumvent this issue. Assuming the AOT, CLMVAP, and ozone values derived from MODIS are the best approximations for Shark Bay, the second spectral effect may then be due to the atmospheric and/or aerosol models used within Tafkaa 6S. It is likely these models used may be sub-optimal for the semi-arid coastal climate of Shark Bay however, improvements to these are beyond the scope of this work. Further, Goodman et al. (2008) noted that using the full geometry implementation of Tafkaa (i.e. with cross-track pointing information) can reduce the magnitude of the spectral effects observed in the R_{rs} . The third artefact is more problematic with respect to accurate retrieval of geophysical parameters using the BRUCE model.

When examining Figure 3.4a, the reflectance spectra of the quasi-deep water pixel on both 21 January 2012 and 27 February 2012 appear to have similar spectral shapes to those of the other dates, with the main difference being a vertical offset/shift. This implies an over-correction of the atmospheric signal that may be due to an over-estimation of one or more MODIS-derived atmospheric parameter. Indeed, the vertical column water vapour and AOT for these two dates were amongst the highest (see Table 3.1). After sun-glint correction, the third spectral artefact is removed but accentuates the second spectral artefact (see Figure 3.4b).

Analysis of the reflectance spectra of the shallow water pixel (Figure 3.4c) also shows the occurrence of the three spectral artefacts. However, the magnitude of the reflectance spectra is significantly larger than the magnitude of these spectral artefacts. Moreover these artefacts have marginal impacts across the water penetrating bands between 450 and 600 nm, and as such are deemed less likely to dramatically impair depth retrievals. Negative reflectances at long wavelengths (third spectral artefact) after Tafkaa's atmospheric correction, was also observed by Goodman et al. (2008) over bright shallow water (sandy substrate) pixels. Goodman et al. (2008), illustrated that this spectral feature does not undermine accurate depth retrievals, as

the de-glinting procedure effectively normalises the reflectance at 750 to low positive values (see Figure 3.4d).

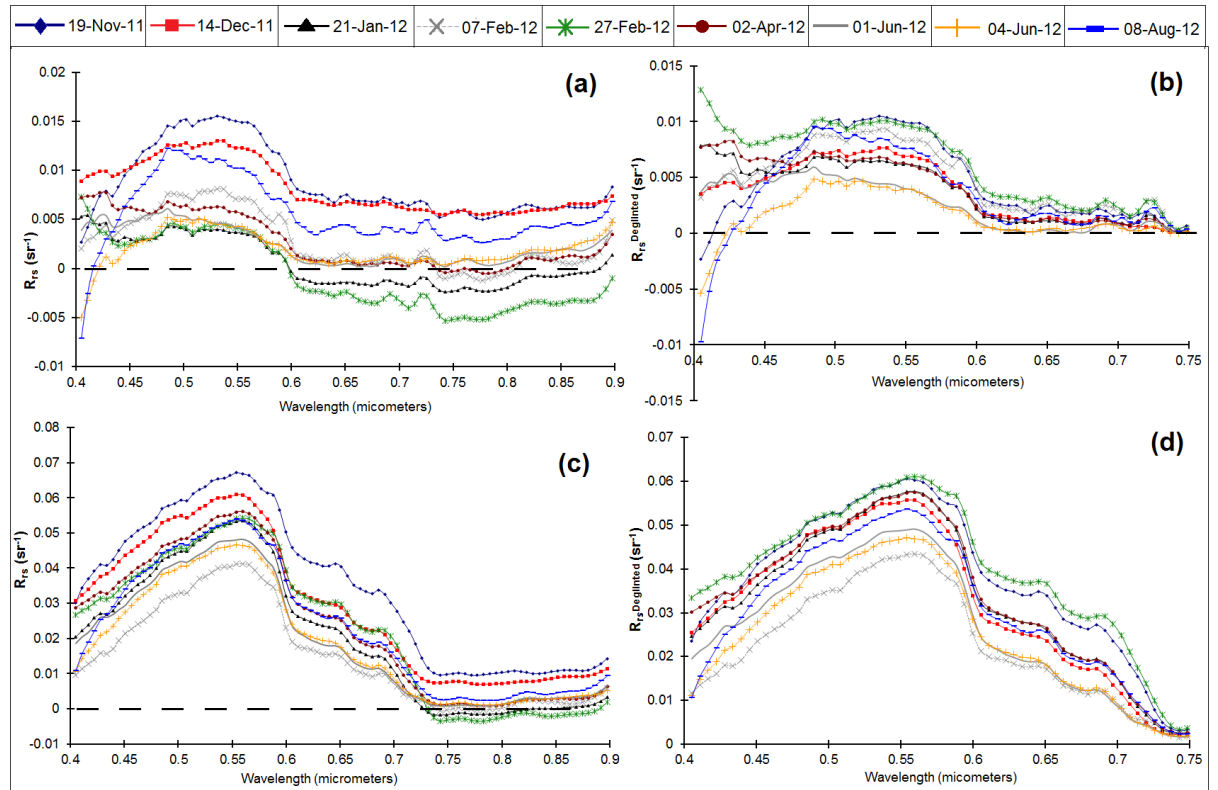


Figure 3.4: The remote sensing reflectance of a quasi-deep water pixel (a), (25.718 °S/113.978 °E), and a shallow water pixel with a sandy bottom (c), (25.907 °S/113.934 °E), through time. (b) and (d) show the sun-glint corrected R_{rs} spectra of (a) and (c) respectively. Note that the wavelengths past 750-nm are not used in the inversion procedure and are not displayed in (b) and (d).

This comparison has shown the addition of three anomalous spectral artefacts to the remote sensing reflectance spectra after Tafkaa-6S atmospheric correction. The magnitude of these spectral noise are comparable to that of the water-leaving reflectance for deep water pixels, which may lead to inaccurate IOP retrievals. However, as the purpose of this study was to retrieve water column depth, the Tafkaa-derived HICO R_{rs} values over shallow water pixels were deemed suitable in accordance with Goodman et al. (2008).

3.4.2 Bathymetry retrievals and smoothing techniques

Figure 3.5 illustrates the step-wise modification of the HICO-derived water column depth product of Shark Bay, 19 November 2011, using the proposed smoothing algorithm. Two cross-sectional profiles are presented, each containing: the

raw HICO-derived depth (black curves); pixels classified as impulse noise (red triangles); (c) the depth after impulse noise removal (blue curves), and; the depth after subsequent application of the second order binomial spatial smoother (pink curves). Figure 3.5 also shows the depth uncertainty profile and its subsequent modification.

The raw depth profiles (Figure 3.5) demonstrate how impulse noise pixels introduce unrealistic and abrupt changes in the depth product. These pixels were predominantly encountered when the depth of the immediate neighbourhood was greater than 4.0 m. Additionally, their uncertainties approached, and at times exceeded 100%, of the actual retrieved depth value. Analysis showed that the R_{rs} spectra of impulse noise pixels whose depths have been estimated to over 7.0 m resembled that of quasi-optically deep water (e.g. Figure 3.4a). In such cases, the bottom contribution to the R_{rs} are either weak or non-existent where the geometric depth would be large or precluded by highly absorbing waters. The likely cause for the deeper impulse noise pixels is a low SNR (after atmospheric and sun-glint correction), and where the BRUCE model translates a change in the r_{rs} to large changes in depth (this is explained further in the discussion of Figure 3.6). The BRUCE model can also compensate for a shallower depth by either increasing the water column turbidity or decreasing the benthic albedo coefficient (darker substrate). This phenomenon creates those impulse noise pixels whose depths are unexpectedly shallower than the surrounding pixels.

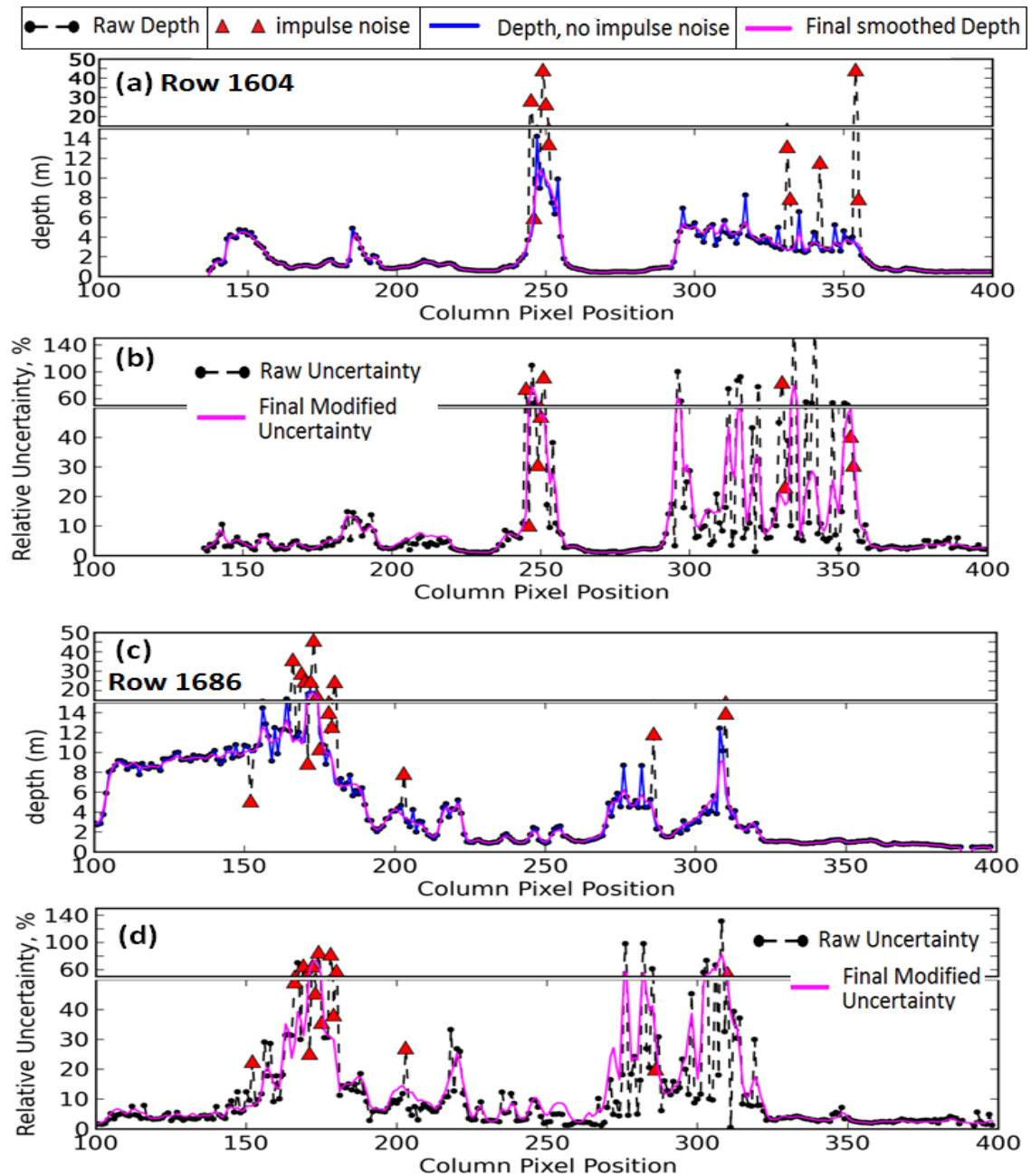


Figure 3.5: Illustration of the three stage smoothing technique applied to HICO derived depth product of Shark Bay on 19 November 2011. Cross-sectional profiles at row number 1604 (top two panels) and at 1686 (bottom two panels). (a) and (c) contain: the raw depth (black dot-dash); impulse pixels (red triangles); depth product after impulse noise pixel removal (solid blue curve), and; the subsequent smoothed depth product. (b) and (d) are the uncertainty profiles of (a) and (c) respectively, and contain: the initial uncertainty (black dot-dash); pixels identified as outliers (red triangles), and; the final modified uncertainty product (pink).

As shown in Figure 3.5, the proposed impulse noise detection algorithm and subsequent adaptive median filter approach successfully identified impulse noise pixels and replaced their depth value with a reasonable estimate. Application of a

second order binomial smoothing kernel then afforded a reasonable spatial uniformity. The smoothed bathymetry images of Shark Bay from 19-Nov-11 to 08-Aug-12 are displayed in Figure 3.7, and show a high level of consistency in depth between different timestamps. In the uncertainty inversion approach, proposed by Hedley et al. (2010), the Cholesky decomposition matrix, L , was used to add spectral noise to the sensor-derived r_{rs} spectra. During per-pixel inversion, the L matrix remained constant with only its magnitude randomly changed. This generated a spectral noise term, δr_{rs} , that is absolute rather than relative to the magnitude of r_{rs} , which thus formed an inverse relationship between $\|r_{rs}\|$ and its relative uncertainty. In other words, the relative uncertainty in r_{rs} for dark or highly absorbing water pixels will be larger than for bright shallow water pixels. This is illustrated in Figure 3.6, which shows the pseudo SNR at 550 nm plotted against the relative uncertainty of the retrieved depth. Here, the pseudo SNR was: (a) derived from r_{rs} spectra, i.e. HICO data that has undergone atmospheric, sunlint and air-to-water corrections, and; (b) computed for each pixel in a HICO scene by dividing the average, μ , of each set of 20 noise perturbed r_{rs} spectra at 550 nm by the standard deviation, σ , at this water penetrating wavelength,

$$SNR (550 \text{ nm}) = \frac{\mu[\{r_{rs}(550) + \delta r_{rs}(550)\}_{i=1\dots 20}]}{\sigma[\{r_{rs}(550) + \delta r_{rs}(550)\}_{i=1\dots 20}]} \quad (3.11)$$

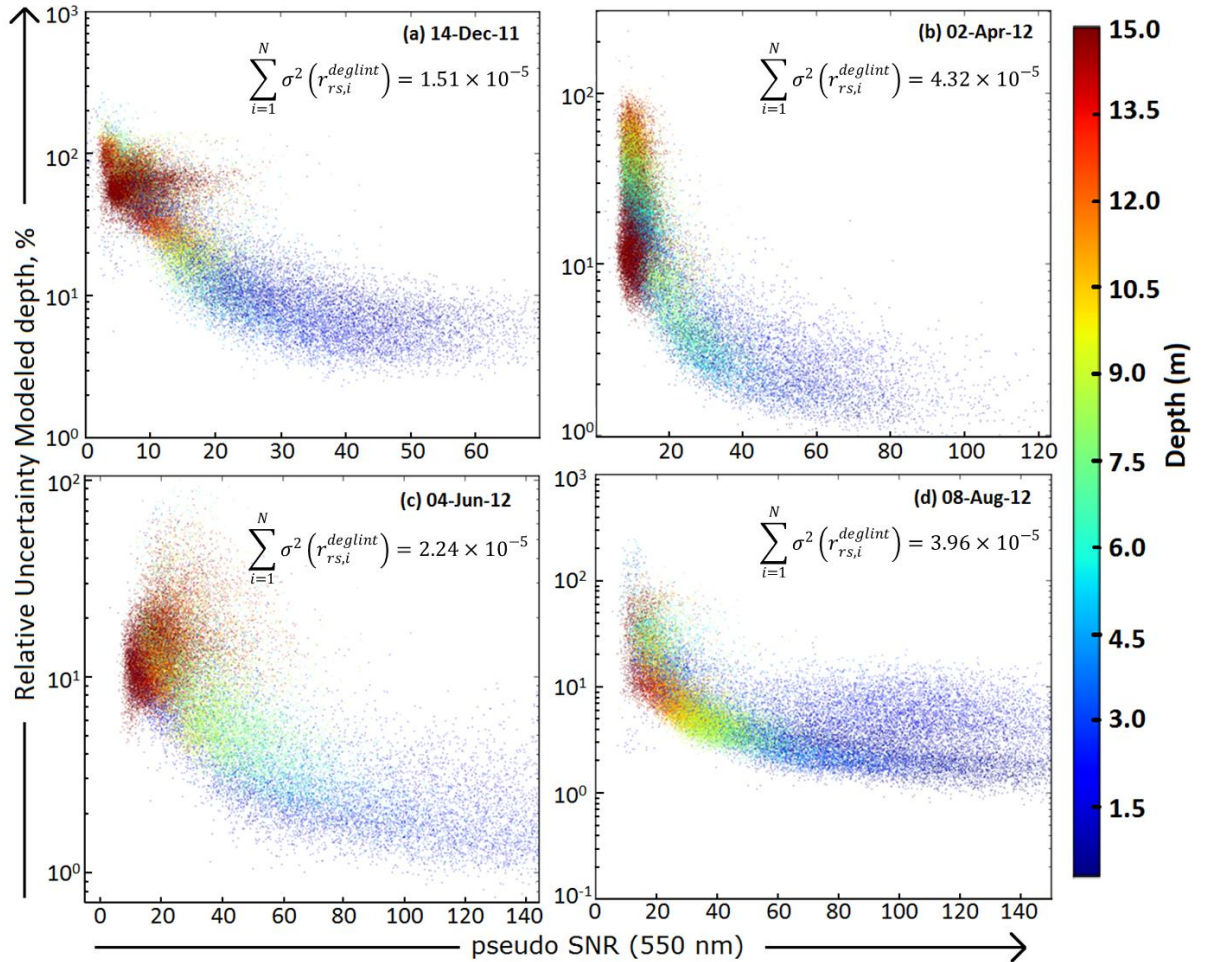


Figure 3.6: Relative uncertainty of the retrieved depth vs. pseudo SNR at 550 nm, obtained from HICO images of Shark Bay on (a) 14-Dec-11; (b) 02-Apr-12; (c) 04-Jun-12, and; (d) 08-Aug-12. Note: (1) vertical axes are displayed in logarithmic form; (2) 35 000 random data points, with depth > 0.3 m, were presented for each panel, and; (3) the summed spectral variance, taken from the deep water region of the given HICO $r_{rs}^{deglint}$ image are also presented.

Figure 3.6 shows a non-linear relationship between the pseudo SNR and the relative uncertainty of the retrieved depth of four HICO scenes of Shark Bay. When the SNR is above 20 the relative uncertainty of the retrieved depth is less than 10% (Figure 3.6). This is an adequate outcome, and analysis of the entire HICO time series for Shark Bay showed that on average 89% of pixels with a retrieved depth less than 5 m had a SNR greater than 20. This average decreases to 74% for pixels whose depths ranged between 5 and 10 m, and to 49% for pixels with a retrieved depth greater than 10 m. Below a SNR of 20, the relative uncertainty in the retrieved depth drastically increases, in most cases to greater than 100%. Such high uncertainties mainly occur for pixels with a retrieved depth greater than 8 metres.

This behaviour can be attributed to the absolute noise term added during the inversion; where, as the SNR decreases below 20 the magnitude of δr_{rs} becomes comparable to $\|r_{rs}\|$. Given the exponential relationship between r_{rs} and depth in the shallow water model; the BRUCE model translates this perturbation of r_{rs} to large changes in depth, and hence why the retrieved depth varies so greatly within the set of 20 noise perturbed r_{rs} spectra for low SNR pixels – e.g. the deeper impulse noise pixels observed in Figure 3.5. Conversely, over bright substrates where $\|\delta r_{rs}(\lambda)\| \ll \|r_{rs}(\lambda)\|$, δr_{rs} is translated to smaller changes in depth. These relationships are demonstrated in Figure 3.5, where pixels with a modelled depth less than 6 m generally had a relative depth uncertainty of less than 10%, and where this relative uncertainty would at times increase with depth.

Figure 3.6 also shows that when environmental noise is included, arising from atmospheric, sun-glint and water-to-air interface corrections, the SNR of HICO – which was initially estimated at approximately 200 at 550 nm (see Lucke et al., 2011) - drops to less than 150 for most cases. This corresponds to an increase in the noise component by a factor of ≥ 1.3 . While this is a modest increase, it does illustrate the importance of accurately removing contaminating signals in a bid to avoid non-uniqueness issues, which lead to higher uncertainties in the retrievals of depth.

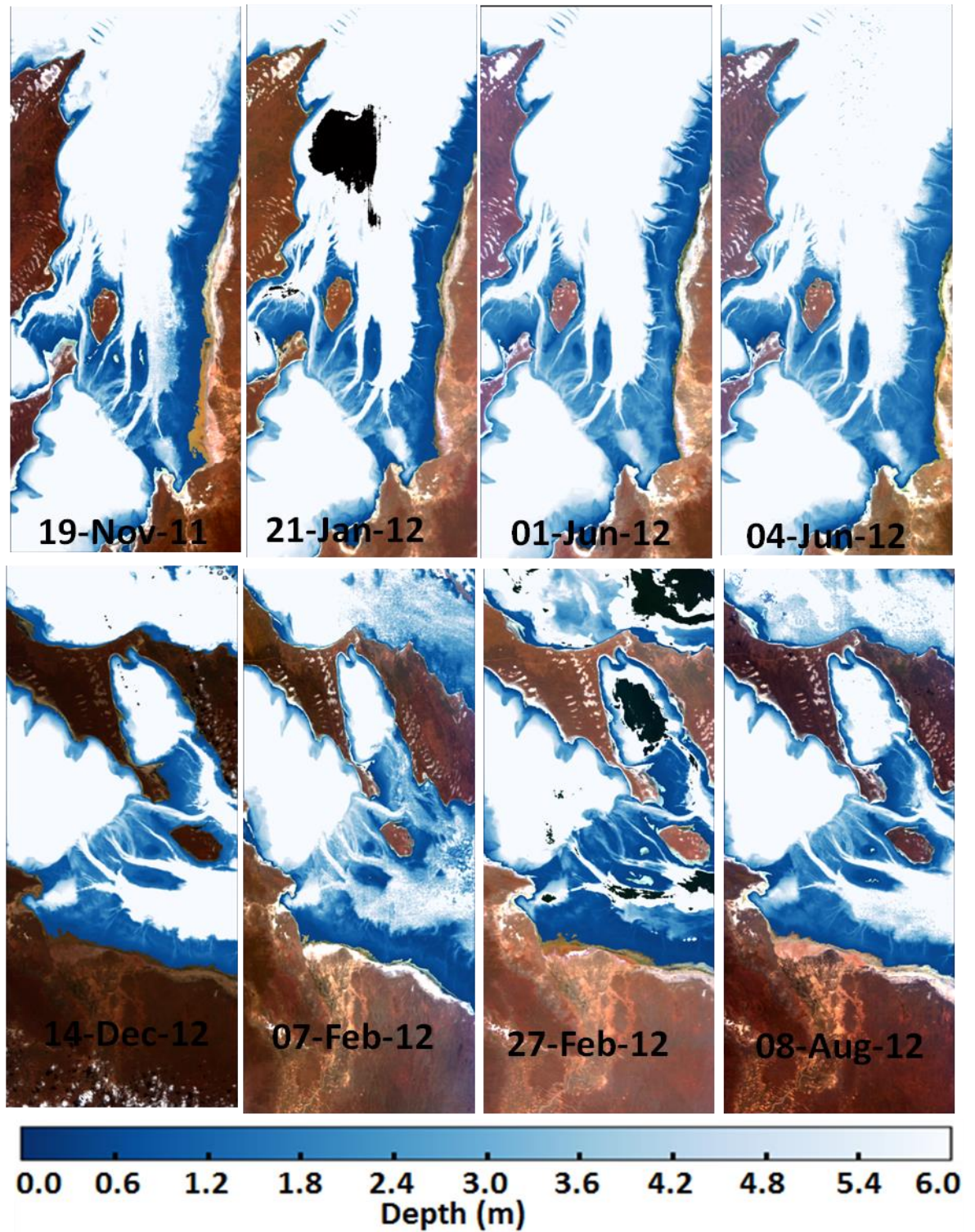


Figure 3.7: Smoothed bathymetry images (before geo-referencing) derived from HICO imagery of the Shark Bay region, from 19-Nov-11 to 08-Aug-12. Note: for simplicity the bathymetry image of 02-Apr-12 is not displayed; black water pixels (e.g. 12-Jan-12 and 27-Feb-12) had $R_{rs}(750) > R_{rs}(400)$ and were not processed, and; blue and white represent shallow and deeper areas respectively.

3.4.3 Tide corrections

3.4.3.1 Harmonic Tidal Analysis

Removing the influence of tide is an important task in delineating changes caused by resuspension and sedimentation from changes in tide heights, particularly since tides can form a significant portion of the variance observed in raw bathymetry products (Egbert and Erofeeva, 2002).

The harmonic tidal analysis begins by extracting the phases of the major tidal constituents from time-adjusted (+02:02 Hrs and -0:32 Hrs) Carnarvon tide data (Figure 3.8a). The correlation coefficients of the curves in Figure 3.8a are given in Table 3.2 and with $r^2 > 0.96$ for all dates, demonstrates high confidence in the values of the modelled phases. The slight differences between the observed and modelled tide heights in Figure 3.8a are likely due to wind induced waves, which do not affect the accuracy of the retrieved phases. Applying these phases with the respective amplitudes taken from Burling et al. (2003), generates modelled tide curves for Monkey Mia and Hamelin Pool as illustrated in Figure 3.8b for 14 December 2011.

One and a half day intervals about the HICO overpass were used to compute the phases of the major tidal constituents as these produced higher correlation coefficients than an expanded time series. The modelled tide heights and their uncertainty at the time of each HICO overpass for Monkey Mia, Hamelin Pool and Faure Sill are given in Table 3.2. The Faure Sill, being a shallow water region containing several narrow water channels (of depths greater than 6 m) exhibits complex tidal harmonics (Burling et al., 2003). Modelling these harmonics are beyond the scope of this paper, however previous research has shown that the Faure Sill diminishes the amplitudes and creates lag in the phases of the tidal constituents (Burling et al., 2003). The net result is a lower tidal height and range in Hamelin Pool than in Monkey Mia. This is observed in the modelled tide data (Table 3.2), where the tide range at Monkey Mia and Hamelin Pool are 81.14 cm and 64.71 cm respectively. Additionally, Table 3.2 suggests little variation in the expected water level height between successive HICO overpasses; evident by the modelled tide ranges of less than 1 m and a standard deviation of tide heights less than 30 cm for Monkey Mia and Hamelin Pool. Indeed a tide height range of approximately 1 m over Shark Bay has been noted by Walker et al. (1988) and modelled by Burling et al. (2003).

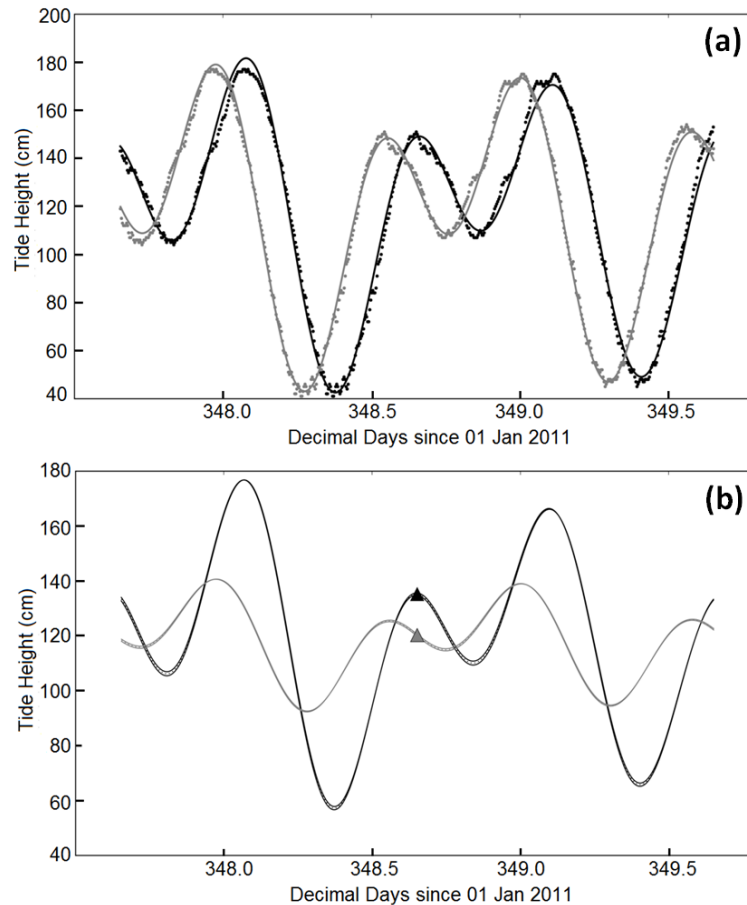


Figure 3.8: Harmonic tidal analysis for a 3 day interval centred on the HICO overpass of 14 December 2011: (a) Time adjusted Carnarvon tide height data for Monkey Mia (+2:02 hrs - Black dots) and Hamelin Pool (-0:32 hrs - Grey dots) overlaid with the respective modelled tide curves using equation (3.8); (b) Modelled tide curves for Monkey Mia (Black line) and Hamelin Pool (Grey line). The triangles in (b) display the modelled water level height at the time of the HICO overpass at Monkey Mia and Hamelin Pool.

Although the modelled tide heights at Monkey Mia and Hamelin Pool appear reasonable based on evidence from the literature, the estimated tide heights over the Faure Sill can be subject to large errors. These errors arise when averaging the tide height between Monkey Mia and Hamelin Pool, which may over simplify the complexity of the shallow water tidal harmonics present over the Faure Sill. In this region, shallow water tidal constituents may cause constructive or destructive interference with the M_2 , S_2 , K_1 , O_1 harmonics, increasing or decreasing the tide height respectively (Doodson & Warburg, 1941). However, with the absence of accurate three-dimensional tide modelling (e.g. Burling et al., 2003) adopting the average is the most pragmatic approach.

Table 3.2: Modelled tide heights (cm), above LAT, during each HICO overpass time for Monkey Mia, Hamelin Pool and the Faure Sill. Also present are the: standard deviation and range of these tide heights, and , correlation coefficients of the tide height curves used to extract the M_2 , S_2 , K_1 , and O_1 tide constituent phases from the time adjusted Carnarvon data.

Date and Time (WST)	Monkey Mia		Hamelin Pool		Faure Sill
	r^2	Modelled tide height (cm)	r^2	Modelled tide height (cm)	Modelled tide height (cm)
19-Nov-2011, 1632 hrs	0.983	124.28 ± 0.01	0.978	114.06 ± 0.04	119.17 ± 0.05
14-Dec-2011, 1539 hrs	0.991	135.21 ± 0.22	0.995	120.23 ± 0.18	127.72 ± 0.40
21-Jan-2012, 1538 hrs	0.983	112.43 ± 0.35	0.991	132.98 ± 0.18	122.70 ± 0.54
07-Feb-2012, 1722 hrs	0.988	115.25 ± 0.44	0.994	133.82 ± 0.19	124.54 ± 0.63
27-Feb-2012, 0940 hrs	0.981	95.19 ± 0.02	0.991	121.92 ± 0.02	108.55 ± 0.05
02-Apr-2012, 1035 hrs	0.966	125.91 ± 0.18	0.983	128.12 ± 0.22	127.01 ± 0.40
01-Jun-2012, 1038 hrs	0.973	173.39 ± 0.18	0.990	127.11 ± 0.07	150.25 ± 0.25
04-Jun-2012, 0932 hrs	0.990	165.61 ± 0.10	0.994	149.56 ± 0.06	157.58 ± 0.15
08-Aug-2012, 1625 hrs	0.962	118.60 ± 0.31	0.988	92.99 ± 0.22	105.79 ± 0.54
Standard deviation of tide heights (cm)	N/A	26.55	N/A	19.30	20.24
Tide range (cm)	N/A	81.14 ± 0.20	N/A	64.71 ± 0.28	69.04 ± 0.69

3.4.3.2 Image based tide correction

To gauge if a tidal signal exists in the HICO derived bathymetry dataset, the predicted tide heights at Monkey Mia (taken from Table 3.2) were plotted against the median HICO derived depth of the shallow water region on the northern side of Faure Island (Figure 3.9). This island is approximately in line with Monkey Mia, and as modelled by Burling (1998) experiences very similar tidal harmonics. Figure 3.9 shows a strong positive correlation ($R^2 = 0.90$) between the predicted tide heights and

the HICO derived bathymetry prior to tide correction, that is, the bathymetry increases with the tide height. Note that a 1:1 line was not expected because: (a) the predicted tide heights are given above LAT; (b) Burling (1998) obtained a normalised RMS of 7% between the predicted and observed tide heights at Monkey Mia with the modelled tidal amplitudes and phases, and; (c) potential random offsets in the bathymetry data caused by sub-optimal atmospheric/sun-glint/air-water interface corrections. Despite this Figure 3.9 implies that the variation in depth between HICO derived bathymetry images are related to tide, and not solely due to random offsets.

The image based tide correction technique is illustrated in Figure 3.10a. This figure shows the median shallow water depth, $\widehat{H}(t)$, computed for each HICO image of Shark Bay. The black horizontal line is the reference depth, \widehat{H}_{ref} , from which the offset of each bathymetry image is calculated. The reference depth in this case is the median water depth computed from all nine HICO scenes. Note that if tide data of the region of interest is available, then the mean water level height or the lowest astronomical tide may instead be used as the reference depth.

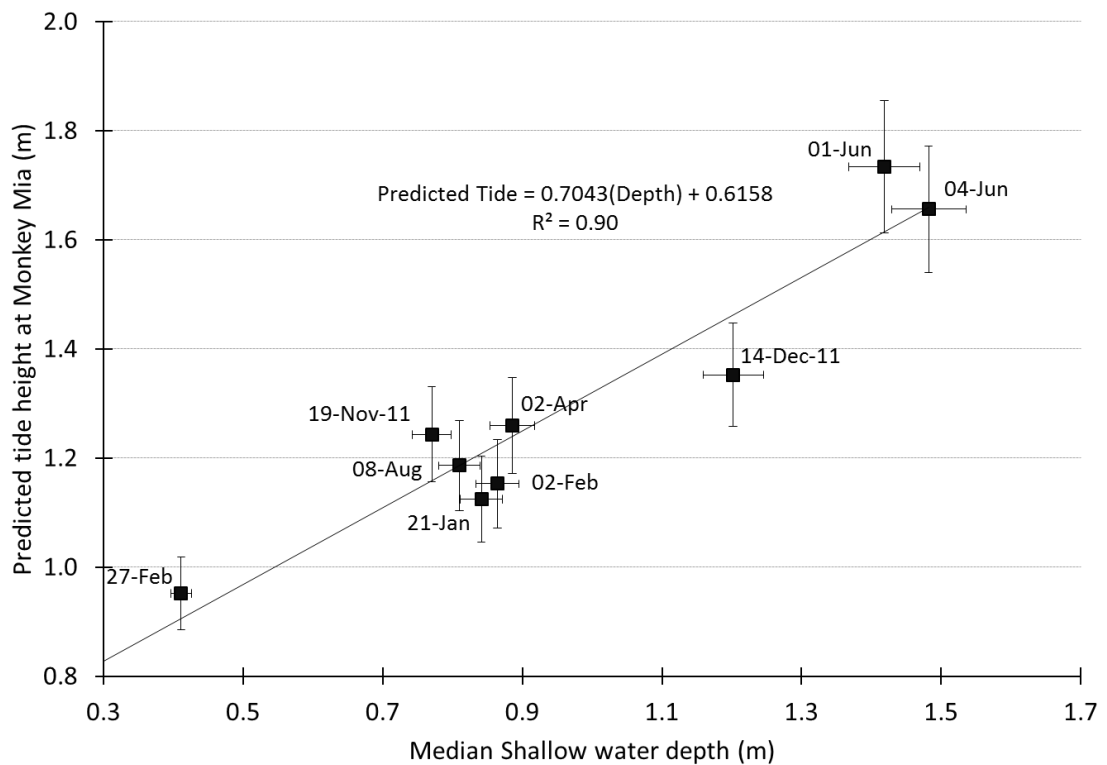


Figure 3.9: Predicted tide heights at Monkey Mia against the median depth of the shallow water pixels surrounding the northern section of Faure Island. The predicted tide heights were taken from Table 3.2, whilst the median shallow water depths were taken from HICO derived bathymetry prior to tide correction. The nine data points represent the nine HICO scenes.

How well the image based and harmonic analysis techniques minimise the tidal influence across the bathymetry time series was tested by computing the standard error in the means (SEM). Here, the mean represents the average depth of the shallow water pixels, $\langle H(t) \rangle$, of each bathymetry image in the time series. Note that applying a tide correction technique to the bathymetry dataset would ideally correct water height variations to a reference depth, and hence yield a SEM near zero. Table 3.3, shows $\langle H(t) \rangle$ and the SEM for the uncorrected, image based and harmonic analysis corrected bathymetry images.

Table 3.3: The mean depth of the shallow water pixels, $\langle H(t) \rangle$, for each HICO derived bathymetry image. The standard error in the means (SEM) of the uncorrected, image based and harmonic tide correction techniques are also present.

Tide method	19-Nov-11	14-Dec-11	21-Jan-12	07-Feb-12	27-Feb-12	02-Apr-12	01-Jun-12	04-Jun-12	08-Aug-12	SEM
Uncorrected	0.91	0.91	1.13	1.41	0.80	1.02	1.42	1.38	1.34	0.24
Image based correction	1.26	1.20	1.26	1.56	1.20	1.24	1.13	1.20	1.17	0.12
Harmonic analysis correction	-0.29	-0.36	-0.10	0.16	-0.28	-0.25	-0.08	-0.20	0.28	0.22

As indicated in Table 3.3, tidal influences over Shark Bay exhibit a SEM of 24 cm with a tidal range of 62 cm. The tidal range is consistent to that modelled using the harmonic tidal analysis (Table 3.2). However, the harmonic analysis tide correction method did not significantly reduce the variability between the bathymetry images, having also overcorrected the depth of the shallow water pixels as noted by the negative averages (Table 3.3). These results suggest that tide correction based on harmonic analysis is inaccurate and does not adequately represent the tidal harmonics encountered over the Faure Sill. In contrast, the image based tide correction approach produces a bathymetry times series with an SEM of 12 cm, indicating that the variations due to tide have at least been minimised. Note that the reason the image based tide correction did not generate an SEM of zero is due to the inclusion of the constraint that forces $\Delta H(t)$ to equal the minimum depth (see equation 3.10) – for some images – to avoid overcorrection. Thus not all bathymetry images were fully

normalised to the imposed reference depth. Figures 3.10b and 3.10c show histograms of the depth of the shallow water pixels for each bathymetry image, before and after empirical tide correction, and illustrate the normalisation achieved by this method. It should be noted that the corrected depth values obtained from this empirical method are relative to an arbitrary reference depth, rather than an absolute tide datum such as LAT.

These results suggest that unless the local tidal dynamics of the region of interest are well characterised, large errors can arise when using tide data recorded at distant tide stations. The lack of *in situ* tide data in close proximity to the region of interest is a constant issue faced for the majority of remote and inaccessible regions for remote sensing studies. Although global tide models are in existence (e.g. Finite Element Solution 2012, Lyard, Lefevre, Letellier, & Francis, 2006 ; Topex Poseidon crossover solution 7.2, Egbert & Erofeeva, 2002), their spatial resolutions are coarse (ranging from $1/16^\circ$ to $1/4^\circ$ longitude and latitude) and do not extend to semi-enclosed embayment's such as Shark Bay. The image based tide correction circumvents the need for a historic tide dataset and eliminates errors from tide models. Although this approach does require at least two bathymetry images of the region of interest at different times, it is the most pragmatic and easiest to implement. Future research would be to compare the empirical tide correction results with estimates obtained from a harmonic analysis whose tidal constituents are derived from high resolution remote sensing imagery, as presented by Mied et al. (2013).

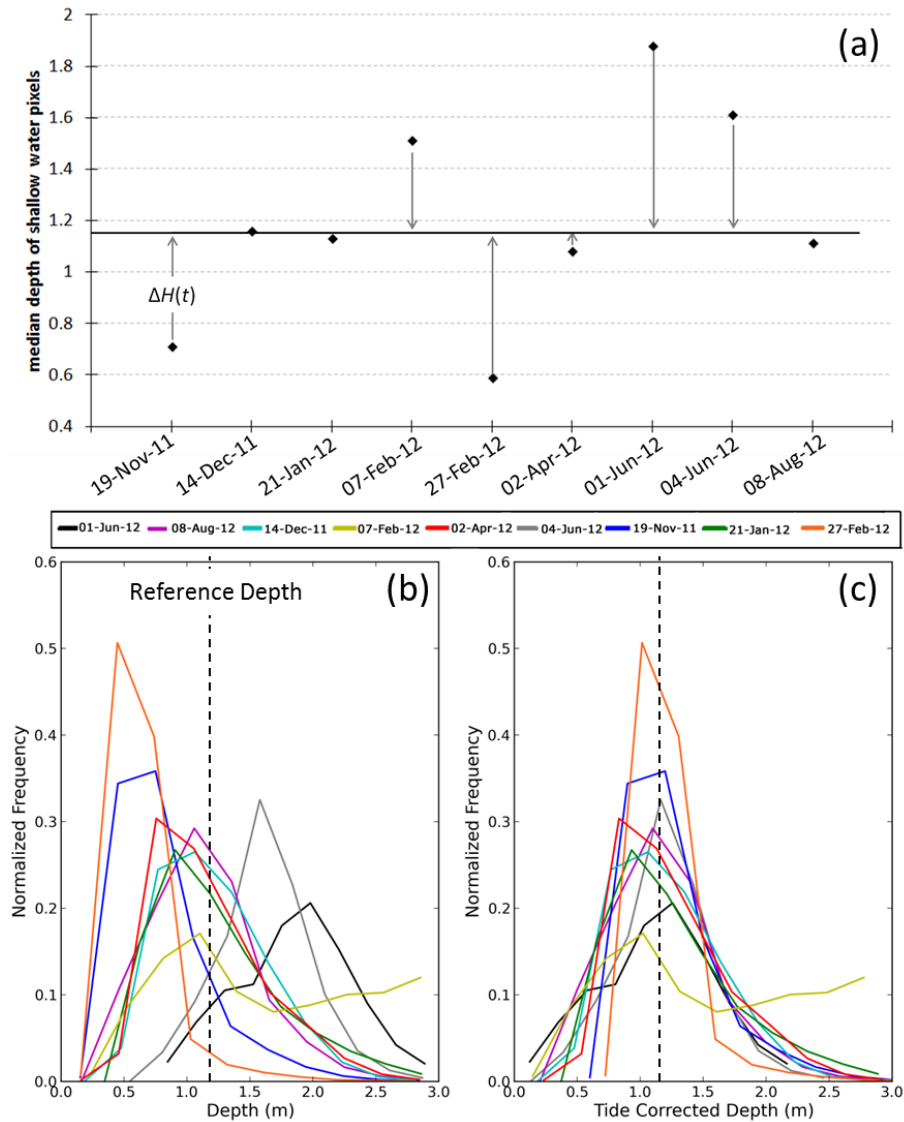


Figure 3.10: (a) illustration of the empirical tide correction technique applied to the HICO dataset of Shark Bay. The horizontal black line represents the reference depth. Histograms of the depth of shallow water pixels (less than 3 m depth) before (b) and after tide correction (c).

3.4.4 Geo-registration

To test the geo-spatial consistency, the spatial ‘pixel drift’ of four test pixels was analysed between HICO images. Pixels A, B, C and D, displayed in Figure 3.3, correspond to different land and seascape features, specifically: A and B are pixels within the birradas (described in section 3.2.6) on the Peron peninsula (25.918 °S/113.737 °E) and Faure Island (25.838 °S/113.862 °E), respectively; C is an intersection point of a distinct and seemingly invariant water channel on the Faure Sill (25.959 °S/113.779 °E) and; D is the southernmost tip of Pelican Island (23.854 °S/114.019°E). A seascape feature (pixel C) was also included because the majority

of GCPs were on the coastal regions surrounding the Faure Sill, and solely choosing test points near these GCPs may bias the result. Additionally, the area surrounding pixel C appeared in both true colour and bathymetry imagery to be invariant through time as expected by the quasi-stable nature of Shark Bay's geology.

The Euclidean distance was used to measure the drift of a given test pixel from its reference position,

$$Distance (^{\circ}) = \sqrt{(\vartheta(A_r) - \vartheta(A_i))^2 + (\varphi(A_r) - \varphi(A_i))^2} \quad (3.12)$$

$$Distance (km) = \frac{Distance (^{\circ})}{0.0009 ^{\circ}} \times \frac{100 m}{1000 m \text{ per } km}$$

where $\varphi(A_r)$ and $\vartheta(A_r)$ are the latitude and longitude coordinates for test pixel A in an arbitrary reference image, and $\varphi(A_i)$ and $\vartheta(A_i)$ are the latitude and longitude coordinates for test pixel A on subsequent HICO images. We set the HICO image of Shark Bay captured on 19 November 2011 as the reference image, and as such the Euclidean distances from equation (3.12) are relative measures but still illustrate geo-spatial consistency through time. Note that these Euclidean distances were converted to kilometres for ease of interpretation, and are presented in Figure 3.11.

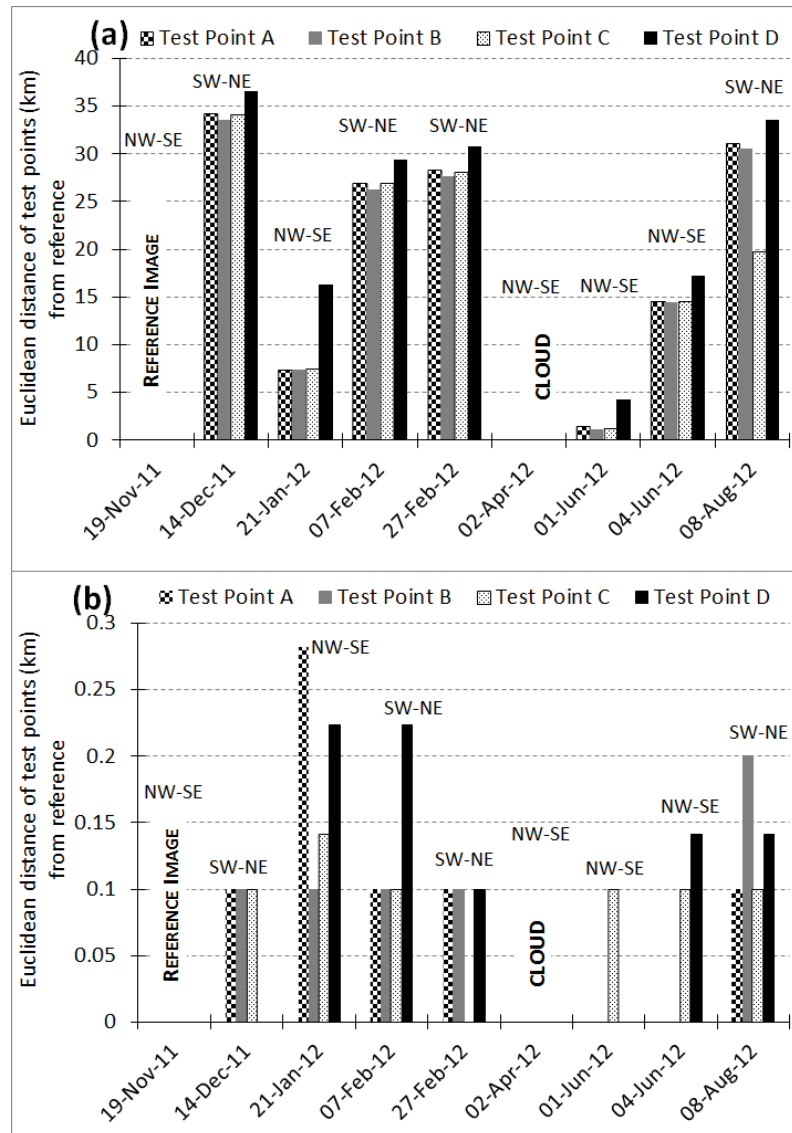


Figure 3.11: Geo-spatial consistency of each HICO image of Shark Bay, relative to 19 November 2011, after (a) Geo-referencing using the provided GLT files, and (b) subsequent Geo-registration using the ground control points. NW-SE and SW-NE refers to the HICO swath orientation.

Figure 3.11a shows that simply geo-referencing a HICO swath with the provided GLT can generate geo-spatial inconsistencies greater than 10 km. The largest geo-spatial inconsistency is encountered when the scene is imaged with different swath orientations. For example, the reference image had a NW-SE orientation whilst the images on the 14 December 2011, 7 February, 27 February, and 8 August 2012 had a SW-NE orientation and where the test pixels encountered drifts greater than 20 km from their reference positions (Figure 3.11a). In contrast, those dates that were imaged with the same swath orientation (21 January, 1 June, 4 June 2012) exhibited much lower geospatial inconsistencies (< 17 km). Such large relative geospatial

displacements will introduce significant errors into change detection analysis, where a change in the geophysical parameter of a pixel is likely due to an evaluation at different locations rather than a temporal change (Townshend, Justice, Gurney, & McManus, 1992). By performing a series of misregistration simulations on Landsat imagery, Dai and Khorram (1998) showed that a geolocation accuracy of less one fifth (<0.20) of a pixel is needed to detect 90% of real temporal changes. For HICO this equates to achieving 20 m geolocation accuracy.

Manual geo-registration using GCPs taken from Google Earth™ imagery significantly improved the geospatial consistency, where the test pixels were now within 300 m of the reference pixels (Figure 3.11b). However, this geospatial consistency is still relatively large compared to the 100 x 100 m HICO pixel footprint. Furthermore, this result is poor compared to other operational satellites, such as MODIS and MERIS both of which achieve sub-pixel geolocation accuracies of ~50 m (Wolfe et al., 2002) and 77 m (Bicheron et al., 2011), respectively and whose ground sampling distance are at least twice as much as that of HICO. This highlights the need for an improved HICO geolocation algorithm that will increase the geolocation accuracy of the resultant GLTs and/or an improved method of using GCPs for subsequent geo-registration. The manual geo-registration employed here has proved troublesome due to: (a) the slight translational drift of the HICO swath, which prohibits the use of a consistent set of GCPs; (b) the amount of GCPs needed to achieve a geospatial consistency of less than 300 m, and; (c) cloud cover, which when present will compromise the accuracy of the geo-registration.

Fortunately, since the commencement of this research, and as part of the transition of HICO data to NASA, the Naval Research Laboratory (NRL) has improved the geolocation accuracies of the provided GLTs to 200-300 m. This improved HICO data is now available through NASA's Ocean Biology Processing Group's data portal:

(<http://oceancolor.gsfc.nasa.gov/cgi/browse.pl?sen=hi>).

3.4.5 Change detection

The ability to detect change in a geophysical parameter from multi-temporal remotely sensed imagery is a key outcome in ecosystem monitoring (Coppin, Jonckheere, Nackaerts, & Muys, 2004). However, literature on detecting change above the uncertainty of multi-temporal datasets is sparse, with exception of Shi and Ehlers

(1996) and Hester, Nelson, Cakir, Khorram, and Cheshire (2010). This section will assess this ability using the HICO-derived, tide corrected, bathymetry dataset. To this end, it is assumed that each geo-registered bathymetry image has sufficient geolocation accuracy to assess temporal change. A two sample, per-pixel, t -test was used to accept or reject the null hypotheses of equal depth (i.e. no change) between pixels (i, j, t_1) and (i, j, t_2) . As described in section 3.2.3, the retrieved depth and its uncertainty were the average and standard deviation, respectively, calculated from a set of 20 noise-perturbed spectra. This is analogous to performing a t -test on two independent sample means, assuming unequal variance, both with a sample size of 20. Here, the upper and lower tail of the Student's t cumulative distribution function at the calculated t statistic and degree of freedom are used to compute the p value. The null hypothesis of “no change in depth” is rejected for pixels with $p < 0.05$ (5% significance level).

Figure 3.12 shows empirically tide corrected bathymetry profiles at row number 1686 for each geo-registered bathymetry image. The uncertainty of the retrieved depth is overlaid around the average depth. This figure illustrates that for shallow waters, of depth less than 6 m, the inversion routine presented can retrieve consistent depths through time – even in the presence of sub-optimal atmospheric correction. However, as the retrieved depth increases, so does its temporal variability, as illustrated by the quasi-deep water pixels of the Faure Sill channels A and B in Figure 3.12. This temporal variability is unlikely caused by natural phenomena, and is more likely the result of variable quality of atmospheric correction and shallow water model inversion. As noted in Section 3.3.1, the magnitude of spectral noise introduced to R_{rs} from atmospheric correction becomes comparable to the reflectance signal as the geometric depth increases. As such, this spectral noise coupled with sun-glint correction would decrease the accuracy in the retrieved depth over quasi-deep water more than it would for shallow water pixels and effectively creates the observed temporal variability in deep water pixels.

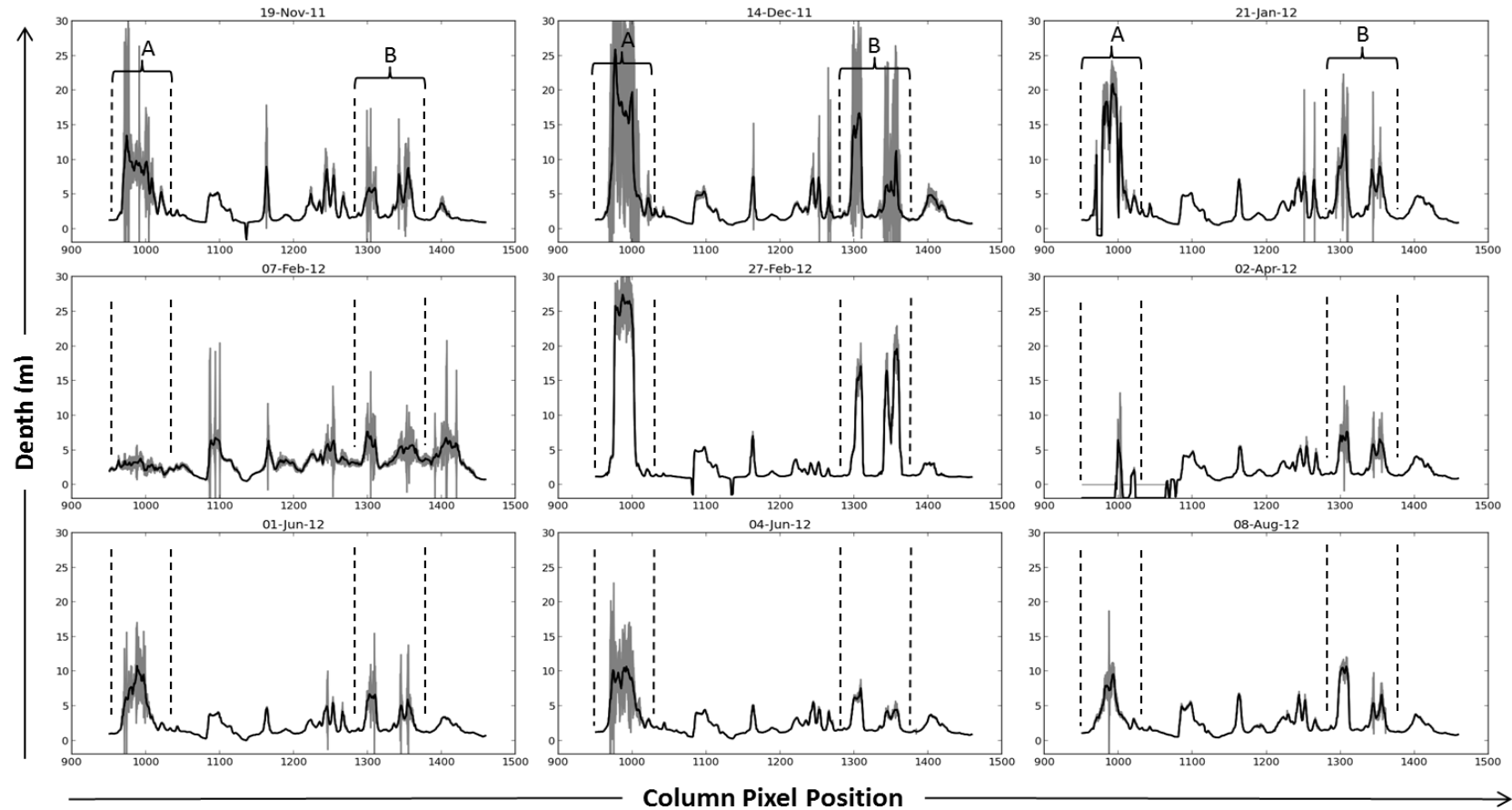


Figure 3.12: Cross-sectional depth profiles of the Faure Sill, at row 1686, taken from geo-registered HICO derived bathymetry images. The solid black line and grey envelope surrounding it represents the retrieved depth and its uncertainty respectively. Highlighted are two sets of deep water channels, A and B, located at column positions 950-1050 and 1280-1380 respectively. The depth of these channels show high temporal variability, the cause of which is discussed in the text.

Despite the normalisation of the bathymetry dataset to a common depth; changes unrelated to tide are expected due to the frequent movement of tidal sandbanks across the Faure Sill. Figure 3.13 shows changes in the HICO-derived, tide corrected bathymetry across the Faure Sill between the dates of: (a) 14 December 2011 and 21 January 2012; (b) 21 January- and 27 February-2012; (c) 27 February- and 04 June-2012 and; (d) 04 June- and 08-August-2012. In this figure, pixels that observed a change had: (1) a difference in depth greater than the baseline variability, and; (2) a p value less than 0.05 (5% interval) at the calculated degree of freedom. Otherwise pixels were classified as having 'no change' and displayed as grey. Here, we define the baseline variability as the residual random fluctuations within the tide corrected bathymetry dataset. Recall that the SEM of the image-based tide corrected bathymetry dataset was 0.12 m (see Table 3.3). Hence, the bathymetry varied on average by 12 cm between each successive timestamp. We set the baseline variability to equal three times the SEM (i.e. 0.36 m), which would encompass: random offsets in depth due to imperfect atmospheric/sun-glint/air-to-water interface corrections, and; imperfect tide normalisation. Therefore any changes in depth greater than the baseline variability of 0.36 m, which are statistically significant with regards to the uncertainty, are plausible and not due to random depth fluctuations caused by corrections performed in the processing.

The change detection analysis shown in Figure 3.13 does not include the bathymetry images on 7th February and 2nd April 2012, as the bathymetry profiles of these dates (see Figure 3.12) appear inaccurate. This is evident from the derived depth values of channels A and B when compared to the other profiles. Furthermore these two bathymetry images were included (results not presented here), the change detection analysis afforded significant, yet unrealistic changes in depth across the Faure Sill. Additionally, deep-water pixels were flagged in Figure 3.13, due to their temporal variability as noted in Figure 3.12.

For the purpose of change detection, separate image based tide corrections were performed for the different regions of Shark Bay, shown by the dashed magenta regions in Figure 3.13a. These regions were: (1) the eastern and western shallow areas of Hamelin Pool, and: (2) the Wooramel bank containing water channels orientated perpendicular to the coast. These two additional tide corrected subsets were merged to the tide corrected bathymetry dataset of the Faure Sill (Section 3.3.2) to form a complete tide corrected bathymetry image of lower Shark Bay for each HICO

overpass. This latter dataset was used to assess the temporal changes in depth with the method described above.

Separate tide correction over Hamelin Pool and the Wooramel bank were performed to take into account the differing tidal variations across the Shark Bay region. For instance, the tidal regime at Hamelin Pool is particularly complex in which the astronomical tide accounts for only 15% of the variation in water height (Burne & Johnson, 2012). Over this enclosed embayment, the mean sea-level varies in an irregular manner due to seasonal winds. Specifically southerly winds, that during summer, when they are more persistent and strongest, act to reduce the mean sea level by approximately 50 cm compared to that in winter when the southerly winds subside (Burne & Johnson, 2012).

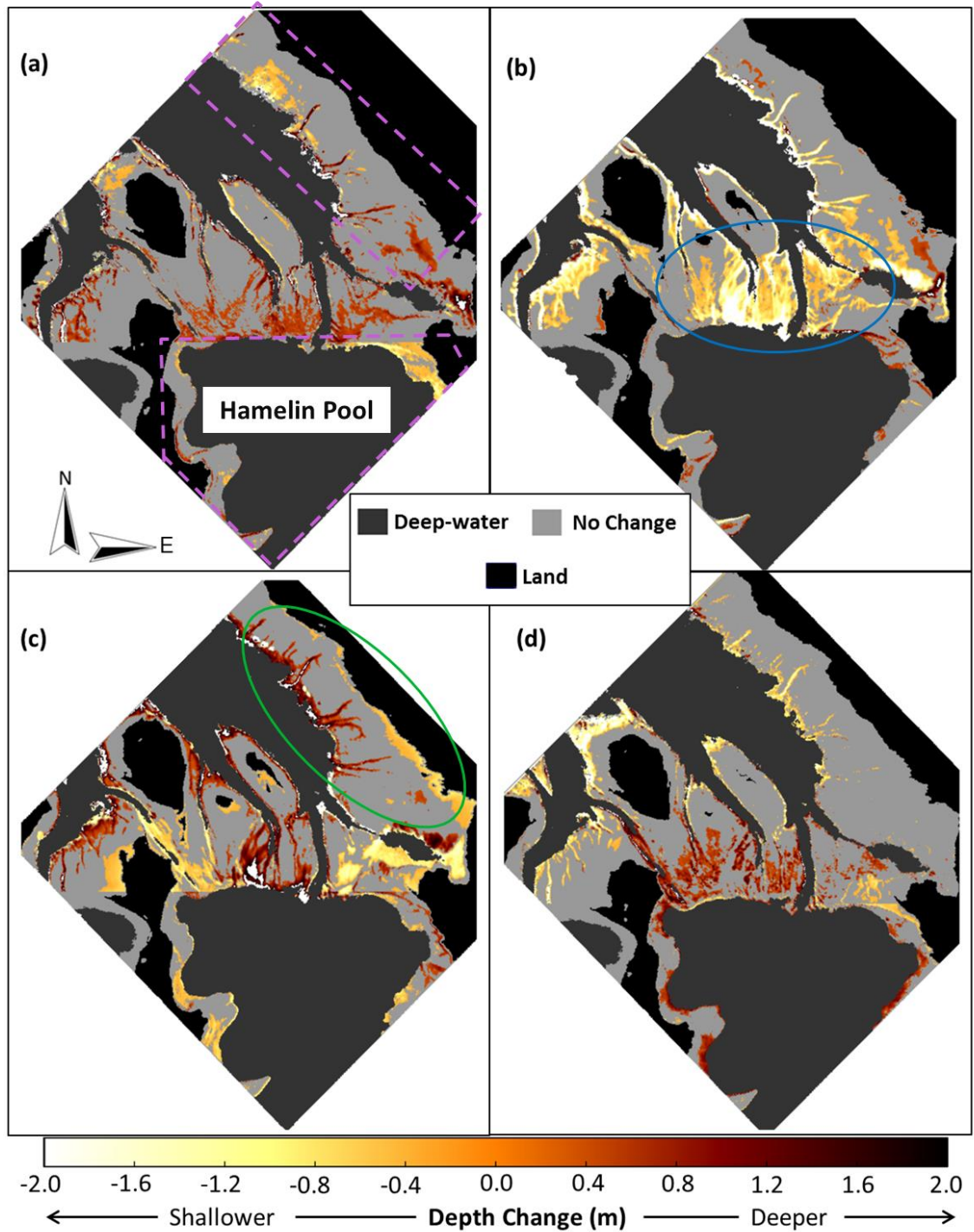


Figure 3.13: Change detection analysis of HICO-derived, tide corrected bathymetry of the Faure Sill between the dates of: (a) 14-Dec-2011 and 21-Jan-2012; (b) 21-Jan- and 27-Feb-2012; (c) 27-Feb- and 04-Jun-2012 and; (d) 04-Jun- and 08-Aug-2012. Deep-water and land are presented as dark and black pixels respectively. The blue and green circles in (b) and (c) highlight regions of change discussed in the text. Separate image-based tide corrections were performed for the dashed magenta presented in (a).

The HICO-derived bathymetry dataset spans both summer and winter and thus it is likely that the Faure Sill, Hamelin Pool and the Wooramel bank have substantially different tide heights. The normalisation to a reference depth over the Faure Sill can therefore introduce large artificial depth changes at the other regions, and as such, separate image-based tide corrections were performed. It should be noted that separate regional tide correction and subsequent merging to a single bathymetric image can only be used to analyse temporal changes; as these images would contain steps in the depth between adjacent tide corrected regions. Tidal modelling would be necessary to interpolate (either linearly or non-linearly) the tide correction offsets for the different regions to generate a homogeneous tide corrected bathymetry image. However this is beyond the scope of this study.

The change detection analysis (Figure 3.13) indicates constant bathymetry for the majority of the Faure Sill. Though there are three regions that experience bathymetric fluctuations between the five successive dates. These regions are predominantly shallow water areas: (i) on the western and eastern sides of Hamelin Pool; (ii) on the southern Faure Sill (see blue circle in Figure 3.13b), and; (iii) on the Wooramel bank (green circle in Figure 3.13c).

The extent of change observed ranged between approximately -1.6 m (shallower) and 1.6 m (deeper); this appears to be an unrealistic depth change in the timeframe of one month. For example on the western shallow regions of Hamelin Pool, the depth decreased by approximately 1 m from 27 February to 4 June 2012. This is unlikely to occur as the benthos of this region consists of hard microbial pavement that is not susceptible to erosion from water movement (Jahnert & Collins, 2011). Although the deposition of motile sediment and its subsequent removal is possible, the extent of change observed through the HICO-derived bathymetry is unlikely. However, we are encouraged by the spatial consistency of several features in this region, whose depth fluctuates through time.

The change in depth detected on the southern Faure Sill between 21 January and 27 February 2012 (blue circle in Figure 3.13b) and 27 February and 4 June 2012 (Figure 3.13c) appears to be due to a plume of turbid water at this location on the 27 February (see red square in Figure 3.14). The true colour imagery on 27 February does indicate the formation of new water channels; however the change detection (Figure 3.13) shows that the bathymetry at this date is approximately 1 m shallower than on 21 January – contrary to the formation of new water channels. Additionally, R_{rs} spectra

of this region indicate higher absorption between 400 to 500 nm than the adjacent areas, suggestive of higher CDOM/phytoplankton. The retrieved model parameters over the plume on 27 February 2012 are: $a_{\phi}(440) = 0.11 \text{ m}^{-1}$, $a_{dg}(440) = 0.18 \text{ m}^{-1}$, $b_{bp}(550) = 0.12 \text{ m}^{-1}$, depth = 0.50 m, $B_{sand} = 0.115$, and $B_{seagrass} = 0.005$. The same region on the 21 January 2012 had lower IOP values, larger depth and a brighter substrate: $a_{\phi}(440) = 0.035 \text{ m}^{-1}$, $a_{dg}(440) = 0.07 \text{ m}^{-1}$, $b_{bp}(550) = 0.035 \text{ m}^{-1}$, depth = 3.5 m, $B_{sand} = 0.45$, and $B_{seagrass} = 0.02$. Given the high IOPs, very shallow depth and low bottom albedo coefficients implies that the bottom contribution to R_{rs} is very low or non-existent over this plume, and as such the retrieved depth is unreliable. In operational satellite processing, such pixels should be flagged as deep-water pixels and not used in the change detection analysis.

The shallow water region with water channels orientated perpendicular (green circle in Figure 3.13) appears to have undergone changes in depth due to resuspension and movement of sediment near the mouth of the Wooramel River. This was observed on the 14 December 2011, where the sediment plume appeared to enter the numerous channels and flow northward (Figure 3.14). It is possible that some sediment would have settled down, given that modelled tidal flow (Burling, 1998) is perpendicular to the channels' orientation (i.e. trapping sediment) with a modelled speed of approximately 0.5 m/s at high and low tide (Burling, 1998). Retrieved $b_{bp}(550)$ imagery on 21 January 2012 revealed that the amount of suspended sediment in the water column was considerably less, and where the change detection analysis showed an increase in depth by approximately 1.2 m (Figure 3.13a). In other words, on the 14 December the water channels were 1.2 m shallower, presumably due to the high sediment deposition that was subsequently eroded over 38 days until 21 January 2012. Note the fluctuating depth changes (shallower, then deeper) for these channels are observed in Figures 3.13b and 3.13c, due to more resuspension and movement of sediment from the mouth of the Wooramel River on 27 February 2012.

The change detection analysis highlights that though some of the changes observed are feasible, the extent of change (approximately 1 m) is unlikely. The magnitude of detected change depends on the accuracy and precision of the depth retrievals and on the tide correction scheme. Firstly a relatively high precision is needed to detect change above the uncertainty. Here the low relative uncertainty in the retrieved depths of shallow water pixels (< 10%, see Figure 3.6) allowed the detection of subtle changes to as low as 40 cm (see Figure 3.13). Secondly, high accuracy in the

retrieved depth (prior to tide correction) is required to infer accurate magnitudes of change. This in turn necessitates adequate atmospheric correction and a robust optimisation scheme that converges to the global minimum. Here, the sub-optimal radiometric corrections have likely reduced the accuracy, particularly over the quasi-deep water pixels, whilst the convergence to local minima is the likely cause of the inaccuracy in some shallow water pixels. Future improvements to atmospheric and sun-glint corrections and optimisation schemes will increase the accuracy in change detection analysis, however, this study has shown that even with sub-optimal corrections, it is possible to detect change above the uncertainty in the retrievals due to environmental and sensor noise.

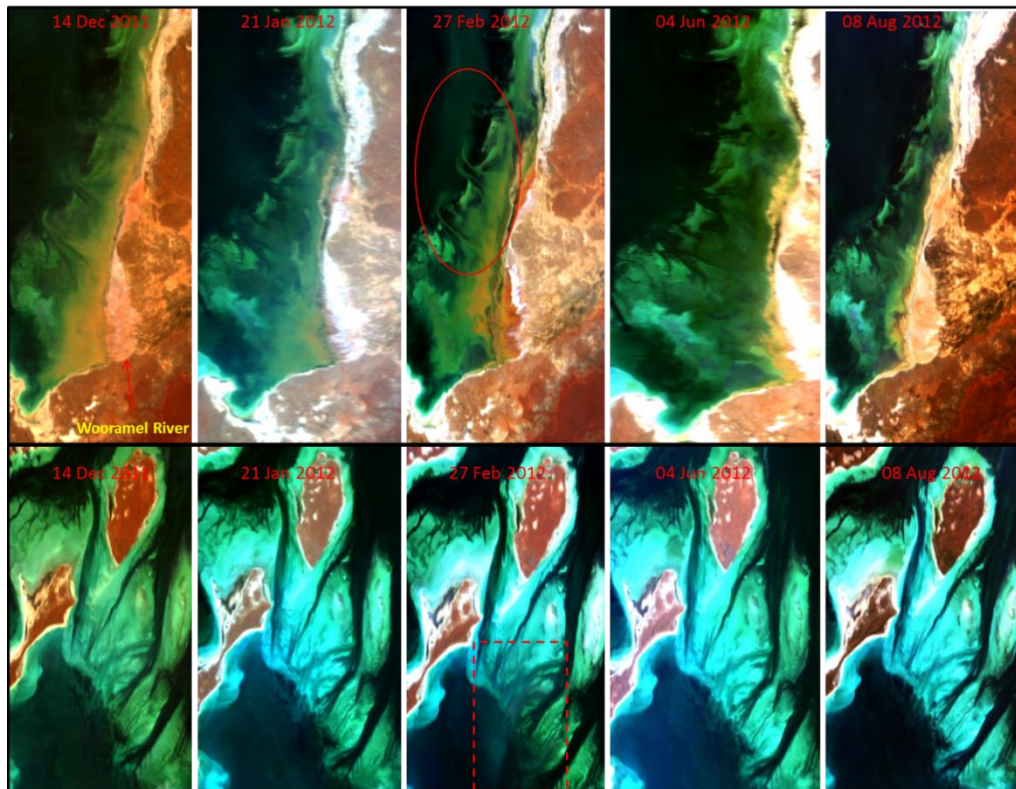


Figure 3.14: HICO derived pseudo true colour images of: the shallow water region parallel to the coast, north of the Wooramel River (top panels), and; the Faure Sill (bottom panels). The top panels show sediment flowing north from the Wooramel River, and through the seagrass channels orientated perpendicular to the coast, indicated by the red circle. The red square on 27-Feb-2012 highlights a plume of turbid water on the southern Faure Sill (bottom panel).

3.5 Conclusion

The accuracy and precision of the HICO-derived bathymetry dataset was dependent on the quality of the atmospheric/sun-glint correction and on the BRUCE

shallow water semi-analytical inversion scheme respectively. For many atmospheric correction algorithms, such as Tafkaa (Gao et al., 2000), the lack of spectral bands past 900 nm inhibits the selection of the appropriate atmospheric aerosol model and an estimation of vertical column water vapour in a per-pixel basis. To overcome this information gap, coincident MODIS level-2 products of the Shark Bay region were processed and used to obtain several of the input parameters that Tafkaa-6S required. This study has shown that the procedure introduced three spectral artefacts to the remote sensing reflectance spectra. Unfortunately, the high absorption of light in the water column throughout Shark Bay causes the magnitude of the water-leaving reflectance to become comparable to that of the spectral artefacts – particularly over quasi-deep and optically deep water pixels. This potentially leads to inaccurate depth retrievals over these pixels. Conversely, the accuracy of the depth retrievals for shallow water were shown to be not greatly affected as the magnitude of R_{rs} for these pixels were substantially higher relative to the spectral artefacts.

Addition of spectral artefacts enhanced the complexity of the parameter space with the addition of more local minima. To increase the likelihood of the LM algorithm localising to a global minimum, a brief search of parameter space was performed to locate the parameter values that corresponds to a local minimum with the lowest Euclidean distance. These parameter values were then passed as the initial values to the uncertainty inversion scheme proposed by Hedley et al. (2010). This per-pixel parameter space ‘update-repeat’ search and uncertainty determination afforded improved retrievals of bathymetry, where the majority of the bathymetry image had a relative uncertainty of less than 20%. A per-pixel *t*-test analysis between bathymetry images at consecutive timestamps revealed the ability to detect changes in HICO-derived depth to as low as 0.4 m. This reinforces the use of satellite-based hyperspectral remote sensing techniques in analysing time series datasets when uncertainty is taken into account.

HICO’s ability to detect temporal change is not only dependent on precision of the bathymetric dataset but also on its geolocation accuracy. Thorough georegistration using ground control points taken from Google Earth™ imagery has increased the relative geolocation accuracy, from more than 30 km using the distributed geographic lookup tables, to better than 300 m (i.e. 3 pixels). However, despite this improvement, analysing temporal change from remotely sensed imagery requires sub-pixel geolocation accuracy, that is, less than 100 m for HICO. Thus

enabling time series analysis of HICO data requires further work in either creating automated geo-registration algorithms.

Relating changes in bathymetry to factors such as sedimentation/erosion necessitates the removal of the tidal contribution to the retrieved water column depth. Correcting tide height over the Faure Sill has proved problematic. An empirical tide correction scheme is presented that corrects each bathymetry image in the time series to a reference depth. This reference depth is arbitrary and in this case was set to the median depth across the time series. However, this reference depth can be set to a datum such as lowest astronomical tide or mean water height if these values are known for the region. Even so, with this image based normalisation of depth, it was shown that detecting changes in depth due to sedimentation/deposition of as low as 0.4 m is possible. The fluctuating changes in depth (increasing then decreasing) of several spatially consistent features are particularly encouraging. Though the extent of change is at present over-estimated, improvements to atmospheric/sun-glint/air-to-water interface corrections would directly enhance the accuracy of the depth retrievals and hence extent of change.

The issues faced here in regards to atmospheric and sun-glint corrections are by no means inherent to HICO, but to all ocean colour sensors. Though HICO was built as a prototype low cost sensor, its data can be manipulated to retrieve precise bathymetry. The development of future sensors that have: (1) higher SNR and SWIR bands in combination with more advanced atmospheric/sunglint correction and in water inversion algorithms could substantially improve bathymetry retrievals, and; (2) sophisticated geo-location and –registration algorithms to afford sub-pixel geolocation accuracies will also lead to the ability in monitoring changes in the bathymetry of key coastal regions.

CHAPTER 4

IMPROVING THE OPTIMISATION SOLUTION FOR A SEMI-ANALYTICAL SHALLOW WATER INVERSION MODEL IN THE PRESENCE OF SPECTRAL NOISE

*This chapter and the associated appendices have been published in the journal:
Limnology and Oceanography: Methods*

Rodrigo A. Garcia, Lachlan, I. W. McKinna, John D. Hedley, Peter R. C. S. Fearn.

Improving the optimisation solution for a semi-analytical shallow water inversion model in the presence of spectrally correlated noise. *Limnology and Oceanography: Methods*, 12 (2014), pp. 651-669. DOI: 10.4319/lom.2014.12.651.

<http://onlinelibrary.wiley.com/doi/10.4319/lom.2014.12.651/abstract>

4.1 Abstract

In coastal regions, shallow water semi-analytical inversion algorithms may be used to derive geophysical parameters such as inherent optical properties (IOPs), water column depth and bottom albedo coefficients by inverting sensor-derived sub-surface remote sensing reflectance, r_{rs} . The uncertainties of these derived geophysical parameters due to instrumental and environmental noise can be estimated numerically via the addition of spectral noise to the sensor-derived r_{rs} prior to inversion. Repeating this process multiple times allows the calculation of the standard error and average for each derived parameter. Apart from spectral non-uniqueness, the optimisation algorithm employed in the inversion must converge onto a single minimum to obtain a true representation of the uncertainty for a given set of noise-perturbed r_{rs} . Failure to do so inflates the uncertainty and affects the average retrieved value (accuracy). We show that the standard approach of seeding the optimisation with an arbitrary, fixed initial guess, can lead to the convergence to multiple minima, each having substantially different centroids in multi-parameter solution space. We present the Update-Repeat Levenberg-Marquardt (UR-LM) and Latin Hypercube Sampling (LHS) routines that dynamically search the solution space for an optimal initial guess; that when applied

to the optimisation allows convergence to the best local minimum. We apply the URLM and LHS methods on HICO-derived and simulated r_{rs} , and demonstrate the improved computational efficiency, precision and accuracy afforded from these methods compared to the standard approach. Conceptually, these methods are applicable to remote sensing based, shallow water or oceanic semi-analytical inversion algorithms requiring non-linear least squares optimisation.

4.2 Introduction

The implicit inverse modelling approach is commonly used in optical remote sensing applications to derive geophysical parameters from sensor-observed radiometric data. A typical semi-analytical inversion algorithm comprises of three key components: (i) a forward semi-analytical model, (ii) a set of internal geophysical parameters, and (iii) an inverse spectral optimisation method (Werdell et al., 2013). In shallow waters, a forward semi-analytical model simulates the sub-surface remote sensing reflectance, r_{rs} , as a function of the water column's inherent optical properties (IOPs), depth and the bottom albedo coefficients (Maritorena et al., 1994; Lee et al., 1998; Albert & Mobley, 2003; Klonowski et al., 2007; Brando et al., 2009). Using an optimisation method, the internal geophysical parameters (i.e. IOPs, depth, and bottom albedos) are iteratively varied until the modelled sub-surface remote sensing reflectance, r_{rs}^M , best matches the sensor-derived r_{rs} . At this point, the set of internal geophysical parameters are deemed the optimal solution.

Two spectral optimisation methods implemented by semi-analytical ocean colour inversion models are the Levenberg-Marquardt (LM; Marquardt, 1963, e.g. Klonowski et al., 2007; Werdell et al., 2013) and Downhill simplex algorithms (Nelder & Mead, 1965, e.g. Brando et al., 2009). These optimisation algorithms iteratively change the model parameters in the direction of the lowest cost function; where the cost function is a measure of the similarity between the forward modelled r_{rs}^M and the sensor-derived r_{rs} . Thus the objective of these optimisation schemes is to find the global minimum, that is, the set of model parameters whose modelled r_{rs}^M matches perfectly with r_{rs} . Unfortunately such optimisation algorithms are understood to potentially converge to local minima – rather than the global minimum – particularly if the initial guess used to seed the optimisation is sufficiently close to a local minimum (Kirkpatrick, Gelatt, & Vecchi, 1983; Press, Teukolsky, Vetterling, & Flannery, 2007).

Several global optimisation algorithms have been implemented in the inversion of ocean colour data. Maritorena, Siegel, and Peterson (2002) used a downhill simplex-coupled simulated annealing procedure (see Kirkpatrick et al., 1983; Press et al., 2007) to retrieve chlorophyll concentration, absorption coefficient for dissolved and detrital material, $a_{dg}(443)$, and the particulate backscattering coefficient, $b_{bp}(443)$, from ocean colour radiometry. Similarly, Salinas, Chang, and Liew (2007) used the native simulated annealing procedure (Kirkpatrick et al., 1983) to derive $a_{dg}(440)$, $b_{bp}(550)$ and the absorption coefficient of phytoplankton, $a_{phy}(440)$. Slade, Resson, Musavi, and Miller (2004) and Zhan, Lee, Shi, Chen, and Carder (2003) used particle swarm optimisation and genetic algorithms, respectively (both global optimisation methods) to derive $a_{phy}(440)$, $a_{dg}(440)$ and $b_{bp}(550)$ from ocean colour radiometry of optically deep waters.

The basis behind these global optimisation algorithms is a preliminary search of the multi-parameter solution space from which the global minimum is then located. The only disadvantage of these global optimisation techniques is the processing time required to invert a single reflectance spectrum. Processing time becomes particularly critical when propagating uncertainty through the inversion-optimisation procedure to derive the uncertainty for each retrieved parameter. Huang, Li, Shang, and Shang (2013) demonstrated the application of a hybrid simulated annealing-downhill simplex (HSADS) routine to derive $a_{phy}(440)$, $a_{dg}(440)$ and $b_{bp}(440)$ from simulated and measured R_{rs} with high accuracy. In a comparison between different optimisation schemes, Huang et al. (2013) showed that the Levenberg-Marquardt (LM) algorithm was computationally faster (by a factor of 800) than HSADS, and both methods achieved similar inversion results. Indeed the standardised error and root mean square error between the actual and retrieved IOP values obtained from LM was comparable to that obtained from HSADS. However, HSADS produced 47 more valid retrievals (out of 500 retrievals) than the LM algorithm.

An analysis of the propagation of noise caused from sensor and environmental conditions (e.g. atmospheric fluctuations, sea surface state), through the inversion process to the retrieved geophysical parameters has recently been applied to imagery from several satellite platforms (Garcia et al., 2014; Hedley et al., 2012a). In this method, the derived r_{rs} is perturbed multiple times by the addition of spectrally correlated noise, of various magnitudes, and inverted to obtain a range of IOPs, depth and bottom albedo values from which the uncertainties are calculated. This is a

computationally demanding procedure where each derived r_{TS} is perturbed, for example, twenty times by the sensor-environment spectral noise (e.g. Hedley et al., 2012a). This effectively means that a given satellite image is inverted 20 times which, when combined with the iterative process of an optimisation algorithm, can result in potentially large processing times. Consequently, optimisation routines that offer high computational efficiency are desired.

The inclusion of spectrally correlated noise taken from the spectral covariance matrix of an imaged homogeneous deep-water region, potentially introduces more local minima to the multi-parameter solution space. Such minima add more convergence points on which local optimisation algorithms may converge. Use of HSADS or any other global optimisation algorithms, though desirable, is computationally prohibitive. Thus in this paper we investigate two simple and computationally faster methods, the Update Repeat Levenberg-Marquardt (UR-LM) and Latin Hypercube Sampling (LHS), that guide the LM algorithm to the optimum (if not global) minimum. Here the optimum minimum refers to the minimum with the lowest cost function found during the initial search of parameter space. The UR-LM locates the optimum minimum by taking a finite step away from a local minimum and discerning whether the optimisation returns to the same minimum or one with a lower cost function. The UR-LM repeats this procedure if the latter occurs, until either the same minimum is converged to or the number of repeats exceeds ten. The LHS method, on the other hand, locates local minima from a wide variety of initial guesses. The local minimum with the lowest cost function is then defined as the optimum. We adopted the LM algorithm as implemented in MPFIT (in C language; Markwardt, 2009) that allows for upper and lower bounding constraints. Unlike the LM algorithm employed by Huang et al. (2013), these constraints eliminate issues dealing with non-physical retrievals.

The UR-LM and LHS methods are in a sense a common tactic in finding the global minimum when using the LM algorithm (Press et al., 2007). Within this study we apply the UR-LM and LHS optimisations schemes, in combination with the semi-analytical shallow water algorithm proposed by Klonowski et al. (2007), to invert a selection of r_{TS} observed by the Hyperspectral Imager for the Coastal Ocean (HICO) and a set of simulated r_{TS} spectra. Both the HICO-derived and simulated r_{TS} were selected/simulated for coastal waters with varying benthic substrates, depths and in-water optical properties. We show that these two methods: (1) are more

computationally efficient – requiring fewer LM iterations when inverting the noise-perturbed r_{rs} compared to the standard approach where the initial guesses are arbitrarily set and fixed; (2) provide lower uncertainties and high accuracies in the presence of spectrally correlated noise compared to the standard approach, and; (3) are not affected by changes to the lower bounds in the constrained LM algorithm, unlike the inversions from the standard approach.

4.3 Methods and data

4.3.1 Shallow water model

The semi-analytical Bottom Reflectance Un-mixing Computation of the Environment algorithm, BRUCE (Klonowski et al., 2007), was used to retrieve water column inherent optical properties (IOPs), geometric depth and key benthic substrates from both simulated and satellite-derived hyperspectral r_{rs} . Klonowski et al. (2007) and Fearn et al. (2011) extensively describe the forward model of the BRUCE algorithm; briefly the r_{rs} is modelled as a function of the absorption (a) and backscattering coefficients (b_b) of the water column, the geometric depth (H), the bottom reflectance (ρ) and the sun-sensor viewing geometries (Lee et al., 1999),

$$r_{rs}(\lambda) \approx (0.084 + 0.170u)u \left(1 - \exp \left\{ - \left[\frac{1}{\cos\theta_w} + \frac{1.03(1 + 2.4u)^{0.5}}{\cos\theta_v} \right] \kappa H \right\} \right) + \frac{\rho}{\pi} \exp \left\{ - \left[\frac{1}{\cos\theta_w} + \frac{1.04(1 + 5.4u)^{0.5}}{\cos\theta_v} \right] \kappa H \right\} \quad (4.1)$$

$$u(\lambda) = \frac{b_b(\lambda)}{a(\lambda) + b_b(\lambda)} \quad (4.2a)$$

$$\kappa(\lambda) = a(\lambda) + b_b(\lambda) \quad (4.2b)$$

where θ_v and θ_w are the subsurface sensor-viewing zenith and solar zenith angles respectively. The spectral absorption and backscattering coefficients are themselves functions of the following: (1) the absorption coefficient of phytoplankton at 440 nm, P ; (2) the absorption coefficient of coloured dissolved and detrital matter at 440 nm, G ; and (3) the backscattering coefficient of suspended particles at 550 nm, X , as given by (Lee et al., 1999)

$$a(\lambda) = a_w(\lambda) + Pa_{phy}^*(\lambda) + Ge^{-0.015(\lambda-440)} \quad (4.3)$$

$$b_b(\lambda) = b_{bw}(\lambda) + X \left(\frac{550}{\lambda} \right) \quad (4.4)$$

where $a_w(\lambda)$ and $b_{bw}(\lambda)$ are the spectral absorption and backscattering coefficients of pure water respectively, and $a^*_{phy}(\lambda)$ is the specific absorption coefficient of phytoplankton normalised to a value of 1.0 at 440-nm. The exponent in equation (4.3) parameterises the spectral shape of the absorption coefficient of coloured dissolved and detrital matter, $a^*_{dg}(\lambda)$. In BRUCE (Klonowski et al., 2007) the net benthic albedo, $\rho(\lambda)$, is expressed as a linear combination of the albedos of three key benthic substrates (typically sediment, seagrass and brown algae),

$$\rho(\lambda) = \sum_{i=1}^3 B_i(550 \text{ nm}) \rho_i^*(\lambda) \quad (4.5)$$

where B_i is the albedo at 550 nm and $\rho_i^*(\lambda)$ is spectral irradiance reflectance normalised to a value of 1.0 at 550 nm for the i^{th} benthic class respectively. Both $\rho_i(\lambda)$ and the number of benthic classes can be varied depending on the likely benthos present in the region-of-interest. For HICO imagery of Shark Bay, Western Australia, the bottom albedo was expressed as a linear mix of sand and mixed seagrass (50% *Posidonia australis* and 50% *Amphibolis antarctica*) whilst sand, *Posidonia sp.* (seagrass) and *Sargassum sp.* (brown macroalgae) were used for the simulated hyperspectral dataset.

4.3.2 Hyperspectral data

4.3.2.1 Hyperspectral satellite imagery

The HICO sensor aboard the International Space Station captured a spectral image of Shark Bay (see Figure 4.1), Western Australia, on 14th December 2011. The HICO image data provided by the Oregon State University were at-sensor calibrated top-of-atmosphere radiances. These image data were atmospherically corrected using Tafkaa 6S (Gao et al., 2000) to obtain surface remote sensing reflectance (R_{rs}). Here, the aerosol and atmospheric models were set to “maritime” and “mid-latitude summer” respectively. The Tafkaa 6S inputs for aerosol optical thickness at 550 nm, vertical column water vapour and ozone concentrations were obtained from a coincident MODIS image of Shark Bay. Sun-glint and air-water interface corrections were performed on a per-pixel basis to obtain r_{rs} imagery, from which the improved optimisations of the BRUCE algorithm (Klonowski et al., 2007) were tested and compared. Further details on the Shark Bay study site as well as atmospheric, sun-glint

and air-water corrections are given in section 3.3.2. Note that HICO imagery was obtained through the Oregon State University, College of Earth, Ocean, and Atmospheric Sciences, HICO web portal (hico.coas.oregonstate.edu).

4.3.2.2 Simulated spectra from forward modelling

A total of 4375 simulated hyperspectral r_{rs} spectra of various IOP combinations, depths, bottom types and bottom type mixtures were generated via the BRUCE algorithm's forward model (equation 4.1). These modelled r_{rs} spectra were then convolved with HICO's relative spectral response functions (SRF), using a full width at half maximum of 5.1 nm (Gao et al., 2012) for each band. The resultant simulated r_{rs} dataset therefore had the same spectral resolution and wavelengths as the HICO sensor. The input parameters used to simulate the 4375 HICO r_{rs} are displayed in Table 4.1 where the range of values shown are similar to those used by Klonowski et al. (2007) in validating the BRUCE algorithm. Here, however, the sensor viewing and solar zenith angles were kept constant at 6.3° and 45.2° respectively. These angles were used to match the sensor and solar angle geometries of the HICO Shark Bay image from which spectral noise was extracted and added to the simulated r_{rs} spectra.

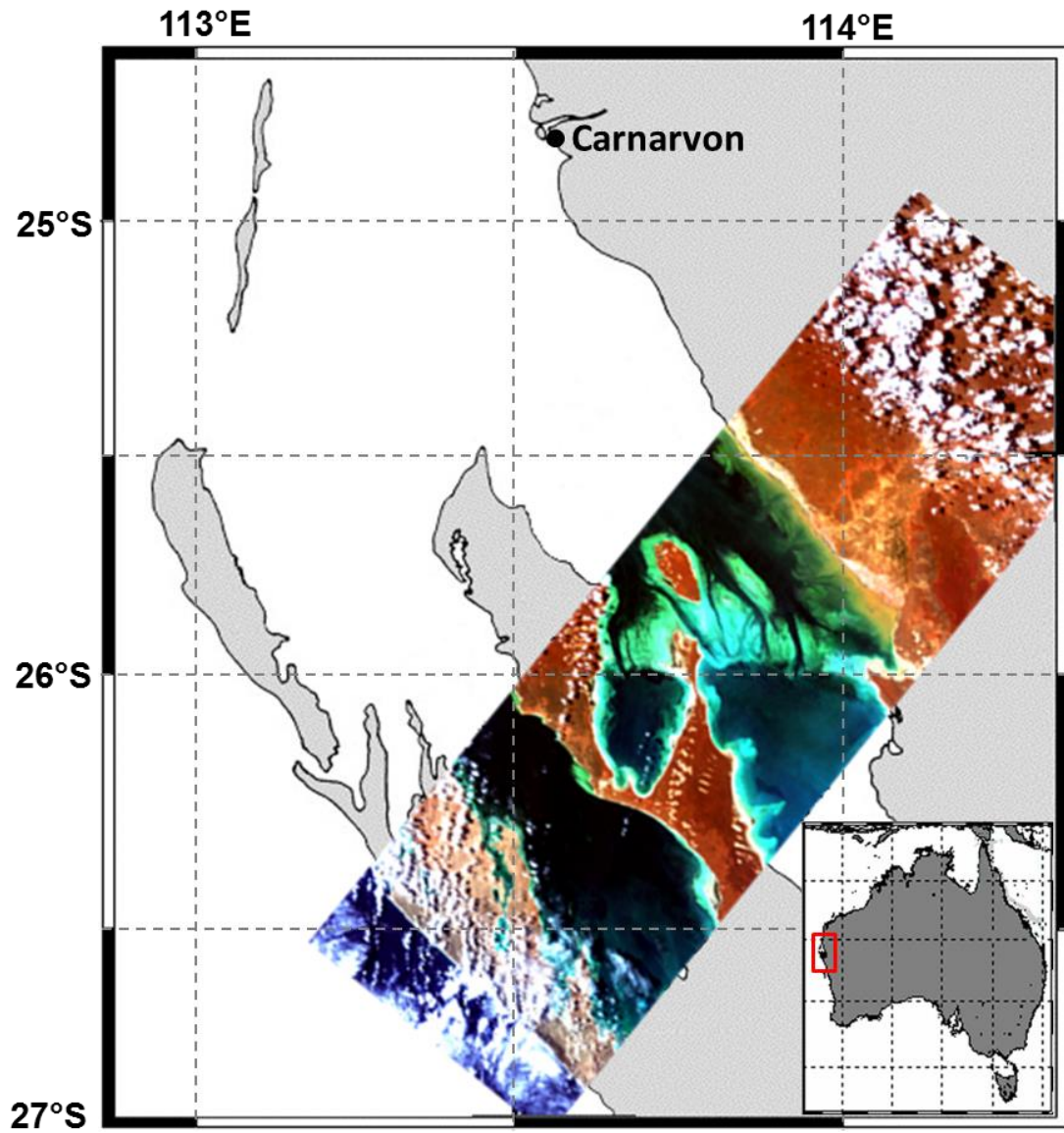


Figure 4.1: Map of Shark Bay, Western Australia, Australia, with HICO-derived R_{rs} pseudo true colour imagery captured on 14 December 2011.

Table 4.1: The set of input model parameters used to generate the 4375 simulated HICO r_{rs} spectra via forward modelling. A view angle of 6.3° from nadir and a solar zenith angle of 45° were used.

BRUCE model parameter	Value
$a_{phy}(440 \text{ nm}), P \text{ (m}^{-1}\text{)}$	0.01, 0.03, 0.05, 0.07, 0.10
$a_{dg}(440 \text{ nm}), G \text{ (m}^{-1}\text{)}$	0.01, 0.1, 0.25, 0.35, 0.50
$b_{bp}(550 \text{ nm}), X \text{ (m}^{-1}\text{)}$	0.006, 0.010, 0.03, 0.07, 0.10
Depth, $H \text{ (m)}$	1, 3, 6, 11, 20
Benthic substrate	Sand, $B_{sand} = 0.227$
albedo, $B_i \text{ (550 nm)}$	<i>Posidonia sp.</i> , $B_{seagrass} = 0.053$ <i>Sargassum sp.</i> , $B_{algae} = 0.033$ Mixture 1: 50% sand ($B_{sand} = 0.113$), 50% <i>Posidonia sp.</i> ($B_{seagrass} = 0.026$) Mixture 2: 50% sand ($B_{sand} = 0.113$), 50% <i>Sargassum sp.</i> ($B_{algae} = 0.016$) Mixture 3: 50% <i>Posidonia</i> ($B_{seagrass} = 0.026$); 50% <i>Sargassum sp.</i> ($B_{algae} = 0.016$) Mixture 4: 33.3% sand ($B_{sand} = 0.076$), 33.3% <i>Posidonia sp.</i> ($B_{seagrass} = 0.018$) and 33.3% <i>Sargassum sp.</i> ($B_{algae} = 0.011$)

One of the aims of this paper is to gauge the accuracy of the UR-LM and LHS methods in the presence of real environmental and sensor noise. Such noise not only should account for instrumental noise, but also environmental noise produced from atmospheric variability, sun-glint, sky radiance and the effects of the air-to-water interface present in image data of aquatic systems. To this end, an estimate of the magnitudes and spectral characteristics of such noise were obtained from the HICO r_{rs} image of Shark Bay captured on 14 December 2011. The procedure of extracting spectrally correlated noise from the image data and adding it to the r_{rs} (simulated or sensor-derived) is explained in the following section. Here, spectrally correlated noise of varying magnitudes and shapes were added to each simulated r_{rs} spectrum to obtain 100 noise-perturbed r_{rs} spectra. These were then inverted using (i) the standard LM (SLM), (ii) UR-LM and (iii) LHS implementations of the BRUCE algorithm.

4.3.3 Optimisation and uncertainty propagation

As alluded previously, two datasets were used within this study: (1) the HICO-derived r_{rs} image data, and; (2) the simulated r_{rs} dataset that mimics the spectral resolution of the HICO sensor (henceforth referred to as simulated r_{rs} dataset). In both datasets, the constrained non-linear Levenberg-Marquardt (LM) algorithm (Marquardt, 1963; Markwardt, 2009) was used to derive the model parameters P , G , X , H , B_{sand} , and $B_{seagrass}$. For the simulated r_{rs} dataset, B_{algae} was additionally derived. With this approach, we could observe the effect of the SLM, UR-LM, and LHS optimisation implementations on the ‘best case’ simulated r_{rs} data and on ‘real world’ HICO-derived r_{rs} data. To ensure spectral consistency between the forward modelled r_{rs}^M and the HICO-derived and simulated r_{rs} data, the optically active spectral coefficients within the BRUCE algorithm (a_{pw} , a_{dg}^* , a_{phy}^* , b_{pw} , b_{bp}^* , and ρ_i^*) were convolved with HICO’s relative SRFs.

The uncertainties of the derived geophysical parameters were estimated by the noise propagation technique developed by Hedley et al. (2010; 2012a) that takes into consideration both sensor and environmental noise. Note that this propagation technique does not take into account uncertainties caused by differing spectral shapes of IOPs as done in Wang et al. (2005). The uncertainty of each model parameter was determined in the following manner: (i) the spectral covariance matrix, C_{rrs} , of a homogeneous deep-water region was computed from the HICO-derived r_{rs} image of Shark Bay, 14 December 2011; (ii) the spectral noise term, δr_{rs} , was then computed as the dot product between an n -band amplitude vector and the Cholesky decomposition matrix, L_{rrs} , of C_{rrs} ; (iii) δr_{rs} was then added to the r_{rs} to generate a noise-perturbed spectrum, $r_{rs} + \delta r_{rs}$; (iv) steps (ii) and (iii) were repeated to generate a set of m noise-perturbed spectra that were inverted to obtain a set of m optimised model parameters (P , G , X , H , B_{sand} , etc.). The standard error and average from this set were taken as the uncertainty and retrieved value respectively. Note that: (a) the values of the n -band amplitude vector are normally distributed random numbers ($\mu = 0$, $\sigma = 1$) and represent the magnitude of the spectrally correlated noise; (b) the L_{rrs} matrix, which was kept constant throughout the procedure, contains information on the spectral variance of each band and how the spectral bands covary, and; (c) the number of m noise-perturbed spectra varied for the two datasets. For the HICO-derived r_{rs} image data m was set to 3000, whilst $m = 100$ for the simulated r_{rs} dataset. Recall that the HICO-derived r_{rs} dataset underwent atmospheric/sun-glint/air-water interface corrections that add

spectral artefacts to r_{rs} . These artefacts introduce more minima to the solution space, and thus m was set to 3000 to observe all the possible convergence points.

The SLM, UR-LM and LHS implementations of the BRUCE model were tested on four pixels from the HICO-derived r_{rs} image and the set of noise perturbed, simulated r_{rs} spectra. The four pixels selected from the HICO image – based on pseudo true colour imagery and previous benthic surveys (Walker et al., 1988) – have the following geometric depths and benthic substrates: Pixels A and B are shallow water pixels whose substrates are dominated by bright sediment and seagrass respectively; C is a quasi-deep water pixel with a sandy bottom, and; D is an optically deep water pixel. The r_{rs} of these four pixels underwent the uncertainty propagation technique described above using the three implementations of the BRUCE model.

The lower bounds of the derived IOPs, geometric depth and bottom albedos were set to slightly negative values for the constrained LM optimisation. This concept follows Werdell et al. (2013) who allowed the range of valid IOP retrievals to be slightly negative in order to account for noise in the inverted r_{rs} spectrum. Preliminary analysis showed that the bottom albedo coefficients typically produced uncertainties in excess of 40% and hence the need for more relaxed upper and lower bounds.

$$\begin{aligned}
 -0.10 a_w(490 \text{ nm}) < P < 2 \text{ m}^{-1} \\
 -0.10 a_w(490 \text{ nm}) < G < 2 \text{ m}^{-1} \\
 -0.10 b_{bw}(550 \text{ nm}) < X < 2 \text{ m}^{-1} \\
 -0.05 \text{ m} < H < 40 \text{ m} \\
 -0.40 \rho_i(550) < B_{\text{seagrass}}, B_{\text{sand}}, B_{\text{algae}} < 1.4 \rho_i(550)
 \end{aligned} \tag{4.6}$$

4.3.4 Optimising initial guess

An initial guess for each model parameter is required to initiate the LM optimisation. Preliminary investigations showed that the LM algorithm converges to different local minima when the optimisation is seeded with different initial guesses. The LHS and UR-LM methods (see flowchart in Figure 4.2) that search for the initial guess that guides the LM to the optimum, if not global, minimum are presented.

4.3.4.1 Latin hypercube sampling

Latin hypercube sampling (LHS) is an efficient sampling strategy used to sample the parameter space for an optimal, yet minimal set of initial guess parameters. LHS is an alternative method to simple random sampling, and where the selected

samples are guaranteed to cover the full range of variability in the data. The LHS routine has been described extensively by Helton and Davis (2003), Huntington and Lyrantzis (1998) with a step-by-step implementation given by Wyss and Jorgensen (1998). Here, the LHS was used to obtain seven sets of initial guesses,

$$LHS\ Guess = \left\{ \begin{matrix} P_1 & G_1 & X_1 & H_1 & B_{sd1} & B_{sg1} \\ P_2 & G_2 & X_2 & H_2 & B_{sd2} & B_{sg2} \\ \ddots & \ddots & \ddots & \ddots & \ddots & \ddots \\ P_7 & G_7 & X_7 & H_7 & B_{sd7} & B_{sg7} \end{matrix} \right\} \quad (4.7)$$

where each set was used to seed the inversion of the HICO-derived and simulated r_{rs} spectrum. The set that generated the lowest Euclidean distance was used to seed the inversions of the noise perturbed r_{rs} spectra. For a given spectral image or spectral dataset, obtaining the seven sets of initial guesses (equation 4.7) is only performed once at the start. These initial guesses are then reused throughout the processing to find the optimum initial guess.

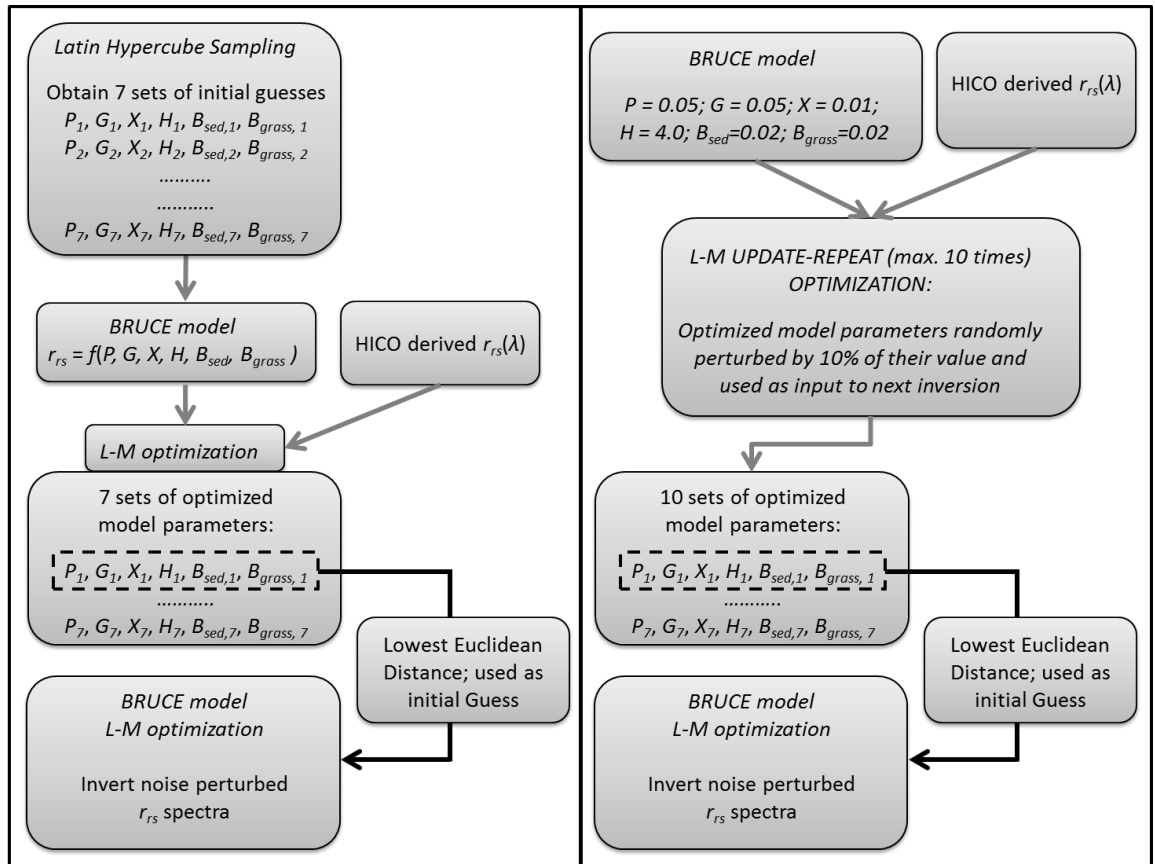


Figure 4.2: Flow chart of the Latin Hypercube Sampling (left panel) and Update-Repeat LM optimisation (right panel) techniques.

Although simple random sampling could have been used to sample the parameter space for initial guesses, it has the following drawbacks: (1) it can potentially exclude sub-ranges of model parameters that have low probability of occurring but have significant impacts on the model output, and; (2) would require a large number of samples to effectively sample all of the model parameters' sub-ranges (Helton & Davis, 2003). LHS overcomes this by specifying the sub-ranges (or subsets) of the model parameter from which one random sample is selected (Helton & Davis, 2003; Press et al., 2007, p. 410). The sub-ranges are selected based of equal probability of the parameters' probability distribution function (PDF). Here, each model parameter was assumed to have a normal PDF bounded by the imposed optimisation constraints. With exception, the depth parameter was assumed to have a normal PDF whose mean and standard deviation were 9.5 m and 2.5 m respectively. The LHS routine of the model parameters in BRUCE followed the program created by Sandia National Laboratories (Wyss & Jorgensen, 1998).

4.3.4.2 Update-Repeat LM optimisation (UR-LM)

In the update-repeat LM method, the model parameters that are derived from the optimisation process, which represent the solution at a local or global minimum, are randomly perturbed by a finite amount and used to seed a subsequent optimisation. This process is continued until either the LM algorithm converges to a minimum with a Euclidean distance of $\leq 1.0 \times 10^{-5}$ or a set number of perturbations have elapsed. This procedure is as follows: an initial inversion of the sensor-derived (or simulated) r_{rs} spectrum is performed with the standard set of LM initial guess values (equation 4.8). If within the first inversion the LM optimisation achieved a Euclidean distance $\leq 1.0 \times 10^{-5}$, then the optimised values of the model parameters are used to seed the inversions of the (same) set of noise-perturbed r_{rs} spectra. If, however, the Euclidean distance of the initial inversion was greater than 1.0×10^{-5} , then the optimised values of the model parameters are randomly perturbed by 10% of their value and used as the initial guess for a subsequent inversion of r_{rs} . This perturbation/inversion step is repeated until either the Euclidean distance falls below 1.0×10^{-5} or the number of repetitions occurs more than 10 times. In the latter case, the set of optimised values that generated the lowest Euclidean distance were used as the initial guess for the optimisation of the set of noise perturbed spectra. For ease of interpretation, a flowchart of both the LHS and UR-LM methods are presented in Figure 4.2.

4.4 Results and Discussion

4.4.1 Inverting measured hyperspectral data

Figure 4.3 (left panel) shows 3000 noise-perturbed r_{rs} spectra for each of the four pixels (A , B , C and D) selected from HICO imagery of Shark Bay, 14 December 2011. Each of these noise-perturbed spectra underwent inversion using the BRUCE algorithm with SLM optimisation to derive 3000 optimised values for each model parameter. In the standard algorithm as implemented by Klonowski et al. (2007), the initial guess values were arbitrarily set to

$$\begin{aligned} P &= 0.05; G = 0.05; X = 0.01; H = 4.0; \\ B_{\text{sediment}} &= 0.02; B_{\text{seagrass}} = 0.02 \end{aligned} \quad (4.8)$$

The results for this set of inversions, using these same seed values, are presented in Figure 4.4 which shows the five different retrieved model parameters P , G , X , B_{sand} and B_{seagrass} , as well as the Euclidean distance plotted against the retrieved depth, H , for the inversions of Pixel A (HICO image row 1082, column 317).

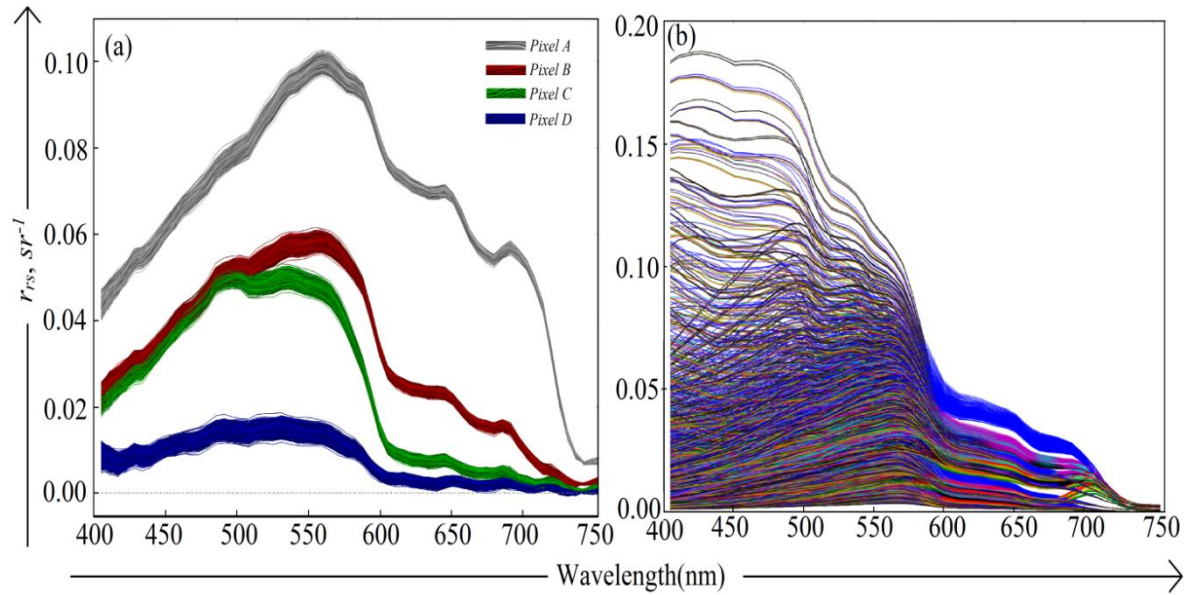


Figure 4.3: (a) Tafkaa-6S atmospherically corrected and deglinted, noise-perturbed r_{rs} of pixels A (row 1082, col 317), B (row 1083, col 212), C (row 1031, col 210) and D (row 1200, col 445). Note that 3000 noise-perturbed r_{rs} spectra were generated and shown for each of these four HICO pixels. (b) The ‘noise-free’ simulated HICO r_{rs} dataset.

The inversion results in Figure 4.4 show that two distinct solution groups exist at three very different retrieved depths. Group 1, highlighted red in Figure 4.4,

predominantly had Euclidean distances $< 1.0 \times 10^{-4}$ with retrieved depths between 0.59 – 0.62 m, and Group 2, had an average Euclidean distance of 3.0×10^{-3} with retrieved depths between 10 – 13 m. Note, a small set of outliers were also retrieved existing at depths greater than 25 m (see Figure 4.4). Groups 1 and 2 represent very different retrieved IOPs, depth, B_{sediment} and B_{seagrass} . Table 4.2 provides an overview of the mean values and uncertainties of each parameter based on the results of the inversions displayed in Figures 4.4, 4.5 and 4.6. The points displayed in Figure 4.4 are presented in the column labelled “SLM BRUCE” in Table 4.2 for each of the four test pixels selected from the HICO image. Here SLM stands for the Standard Levenberg-Marquardt implementation of BRUCE. The results of the SLM for HICO pixel *A* collectively produced high uncertainties including retrieved parameter averages that were larger relative to the UR-LM and LHS approaches (see Table 4.2).

Arguably one might consider that a given r_{rs} spectrum should have a unique point in retrieved parameter space that generates the lowest possible Euclidean distance. Thus for situations where non-uniqueness is not an issue, one would assume that adding spectral noise to the r_{rs} spectrum would simply create dispersal about this unique point in parameter space rather than dispersals about two or more different minima. Note that in parameter space, the non-uniqueness of the r_{rs} spectrum would represent a situation where two or more local minima exist that have very similar Euclidean distances but very different solutions. For HICO pixel *A* (Figure 4.4), each solution cluster has a substantially different Euclidean distance. Thus non-uniqueness was not deemed the cause, but rather the convergence onto two substantially different minima.

Without ground truth data it is unknown which of the two minima in Figure 4.4 is representative of the true environmental parameters. However, pragmatically we can assume the minimum with the most realistic solution being the one with the best model fit (i.e. lowest Euclidean distance). In the case of HICO pixel *A* (Figure 4.4) this would be Group 1 where the model parameters range between $0.0 < P < 0.05 \text{ m}^{-1}$, $0.17 < G < 0.26 \text{ m}^{-1}$, $0.03 < X < 0.08 \text{ m}^{-1}$, $0.59 < H < 0.62 \text{ m}$, $0.28 < B_{\text{sediment}} < 0.31$, and $0.05 < B_{\text{seagrass}} < 0.07$. The depth taken from the nautical chart of Shark Bay, Western Australia, at the approximate area of HICO pixel *A* ranged between 0.3 to 0.4 m (above lowest astronomical tide, LAT). We note that the retrieved depth of 0.6 m was the depth at the time of the HICO overpass, and was not corrected for tide to a chart datum such as LAT. Thus taken into consideration, the tide and possible depth offsets caused by

atmospheric correction, a retrieved depth of 0.6 m is quite possible.

A method that guides the LM optimisation is clearly needed to avoid multiple solution minima so that a true representation of the mean and standard deviation for each retrieved model parameter can be obtained. Although it is possible to perform a post-processing density based cluster analysis to isolate the solution group with the lowest Euclidean distance, it is more ideal (with regards to processing time) to have a robust method that only converges to one minimum. Figures 4.5 and 4.6 present the results of the inversions of HICO pixel *A* using the UR-LM and LHS implementation of the BRUCE model respectively. In these two methods the inversions show only one group of solutions indicative of the convergence to a single minimum. Moreover, this minimum is the same as Group 1 of Figure 4.4, and demonstrates that the UR-LM and LHS methods both guided the LM optimisation to the optimal solution (based on lowest Euclidean distance). Indeed the inversions using these methods were considerably more precise; for example, the retrieved depth from the SLM was 5.97 ± 5.16 metres ($5.97 \text{ m} \pm 87\%$ - see Table 4.2) whilst through the UR-LM method the retrieved depth changed to 5.18 ± 0.16 metres for HICO pixel *C* (see Table 4.2). Additionally, the IOP retrievals for pixel *A* appear to have been improved with the UR-LM and LHS methods relative to the SLM approach. Recall that pixel *A* is characterised as very shallow with a bright sand substrate, thus the majority of the magnitude of the r_{rs} arises from bottom reflectance. Retrievals of the absorption and backscattering coefficients and the depth, using the SLM for HICO pixel *A* were considerably larger compared to values retrieved using the UR-LM and LHS methods. This implies that the SLM preferentially translates the magnitude of the r_{rs} signal to a higher signal from the water column (i.e. higher backscattering coefficient), and therefore decreases the bottom reflectance signal by both increasing the depth and absorption coefficients. In contrast, the UR-LM and LHS methods avoided the over-contribution of the water column reflectance, allowing both methods to retrieve a shallower, more realistic depth.

Appendix A shows the inversion results of the other HICO pixels (*B*, *C*, and *D*). The basis behind the UR-LM and LHS methods is the selection of an optimised initial set of LM guess parameters that correspond to the lowest minimum found during the initial parameter search. Using this optimised guess to seed the inversion of the noise perturbed r_{rs} spectra generally increases the computational efficiency of the inversions. Here, computational efficiency is defined as the total number of iterations

(T_i) that the LM algorithm performed. This enhanced efficiency is presented in Table 4.2, which compares the retrieved model parameters, average Euclidean distance and number of iterations between the SLM, UR-LM and LHS BRUCE implementations. For the SLM, T_i accounts for the number of iterations incurred during 3000 spectral inversions, whilst for the UR-LM and LHS, T_i also includes the number of iterations incurred during the search for the optimised initial guess. The results shown in Table 4.2 indicate that the UR-LM and LHS methods are comparable and at least twice more computationally efficient than the SLM.

Although the UR-LM and LHS methods can yield improved optimisations for optically shallow to quasi-deep pixels, it does not improve the inversion of optically deep-water pixels (see Table 4.2, HICO pixel D). This, however, is due to the BRUCE model attempting to retrieve depth and bottom albedo coefficients from an r_{rs} spectrum that has negligible bottom contribution. It is therefore important to have a method of determining whether a pixels' r_{rs} spectrum relates to deep-water or not (e.g. Brando et al., 2009) and to be able switch between ocean colour models such as the Generalized IOP algorithm (Werdell et al., 2013) and a shallow water model such as BRUCE.

Table 4.2: A comparison between the mean and relative standard deviations of the retrieved model parameters, average Euclidean distance and total number of iterations obtained from the SLM, UR-LM and LHS implementation of the BRUCE model. Presented are the retrieved model parameters from the four pixels in the HICO image of Shark Bay, 14th December 2011.

Pixel type	SLM BRUCE	UR-LM BRUCE	LHS BRUCE
Shallow, sediment substrate (A)			
$P (m^{-1})$	0.223 ± 134.29%	0.012 ± 77.15%	0.012 ± 77.96%
$G (m^{-1})$	0.288 ± 37.25%	0.212 ± 5.36%	0.213 ± 5.46%
$X (m^{-1})$	0.203 ± 99.74%	0.060 ± 11.75%	0.061 ± 11.66%
$H (m)$	4.37 ± 127.81%	0.60 ± 0.83%	0.60 ± 0.86%
$B_{sediment}$	0.176 ± 94.5%	0.294 ± 1.11%	0.294 ± 1.08%
$B_{seagrass}$	0.071 ± 18.56%	0.061 ± 4.27%	0.061 ± 4.28%
Average Euclidean Dist.	1.11×10^{-3}	9.05×10^{-5}	9.04×10^{-5}
Total Number LM iterations	100,278	31,529	31,596
Shallow, seagrass substrate (B)			
$P (m^{-1})$	0.020 ± 75.27%	0.025 ± 40.35%	0.026 ± 39.4%
$G (m^{-1})$	0.254 ± 17.97%	0.269 ± 5.62%	0.269 ± 6.04%
$X (m^{-1})$	0.080 ± 17.0%	0.084 ± 6.13%	0.084 ± 6.25%
$H (m)$	1.81 ± 30.89%	2.06 ± 4.6%	2.06 ± 4.55%
$B_{sediment}$	0.152 ± 15.69%	0.159 ± 12.64%	0.159 ± 13.64%
$B_{seagrass}$	0.001 ± 1882.15%	-0.003 ± 396.64%	-0.003 ± 405.57%
Average Euclidean Dist.	1.0×10^{-3}	5.83×10^{-5}	5.81×10^{-5}
Total Number LM iterations	63,764	33,990	33,735
Quasi deep, sediment substrate (C)			
$P (m^{-1})$	0.015 ± 37.66%	0.015 ± 33.94%	0.015 ± 34.0%
$G (m^{-1})$	0.106 ± 9.45%	0.105 ± 5.58%	0.105 ± 5.65%
$X (m^{-1})$	0.027 ± 12.85%	0.027 ± 8.96%	0.027 ± 8.73%
$H (m)$	5.97 ± 86.42%	5.18 ± 3.08%	5.18 ± 3.13%
$B_{sediment}$	0.361 ± 10.61%	0.361 ± 9.69%	0.361 ± 9.82%
$B_{seagrass}$	0.003 ± 792.87%	0.002 ± 1221.57%	0.002 ± 1148.18%
Average Euclidean Dist.	5.74×10^{-5}	4.44×10^{-5}	4.43×10^{-5}
Total Number LM iterations	76,675	35,623	35,657
Optically deep (D)			
$P (m^{-1})$	0.026 ± 72.51%	0.027 ± 70.78%	0.026 ± 70.32%
$G (m^{-1})$	0.138 ± 15.1%	0.137 ± 15.42%	0.138 ± 15.3%
$X (m^{-1})$	0.012 ± 15.97%	0.012 ± 15.69%	0.012 ± 15.75%
$H (m)$	11.90 ± 50.69%	11.61 ± 44.89%	11.50 ± 45.08%
$B_{sediment}$	0.054 ± 220.44%	0.056 ± 208.12%	0.055 ± 207.31%
$B_{seagrass}$	0.021 ± 210.29%	0.020 ± 212.46%	0.021 ± 210.91%
Average Euclidean Dist.	2.11×10^{-5}	2.06×10^{-5}	2.06×10^{-5}
Total Number LM iterations	66,383	57,425	57,196

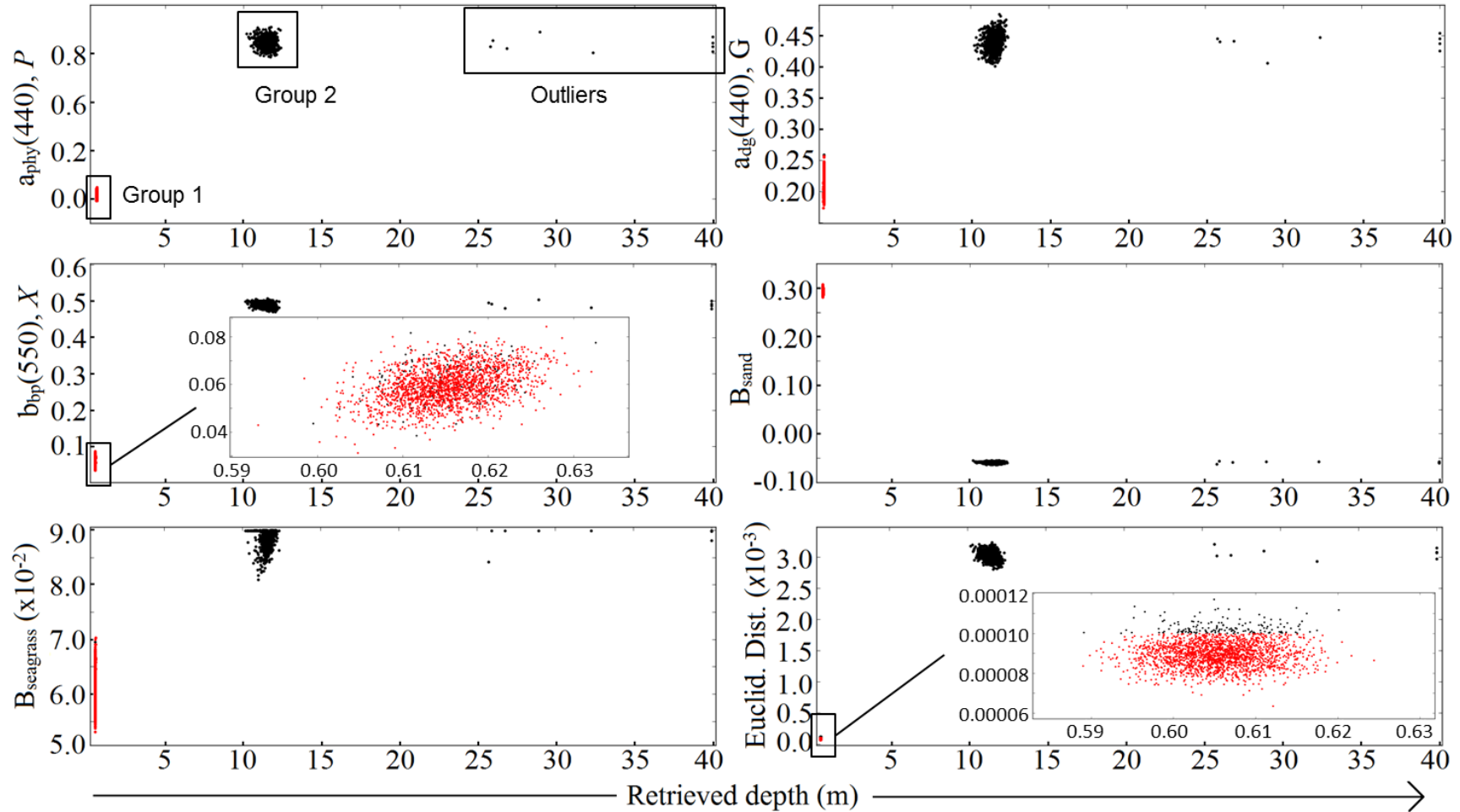


Figure 4.4: Retrieved BRUCE model parameters vs. retrieved depth for the 3000 noise perturbed r_{rs} spectra of HICO pixel A (row 1082, col 317) using SLM optimisation. The seed guess parameters were arbitrarily set. The red dot points are those retrievals whose inversion obtained a Euclidean distance $< 1.0 \times 10^{-4}$.

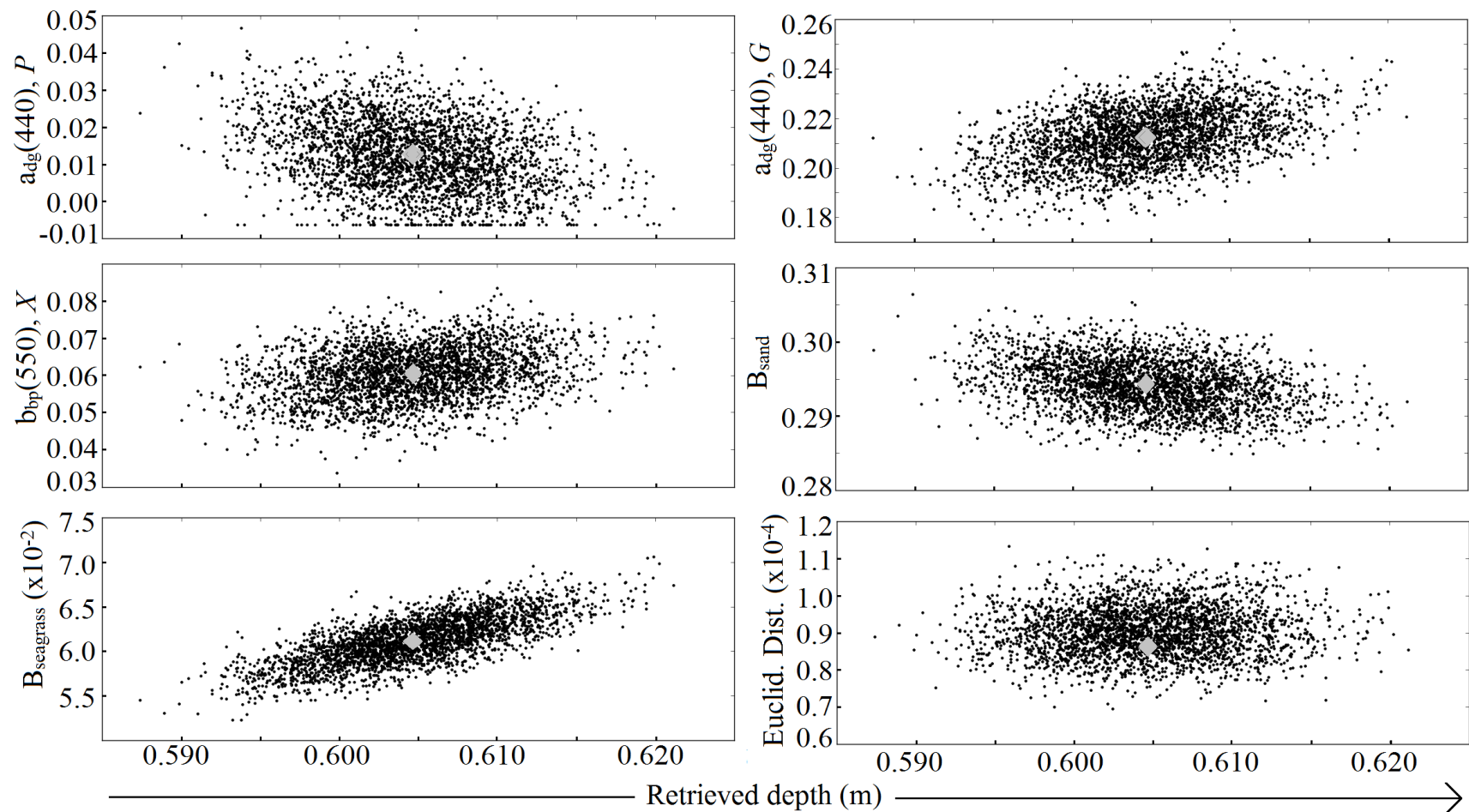


Figure 4.5: Retrieved BRUCE model parameters vs. retrieved depth for the 3000 noise perturbed r_{rs} spectra of the HICO pixel A (row 1082, col 317). The optimised guess values used to seed the LM optimisation were dynamically chosen using the UR-LM method shown as grey diamonds.

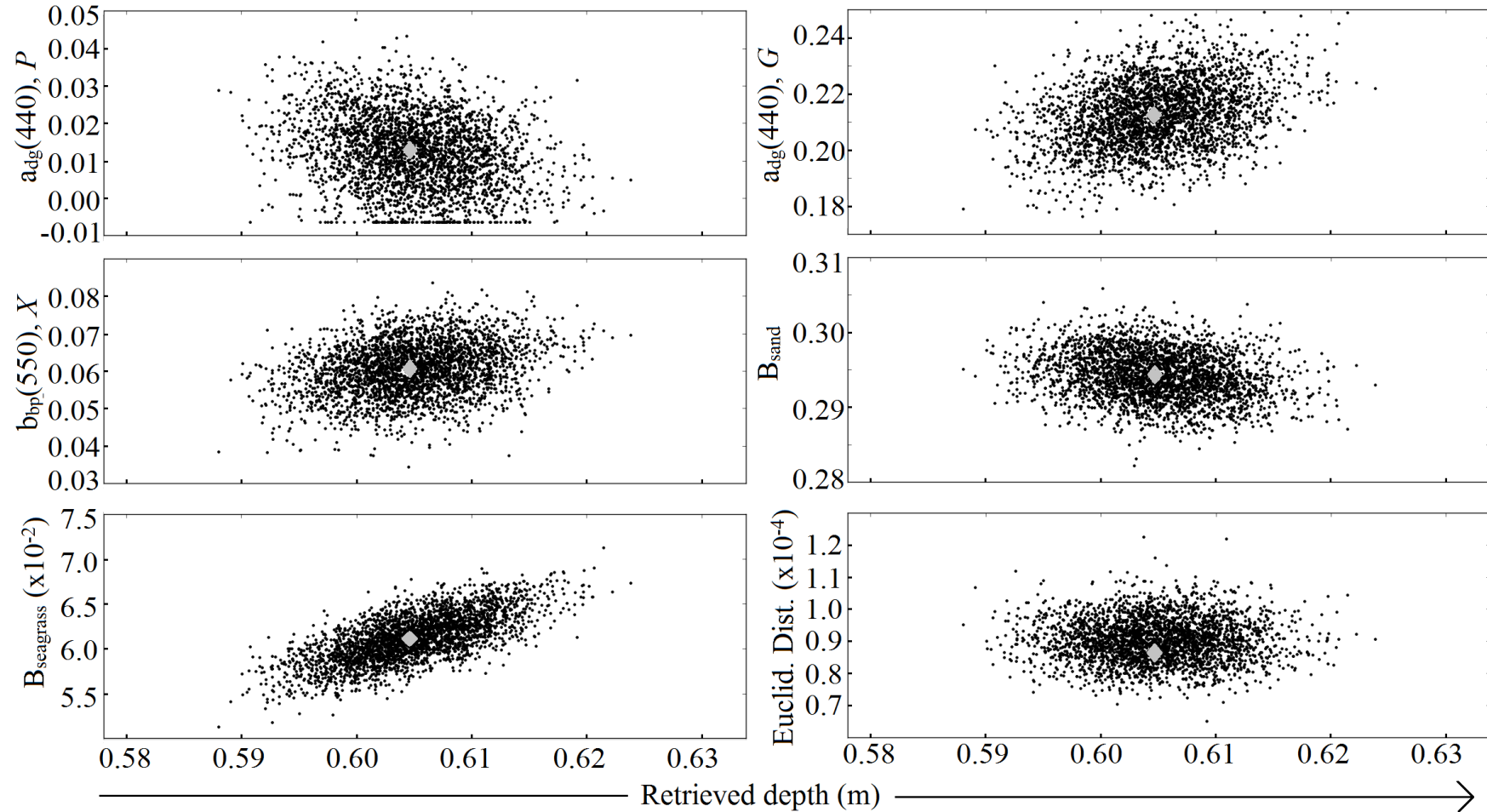


Figure 4.6: Retrieved BRUCE model parameters vs. retrieved depth for the 3000 noise perturbed r_{rs} spectra of the HICO pixel A (row 1082, col 317). The optimised guess values were dynamically chosen using the LHS method, shown as grey diamonds.

4.4.2 Inverting simulated hyperspectral data

An assessment of the sensitivity to noise and accuracy of the retrieved geophysical parameters from the three optimisation approaches was carried out by inverting noise-perturbed, simulated r_{rs} spectra. Specifically, the BRUCE model was implemented in a forward sense where a range of values for the model inputs (see Table 4.1) was used to obtain 4375 modelled r_{rs} . For each of these modelled spectra, the uncertainty propagation technique produced 100 noise-perturbed r_{rs} spectra (i.e. a total of 437,500 spectra) that were inverted to retrieve the uncertainty and average value of the model parameters. Note that we have chosen to use forward modelling rather than relying on Radiative transfer numerical models such as Hydrolight (Mobley & Sundman, 2000) or PlanarRad (Hedley, 2008) to exclude sources of uncertainty from the BRUCE model parameterisation. Such uncertainties arise from assumptions made regarding the bottom albedo, chlorophyll model, phase functions and sun-sensor viewing geometries. Thus in this context forward modelling is an ideal situation, because prior to the addition of spectrally correlated noise the optimisation procedures would be expected to produce 100% accuracy between the retrieved and input model parameters.

Figures 4.7 to 4.9 compare the retrieved versus input BRUCE model parameters using the SLM, UR-LM and LHS optimisation methods. Table 4.2 presents the accuracy, average uncertainty, average retrieved value and root mean square error (RMSE) between the retrieved and input model parameter for these three methods. The accuracy of the three methods was assessed based on the proportion of retrievals that were within 1% of the input model parameter. Thus, the ideal scenario of 100% accuracy implies that all the retrievals were within 1% of the input model parameter. Here the average retrieved value (henceforth referred to as centroid) was used to assess how close the retrievals are to the input model value, whilst the RMSE was used as a measure of the scatter the retrievals have about the “true” value

$$RMSE = \left[\frac{\sum_{i=1}^M (\hat{x}_{i,j} - x_j)^2}{M - 1} \right]^{1/2} \quad (4.9)$$

where $\hat{x}_{i,j}$ is the i^{th} retrieval of the j^{th} BRUCE model parameter (P , G , X etc.), x_j is the true value of the j^{th} model parameter, and M being the number of retrievals. The normalised RMSE (equation 4.9 divided by the average retrieved value of the scatter) was not used as this tends to very large values as the average retrieved value

approaches zero. Here, the optimisation method that generated the lowest RMSE, relative uncertainty and highest accuracy was considered the most optimal. Note that the accuracies presented in Table 4.3 will be lower when inverting sensor-derived subsurface remote sensing reflectance due to uncertainty in the model parameterisation, and potentially erroneous radiometric corrections arising from atmospheric fluctuations and sea surface state (sun-glint and air-water interface).

Table 4.3: An inter-comparison of the RMSE (scatter), percent accuracy, average relative uncertainty and average retrieved value for each BRUCE model parameter between the three optimisation approaches. Recall that 100% accuracy is ideal as all the retrievals would be with 1% of the input model parameter.

Actual values	Average retrieved value (centroid)			Average uncertainty			RMSE			Accuracy (%)		
	SLM	URLM	LHS	SLM	URLM	LHS	SLM	URLM	LHS	SLM	URLM	LHS
<i>P</i> (m ⁻¹)												
0.01	0.058	0.021	0.019	0.085	0.033	0.030	0.117	0.047	0.023	1.37	4.11	4.69
0.03	0.067	0.034	0.034	0.097	0.038	0.036	0.115	0.037	0.021	1.83	7.77	9.26
0.05	0.078	0.052	0.051	0.107	0.041	0.041	0.108	0.074	0.020	2.06	10.74	13.14
0.07	0.087	0.071	0.067	0.113	0.048	0.045	0.103	0.081	0.018	3.09	13.71	16.11
0.1	0.105	0.097	0.094	0.126	0.055	0.053	0.101	0.049	0.018	4.80	19.77	20.23
<i>G</i> (m ⁻¹)												
0.01	0.120	0.054	0.008	0.078	0.031	0.007	0.250	0.172	0.004	1.37	7.66	10.63
0.1	0.450	0.138	0.082	0.177	0.027	0.021	0.517	0.153	0.004	2.74	29.37	36.57
0.25	0.669	0.218	0.215	0.362	0.046	0.045	0.544	0.059	0.010	4.57	40.00	40.00
0.35	0.670	0.311	0.312	0.385	0.063	0.064	0.402	0.020	0.020	2.86	37.14	37.26
0.5	0.643	0.475	0.475	0.328	0.093	0.093	0.231	0.040	0.040	5.60	29.71	29.71
<i>X</i> (m ⁻¹)												
0.006	0.096	0.026	0.006	0.077	0.009	0.004	0.136	0.067	0.001	0.00	2.86	5.83
0.01	0.108	0.030	0.010	0.074	0.009	0.004	0.144	0.070	0.001	0.23	4.34	7.77
0.03	0.154	0.059	0.025	0.088	0.014	0.004	0.177	0.111	0.001	0.80	17.14	24.46
0.07	0.163	0.050	0.050	0.084	0.004	0.004	0.121	0.001	0.001	4.23	46.51	46.51
0.1	0.180	0.082	0.082	0.068	0.004	0.004	0.124	0.001	0.001	7.20	69.94	70.06
<i>H</i> (m)												
1	0.98	0.98	1.00	0.18	0.05	0.04	0.15	0.10	0.01	47.89	85.03	88.69
3	1.59	2.88	3.00	0.98	0.30	0.30	1.62	0.54	0.07	1.71	48.80	51.31
6	2.44	4.58	5.30	2.01	1.37	1.42	3.83	2.00	0.50	0.00	6.63	11.89
11	3.60	4.83	6.21	3.89	4.27	4.69	7.82	5.02	3.22	0.23	0.34	2.29
20	3.75	4.99	6.46	4.35	5.28	6.25	16.55	11.75	9.76	0.00	0.46	0.80
<i>B_{sand}</i>												
0	-0.011	0.017	0.023	0.060	0.056	0.061	0.043	0.054	0.052	0.00	0.00	0.00
0.0757	0.009	0.055	0.067	0.069	0.060	0.065	0.087	0.053	0.034	2.08	12.00	13.44
0.1135	0.018	0.072	0.089	0.073	0.061	0.065	0.116	0.065	0.036	4.48	14.88	17.44
0.227	0.056	0.134	0.156	0.089	0.061	0.065	0.199	0.112	0.072	11.36	24.00	25.12

<i>B_{posidonia}</i>												
0	0.014	0.010	0.009	0.020	0.020	0.022	0.022	0.019	0.018	0.00	0.00	0.00
0.0177	0.020	0.018	0.018	0.020	0.021	0.023	0.014	0.011	0.010	3.04	7.84	7.84
0.0265	0.023	0.022	0.023	0.020	0.021	0.023	0.014	0.009	0.009	5.60	9.52	9.92
0.053	0.031	0.034	0.036	0.020	0.021	0.023	0.029	0.019	0.017	8.00	12.48	12.80
<i>B_{sargassum}</i>												
0	-0.003	0.003	0.004	0.013	0.014	0.015	0.007	0.008	0.007	0.00	0.00	0.00
0.011	0.000	0.008	0.009	0.013	0.015	0.016	0.013	0.007	0.005	4.00	4.64	4.96
0.0165	0.002	0.010	0.012	0.014	0.015	0.016	0.017	0.009	0.007	4.96	6.40	6.96
0.033	0.007	0.017	0.019	0.015	0.015	0.016	0.029	0.017	0.016	6.56	10.88	12.32
				Number of L-M iterations								
				SLM								
				42,380,282								
				UR-LM								
				13,150,908								
				LHS								
				11,132,485								

Figures 4.7 to 4.9 show that in the presence of spectral noise the SLM leads to retrievals that have much greater scatter and variation about the actual (or true) parameter value. This is seen for example, in the retrievals of the phytoplankton absorption coefficient, P (Figure 4.7), where there appears to be little or no correlation between the retrieved and actual values for the SLM. In contrast the results for the UR-LM and LHS show a much improved agreement between input and retrieved values for P . Indeed, the scatter (RMSE) for the majority of the model parameters were consistently greater than the input value for the SLM method. The LHS method has considerably lower RMSE than the SLM method; in fact the LHS method reduced the scatter on average by factors of 5, 56, 194 and 11 for parameters P , G , X and H respectively, when compared to the SLM. The UR-LM method on the other hand has only reduced the scatter, on average by factors of 2, 8, 78 and 1.9 for P , G , X and H respectively when compared to the SLM. In addition to the reduced RMSE, the UR-LM and LHS methods have centroids for the IOPs and depth closer to the actual value than the SLM (see Table 4.3).

Figure 4.10 displays density plots of the bias in the down-welling diffuse attenuation coefficient at 490 nm, $K_d(490)$ plotted against bias in depth; and the bias in B_{sand} , B_{seagrass} and B_{algae} versus depth bias, for the SLM and LHS optimisation approaches. The bias was defined as the retrieved minus actual parameter value, thus negative bias represents under-estimation and vice-versa for a positive bias. Here, $K_d(490)$ was computed by

$$K_d(490) = \frac{a(490) + b_b(490)}{\cos(\theta_w)} \quad (4.10)$$

where $a(490)$ and $b_b(490)$ are the absorption and backscattering coefficients of the water column at 490 nm. The retrieved and true values of P , G and X were used as inputs to equations (4.3) and (4.4) to compute $a(490)$ and $b_b(490)$ respectively. Also, θ_w was set to the sub-surface solar zenith angle at the time of the HICO overpass on 14 December 2011. The bias in $K_d(490)$ was thus computed by $K_{d, \text{retrieved}}(490) - K_{d, \text{actual}}(490)$. The results in Figure 4.10 show that the SLM procedure, for the majority of the inversions, simultaneously over-estimated $K_d(490)$ and under-estimated depth and the bottom albedo coefficients. This implies that the BRUCE model, when initiating the SLM optimisation with a fixed initial guess, preferentially under-estimates the depth by compensating for a more turbid water column and darker substrate. This is an example of the LM algorithms' inability to move beyond local minima. In the SLM

approach the initial guess for depth was 4 m (see equation 4.8), thus as the LM algorithm increased or decreased the depth parameter in the direction of lowest Euclidean distance, it encountered and converged to a local minimum rather than continuing the optimisation process towards the global minimum.

When comparing the bias in $K_d(490)$ with the bias in depth (Figure 4.10a), the LHS method produced depth retrievals more centred on a bias of zero than the SLM approach. Indeed, the SLM had biases in depth up to -20 m where the $K_d(490)$ bias predominantly ranged between 0 and 1.5 m^{-1} . The LHS method in contrast, had $K_d(490)$ bias ranging between -0.05 and 0.10 m^{-1} , and a bias in depth that ranged between -15 and 10 m. It should be noted that these large biases in depth of the LHS method had: (i) a substantially lower frequency of occurrence (see the colour bar in Figure 4.10) compared to the SLM method; and (ii) were obtained for the inversions of simulated r_{rs} whose input depths were greater than 10 metres – as illustrated by the large scatter about these retrieved depths in Figure 4.8. This latter result emphasises the optical depth limit of shallow-water inversion models.

In the LHS method, the depth was still preferentially under-estimated though not the extent of the SLM. This is also observed by centroids of the depth retrievals (Table 4.3), which plateau to around 3 to 4 m for input depths greater than 6 m using the SLM method, whereas the centroids reach 6.48 m using the LHS method. Importantly, the LHS method has improved the bias of $K_d(490)$, which in turn relates to improved accuracies of the retrieved IOPs over a range of depths – particularly over shallow water where the bottom reflectance can contribute more to the net water-leaving signal than water column optics.

The UR-LM and LHS methods have significantly increased the accuracy of the depth retrievals and indeed the other retrieved parameters. In the SLM approach, the accuracies of retrieved depths greater than or equal to 3 metres are less than 2%. This has increased to accuracies of 51.3%, 11.9%, 2.3% and 0.80% for retrieved depths of 3, 6, 11 and 20 m respectively using the LHS method. The rapid decline in accuracy and increased scatter about the true value with depth is associated with the exponential nature of light attenuation. At depths greater than 10 m, the bottom contribution to the r_{rs} signal is typically very small, resulting in minor differences between an r_{rs} spectrum at, say 15 metres to that at 20 m for the same set of optical conditions. Hence the BRUCE model can converge to a large range of depths (e.g. 15 – 25 m) without significantly affecting the model fit. Despite these increases in accuracies, the

accuracies of the retrieved depths, IOPs and benthic albedo coefficients are typically less than 50% using the UR-LM and LHS methods, which illustrate the sensitivity of these model parameters to the addition of spectral noise.

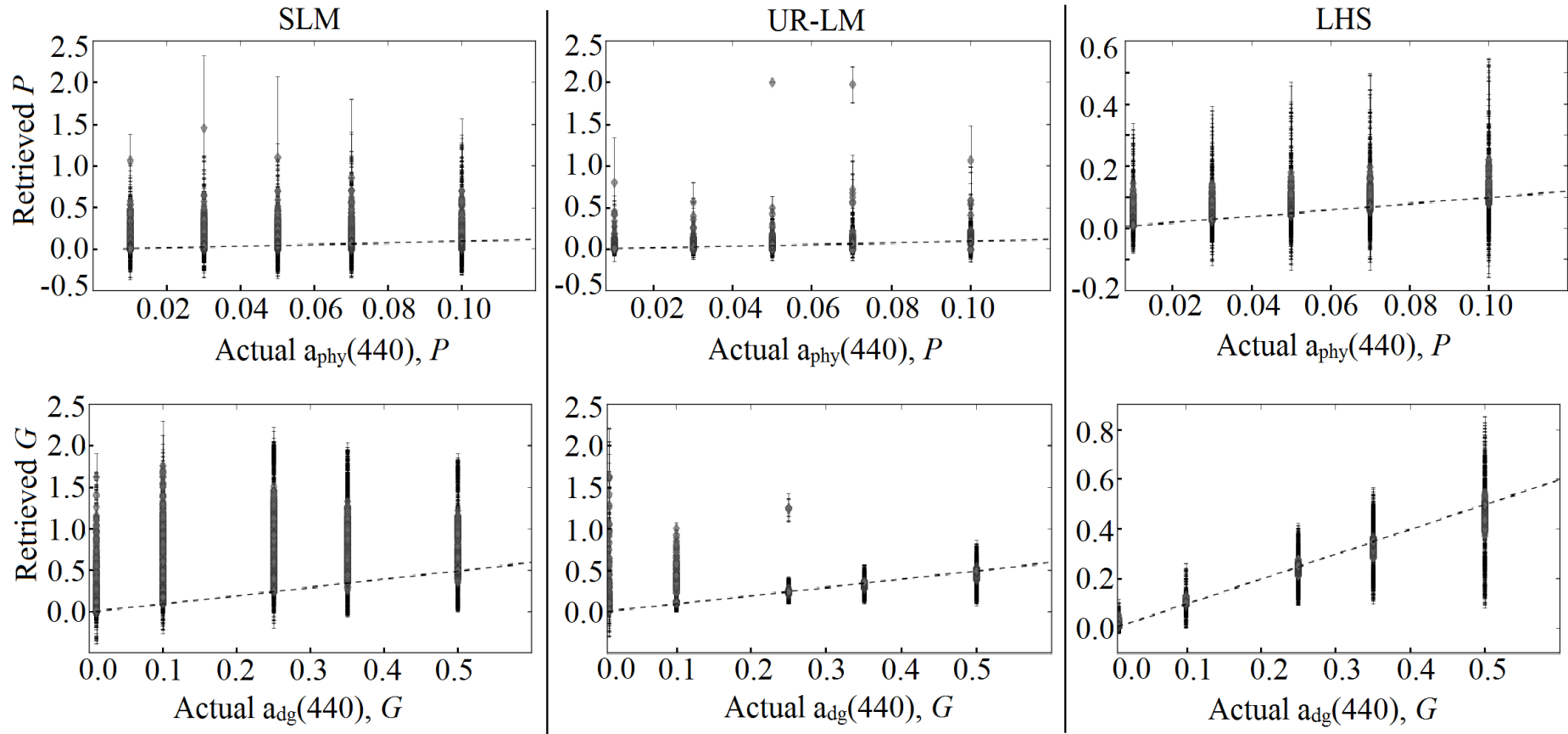


Figure 4.7: Inter-comparison between the SLM (left-hand panels), UR-LM (central panels) and LHS (right-hand panels) optimisation of the noise-added simulated r_{rs} spectra using the BRUCE model. These graphs show the retrieved vs. actual model parameters for P , and G . Note: (1) the uncertainty in each retrieval (grey diamonds) are represented as error bars; (2) the dashed line in each graph represents the ideal 1:1 ratio between retrieved and actual.

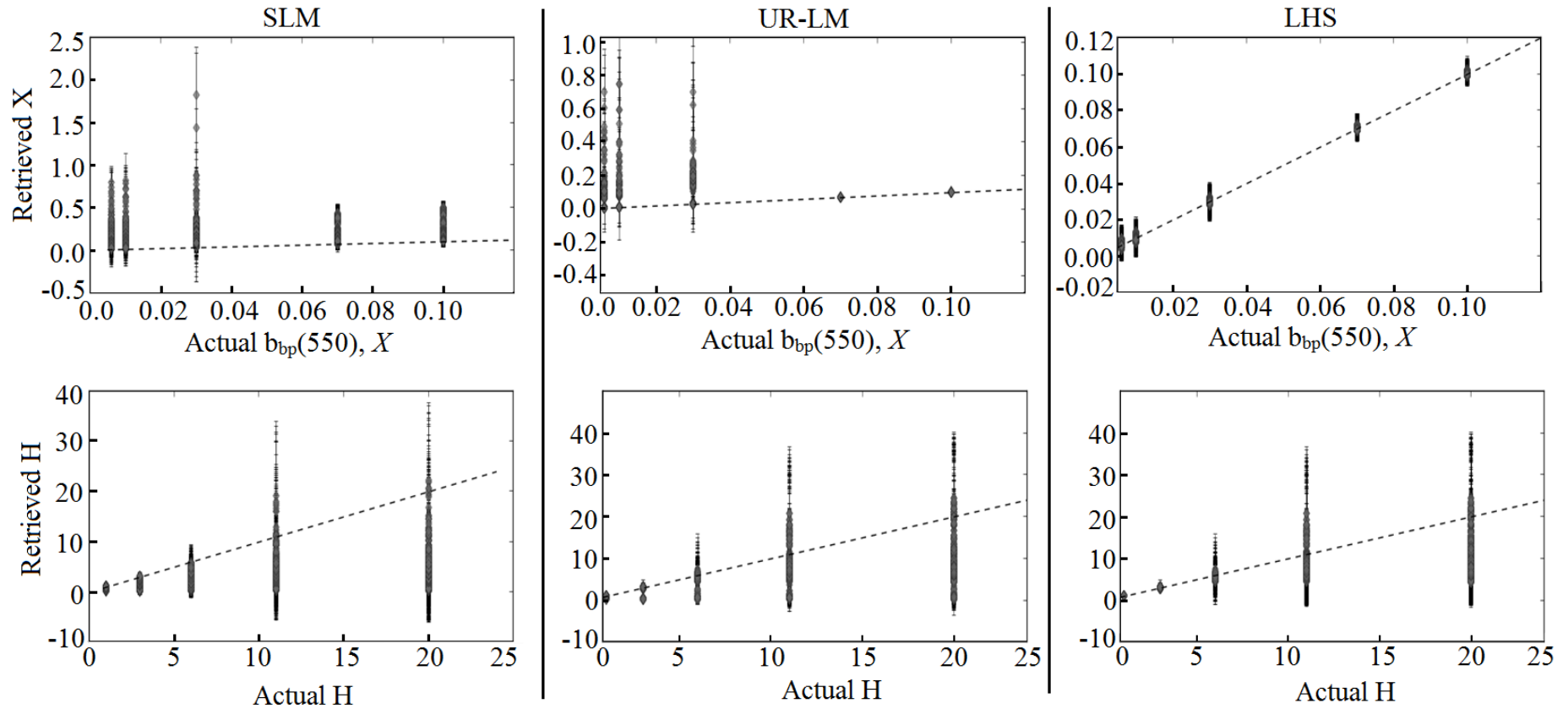


Figure 4.8: Inter-comparison between the SLM, UR-LM and LHS optimisation of the noise-added simulated r_{rs} spectra using the BRUCE model. These graphs show the retrieved vs. actual model parameters for X , and H .

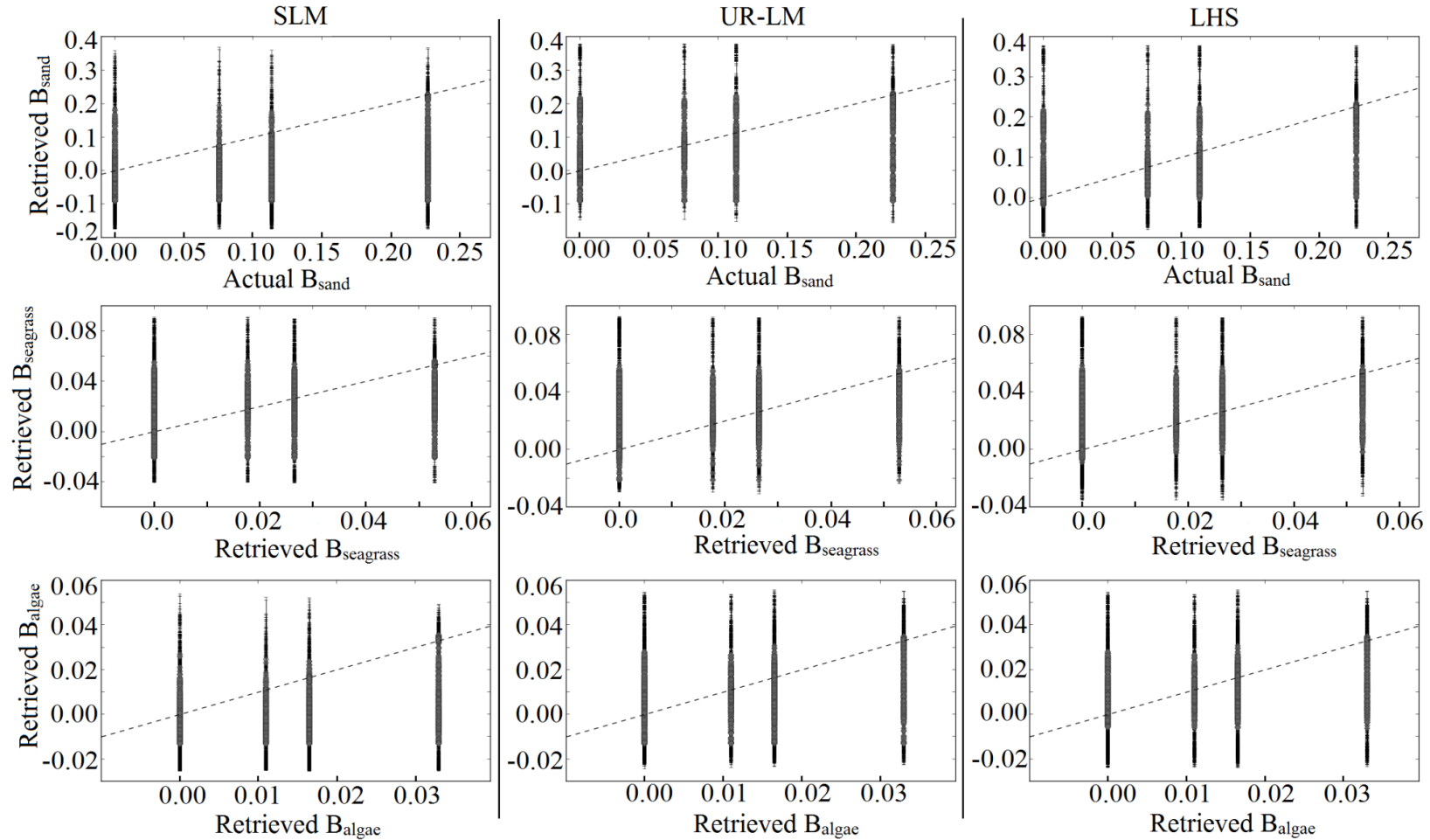


Figure 4.9: Inter-comparison between the SLM, UR-LM and LHS optimisation of the noise-added, simulated r_{rs} spectra using the BRUCE model. These graphs show the retrieved vs. actual model parameters for B_{sand} (top), B_{seagrass} (middle), and B_{algae} (bottom).

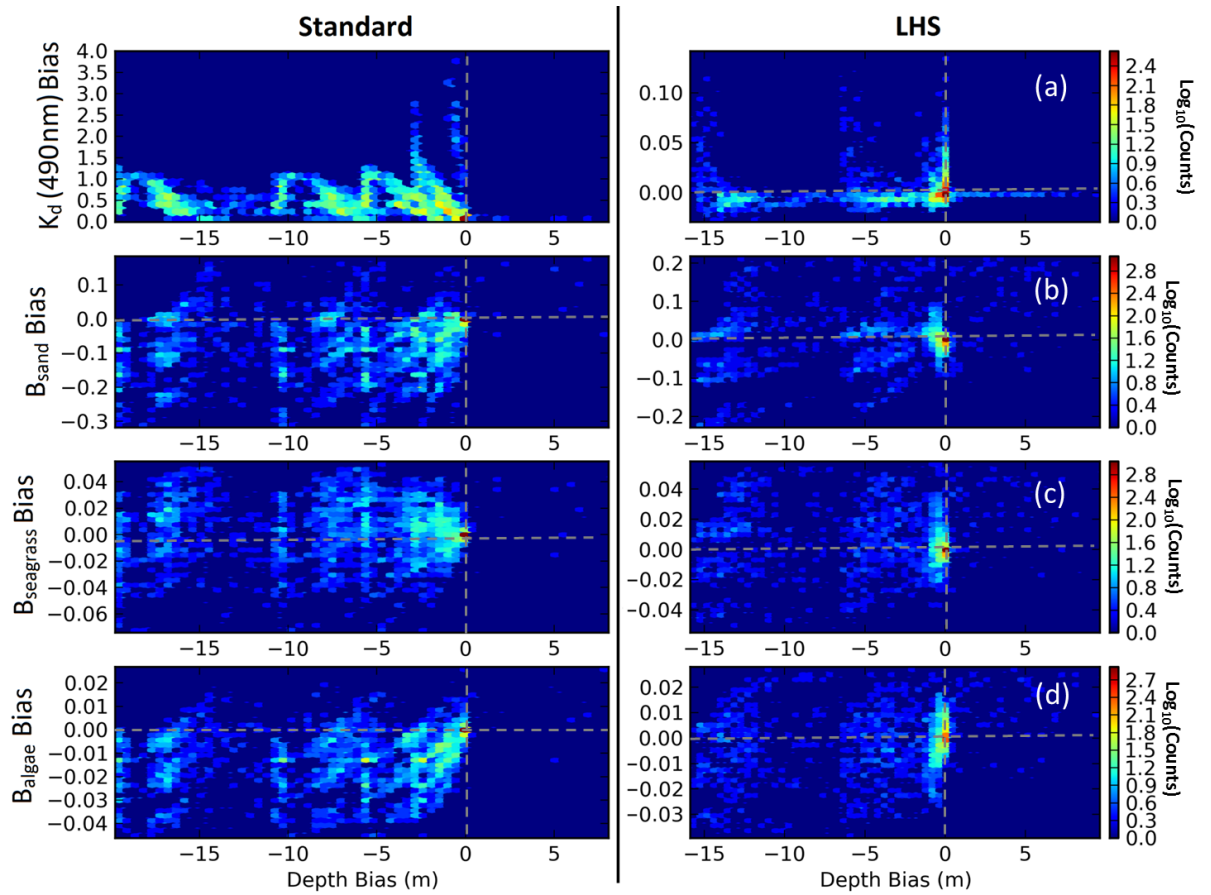


Figure 4.10: Density plots of (a) $K_d(490\text{ nm})$ bias vs. depth bias; (b) B_{sand} bias vs. depth bias; (c) B_{seagrass} vs. depth bias, and; (d) B_{algae} bias vs. depth bias. Each pixel in the density plot has a frequency of occurrence, represented by its colour. The left- and right-hand panels show the bias obtained using the SLM and LHS optimisation methods respectively.

Retrievals of the bottom albedo parameters (B_{sand} , $B_{\text{posidonia}}$, $B_{\text{sargassum}}$) were only marginally improved with the UR-LM and LHS methods. These parameters suffer from very low accuracy ($< 26\%$) and precision ($> 40\%$ relative uncertainty). For these three methods, the highest accuracies were obtained for bright bottom substrates; where 100%, 50% and 33% benthic sediment mixtures obtained accuracies of 25%, 17% and 13%, respectively. These accuracies decreased as the substrate became darker, for instance the accuracy for $B_{\text{sargassum}}$ was on average 2% less than that of $B_{\text{posidonia}}$. These low accuracies are likely due to the over-parameterisation of the BRUCE model where non-zero albedo coefficients are always retrieved even if only one benthic type was modelled (despite having set negative lower bounds ($-0.4\rho_i$, see equation 4.6) in the LM optimisation). Such accuracies have significant implications to benthic classification when total system noise is incorporated in the analysis. Further work is therefore necessary to improve the accuracies of these bottom albedo coefficients.

We found that changing the lower bounds of the BRUCE model parameters can affect the accuracy, RMSE and uncertainty of the retrievals dramatically. So much so that when the lower bounds of the IOPs, depth and bottom albedo coefficients were set to zero, the inversion results using the SLM become similar to the UR-LM and LHS methods (see Appendix B). However, the UR-LM and LHS methods are still more computationally efficient with at least 3.9 times fewer LM iterations than the standard approach. Despite the changes in the quality of the retrievals using the SLM and somewhat the UR-LM method, the LHS technique produced consistent retrievals to that shown in Figures 4.7 to 4.9 and Table 4.3; and so illustrate the robustness and efficiency of this improved optimisation method. Setting the lower bounds to zero should be used with caution as it can underestimate the uncertainty and inflate the average retrieved value, particularly when the value of the model parameter is near zero (see Appendix B). As such, for operational satellite remote sensing we advise that the lower bounds of the LM algorithm to be set as slightly negative values.

4.5 Conclusion

Obtaining a true representation of the uncertainty is crucial for accurate interpretation of ocean colour data. The addition of spectral noise to the derived r_{rs} adds more local minima to the solution space that compromises the convergence to the

“best” local if not global minimum. We have shown through the inversion of noise-perturbed r_{rs} (sensor-derived and simulated) that the standard approach to LM (SLM) optimisation, where the initial guesses are arbitrary and fixed, generated elevated uncertainties because of the convergence to multiple local minima that had different model parameter values. Two methods were presented that searched the multi-parameter space of the BRUCE model, of a given r_{rs} , for the set of parameter values that correspond to a local minimum with the lowest Euclidean distance. The search patterns of these methods differ; in the UR-LM, the optimised values of the inverted r_{rs} were randomly perturbed by 10% of their value and used as the initial guess for a subsequent inversion attempt. This process was repeated until the Euclidean distance fell below 1.0×10^{-5} or if this repetition occurred more than 10 times. In the LHS method, seven sets of initial guesses sampled from the constrained parameter space using Latin Hypercube Sampling were inverted. The optimised values with the lowest Euclidean distance were then used as the initial guesses for the subsequent inversion of noise-perturbed r_{rs} .

Inversions of several HICO derived r_{rs} spectra showed that the UR-LM and LHS method aided the convergence of the LM optimisation to one minimum rather than multiple. As a consequence, the estimated uncertainties of the derived IOPs, depth and bottom albedo decreased and obtained a more accurate representation of the dispersal about the minimum. To test the improvements in accuracy of these two methods (UR-LM and LHS) relative to the SLM approach, we applied these methods to a simulated dataset of r_{rs} spectra whose spectral resolution matched that of HICO. These spectra were generated via forward modelling using the BRUCE model with a range of model parameter values typically encountered in the coastal ocean. Spectrally correlated noise obtained from HICO imagery was added to each simulated r_{rs} to mimic the instrumental noise and imperfect radiometric corrections arising from atmospheric fluctuations and sea surface state. The results showed that the SLM solution approach had substantially lower accuracies, more scatter about true parameter values and higher uncertainties than the UR-LM and LHS methods. Indeed the UR-LM and LHS methods on average increased the accuracies of $a_{phy}(440)$, $a_{dg}(440)$ and $b_{bp}(550)$ by factors of 4, 9 and 14 respectively. On average, the uncertainties for these model parameters were also reduced by factors of 2, 6 and 16 respectively. The retrieved depth also displayed considerable improvement. The SLM method produced accuracies less than 2% for depths greater or equal to 3 metres, while

the LHS method provided accuracies of 51.3%, 11.9% and 2.3% for depths of 3, 6 and 11 m respectively. The UR-LM and LHS methods however did not improve retrievals of the bottom albedo coefficients, which have very poor accuracies, high uncertainties and scatter about the true value. Further analysis revealed that the SLM approach is sensitive to the lower bounds used to constrain the solution space, whilst the LHS (and to a lesser degree, the UR-LM) are considerably more robust and computationally efficient. It should be noted that if spectrally correlated noise is not propagated, and instead just a single reflectance spectrum is to be inverted; then the LHS method would take approximately seven times longer than the SLM. This is due to the search for the optimum initial guess where the LM optimisation is performed seven times.

The UR-LM and LHS methods, like the SLM, are susceptible to spectral non-uniqueness as suggested through the set of inversions presented in Figure 4.11, where two groups (Groups 1 and 2) of different retrieved depths but similar IOP values are present. It is evident that the set of inversions that retrieved a depth greater than 6 m (Group 2, red data points) had negative B_{sand} and B_{seagrass} values, which are not physically possible. Negative bottom albedo values were retrieved as these model parameters were ‘pegged’ to the negative lower bounds of the constrained LM optimisation. Analysis showed (results not shown here) that when the lower bounds were set to zero, the B_{sand} and B_{seagrass} parameters of Group 2 only retrieved values of zero. The MPFIT algorithm used in this study (Markwardt, 2009, Markwardt person. comm. 2014) pegs a model parameter to an upper or lower bound when the cost function (Euclidean distance) exists beyond that boundary; which for this case implies that the minimum is not physically possible and the retrievals should be ignored or flagged. In the situation shown in Figure 4.11, it is possible to determine the correct local minima based on whether the optimisation retrieved any model parameters that ‘bottomed out’. Situations where two or more minima have very similar Euclidean distances and physically possible model parameters are the limit of optimal remote sensing as Hedley et al. (2012b) describes. For example, from *in situ* radiometry it may be possible to identify (through a shallow water model) macroalgae at a shallow depth from sand/seagrass benthos at a deeper depth. However, the satellite/airborne derived r_{TS} spectra of those benthos can contain sensor and environmental noise that can lead not only to indistinguishable spectra but also high uncertainty. These factors can cause the retrieved model parameters of these two benthos to overlap. Although this is an optical remote sensing limit it is still possible and useful to identify these pixels in the

processing using, for example, a post-processing density based cluster analysis, such as DBSCAN (Ester, Kriegel, Sander, & Xu, 1996).

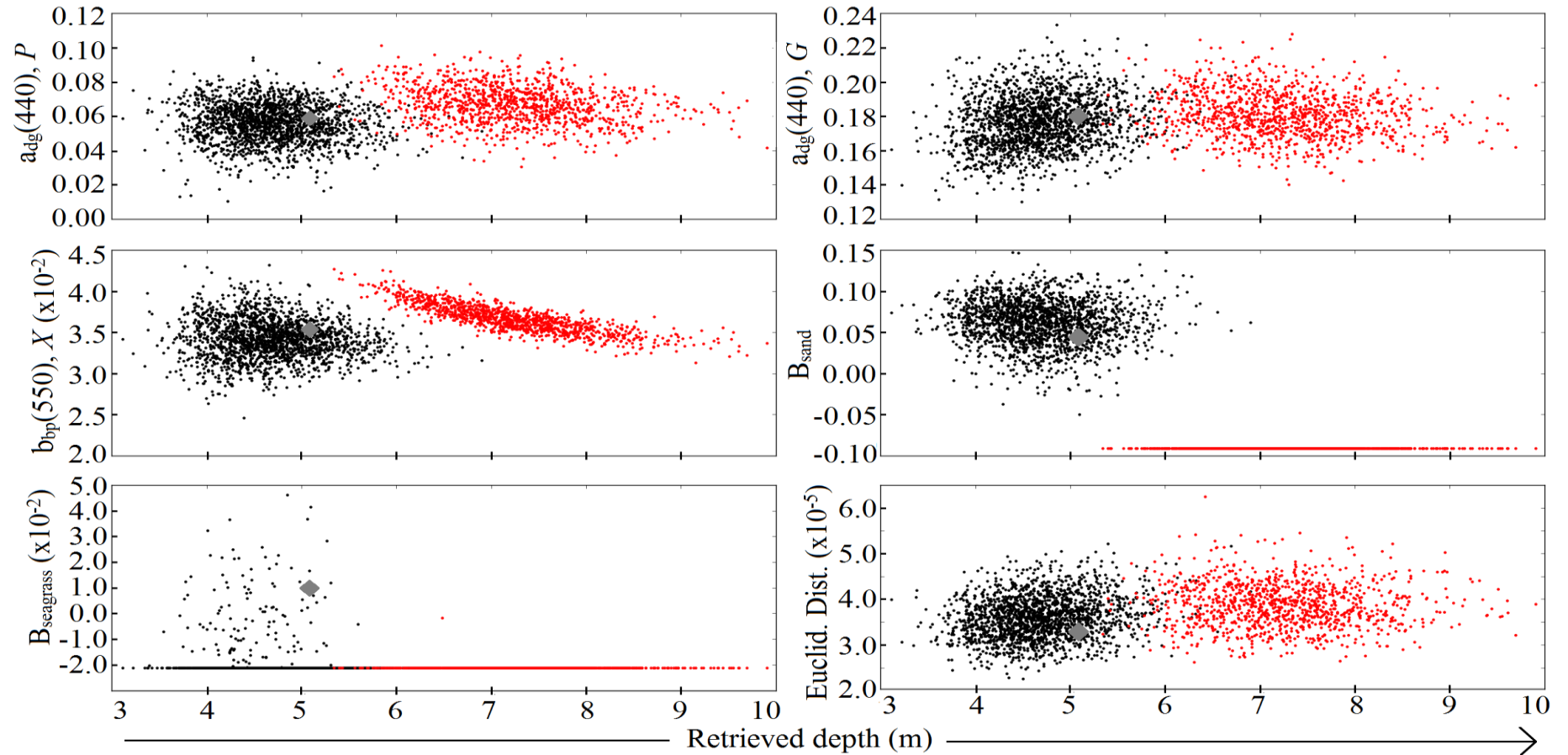


Figure 4.11: Non-uniqueness – retrieved BRUCE model parameters vs. retrieved depth, for the 3000 noise perturbed r_{rs} spectra of quasi-deep HICO pixel at row 1107, column 226, Shark Bay 14-December-2011. The optimised guess values were dynamically chosen using the LHS method and are shown as grey diamonds. The red data points (Group 2) have negative B_{sand} and $B_{seagrass}$ that are not physically possible.

4.6 Recommendations

Based on the analysis presented we recommend the use of the Latin Hypercube Sampling (LHS) procedure to search for the optimal initial guess when implementing the LM optimisation routine within an optically shallow semi-analytical inversion algorithm. The LHS method is simple to implement, more computationally efficient when using the uncertainty propagation technique, and increases the likelihood of converging to the global minimum relative to the standard approach. Furthermore, the LHS (and to a lesser extent the UR-LM) method converges to a single minimum and affords true representation of the uncertainty caused by sensor and environmental noise. Here a complex shallow water algorithm that can have up to seven model parameters was used, and as such it is possible to use the LHS method with other ocean colour models (e.g. Generalized IOP model, Werdell et al., 2013) developed for different sensors. Here the number of noise-perturbed spectra to was set to 3000 per pixel when testing the UR-LM and LHS methods on the HICO spectral image data. For operational processing of satellite/airborne imagery, a recommend 50 noise-perturbed spectra per pixel as illustrated in Figure A.10 (Appendix A), which in C language takes an average of 0.12 seconds per pixel using the LHS method on a standard PC without parallel/GPU processing.

CHAPTER 5

A METHOD TO ANALYSE THE POTENTIAL OF OPTICAL REMOTE SENSING FOR BENTHIC HABITAT MAPPING

This chapter has been published in the journal: Remote Sensing.

Rodrigo A. Garcia, John D. Hedley, Hoang C. Tin, Peter R. C. S. Fearn. A method to analyse the potential of optical remote sensing for benthic habitat mapping. *Remote Sensing*, 7(10), (2015), pp. 13157-13189. DOI: 10.3390/rs71013157. <http://www.mdpi.com/2072-4292/7/10/13157>

5.1 Abstract

Quantifying the number and type of benthic classes that are able to be spectrally identified in shallow water remote sensing is important in understanding its potential for habitat mapping. Factors that impact the effectiveness of shallow water habitat mapping include water column turbidity, depth, sensor and environmental noise, spectral resolution of the sensor and spectral variability of the benthic classes. In this paper, we present a simple hierarchical clustering method coupled with a shallow water forward model to generate water-column specific spectral libraries. This technique requires no prior decision on the number of classes to output: the resultant classes are optically separable above the spectral noise introduced by the sensor, image based radiometric corrections, the benthos' natural spectral variability and the attenuating properties of a variable water column at depth. The modelling reveals the effect reducing the spectral resolution has on the number and type of classes that are optically distinct. We illustrate the potential of this clustering algorithm in an analysis of the conditions, including clustering accuracy, sensor spectral resolution and water column optical properties and depth that enabled the spectral distinction of the seagrass *Amphibolis antartica* from benthic algae.

5.2 Introduction

A fundamental issue with benthic classification of remotely imaged shallow water environments is determining the appropriate definition and number of benthic classes that: (i) optimizes the classification accuracy and precision (Andrefouet et al., 2003); and (ii) standardizes classification maps for ease of inter-comparisons (Mumby & Harbone, 1999). The selection of classes and their descriptive resolution, *i.e.*, biological detail (Mumby et al., 1997), for a spectral library or training dataset, along with the image classification method, have typically been scene and sensor specific (Mumby et al., 1998a). For multispectral imagery, the optimum spectral library could consist of image-derived or *in situ* spectra of pure endmembers (a discrete taxonomic unit *i.e.*, high descriptive resolution) if the benthos in the scene is either homogeneous or was imaged with very high spatial resolution (Mumby et al., 1998b; Mumby et al., 2004; Vahtmae & Kutser, 2007). For a scene with patchy or heterogeneous benthos or that was imaged with moderate to low spatial resolution, the spectral library could contain classes pertaining to merged endmembers (*i.e.*, mixed benthic assemblages) and low descriptive resolution (Mumby et al., 1997; Mumby & Edwards, 2002; Vahtmae, Kutser, Kotta, & Parnoja, 2011). Due to the spectral characteristics of the sensors used (e.g., SPOT, Landsat 5–7, IKONOS; QuickBird), the above studies mostly utilized supervised classification schemes with or without water column correction to produce benthic habitat maps (additional examples include Purkis, Kenter, Oikonomou, & Robinson, 2002; Dekker, Brando, & Anstee, 2005; Gullstrom et al., 2006).

Hyperspectral sensors, in contrast, have enough spectral resolution and bands to potentially facilitate the spectral unmixing of an image spectrum based on the fractional cover of a subset of pure endmembers (Hedley et al., 2004). This has often led to the implementation of a spectral library of pure endmembers which would be linearly mixed either to pre-defined proportions such as in look-up table methods (Mobley et al., 2005; Hedley et al., 2009) or during spectral optimization in shallow-water inversion methods (Lee et al., 1999; Klonowski et al., 2007; Brando et al., 2009). These methods have consequently achieved moderate to high benthic classification accuracies (Mobley et al., 2005; Fearn et al., 2011; Dekker et al., 2011; Kobryn, Wouters, Beckley, & Heege, 2013).

Previous studies with multispectral imagery have shown an inverse relationship between the number of benthic classes and the classification accuracy (Andrefouet et al., 2003; Mumby et al., 1997; Mumby & Edwards, 2002). This same relationship has also been shown for hyperspectral imagery, see (Kobryn et al., 2013; Harvey et al., 2007). This raises the question of how to optimize the class selection, or equivalently how to merge classes of higher descriptive resolution in order to achieve both accurate and useful maps. Karpouzli et al. (2004) observed that agglomerating pure endmembers based on their genera to obtain average spectra of coral, seagrass, macroalgae and sand, reduced the classification accuracy. Specifically high classification accuracy was obtained with more classes at finer descriptive resolution. This was attributed to the fact that the intra-class variability exceeded the inter-class separability – as it has been noted that some species of corals are spectrally similar to macroalgae and vice-versa (Hochberg & Atkinson, 2003). Clearly, averaging pure endmembers based on their genera, which seems a logical and ecologically meaningful step, may not maximise spectral separability between classes, and potentially leads to a higher probability of confusion during classification.

Furthermore increasing the descriptive resolution of the benthic classes may lead to a decrease in the precision of the resultant classification, particularly if sensor and environmental noise is taken into account. Such noise is a component of remotely sensed imagery originating from the sensor and from atmospheric, sunglint and air–water interface corrections that maybe imperfect at times (Brando & Dekker, 2003; Hedley et al., 2012b). The combined impact of sensor and environmental noise and spectral variability of a given taxonomic species observed in local and regional scales (Hochberg, Atkinson, Apprill, & Andrefouet, 2004; Stambler & Shashar, 2007) act to degrade the inter-class spectral separability as described in Hedley et al. (2012b).

Minimising confusion or uncertainty arising from spectrally similar classes necessitates a procedure to re-define the spectral library of endmembers into more distinct classes. Clustering is an approach that can merge those spectrally similar classes thereby reducing the spectral confusion in a spectral library. A variety of indices can be used to define the spectral similarity between two classes including root mean square error, spectral angle mapper (Kruse et al., 1993) or spectral information divergence (Chang, 2000). Though clustering is a common procedure in unsupervised classification (Sohn and Rebelló, 2002; Pu et al., 2012; Maeder et al., 2002; Call et al., 2003), it is seldom performed on the endmember spectra that constitute the spectral

library (for exceptions see Minghelli-Roman, Chisholm, Marchioretti, Ripley, & Jaubert, 2002; Kutser & Jupp, 2006; Purkis & Pasterkamp, 2004). Particularly on benthic spectra that are further modulated by the physical processes occurring in an optically variable water column. In this study we present a hierarchical clustering algorithm, based on linear discriminant coordinates, tailored for shallow-water inversion models that uses the intra-class variability to merge those classes in the benthic spectral library that overlap, i.e., are optically indistinguishable. Here, the intra-class variability incorporates the individual benthos' natural spectral variability plus image-based sensor and environmental noise. The hierarchical clustering ceases when there is no spectral overlap in the variance between groups; and thus outputs a set of classes that are spectrally distinguishable under actual operational conditions. In combination with a shallow water forward model this hierarchical procedure was used to develop depth and water-column specific spectral libraries. The endmembers of which are spectrally distinguishable above the attenuating properties of an optically variable water column at depth. In addition we investigate the effect spectral resolution has on benthic class separability by analysing the clustering from simulations using the following three sensors: Hyperspectral Imager for the Coastal Ocean (HICO); HyVista's HyMap, and; Worldview-2 (WV2). Such information on the number and type (i.e., definition) of distinguishable classes at any given depth and water column optical properties helps to understand the potential of benthic classification from shallow water remote sensing imagery.

5.3 Methodology

The overall goal is the development of a procedure that can quantitate the number and type of classes that are spectrally distinct for any given water column optical properties and depth from a spectral library of representative benthic species. We begin in section 5.3.1 with a description of the benthic irradiance reflectance, ρ_b , library collected from the field and we then describe the hierarchical clustering algorithm in section 5.3.2. Using the measured ρ_b data, the clustering algorithm outputs a library of endmembers that are spectrally separable above the total system's variability but only suitable just below the air-water interface as the attenuating effects of a water column were not modelled. Given an estimated or known range of depths and water column optical properties in a scene, a semi-analytical shallow water

forward model coupled with the clustering algorithm can be used to predict the benthic classes that are optically distinct. This procedure is detailed in section 5.3.3.

5.3.1 Benthic reflectance library

A spectral library of pure endmembers was derived from in-air irradiance reflectance measurements of 22 benthic species collected from the Point Peron (32.2715° S, 115.6865° E) study site, Western Australia, on 22 August 2014 (Table 5.1). Benthic samples were collected with enough material to cover the 25° field of view of the ASD field spectrometer (1 nm resolution, 350–2500 nm coverage). However, the quantities of *Posidonia* sp. and *Metagoniolithon stelliferum* were too small to cover the field of view and these were placed over a substrate (sediment and rock/rubble respectively) that would normally be underneath. These samples were stored overnight in a tank that had aerated, flowing filtered seawater to minimize the effect of pigment degradation. The collected samples were then spectrally analysed the following day on a bench top set up outside on a flat roof. All samples were placed on top of a large flat, non-reflective black tray. The ASD fibre optic was held using a retort stand at a constant 30 cm above the sample and at a small angle off nadir (approx. 10°) and a white reference plate was used to compute the reflectance for each spectral measurement at the same angular geometry. Furthermore, each benthic sample was stirred and mixed every three spectral measurements to capture the sub local-scale taxonomic spectral variability. With this setup approximately 30–40 in-air reflectance measurements were recorded for each (wet) benthos collected. At the time of sample collection (winter) the leaves of *Posidonia* sp. were in the dormant phases, and new leaves were not visible in the collection area. The leaves that were collected, however, were already detached and slightly senescent.

The benthic irradiance reflectance spectra, ρ_b , between 400 and 680 nm were then convolved with the spectral response functions (SRF) of the HICO, WV2 and HyMap sensors to generate three spectral libraries (Figure 5.1). The clustering algorithm was used on these spectral libraries to assess the impact of reducing spectral resolution. Here, wavelengths past 680 nm were not considered due the high absorption of light in the water column. This reduced the number of bands of HICO and HyMap to 49 and 16 respectively. For WV2 the five spectral bands between 400 and 680 nm were used.

Table 5.1: List of the benthic species collected from the Point Peron study site.

Genera	Species
Brown alga (BA)	<i>Sargassum linearifolium</i>
	<i>Sargassum spinuligerum</i>
	<i>Ecklonia radiata</i>
	<i>Colpomenia sinuosa</i>
Red alga (RA)	<i>Asparagopsis armata</i>
	<i>Hypnea ramentacea</i>
	<i>Ballia</i> sp.
	<i>Amphiroa anceps</i>
	<i>Euptilota articulata</i>
	<i>Ballia callitrichia</i>
Green alga (GA)	<i>Metagoniolithon stelliferum</i> on rubble
	<i>Ulva australis</i>
	<i>Enteromorpha</i> sp.
	<i>Codium duthieae</i>
	<i>Caulerpa germinata</i>
	<i>Caulerpa flexis</i>
Seagrass (SG)	<i>Bryopsis vestita</i>
	<i>Amphibolis antarctica</i>
Sand/sediment (SD)	<i>Posidonia</i> sp. on sediment
	Sediment
	Sediment/Rubble
	Rocks with encrusting red coralline algae

5.3.2 Clustering

5.3.2.1 Measure of interclass overlap

A measure of the degree of overlap or misclassification between a pair of classes was used in the clustering algorithm to identify which classes to merge per iteration. Specifically, the closest (most similar) pair of classes whose misclassification proportion, τ_m , exceeded a user-defined amount were combined. We have defined τ_m between two classes i and j as the proportion of misclassified spectra in Linear Discriminant (LD) coordinates as given by Rencher and Christensen (2012, p. 288-319),

$$\tau_m = \frac{n_{mi} + n_{mj}}{n_i + n_j} \times 100\% \quad (5.1)$$

where n_i and n_j are the number of LD points (i.e. spectra) in classes i and j , whilst n_{mi} and n_{mj} are the number of misclassified LD points from those respective classes. We consider a point misclassified if it is closer or equal in distance to the mean of a different class than to its own class mean (exemplified in Figure C.4, Appendix C). Here the straight line distance between a point and a class mean in LD coordinates is computed using the RMSE, where similar spectra have low RMSE. This approach is equivalent to inserting a separating plane between two classes and counting the number of spectra on their incorrect side as done in Hedley et al. (2012b). This per-point per-class comparison was performed for all possible pairs of benthic classes in the clustering procedure per iteration.

5.3.2.2 Linear Discriminant Hierarchical Clustering (LDHC) algorithm

The measured ρ_b spectra (initial spectral library) may contain many benthos that are indistinguishable in terms of their reflectance when sensor and environmental noise $NE\Delta r_{rs}$ (Brando et al., 2009) and the species natural spectral variability are taken into account. To assess this, an agglomerative centroid hierarchical clustering algorithm based on linear discriminant coordinates (hereafter referred to as HDC) was developed. Here classes were merged that had a misclassification proportion (τ_m) greater than a user-specified threshold. This threshold, set at 5% in this study, is inversely proportional to the number of benthic classes generated from the HDC algorithm. We define the class-merging (or clustering) accuracy as $100 - \tau_m$, and thus would allow a user to set a threshold for the level of class separability. This is a more quantitative and intuitive approach than predetermining, arbitrarily, the number of

classes that the clustering should output. The HDC algorithm can be summarized in the following three steps (flowchart A, Figure 5.2): (1) the addition of $NE\Delta r_{rs}$ to the measured ρ_b spectra; (2) the transformation from spectral space to LD coordinates; and (3) subsequent hierarchical clustering. The advantage of this approach is that no prior decision on the number of resultant clusters to output is needed. This is a common issue faced by conventional hierarchical clustering (Holden & LeDrew, 1998; Anderberg, 1973, p.15). Here the number of output clusters is dependent on the following: (a) the magnitude of the error given by the covariance matrices—pertaining to $NE\Delta r_{rs}$ and the taxonomic spectral variability; (b) the spectral resolution of the sensor; and (c) the τ_m threshold. Note an extended description of the HDC procedure with accompanying figures are given in Appendix C.

To account for the total noise in the system just below the air–water interface in step (1), we perturb the measured ρ_b spectra with $NE\Delta r_{rs}$ using the procedure developed by Hedley et al. (2010; 2012a). As such spectral noise caused from the sensor and any spatial noise from atmospheric, sunglint and air-to-water interface corrections were included. Briefly, the spectral covariance matrix, C_{SE} , was extracted from an imaged homogeneous deep-water region of subsurface remote sensing reflectance (r_{rs}) imagery. A set of pseudo-random spectral noise terms, $\delta\rho_{SE}$, were computed from C_{SE} and were added to a single ρ_b spectrum to generate a number of noise-perturbed spectra, $\rho_b \pm \delta\rho_{SE}$. This number varied for a given class but was such that it would generate 2000 noise-perturbed benthic reflectance spectra (Figure C.1 in Appendix C). A total of 44,000 spectra from the 22 classes were consequently produced. A detailed description of the computation of $\delta\rho_{SE}$ (presented as δr_{rs}) is given in section 4.3.3.

In this developmental study, we estimated the spectral shape and magnitude of $NE\Delta r_{rs}$ from an imaged homogeneous deep-water region of the HICO-derived r_{rs} image of Shark Bay 14th December 2011. Interpolation to the wavelength centres of HyMap and WV2 were performed to keep the magnitude and spectral shapes of $NE\Delta r_{rs}$ consistent between sensors. The spectral covariance matrices C_{SE}^{WV2} and C_{SE}^{HyMap} were then computed and used in the HDC algorithm for the respective sensors. The atmospheric, sunglint and air-to-water interface corrections used on the HICO image of Shark Bay to convert top-of-atmosphere calibrated radiances to r_{rs} are described in section 3.3.2.

In step (2) the Linear Discriminant Analysis (LDA) procedure for the case of several classes was implemented (Rencher & Christensen, 2012, p. 288-319) to convert the 44,000 ρ_b spectra into LD coordinates. The optimal number of eigenvectors, s , of the resultant LD points was chosen through an iterative approach, where s was successively increased to maximise the number of classes, k , generated from the subsequent clustering. If k remained constant with increasing s for more than three successive increments of s then the iteration was ceased and the eigenvector that produced the last improvement in k was selected.

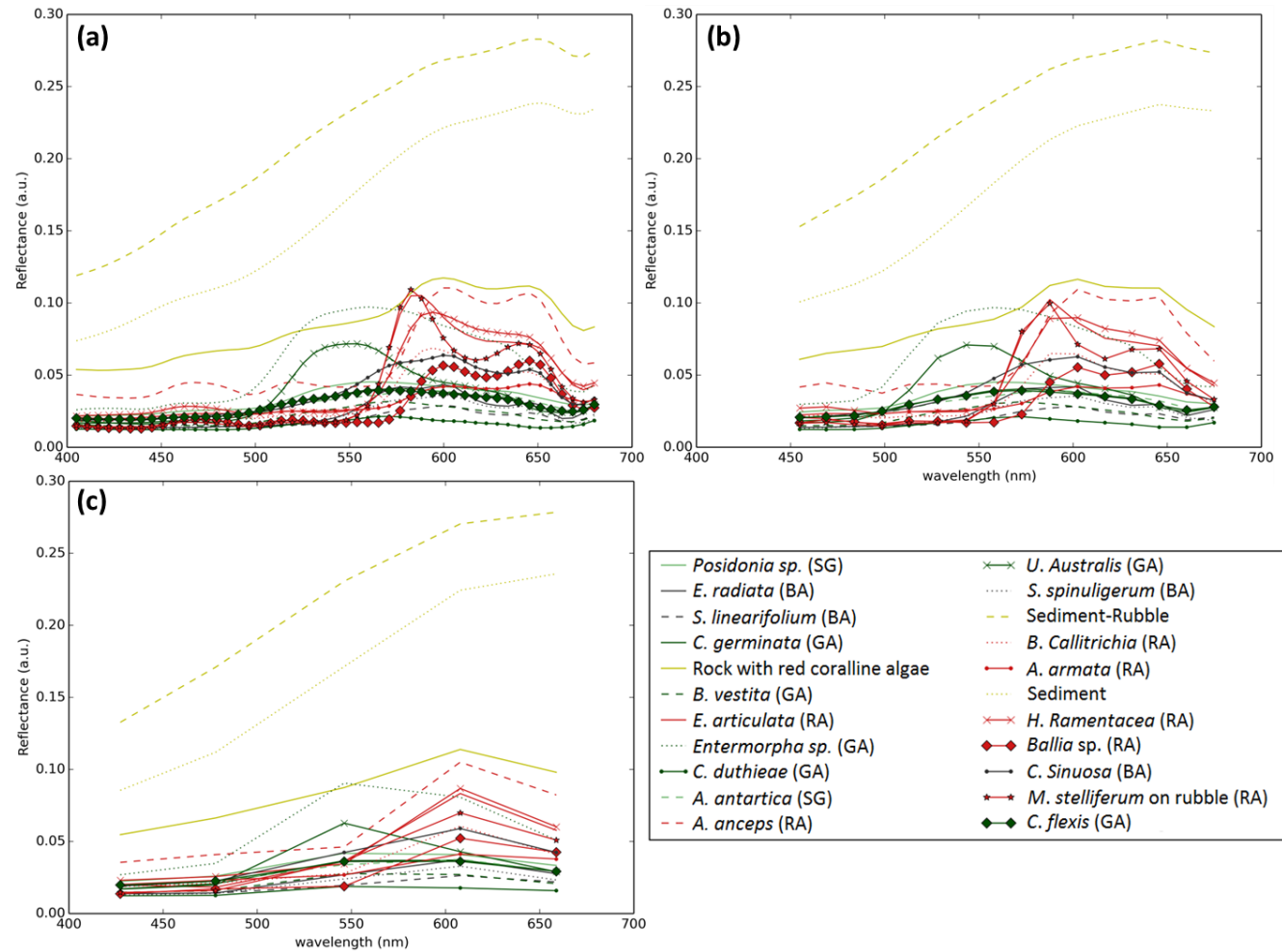


Figure 5.1: The average irradiance reflectance spectra of the benthos collected, convolved to the spectral resolutions of (a) HICO (b) HyMap and (c) WV2.

For a given eigenvector number an iterative centroid-based hierarchical clustering procedure was implemented to merge overlapping benthic classes. Here a single pair of classes was merged per iteration with τ_m set to 5%. The iterative clustering begins with the computation of the RMSE between all possible pairs of class means, and τ_m between those pairs. The pair of classes that had the lowest RMSE and whose $\tau_m > 5\%$ were merged to form a single class. In this step the LD coordinates of the two merging classes remain unchanged only that they are labelled as one. The ρ_b spectra of these two classes were used to compute the weighted average of the newly merged class. This iteration continues until the remaining classes all have a $\tau_m \leq 5\%$; in other words the clustering ceases when there is a 95% accuracy that all classes are optically separable above the sensor and environmental noise and the benthos' natural spectral variability. This clustering accuracy can be reduced (with a corresponding increase in the number of "separable" classes) according to the desire of the user or application. The output of this entire procedure is a spectral library that contains the optimum set of endmembers for classifying the set of substrates of interest.

We compare the resultant classes from the HDC algorithm with an agglomerative centroid-based hierarchical clustering procedure taken from Everitt, Landau, Leese, and Stahl (2011, p.76) using only bottom reflectances. For simplicity in this text we refer to this type of clustering as the standard hierarchical clustering. In this standard hierarchical clustering the pair of classes with the lowest RMSE were merged per iteration. Note, the mean class ρ_b spectra were used to compute the RMSE between all possible pairs, and the weighted average spectrum was computed for a newly merged group. The merging continues until all groups have clustered into one class. We estimate the appropriate number of clusters by locating the knee from a bi-plot of the linkage distance against the number of clusters (Salvador & Chan, 2004). Here, the linkage distance is simply the RMSE between the pair of groups that are merged at a given cluster iteration. We utilize the definition of "knee of the plot" as the point that experiences an abrupt change in the RMSE as done by Torrecilla, Stramski, Reynolds, Millan-Nunez and Piera (2011).

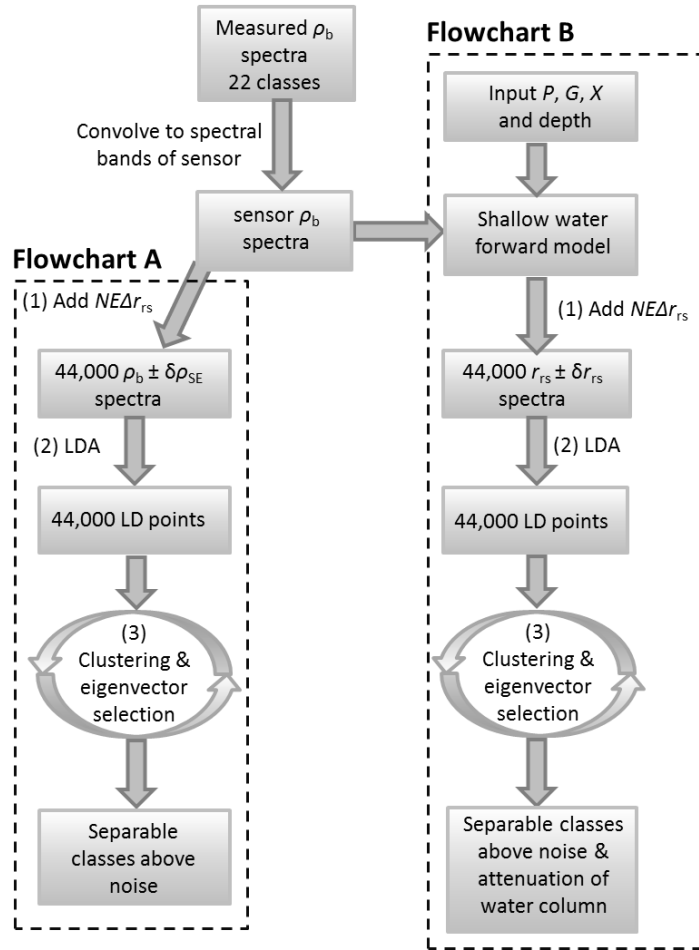


Figure 5.2: The LDHC algorithm using the basic bottom reflectances (flowchart A) and coupled with a shallow water forward model to include a water column (flowchart B).

5.3.2.3 Depth and water column specific spectral libraries

Without incorporating the attenuating properties of a water column to ρ_b the HDC generated spectral library would only be suitable just below the water's surface. Employing such a spectral library into a physics-based inversion, for instance, may not give a realistic representation of benthic classification at increased depth and/or turbidity (discussed in Section 5.4.4) as fewer classes would be optically separable (Hedley et al., 2012b; Botha, Brando, Anstee, Dekker, & Sagar, 2013). To include the attenuating properties of a water column and water depth we used the semi-analytical (SA) shallow water forward model given by Lee et al. (1999). This model estimates r_{rs} from the following scalars: (a) the absorption coefficient of phytoplankton at 440 nm, P (m^{-1}); (b) the absorption coefficient of dissolved and detrital matter at 440 nm, G (m^{-1}); (c) the backscattering coefficient of suspended particles at 550 nm, X (m^{-1}); (d) depth, H (m); (e) and the bottom reflectance, ρ . This SA model was used to compute r_{rs} over each measured ρ_b spectrum described Section 2.1 from a given set of

P , G , X and depth. The set of r_{rs} spectra were then passed through the HDC (flowchart B in Figure 5.2) to merge those classes that were optically indistinguishable above the total system's noise and attenuating water column. After the clustering based on r_{rs} , the corresponding benthic reflectances (ρ_b) were merged to produce the mean bottom endmember spectra. Note that in this SA model the phytoplankton spectral absorption shape is almost fixed. Though in reality this spectral shape is likely to change with the presence of different phytoplankton functional groups (spatially and temporally); benthic classification from remote sensing, which this algorithm is tailored towards, is typically performed in relatively clear shallow waters with relatively low chlorophyll concentrations. In these conditions, the shape of the phytoplankton absorption spectrum would likely have very minor impact to the clustering outputs.

The impact of water column depth and optical properties on the classes produced from the HDC algorithm was modelled by selecting specific depths between 0.5 and 20 m for the following water column optical properties: (1) $P = 0.01 \text{ m}^{-1}$, $G = 0.01 \text{ m}^{-1}$, $X = 0.001 \text{ m}^{-1}$ ($\kappa = 0.03 \text{ m}^{-1}$; $Z_{SD} = 48 \text{ m}$); (2) $P = 0.05 \text{ m}^{-1}$, $G = 0.1 \text{ m}^{-1}$, $X = 0.01 \text{ m}^{-1}$ ($\kappa = 0.11 \text{ m}^{-1}$; $Z_{SD} = 13 \text{ m}$); (3) $P = 0.1 \text{ m}^{-1}$, $G = 0.2 \text{ m}^{-1}$, $X = 0.02 \text{ m}^{-1}$ ($\kappa = 0.21 \text{ m}^{-1}$; $Z_{SD} = 6.8 \text{ m}$); and (4) $P = 0.5 \text{ m}^{-1}$, $G = 0.5 \text{ m}^{-1}$, $X = 0.05 \text{ m}^{-1}$ ($\kappa = 0.68 \text{ m}^{-1}$; $Z_{SD} = 2 \text{ m}$). κ and Z_{SD} are the attenuation coefficient at 490 nm and the estimated Secchi depth respectively, $\kappa Z_{SD} = 1.44$ (Holmes, 1970). Here, Z_{SD} was used as a qualitative and readily interpretable measure of water clarity. An analysis of the conditions (clustering accuracy, spectral resolution, water column depth and optical properties) where the seagrass species *A. antarctica* is spectrally resolvable against benthic algae was performed. For this analysis the clustering was run iteratively over a range of depths (0.25 to 25 m at 0.25 m increments) at the four water clarities mentioned above for eight different clustering accuracies (60% to 95% at 5% increments).

5.4 Results and Discussion

5.4.1 Hierarchical clustering of benthic irradiance reflectance spectra

The HDC-derived dendrogram using the basic ρ_b spectra at HICO bands describes which benthic classes merge and the RMSE of that union (Figure 5.3a). The respective dendrogram generated from the standard hierarchical clustering is presented in Figure 5.3b. Here, the RMSE refers to the spectral difference (in LD coordinates)

between one class mean and another, where the larger the value the larger the spectral difference. Based on the simulated spectral variability, occurring just below the air–water interface, the clustering output 18 classes for HICO (Figure 3a) and HyMap (Figure 5.4) and 14 classes using WV2 bands (Figure 5.5). The clusters that were formed using HICO and HyMap bands were identical except that the merging of the clusters occurred at lower RMSE for HyMap (Figure 5.4). For example the merging of *C. sinuosa* with the cluster *S. linearifolium*/*S. spinuligerum* occurred at an RMSE of ~0.035 for HICO and ~0.032 for HyMap. This slight decrease in RMSE is likely due to the lower spectral resolution of the HyMap sensor or due to the lack of spectral bands below 450 nm (*i.e.*, less spectral bands to facilitate separation). The dendrogram for HICO (Figure 5.3a) and HyMap (Figure 5.4) show the formation of two green algae clusters (*C. germinata*/*C. flexis* and *B. vestita*/*C. duthieae*) and a brown algae cluster (*C. sinuosa*/*S. linearifolium*/*S. spinuligerum*) with the other benthic classes remaining optically separable. The dendrogram produced from the standard hierarchical clustering (Everitt et al., 2011, p.76) (Figure 5.3b) illustrates the potential indecision of what RMSE to cut the dendrogram and extract the relevant clusters. Here clustering continues to a single class with no indication of the optimum number of classes. At ~0.003 RMSE, 18 classes were extracted with the following clusters: (a) seagrass-green algae *A. antarctica*/*C. germinata*/*C. flexis*; (b) mixed brown algae *E. radiata*/*S. spinuligerum*; and (c) brown-green algae *S. linearifolium*/*B. vestita*. A post clustering approach was utilized to estimate the appropriate number of classes from the standard hierarchical clustering (Figure 5.3b). Here, nine classes was chosen as the optimum number, where the following general clusters remained: (a) two separate green algae species (*Entromorpha* sp. and *U. australis*); (b) two separate sediment classes (sediment/rubble and sediment); (c) mixed red/brown algae; (d) mixed brown, red, green algae and seagrass; and (e) a mixed red algae class. The number of classes selected by this post-clustering approach is much lower than that selected by the HDC. Moreover the HDC preferentially merges classes of the same genera first. For example the centroid hierarchical clustering merges the seagrass *Posidonia* sp. with the mixed *C. germinata*/*C. flexis* algae green class at the second iteration (Figure 5.3b, RMSE ~0.0135), whereas the HDC considers these two classes optically distinct.

These two clustering algorithms generate different classes because the HDC first identifies pairs of classes with $\tau_m > 5\%$ (the user defined threshold) and then merges the pair with the lowest RMSE (Mahalanobis distance in spectral space). The

centroid based hierarchical clustering (Figure 5.3b) instead merges the most similar class pairs regardless of whether their variance overlap or not. In other words a pair of classes may be grouped even if they could be considered optically distinct. An added advantage of the HDC is that the number of classes selected is imbedded inside the clustering, where the merging of clusters ceases when the variance overlap between groups is below a user defined threshold. Thus the criterion for stopping is statistically meaningful and aligns with the sensor and environmentally limited system of remote sensing as described and illustrated in Hedley et al. (2012b) (see Figure 1 in Hedley et al., 2012b). The user defined threshold describes the proportion of misclassification that a pair of classes should have before they are considered optically indistinguishable and hence merged. For example using HICO bands, the two classes *C. germinata* and *C. flexis* had a τ_m of 20%, *i.e.*, 20% of the total spectra of these two classes were located in the overlap region and hence inseparable. Given that $\tau_m > 5\%$ and proximity of the class means the HDC clustered these *C. germinata* and *C. flexis* after the second iteration.

The much lower spectral resolution and fewer wavebands of the WV2 sensor only facilitated the separation of 14 classes with the HDC. The dendrogram (Figure 5.5) shows the formation of the following clusters: (1) all the brown algae classes; (2) the green alga cluster *Enteromorpha* sp./*U. australis*; (3) the mixed seagrass-green algae class of *Posidonia* sp./*C. germinata*/*C. flexis*/*B. vestita*; and (4) the red alga cluster *E. articulata*/*M. stelliferum*. Thus out of the seagrass species, only *A. antarctica* was spectrally separable using WV2 bands. At the time of collection the seagrass *Posidonia* sp. samples were senescent and less spectrally distinct (using WV2 bands at least), which likely lead to its inclusion into the green algae cluster. Fyfe (2003) compared the in-air reflectance of several unfouled and fouled seagrass species and showed that the latter had broader and less reflective peaks between 520–580 nm compared to the unfouled case. It is likely that this seagrass species can be optically separated if their reflectance spectra are collected during their growing season.

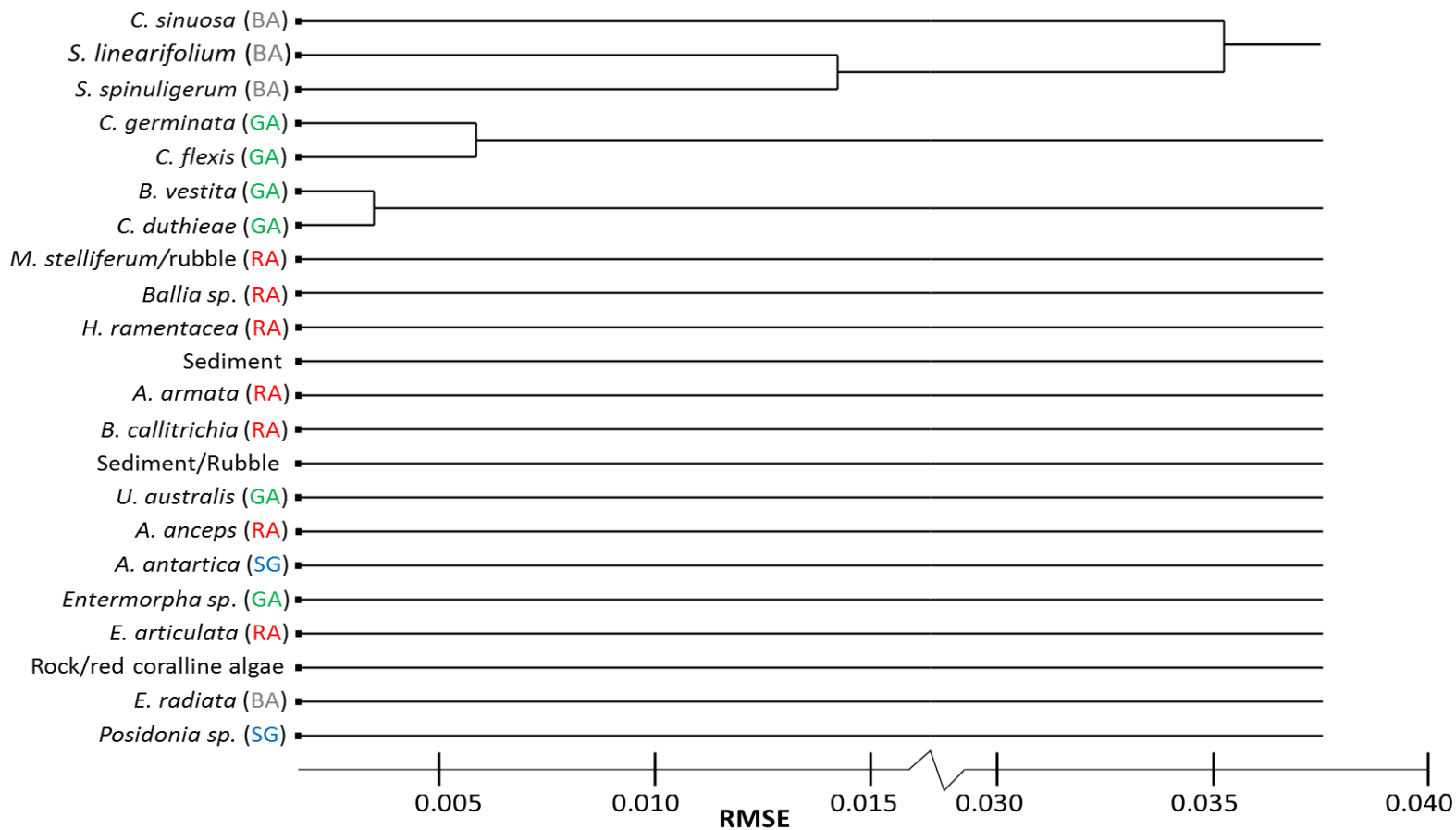


Figure 5.3a: HDC dendrogram of ρ_b spectra using HICO's spectral bands. The iterative selection of eigenvectors chose the first six that produced 18 classes.

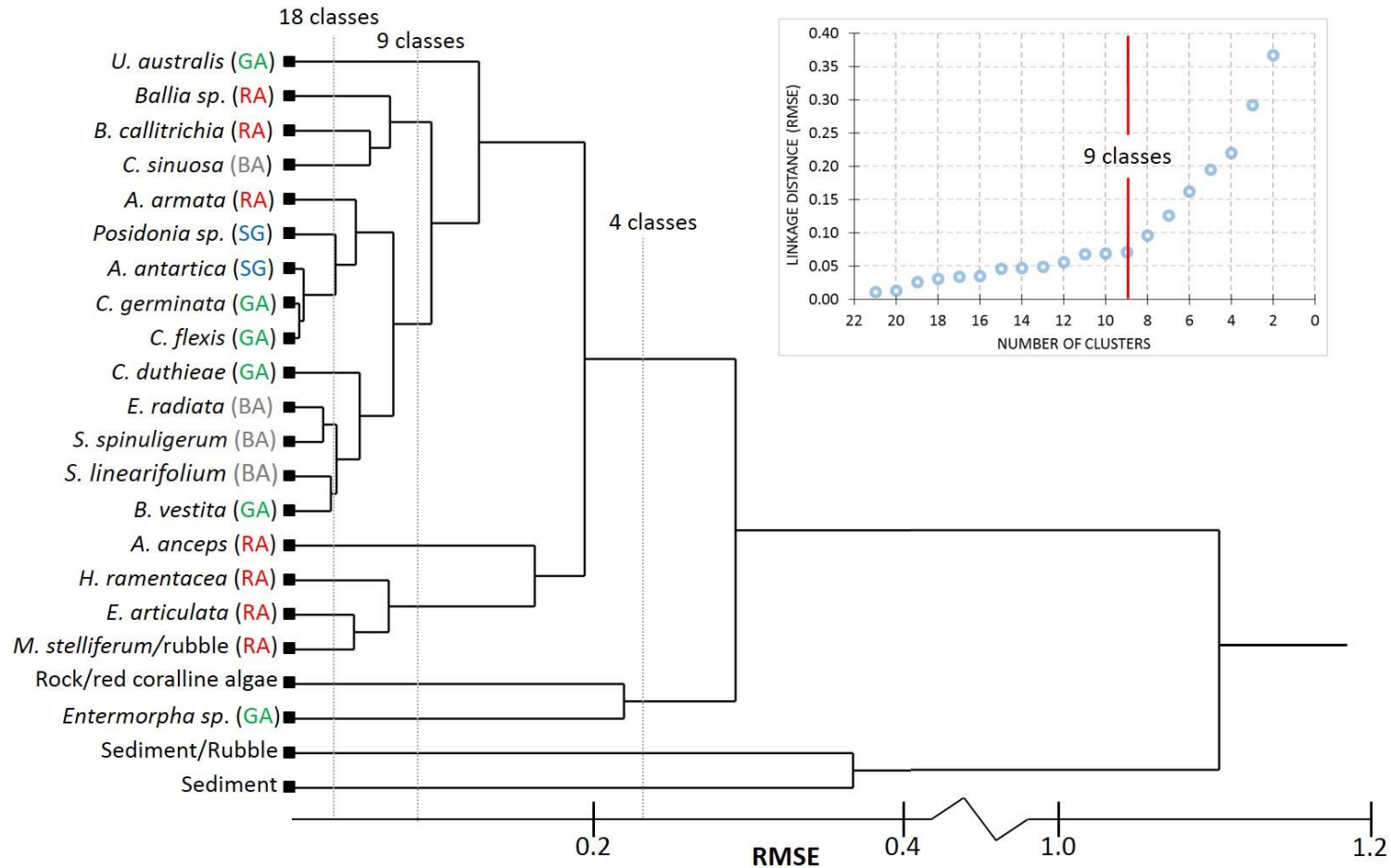


Figure 5.3b: Centroid hierarchical clustering dendrogram of ρ_b spectra using HICO's spectral bands. The top right panel shows the linkage distance vs. number of clusters, where nine classes were selected as the optimal based on the location of the knee of the curve.

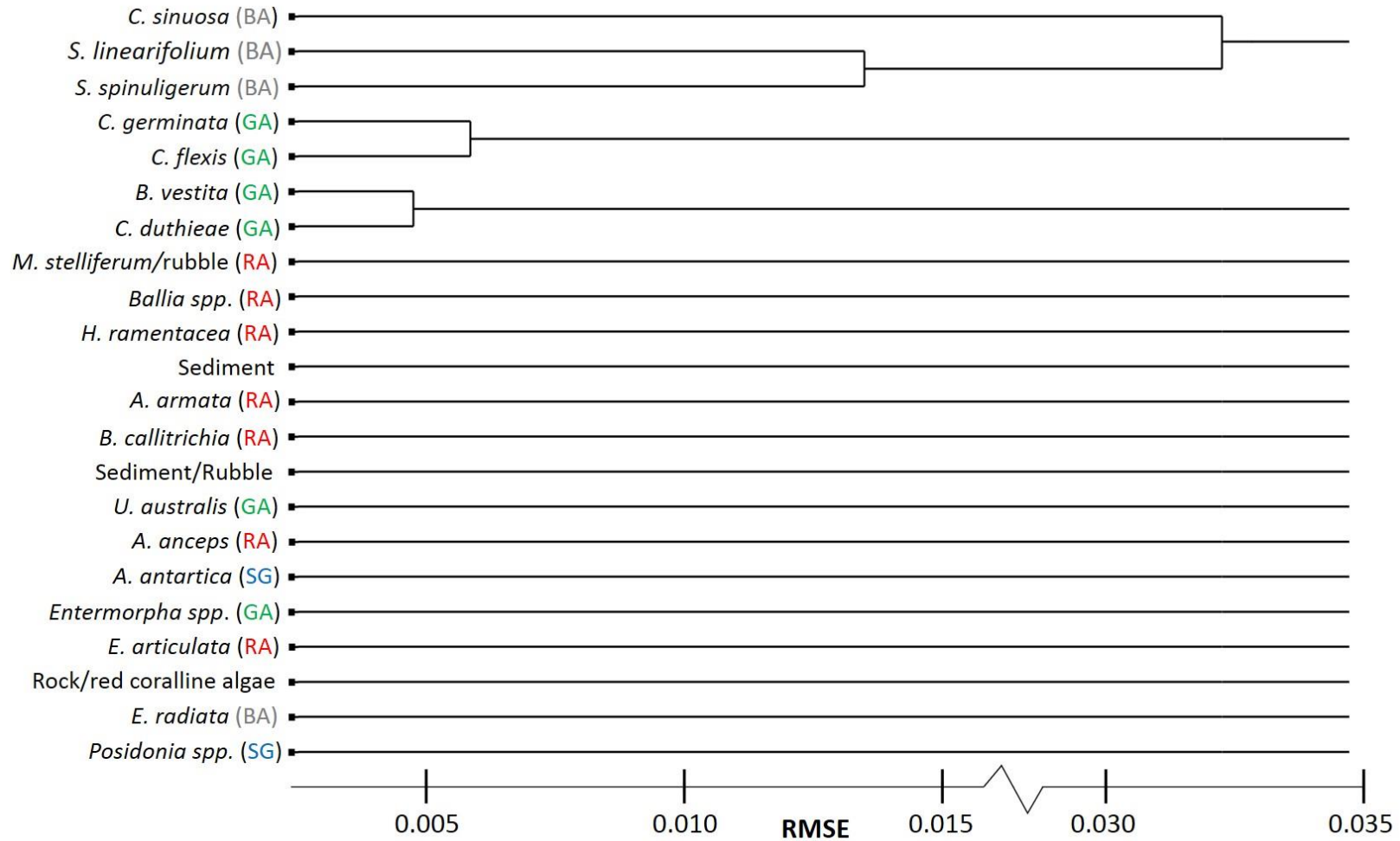


Figure 5.4: HDC dendrogram of ρ_b spectra using HyMap spectral bands. The iterative selection of eigenvectors chose the first seven that produced 18 classes.

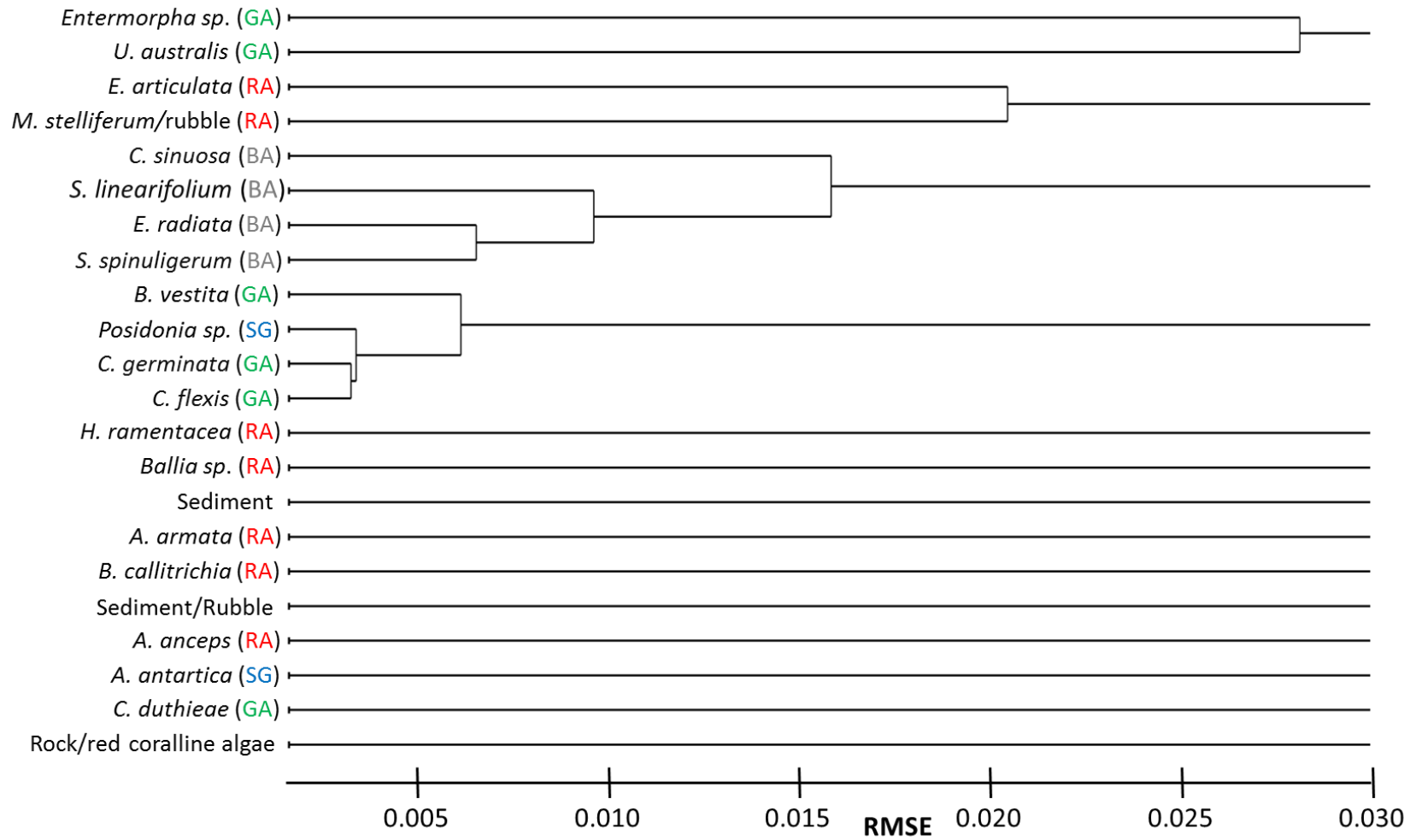


Figure 5.5: HDC dendrogram of ρ_b spectra using WV2's spectral bands. The iterative selection of eigenvectors chose the first four that produced 14 classes.

5.4.2 Water-column specific benthic spectral libraries

Two spectrally distinct benthic classes remain at a modelled water depth and optical properties of 15.0 m, $P = 0.05 \text{ m}^{-1}$, $G = 0.10 \text{ m}^{-1}$ and $X = 0.010 \text{ m}^{-1}$ using HICO bands (Figure 5.6). Here the HDC has merged all benthic vegetation species into a mixed vegetation class and merged the remaining two sediment classes. Thus at this water column optical property and depth it is not possible to distinguish between any of the initial benthic vegetation species above the total system noise, and only a bright (i.e., sediment) and dark (i.e., vegetation) substrate can be distinguished, assuming completely filled pixels of each type. Figure 5.6 shows the possibility of determining *a priori* which benthic classes are separable in a single image pixel at a fixed depth and optical property. Thus for an image with varying depths and water column optical properties the HDC clustering will need to be applied per-pixel. Physics-based inversion methods can be used to derive the depth and water column optical properties as will be discussed in Section 5.4.3.

The decrease in the number of optically separable benthic classes for increasing depth and water column turbidity at HICO, HyMap and WV2 bands was quantified with the HDC clustering (Figure 5.7). Clear to turbid water columns (Figure 5.7, water types 1 and 4 respectively) were modelled to assess their impact on benthic class optical separation. For a given water clarity the number of optically distinguishable benthic classes decreased in a near exponential manner with increasing depth, as has been described in the literature (Hedley et al., 2012b; Botha et al., 2013). Increasing the water turbidity also reduces the number of separable classes dramatically with increasing depth. With HICO spectral bands, 13 classes can be optically distinguished at 5 m depth for water type 1 (48 m Secchi depth, Figure 5.7a), whereas only 11, 6 and 2 classes are separable for water types 2, 3 and 4 (Secchi depths of 13, 6.2 and 2 m) respectively at that depth. The water column saturation point, that is, where the water column contributes to nearly all of the water leaving radiance, is located when none of the benthic classes can be distinguished (i.e., number of classes = 1). For water types 2, 3 and 4 these occur at depths 20 m, 12 m and 5.5 m respectively using HICO bands.

Decreasing the number of spectral bands also increases the slope of the exponential curve as illustrated when comparing Figures 5.7a (HICO) and 5.7c (WV2). For water type 3 at 3 m depth the HICO, HyMap and WV2 wavebands, according to the HDC, can distinguish 12, 11 and 5 classes respectively. Increasing the depth to 5

m reduced the number of classes to 6, 6 and 3 respectively. For depths less than the water column saturation point, the five WV2 bands between 400 and 680 nm can generally separate half as many benthic classes as HICO. Based on the modelling shown in Figure 5.7 and a comparison between the exponential slopes, there appears to be minor differences in the number of classes distinguishable at depth between HICO and HyMap wavebands. In this analysis, wavelengths between 400 and 680 nm were used which reduced the number of bands to 49 and 16 for HICO and HyMap respectively. This may seem like a large reduction of wavebands without greatly affecting the benthic separability. We should note that unlike HICO, HyMap does not have bands below 450 nm (Kruse, Broadman, Lefkoff, Young, & Kierein-Young, 2000), hence both sensors have wavebands that emphasize the spectral differences between the benthic classes analysed. The literature has shown that specific wavelength ranges predominantly within 520–680 nm are useful for identifying substrate types, such as healthy coral, bleached coral, seagrass, sand and algae (Call et al., 2003; Holden & LeDrew, 1998; Fyfe, 2003; Clark, Mumby, Chisholm, Jaubert, & Andrefouet, 2000; Hochberg & Atkinson, 2000). Therefore, it is likely that the difference in bandwidth is the cause where the spectral resolution of HICO and HyMap are 5.7 and 15 nm (Kruse et al., 2000) respectively. This is in line with what Hochberg and Atkinson (2003) showed where the separation of coral, algae and sand using LDA were nearly identical for spectra at 10, 5.5 and 1 nm spectral resolutions.

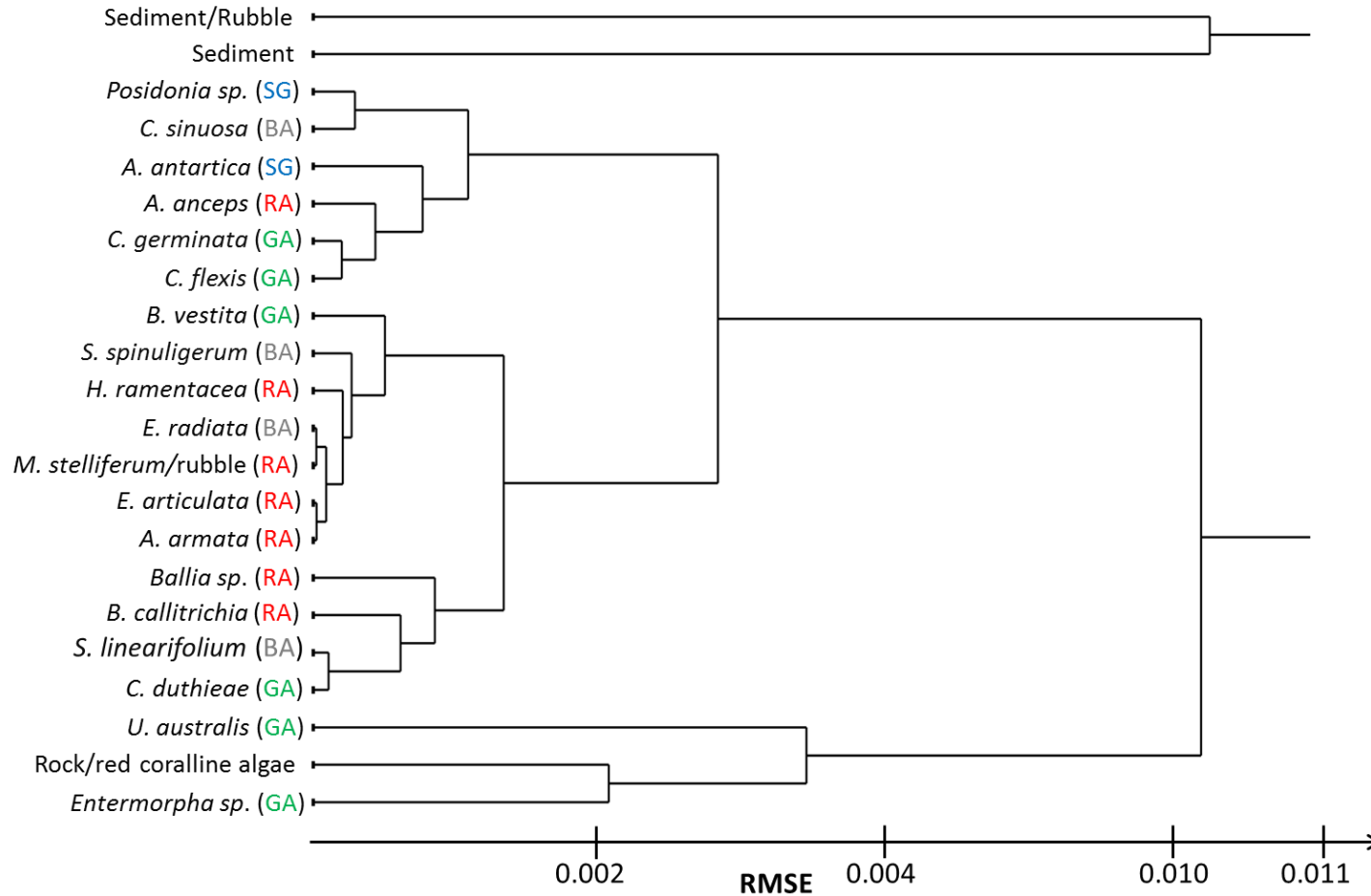


Figure 5.6: Dendrogram from the LDHC of modelled r_{rs} spectra using HICO's spectral bands. The water column was modelled with depth 15 m and $P=0.05$, $G=0.1$ and $X=0.010 \text{ m}^{-1}$. Here the iterative selection of eigenvectors chose only one eigenvector.

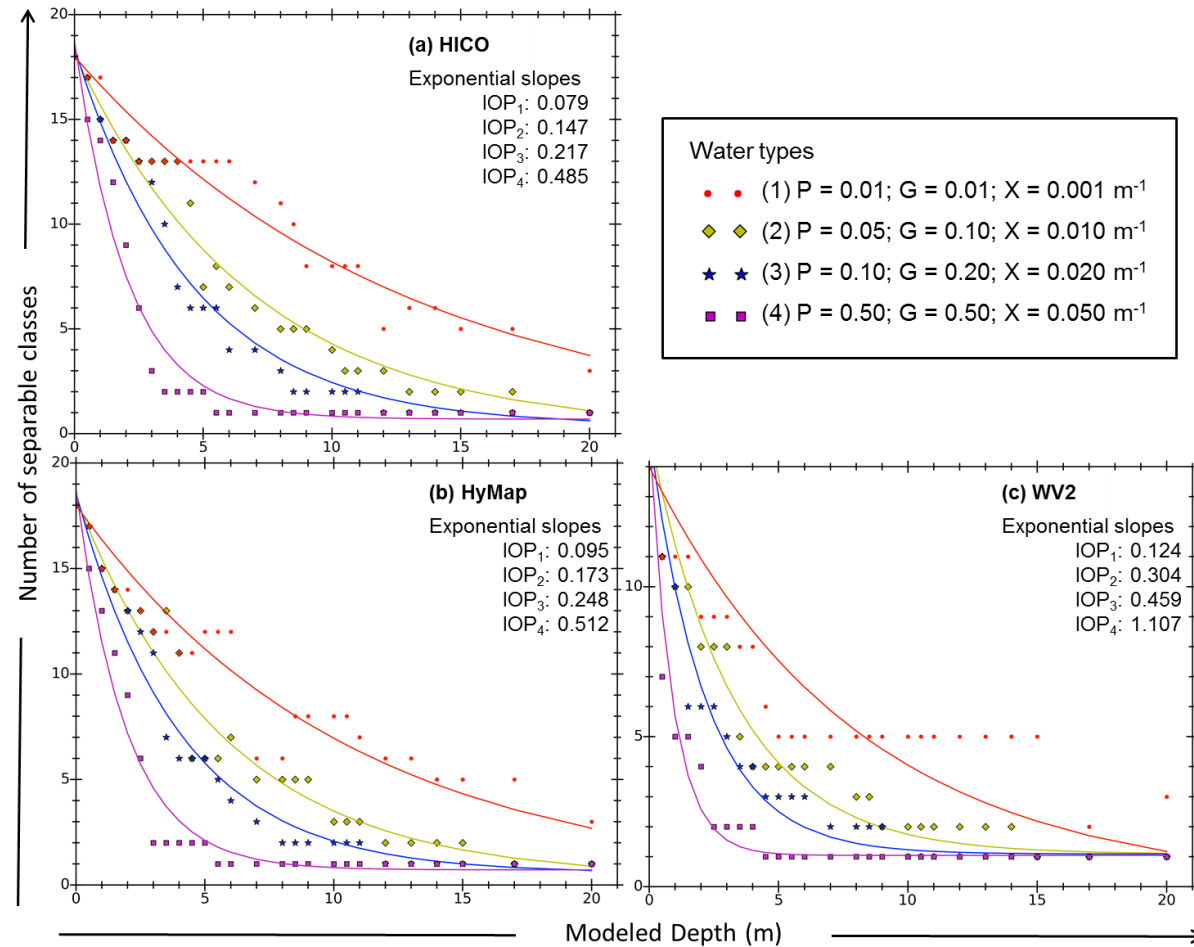


Figure 5.7: Number of optically separable classes vs. depth using the spectral bands and resolutions for (a) HICO; (b) HyMap, and; (c) WV2. Four water-columns were modelled with varying water turbidity representing very clear to turbid waters. The exponential curves were derived through a least squares fit.

Table 5.2: The classes from the HICO spectral libraries at depths 3-6 m using water column optical properties of $P = 0.01 \text{ m}^{-1}$, $G = 0.01 \text{ m}^{-1}$, and $X = 0.001 \text{ m}^{-1}$. The superscripts represent the number of species that form that cluster, for example mixed brown algae⁴ means that four brown algae species were merged to form one mixed brown algae class. The spectral libraries at 5 and 6 m depth are identical.

Depth (m)	3	4	5	6
N°. Eigenvectors	6	7	6	7
N°. Classes	13	13	13	13
Clusters	1. Brown algae ⁴ /seagrass ² /green algae ⁴ class; 2. Sediment; 3. Sediment-Rubble; 4. Rock-red coralline algae; 5. <i>Enteromorpha</i> sp. (GA); 6. <i>U. australis</i> (GA); 7. <i>E. articulata</i> (RA); 8. <i>M. stelliferum</i> (RA); 9. <i>Ballia</i> sp. (RA); 10. <i>H. ramentacea</i> (RA); 11. <i>A. armata</i> (RA); 12. <i>B. callitrichia</i> (RA); 13. <i>A. anceps</i> (RA).	1. Brown algae ⁴ /seagrass ² /green algae ⁴ class; 2. Sediment; 3. Sediment-Rubble; 4. Rock-red coralline algae; 5. <i>Enteromorpha</i> sp. (GA); 6. <i>U. australis</i> (GA); 7. <i>E. articulata</i> (RA); 8. <i>M. stelliferum</i> (RA); 9. <i>Ballia</i> sp. (RA); 10. <i>H. ramentacea</i> (RA); 11. <i>A. armata</i> (RA); 12. <i>B. callitrichia</i> (RA); 13. <i>A. anceps</i> (RA).	1. Brown algae ² /seagrass ² /green algae ⁴ class; 2. <i>E. radiata</i> / <i>C. sinusoa</i> brown algae class; 3. Sediment; 4. Sediment-Rubble; 5. Rock-red coralline algae; 6. <i>Enteromorpha</i> sp. (GA); 7. <i>U. australis</i> (GA); 8. <i>E. articulata</i> / <i>M. stelliferum</i> red algae class; 9. <i>Ballia</i> sp. (RA); 10. <i>H. ramentacea</i> (RA); 11. <i>A. armata</i> (RA); 12. <i>B. callitrichia</i> (RA); 13. <i>A. anceps</i> (RA)	1. Brown algae ² /seagrass ² /green algae ⁴ class; 2. <i>E. radiata</i> / <i>C. sinusoa</i> brown algae class; 3. Sediment; 4. Sediment-Rubble; 5. Rock-red coralline algae; 6. <i>Enteromorpha</i> sp. (GA); 7. <i>U. australis</i> (GA); 8. <i>E. articulata</i> / <i>M. stelliferum</i> red algae class; 9. <i>Ballia</i> sp. (RA); 10. <i>H. ramentacea</i> (RA); 11. <i>A. armata</i> (RA); 12. <i>B. callitrichia</i> (RA); 13. <i>A. anceps</i> (RA)

Table 5.3: The classes from the HyMap spectral libraries at depths 3-6 m using water column optical properties of $P = 0.01 \text{ m}^{-1}$, $G = 0.01 \text{ m}^{-1}$, and $X = 0.001 \text{ m}^{-1}$.

Depth (m)	3	4	5	6
No Eigenvectors	4	4*	5	5
No Classes	12	11	12	12
Clusters	1. <i>E. articulata</i> / <i>M. stelliferum</i> red algae class; 2. Mixed brown algae ⁴ ; 3. Mixed seagrass ² /green algae ⁴ ; 4. Sediment-Rubble/Sediment; 5. <i>Enteromorpha</i> sp.; 6. <i>U. australis</i> ; 7. Rock-red coralline algae; 8. <i>Ballia</i> sp.; 9. <i>H. ramentacea</i> ; 10. <i>A. armata</i> ; 11. <i>B. callitrichia</i> ; 12. <i>A. anceps</i>	1. <i>E. articulata</i> / <i>M. stelliferum</i> red algae class; 2. <i>E. radiata</i> / <i>C. sinusoa</i> brown algae class; 3. Brown algae ² /seagrass ² /green algae ⁴ class; 4. Sediment-Rubble/Sediment; 5. <i>Enteromorpha</i> sp./ <i>U. australis</i> green algae class; 6. Rock-red coralline algae; 7. <i>Ballia</i> sp.; 8. <i>H. ramentacea</i> ; 9. <i>A. armata</i> ; 10. <i>B. callitrichia</i> ; 11. <i>A. anceps</i>	1. <i>E. articulata</i> / <i>M. stelliferum</i> red algae class; 2. <i>E. radiata</i> / <i>C. sinusoa</i> brown algae class; 3. Brown algae ² /seagrass ² /green algae ⁴ class; 4. Sediment-Rubble; 5. Sediment; 6. <i>Enteromorpha</i> sp./ <i>U. australis</i> green algae class; 7. Rock-red coralline algae; 8. <i>Ballia</i> sp.; 9. <i>H. ramentacea</i> ; 10. <i>A. armata</i> ; 11. <i>B. callitrichia</i> ; 12. <i>A. anceps</i>	1. <i>E. articulata</i> / <i>M. stelliferum</i> red algae class; 2. <i>E. radiata</i> / <i>C. sinusoa</i> brown algae class; 3. Brown algae ² / seagrass ² /green algae ⁴ class; 4. Sediment-Rubble; 5. Sediment; 6. <i>Enteromorpha</i> sp./ <i>U. australis</i> green algae class; 7. Rock-red coralline algae; 8. <i>Ballia</i> sp.; 9. <i>H. ramentacea</i> ; 10. <i>A. armata</i> ; 11. <i>B. callitrichia</i> ; 12. <i>A. anceps</i>

*six eigenvectors generated 12 classes identical to those at 5 and 6 m.

The number of classes within a spectral library can be stratified with depth, for instance using water type 1, the spectral library for WV2 (Figure 5.7c) has the same number of classes from 5 m to 15 m. Stratification in the number of classes is expected as they are integer values and hence more emphasized in slowly decreasing curves and less observed in areas of rapid change (e.g., 0–3 m depth of Figure 5.7b for water type 3). Analyses of the spectral libraries from all three sensors within the stratified regions of a given water type indicate that at >5 m the output classes produced are identical though subtle differences exist in the RMSE of when classes merge. At shallower depths, however, the spectral libraries in the stratified regions have minor differences in the classes that merge and thus in the output classes. For HICO spectral bands 13 classes were generated in the stratified region between 3 and 6 m depth with water type 1. The spectral libraries at 3 and 4 m are identical as are the spectral libraries at 5 and 6 m (Table 5.2). Between these two sets of spectral libraries the following differences occur: (1) the brown alga *E. radiata* and *C. sinuosa* from the mixed vegetation class (at 3 m) split to form an individual mixed brown algae class; and (2) the union of *E. articulata* and *M. stelliferum* (Table 5.2).

The classes from the HyMap spectral libraries for depths 3 to 6 m with water type 1 are given in Table 5.3. A stratified region (Figure 5.7b) is formed in this depth range and water type, where 12 classes are optically separable at 3, 5 and 6 m depth. At 3 m depth four species of brown algae merge to form one cluster, however at 4, 5 and 6 m two of those brown algae species (*E. radiata* and *C. sinuosa*) form a separate mixed class and the other two merge into a mixed brown algae/green algae/seagrass class (Table 5.3). Other differences include: (1) the separation of the Sediment-Rubble/Sediment class (3 and 4 m) to their individual class at 5 and 6 m; and (2) the union of the green alga *Enteromorpha* sp. and *U. australis* at >3 m depth. Some clusters are consistently generated within this depth range which include Rock-red coralline algae and six red algae classes *E. articulata*/*M. stelliferum*, *Ballia* sp., *H. ramentacea*; *A. armata*; *B. callitrichia*, and *A. anceps*. Indeed each spectral library between 3 and 6 m has six red algae classes, >1 sediment class, >1 green algae class and a mixed vegetation class. At 4 m depth the HDC procedure generated 11 classes using three eigenvectors, analysis has shown that using six eigenvectors facilitates the separation of 12 classes identical to that produced at 5 and 6 m (Table 5.3). Here six eigenvectors were not used because the fourth and fifth eigenvectors did not increase the number of clusters generated and thus the iterative eigenvector selection procedure chose the first

three. Like for HICO (Table 5.2) there are minor differences between spectral libraries in these stratified regions, as such we propose the use of a single spectral library for such regions.

5.4.3 Resolving seagrass species from algae

An important ecological application of optical remote sensing is mapping seagrass meadows (Roelfsema et al., 2013). Using the HDC algorithm, we consider the clustering accuracy, sensor spectral resolution, water column depth and optical properties that enable the optical distinction of the seagrass species *A. antarctica* from green and brown alga. Figure 5.8 shows the modelled depth at which we can no longer resolve *A. antarctica* from the green algae species (Table 5.1) for clear to turbid water clarities (water types 1 to 4 respectively) using the different sensors. Thus for HICO bands *A. antarctica* is optically distinguishable from green algae to a depth of approximately 4.25 m at 90% clustering accuracy for a clear water column (water type 1, Figure 5.8a). Beyond this depth at 90% accuracy *A. antarctica* cannot be spectrally distinguished. Note that the results for WV2 in Figure 5.8c relates to the ability of distinguishing *A. antarctica* from the *Posidonia* sp./green algae cluster, as the latter seagrass species could not be resolved using bottom reflectances (Figure 5.8).

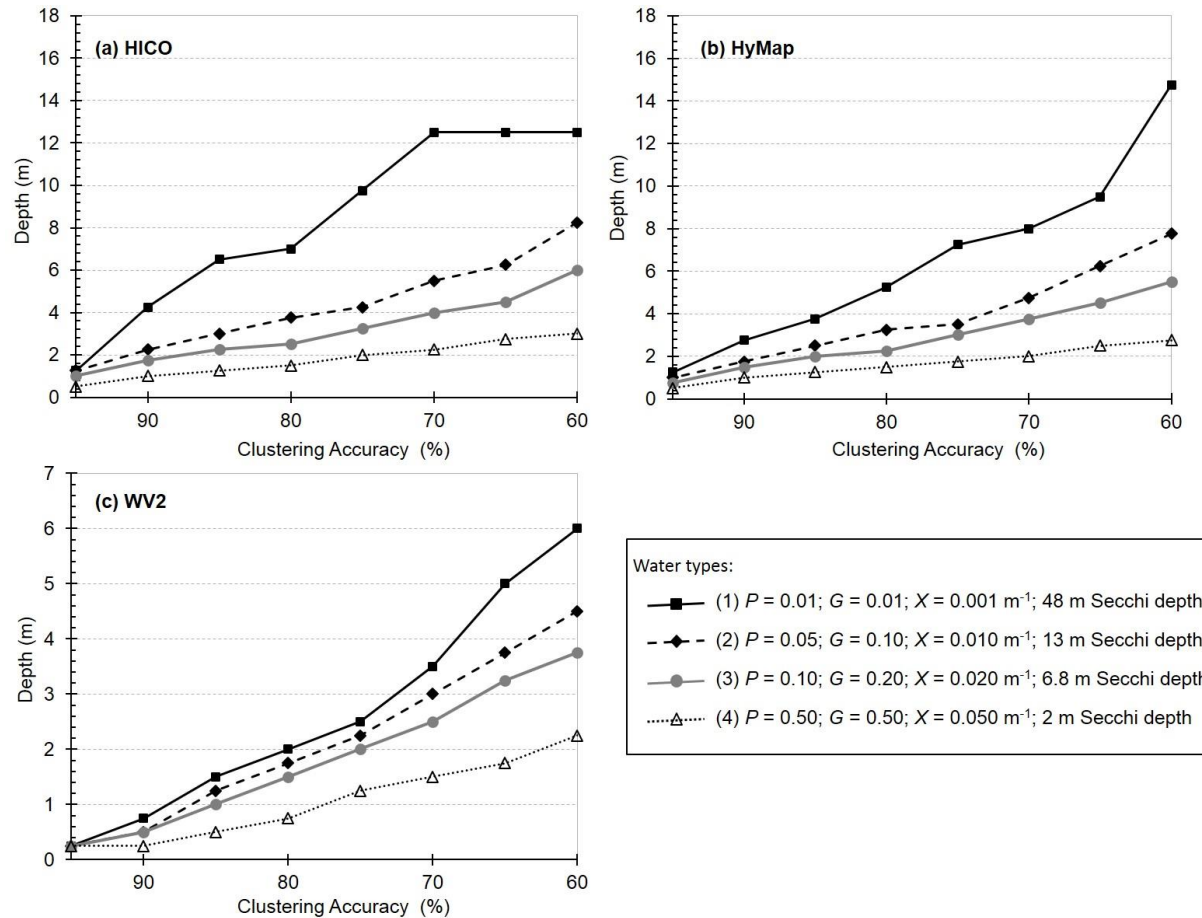


Figure 5.8: The estimated modelled depth (m) at which *A. antarctica* can no longer be distinguished from green algae at various clustering accuracies for (a) HICO; (b) HyMap, and; (c) WV2 wavebands. Clear (water type 1) to turbid (water type 4) water clarities were modelled. The depths given here are estimates as the clustering at every 0.25 m depth increment were analysed.

For a given water type, decreasing the clustering accuracy enables the ability to spectrally resolve seagrass from green algae to greater depths. The reason being that the HDC allows for greater misclassification proportion between pairs of classes before they are considered “indistinguishable”. For example, using HyMap bands *A. antartica* can be distinguished at 2.5 and 3.75 m for water type 2 at 85% and 75% clustering accuracies respectively (Figure 5.8b). Therefore if the user desires the ability to map *A. antartica* up to a depth of 4 m with HyMap, then 75% clustering accuracy should be used for water columns with Secchi depths greater than 13 m. A reduction of the water clarity also decreases the ability to resolve species at depth, as observed by the ability of WV2 to distinguish *A. antartica* to 2 m and 0.75 m for water types with Secchi depths 48 and 2 m (Figure 5.8c) respectively at 80% accuracy. Therefore as the modelled water depth or turbidity is increased the distances between classes decreases such that neighbouring classes experience more overlap (Hedley et al., 2012b). Hence a greater τ_m accounts for the decrease in the inter-class distance, where classes are considered optically distinct despite their increase in overlap. We have low confidence for results that used clustering accuracies less than 70% as, for example, HyMap bands can distinguish *A. antartica* to 2.25 m for water type 4 (Figure 5.8b) that has an estimated Secchi depth of 2 m.

The advantage of using hyperspectral sensors is clearly demonstrated in Figure 5.8, where HICO and HyMap have the ability to resolve seagrass from green algae to much greater depths for a given clustering accuracy and water clarity compared to WV2. Indeed at 85% clustering accuracy, HICO and HyMap spectral bands can distinguish *A. antartica* to an estimated depth of 6.5 and 3.75 m respectively for water type 1 (48 m Secchi Depth), whilst WV2 can only resolve it to a depth of 1.5 m. On average HICO bands can detect *A. antartica* to depths 2.7 times greater than WV2 bands across the clustering accuracies and water types. In most conditions analysed there is close similarity in the depth limits at which *A. antartica* can be resolved using HICO and HyMap bands, where on average HICO can detect this species to depths 1.2 times greater than HyMap.

The ability to spectrally resolve mixed seagrass/green algae from brown algae was analysed for the same conditions presented in Figure 5.8. However, a direct comparison between seagrass and brown algae was not possible for HICO, HyMap and WV2 at any of the water column conditions presented. The reason being that *Posidonia* sp. and *A. antartica* both merge with a mixed green algae class. This

seagrass/green algae mix then clusters with a mixed brown algae class at deeper depths. The distinction between mixed seagrass/green algae and brown algae (effectively between green and brown coloured benthic species) follows the same trend as that presented in Figure 5.8 expect that they can be distinguished to much deeper depths.

5.4.4 Implications to shallow water habitat mapping

Modelling for a variety of water turbidities and depth as displayed in Figure 5.7 enables predictions on the number and type of benthic classes that can be expected from a hyperspectral or multispectral image at a constant clustering accuracy. The level of accuracy can be changed according to the needs of the user or application with corresponding changes to the number and type of benthic classes defined by the HDC. Figure 5.9 illustrates that the number of optically separable classes increases as the clustering accuracy decreases for a constant set of water column optical properties at HICO wavebands. These results are similar to those produced by Andrefouet et al. (2003) where the thematic accuracy decreased with increasing number of habitat classes used in the benthic classification scheme. Although thematic and clustering accuracy are applied in different contexts, Figure 5.9 does imply that if a benthic habitat map at a constant classification accuracy is required, then the number of classes used in the classification scheme must change with the range of depths and water column optical properties within an image. Prior knowledge of the depth and optical properties in a given scene therefore becomes a requisite in applying the HDC algorithm. Note the depth, P , G , and X can be determined by applying a shallow water inversion model for sensors with enough spectral bands in the visible (Lee et al., 1999; Klonowski et al., 2007). Here the full benthic spectral library could be used solely to optimize these parameters.

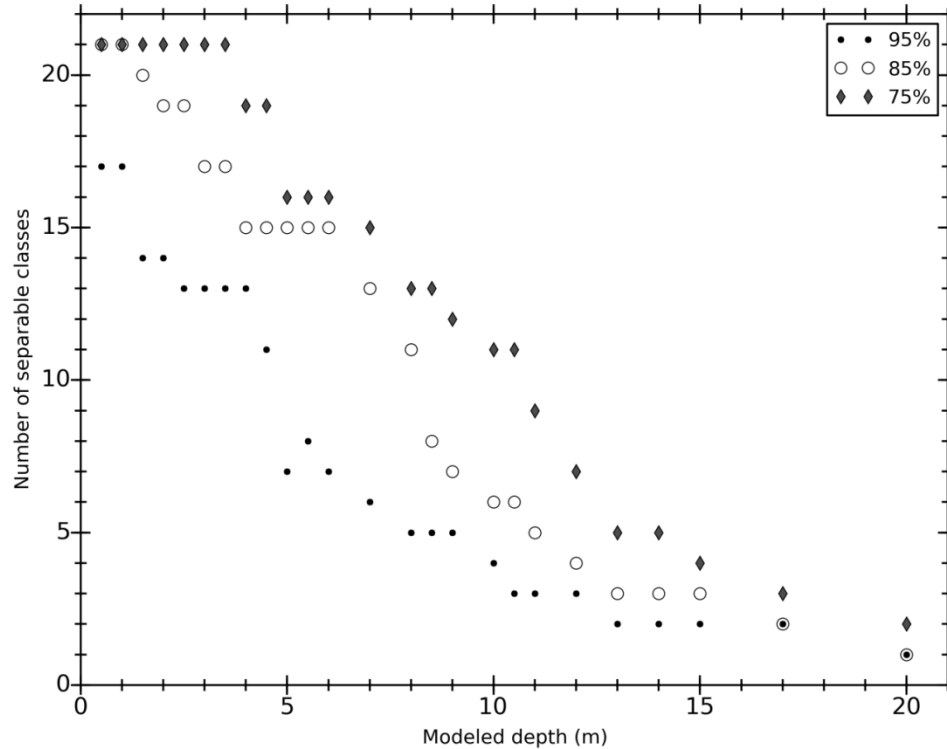


Figure 5.9: Number of optically separable classes vs. depth at three different clustering accuracies using the spectral bands and resolutions for HICO. The water column was modelled with $P=0.05$, $G=0.1$ and $X=0.010 \text{ m}^{-1}$.

Benthic classifications of remotely sensed imagery using physics-based inversion models to date have used a spectral library of representative benthic species (fine descriptive resolution, see Dekker et al., 2011). Depending on the shallow water model used, the inversion process iterates through unique combinations of benthic mixtures and optimizes for their fractional coverage, water column optical properties and depth. The benthic combination and fractional coverage that generated the best fit to the input reflectance are assigned. Therefore distinct benthic species would be assigned to image pixels at any given depth and water column optical property, no matter if it were unlikely to distinguish one benthic species from another.

The research presented here indicates that this type of benthic classification may not be appropriate, particularly when mapping regions of varying water depths or when propagating sensor and environmental noise in the inversion scheme (Hedley et al., 2010; Hedley et al., 2012a; Hedley, 2013). This can be illustrated by the dendrogram presented in Figure 5.6, where the at-surface spectral differences between the benthic vegetation species do not make observable differences to r_{rs} above the total

system noise at the depth and P , G and X modelled. Clearly if a spectral library consisting of the initial 22 benthic classes were used for an inversion of say a pixel having 100% coverage of *E. radiata* with P , G , X and depth used in Figure 5.6; then accordingly a shallow water inversion model would likely not be able to distinguish the forward modelled r_{rs} derived from *E. radiata* from any other benthic vegetation species when $NE\Delta r_{rs}$ is incorporated. In this situation it is likely that equal probability of assignment across the benthic vegetation classes will result. This was illustrated in Figure 5 by Hedley et al. (2012a) where the uncertainty of the bottom type increased with depth and increasing number of endmembers in the spectral library. Furthermore, the assignment of a specific benthic species (even correctly identified *E. radiata*) cannot be made with sufficient certainty, and a classification assignment of “mixed vegetation” would be more appropriate for these optical properties and depth. In fact such a class name would convey that level of uncertainty and lack of spectral separability. Indeed, analysis of HDC-derived output classes has showed that as the water column becomes more turbid or deeper, the ability to distinguish distinct benthic species is lost, where resultant classes consist of mixed clusters. Again in these situations, assigning the appropriate mixed cluster would help convey the level of certainty and optical separability into the classification scheme.

Presently the HDC algorithm assumes 100% substrate coverage of a pixel and as a post-inversion tool would be suited for high spatial resolution image data. In addition, its application would be more appropriate towards constraining the benthic classification of the HOPE inversion model (Lee et al., 1999), if the endmembers of a high descriptive resolution spectral library were cycled through during the optimization process. Note that the HOPE model considers one substrate endmember rather than a linear mixture of two (Brando et al., 2009) or three (Klonowski et al., 2007). The requirement of moderate to high spatial resolution image data does limit the applicability of the HDC algorithm as a post-inversion tool to mostly airborne sensors such as AISA Eagle, HyVista’s HyMap, CASI-2, AVIRIS and Ocean PHILLS. From the current and planned satellite sensors, WV2, Sentinel-2 and VENμS SSC (Crebassol et al., 2010) possess high spatial resolution (≤ 10 m) and enough spectral bands in the visible domain to facilitate optimization using current shallow water inversion models (e.g., Hedley et al., 2012a; Lee, Weidemann, & Arnone, 2013).

Analysis has showed that the HDC-derived water column specific libraries are sensor and scene specific. Sensor specific because the number and type of HDC-

derived benthic classes depend on the sensor's spectral resolution and signal to noise ratio. Scene specific because: (1) the environmental noise in the imagery, such as sunglint which even if corrected (Hedley et al., 2005) leaves residual spatial noise; and (2) The number and type of output classes are dependent on the representative benthic species present. The latter is implied by the clustering of the seagrass *Posidonia* sp. and the green algae *C. germinata*, *C. flexis* and *B. vestita* at WV2 bands (Figure 5.5). If none of the green algae species were present in the scene then *Posidonia* sp. would be spectrally distinct, and would lead to different benthic class mixtures.

As the clustering is based on LD coordinates the ability to distinguish individual classes potentially decreases when the number of initial classes increase. This is illustrated in Figure 5.10, which shows the LD coordinates of the four brown algae *E. radiata*, *S. linearifolium*, *S. spinuligerum* and *C. sinuosa*. Three clusters resulted when the ρ_b spectra (at HICO bands) of these four brown algae species were passed through the HDC algorithm (see Figure 5.10). Recall that two brown algae clusters were considered distinct (*S. linearifolium*/*S. spinuligerum*/*C. sinuosa* and *E. radiata*) when the initial spectral library of 22 classes were passed through the HDC (see dendrogram in Figure 5.3a). The reason for this is that the LDA seeks a projection that maximises the distance between classes whilst minimising the within-class variance (Lachenbruch, Sneeringer, & Revo, 1973; Hastie, Tibshirani, & Friedman, 2009). Thus in the case of Figure 5.10, an optimal projection was found that enabled the distinction of three brown algae clusters. These results imply that only a minimal set of initial benthic classes should be used in the clustering.

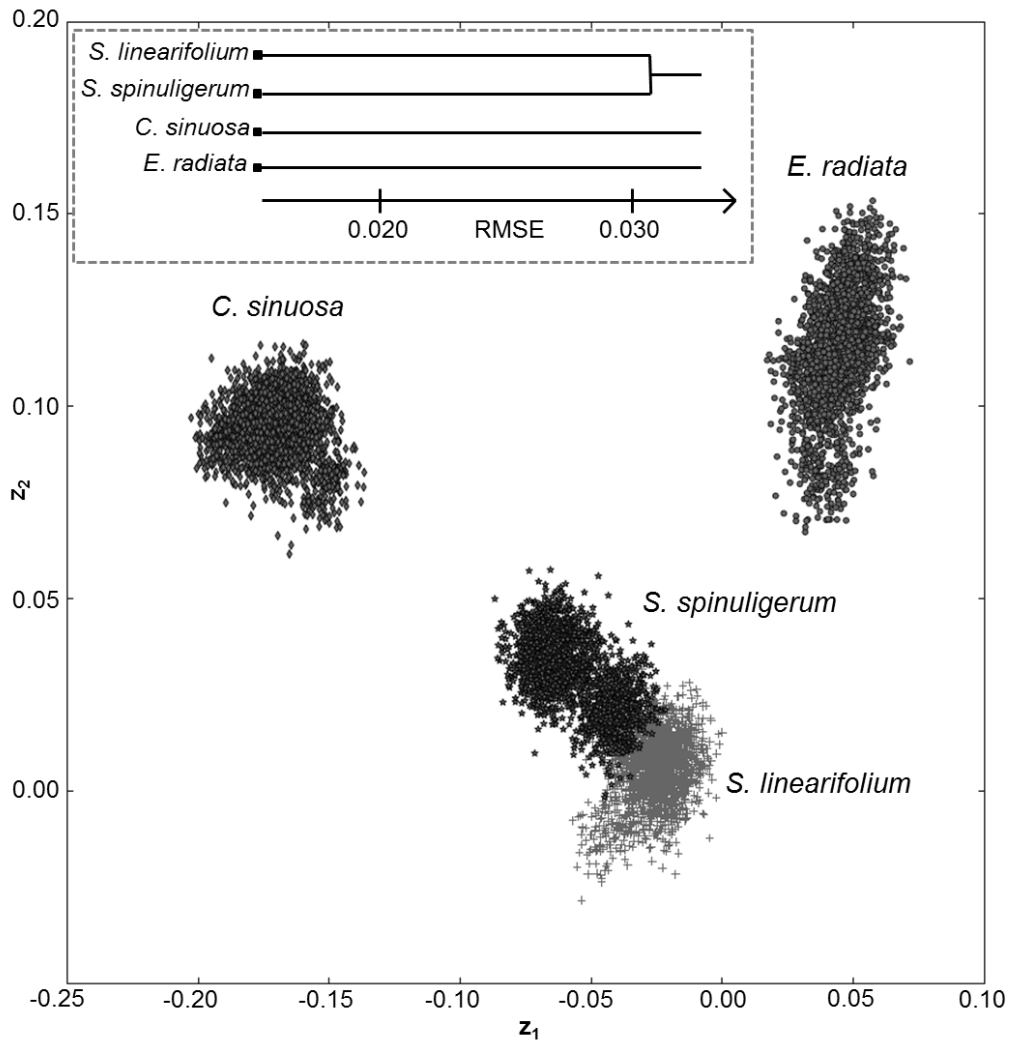


Figure 5.10: LD coordinates of the four brown algae species using HICO wavebands. The HDC-derived dendrogram is shown on the top left corner. Here one eigenvector (z_1) allowed the optimal distinction of the following three clusters: (1) *S. linearifolium*/*S. spinuligerum*; (2) *E. radiata*, and (3) *C. sinuosa*.

Although a sensor's spectral characteristics, total system noise and water column attenuation affect substrate separability; spatial resolution, not accounted by the HDC algorithm, also plays a significant role. Particularly since coastal and coral reefs can be spatially heterogeneous, where a diverse array of spectrally distinct substrates can occur at sub-meter scales (Hedley, 2013). Previous research involving thematic mapping and Object-Based Image Analysis of coral reefs has shown improved benthic classification using imaging platforms with high spatial resolution (<10 m) compared to those with moderate resolution (30 m) (Benfield et al., 2007). Thus although a sensor, such as HICO, with high spectral resolution can spectrally discriminate between many benthos to deeper depths, its spatial resolution (~90 m)

will significantly affect the ability to resolve individual substrates compared to HyMap or even WV2 with resolutions less than 10 m. For moderate spatial resolution sensors broad classification of pixels into key substrate components would be a more feasible approach (e.g. Klonowski et al., 2007; Goodman & Ustin, 2007).

As a final note, a sensor's radiometric calibration and the atmospheric correction can significantly affect the accuracy of the retrievals from inversion models (Dekker et al., 2011), and hence on subsequent results from the HDC-algorithm as a post-inversion tool. Image pre-processing steps have been used, prior to shallow water inversion models, to minimise the effect of residual under- or over-atmospheric correction (Klonowski et al., 2007; Lee et al., 2001). In Klonowski et al. (2007) the R_{rs} of an image were vertically shifted to make $R_{rs}(750) = 0$, this approach was later modified where the R_{rs} were subtracted by the median value between 650 and 800 nm (Dekker et al., 2011). In Lee et al. (2001) the R_{rs} were adjusted by setting the $R_{rs}(750)$ to a value computed from an empirical relationship. These approaches are therefore useful if the atmospheric parameters were assumed constant for an image and the atmospheric correction produced a systematic offset. Atmospheric correction that deduce atmospheric parameters per-pixel can potentially use different aerosol models in an image and thereby cause variation in the spectral shape of the derived R_{rs} . If imprecise the pre-processing steps will not be able to account for an incorrect spectral shape of the R_{rs} . Radiometric sensor calibration can also significantly affect both the shape and offset of sensor-derived R_{rs} . Indeed, Lewis, Gould, Weidemann, Ladner, and Lee (2013) showed substantial improvement in match ups between *in situ* and HICO-derived water leaving radiance after vicarious calibration. Minimising errors from calibration and atmospheric correction is particularly crucial over dark targets such as deep water or submerged aquatic vegetation. This is due to a reduced signal-to-noise ratio and where a higher proportion of the at-sensor radiance is contaminated by the atmospheric path radiance compared to bright shallow targets. Hence small errors in the calibration or deviations of the actual atmospheric parameters compared to what is used during atmospheric correction can produce negative reflectances (Richter, 1990; Jacobsen, Heidebrecht, & Goetz, 2000; Moses, Bowles, & Corson, 2015). Improvements to a sensor's SNR, accurate calibration and atmospheric correction will lead to improved benthic classification from shallow water inversion models. We note that the use of the HDC algorithm to examine the ability of spectrally resolving a set

of representative substrates for various environmental conditions takes into account noise introduced from inaccurate atmospheric or sunglint correction.

5.5 Conclusions and future work

We have presented an agglomerative hierarchical clustering using linear discriminant coordinates (HDC), which when used on a spectral library of benthic endmembers outputs those classes that are optically distinguishable above the total system's variability. The HDC clustering differs from other hierarchical clustering schemes by the inclusion of the system's total variability onto each data point and the clustering based on pairwise distance and misclassification proportions. The iterative merging of classes in the HDC ceases when the remaining classes have a misclassification rate below a user specified threshold. Thus the user does not need to decide beforehand or post-clustering the number of classes to output – a common problem faced in the application of clustering procedures. Rather the total system's variability controls this outcome where a noisier system would lead to fewer output classes for a given misclassification threshold and vice-versa. In the context of benthic classification from shallow water remote sensing, variability arises from the sensor and environment (imperfect atmospheric, sunglint and air–water interface corrections) and the spectral variability observed within a given benthic species. Both sources degrade the spectral separability between benthic classes.

The HDC was applied to a set of measured reflectance spectra of 22 benthic classes collected from the Point Peron study site, Western Australia. This initial spectral library contained the sub-local scale spectral variability of each benthic class and with the addition of sensor and environmental noise taken from a HICO image, accounted for the total system's variability. Analysis of the clustering on datasets convolved to the wavebands of WV2, HyVista's HyMap and HICO sensors showed a reduction in spectral resolution reduced the spectral separability between classes and hence reduced the number of distinct classes. For instance, at WV2 and HICO wavebands 14 and 18 classes were spectrally separable just below the water's surface respectively, from the initial 22. Dendrograms from the HDC have showed that benthic species from a given genera preferentially merge first before clustering with species of other genera.

Depth and water column turbidity have been demonstrated in the literature as the most influential factor inhibiting benthic classification, where fewer classes are optically separable with increasing depth and/or turbidity. Using the measured benthic reflectance spectra, a shallow water forward model was used to simulate the water-leaving subsurface reflectance at any specified depth and water column optical property. Combined with the HDC, depth and water column specific spectral libraries were generated and subsequent analysis have quantified that the number of benthic classes decreases with increasing depth and water column turbidity at a constant clustering accuracy. Furthermore, the clustering analysis identifies those benthic classes that merge as a consequence of water column attenuation and the total system's noise.

If the irradiance reflectance spectra of the representative benthos in a scene of interest are known, then the HDC algorithm offers the ability to explore the potential of benthic classification from shallow water remote sensing, where the number and type of classes can be quantified for any given sensor, clustering accuracy, water column optical property and depth. From a management perspective, the HDC can be used to pre-determine which sensor to use so that the mapping requirements match the expected outcomes from the resultant benthic classification map. This was illustrated through the analysis of conditions that include clustering accuracy, water clarity and depth and spectral resolution that enable *A. antarctica* to be spectrally resolved from benthic algae. Such an analysis can aid in an assessment of the feasibility of detecting phase shifts in seagrass meadows, for example, from a variety of sensors; but does not incorporate the effect of spatial resolution, which can decrease spectral distinctions. In situations where local knowledge of the spectral library is absent then the algorithm presented here cannot be applied, as the derived class names are scene specific.

Further research includes the validation of the HDC algorithm with vertical profiling optical measurements and above water radiometry. Such studies would include a comparative analysis of the clustering algorithm to optical measurement based cluster dendrograms using the rand index (Rand, 1971) or cophenetic correlation (Sokal and Rohlf, 1962), in an analogous manner to Torrecilla et al. (2011). Further development includes the application of the HDC-derived spectral libraries into physics-based shallow water inversion models. The purpose of which would be to obtain a benthic classification map with more appropriate class names that help convey the level of certainty and optical separability. It is likely that the resultant benthic

classification map will be depth dependent (and hence layered), as the class names (and numbers) change with depth. Change detection is also an avenue of future research, particularly in assessing the amount of temporal change of a benthic species when it is not spectrally distinct at depth. In other words, assessing which benthic species/clusters we can detect temporal changes in. Mixed benthic assemblages typically occur at spatial resolutions greater than 2 m, how this affects benthic classification using HDC-derived spectral libraries should be investigated.

CHAPTER 6

CONCLUSIONS AND FUTURE WORK

6.1 Conclusions

The overall aims were to utilise uncertainty to examine the potential and limitations of bathymetry and benthic classification from hyperspectral remote sensing of shallow waters. In particular to (1) test the accuracy and precision of inversion model parameters including bathymetry, water column optical properties and benthic classification using the standard implementation of the Levenberg-Marquardt optimisation algorithm; (2) analyse bathymetry and its uncertainty to ascertain the potential and limitations of remote sensing in detecting temporal changes, and; (3) quantify the number and type of optically distinguishable benthic species above the total system noise and attenuating properties of a variable water column at depth in an effort to assess the limitations of benthic classification from remote sensing.

Bathymetry and benthic classification are typically derived through physics-based inversion models that utilise an optimisation procedure. Propagating uncertainty due to noise caused from the sensor and imperfect radiometric, sunglint and air-water interface corrections (environmental noise) is crucial in assigning confidence intervals to water column optical properties, bathymetry and benthic classifications. Thus the first aim was to test the accuracy and precision of inversion model parameters derived with the standard Levenberg-Marquardt optimisation when propagating sensor and environmental noise ($NE\Delta r_{rs}$).

Obtaining a true representation of the variability caused by $NE\Delta r_{rs}$ in parameter space is crucial in acquiring accurate and precise estimates of the desired geophysical parameter. Maximising the accuracy and correctly estimating the uncertainty is crucial for the correct ecological interpretation of remote sensing data. The research presented here shows that propagating sensor and environmental noise through a physics-based inversion model can cause low precision and accuracy (greater spread in parameter space) when a local optimisation procedure such as the Levenberg-Marquardt (LM) algorithm is used. This phenomenon was attributed to the

presence of local minima in the parameter space which local optimisation algorithms may converge.

Although global optimisation routines could be used to converge to the best 'local' if not global minimum in the constrained parameter space, they are often hampered by slow processing speeds compared to local optimisation procedures such as the LM algorithm. Computational efficiency is especially important with the added overhead of propagating uncertainty through the reflectance perturbation and inversion procedure used in this research. We present two new optimisation routines; the Update-Repeat Levenberg-Marquardt (UR-LM) and Latin Hypercube Sampling Levenberg-Marquardt (LHS-LM) algorithms. These two procedures dynamically search the parameter space for the optimal initial guess (i.e. starting point) that when used by the LM optimisation allows the convergence to the best 'local' or global minimum during the perturbation-inversion procedure. We have shown that the UR-LM and LHS-LM algorithms display improved computational speed, accuracy and precision in the derivation of bathymetry, and water column optical properties compared to the standard implementation of the LM algorithm.

Using the UR-LM, bathymetric imagery and associated uncertainty were computed from a time series of HICO imagery of Shark Bay, Western Australia, spanning nine months from November 2011 to August 2012. The overall goal was to assess the potential and limitations of remote sensing to detect temporal changes in depth that were the result of bottom sediment resuspension, transport and deposition. We focus on the Faure Sill, an ecologically important region within the Shark Bay World Heritage Area. Here the bathymetric uncertainty was used to statistically determine whether a change in depth was significant at the 95% confidence interval. Through this statistical analysis we have shown that temporal changes in depth as low as 0.40 m can be detected in shallow waters above the uncertainty and potential random offsets caused by imperfect radiometric corrections and tide normalisation. This analysis also indicated that detecting temporal changes in depth is only viable for shallow waters less than 6 m depth. At greater depths the magnitude of the reflectance signal becomes comparable to the spectral noise and as such bathymetric uncertainty becomes too large to detect temporal changes.

In addition to the temporal analysis, an image-based tide normalisation was developed specifically for a time series of bathymetric imagery. This algorithm minimises the bathymetric variability due to tide in depth in a multi-image dataset and

was shown to perform well in shallow water environments experiencing complex tidal oscillations. A per-pixel temporal statistical procedure was also developed to assess whether a change in depth is statistically significant above the uncertainty at two consecutive time stamps. This statistical analysis could potentially be applied to any ocean colour geophysical parameter and its uncertainty.

Quantifying the number and type of optically resolvable benthic classes above the total system uncertainty and attenuating properties of a water column at depth is crucial in assessing the *a priori* limitations and potential of remotely sensed benthic classification. Here the total system noise includes image-based sensor and environmental noise and the taxonomic spectral variability of individual benthic species. In this research a new hierarchical clustering procedure that uses linear discriminant coordinates (termed HDC) was developed that incorporates the total system noise to merge unresolvable benthic species, i.e. merge classes of higher descriptive resolution in order to obtain a spectral library of separable endmembers. A measure of separability between a pair of benthic classes based on misclassification proportions was used to identify which classes to merge. The clustering ceases when all benthic classes have a misclassification proportion above a user-defined threshold. Choosing such a threshold is a more intuitive approach rather than arbitrarily selecting the number of classes that the clustering should terminate – a common problem faced in current clustering algorithms.

For a given sensor's spectral resolution, the most influential factor prohibiting the optical distinction of benthic classes is the water column. As such we have incorporated a semi-analytical shallow water model to the HDC algorithm to account for the attenuating properties of a water column and depth on the ability to resolve benthic species. This coupled system enables the ability to determine *a priori* the limitations of benthic classification from remote sensing. This was demonstrated with an analysis of the conditions (i.e. clustering accuracy, depth, water column optical properties, sensor spectral resolution and total system noise) that enable the optical distinction of the seagrass *A. antarctica* from benthic algae. Such an analysis is important to match expectations with realistic deliverables based on the limitations of the remote sensing system.

We reiterate that the HDC algorithm is mainly suitable for either high spatial resolution imagery or sites whose benthos are spatially homogeneous and imaged with low spatial resolution. In both cases a given pixel would likely have low benthic

species variability. Thus although this research used the spectral resolution of HICO to exemplify the impact of high spectral resolution on the optical separability of benthic species; its 90 m spatial resolution will reduce HICO's ability to resolve benthic species for sites with high spatial heterogeneity. There are exceptions such as analysing whether it is possible to distinguish different seagrass species for sites that have extensive seagrass meadows e.g. Shark Bay, Western Australia, Florida Bay, USA and the Great Bahama Bank, Bahamas. Future hyperspectral satellite missions such as the EnMAP imager and HypsIRI with higher spatial resolutions may extend the applicability of more refined operational and routine benthic classification of shallow water ecosystems. Such sensors may have the necessary SNR and atmospheric bands that elicit improved benthic classifications, and a re-analysis of their capabilities should be investigated.

6.2 Future work and recommendations

This research reinforces the assumption that accuracy and precision of all parameters derived from physics-based inversion models, including bathymetry and benthic classification, are dependent, in part, on the quality of the radiometric corrections imposed on the at-sensor radiance. These corrections, if not performed adequately, can introduce spectral artefacts and/or offsets to the derived reflectance that are subsequently propagated through to the inversion products and manifest as a decrease in accuracy. We note that imperfect atmospheric and sunglint corrections add spatial noise (Hedley et al., 2005) to remote sensing imagery, from which $NE\Delta r_{TS}$ is derived. Thus, inaccurate corrections potentially introduce higher variability to the spatial noise, which would generate higher uncertainties in the inversion products.

Analysis of the retrieved model parameters ($P, G, X, H, B_1, B_2, B_3$) shows that their accuracy was degraded to typically less than 50% when propagating $NE\Delta r_{TS}$ through the inversion model (Table 4.3). This analysis utilised a dataset of forward modelled r_{TS} spectra, which prior to the addition of $NE\Delta r_{TS}$ did not contain any spectral artefacts that would affect accuracies of any retrieved parameter. The reduction in accuracy is attributed to the dispersal of inversion points in parameter space due to $NE\Delta r_{TS}$ (e.g. Figures 4.5 and 4.6) where the centroid (taken as the retrieved value) can be subsequently offset from the true parameter value. It follows that the larger the dispersal the more offset the centroid would be. Although a sensitivity analysis on how

the magnitude of $NE\Delta r_{rs}$ affects the accuracy of the retrieved model parameters was not performed, it is likely that reducing its magnitude would obtain more accurate retrievals. Given that the magnitude of $NE\Delta r_{rs}$ is computed from spatial noise caused by atmospheric and sunglint corrections. Future work should therefore focus on improving these correction algorithms particularly for HICO imagery that does not have any SWIR to IR bands to facilitate a per-pixel AOT retrieval.

To atmospherically correct HICO imagery with Tafkaa-6S (Chapter 3), the average AOT, ozone concentration and vertical column water vapour were computed from coincident MODIS overpasses. The HICO-derived remote sensing reflectances typically suffered from one of the following three spectral artefacts introduced from this atmospheric correction: (1) an increase in reflectance from 450 to 400 nm; (2) negative reflectances below 420 nm, or; (3) negative reflectances beyond 600 nm. The first two artefacts were likely caused from the wrong aerosol model or poor sensor radiometric calibration, where atmospheric correction gives negative reflectances. The third artefact was caused from over-estimating the AOT which has the effect of vertically shifting the aerosol reflectance. This latter artefact however was compensated by the sunglint correction algorithm specifically developed for the HICO dataset (see equation 3.4). This however is not ideal as sunglint and atmospheric correction are independent and their removal should be uncoupled. Further atmospheric algorithm development is therefore required for HICO and other hyperspectral sensors such as the AISA Eagle that do not have bands in the SWIR to IR. Validation with *in situ* radiometry for multiple sensors and sun-sensor viewing geometries using different atmospheric correction software – such as Tafkaa (Gao et al., 2000), FLAASH (Matthew et al., 2003) and HyCorr – coupled with the different sunglint corrections will give an understanding of which algorithm combination works best and why. An issue not discussed in this thesis is land adjacency effects and its correction. This phenomena is the result of multiple atmospheric scattering events where the upwelling radiance from land are scattered into the viewing angle of adjacent shallow water pixels causing contamination (Santer and Schmechtig, 2000). Sterckx, Knaeps and Ruddick (2011) showed that detectable land adjacency contamination to shallow water pixels can extend to more than 1 km from the shore using airborne hyperspectral imagery. This can represent a substantial amount of ecologically important pixels, and as such further methods of correcting for this effect should be investigated.

Methods for the application of the HDC-derived water specific benthic libraries to guide the classification of physics-based inversion models should also be pursued. To date, benthic classification from inversion models utilise a fine descriptive spectral library of benthic endmembers (see Dekker et al., 2011). The endmember or combination of endmembers that affords the best match to the input reflectance are assigned, regardless of whether the water column obscures the ability to distinguish between such classes. The HDC algorithm could therefore be used, in a post inversion analysis, to provide more appropriate benthic classification tuned to the water column optical properties and depth of each pixel. Specifically the retrieved depth and water column optical properties would be used to generate a list of optically separable benthic classes, which can appropriately modify the classification afforded by the inversion model. In this context appropriate benthic classification refers to the designation of class names such as ‘mixed vegetation’ or ‘mixed brown algae’ etc., and would convey to the user the limitation of physics-based inversion models with regards to benthic classification.

Analysis of the HDC-derived spectral libraries indicates that at certain depths and water clarities seagrass cannot be spectrally distinguished from green algae. However, most species of benthic algae preferentially grow on rock or hard substrates, whereas seagrass exclusively grow on soft sediment substrates. As such these two genera may not exist in the same region of the image, and this information may aid in distinguishing these two spectrally confused classes. Contextual editing has been used in coral reef mapping (see Mumby et al., 1997; Mumby et al., 1998; Benfield et al., 2007) to change the classification produced by per-pixel spectral analysis using a set of rules that are based on environmental variables such as depth, wave exposure, distance to land etc. In a comparison between Landsat and QuickBird sensors, Benfield et al. (2007) showed that contextual editing can improve the classification accuracy of those habitats for which rules are developed. Object-based image analysis (OBIA) in contrast has shown significant improvement in classification accuracy on both high and coarse spatial resolution imagery (Benfield et al., 2007). OBIA first segments the image into fine scale objects, and then pairs of neighbouring objects that produce the lowest increase in spatial heterogeneity are merged. Once a user defined threshold is met – which is scene, sensor and object specific (Benfield et al., 2007; Phinn et al., 2012) – the merging stops. The colour, size and shape of the objects are then used to assign them a classification using fuzzy logic and a set of predefined membership rules

(Benfield et al., 2007; Phinn et al., 2012). Combination of OBIA or contextual editing with benthic classification afforded from physics-based inversion models as a means of including spatial information to further the potential of optical remote sensing has yet to be analysed and should be studied.

This research has quantified that the type and number of optically distinguishable classes changes with both depth and water turbidity. As such it is likely that applying the HDC algorithm to an image that has varying depth and IOPs would result in a depth and water turbidity layered benthic classification map. Figure 5.7 showed that for a given IOP the spectral library can be stratified with depth, in other words the same list of optically distinguishable classes are produced for a range of depths. Hence the depth-layering can be discretised, where one layer could represent the benthic classification for the 4-7 m depth range for instance. Including a water turbidity layer as well could be providing too much information. Figure 5.7 suggested that for a given depth the changes in the number of optically separable benthic classes vary slowly with IOPs. Using HICO bands at 5.5 m depth, 12 and 8 classes were optically separable for water columns with Secchi Depths of 48 m and 13 m respectively (see Figure 5.7a). This large reduction in water clarity only reduced the number of classes by four. This implies that when modelling the number of optically distinguishable classes a single set of IOPs could be used – for instance the averaged derived IOPs from an image – thus avoiding a water turbidity layer. Future work should investigate the feasibility of this approach with the amount of information obtained and the usefulness of the resultant benthic classification, from a management perspective, on high spatial resolution hyperspectral imagery of shallow water environments. Focus should be placed on whether such benthic classification is suitable for managing and monitoring shallow water environments, and whether other forms of classification can be used in conjunction to provide management deliverables.

APPENDIX A

Figures A.1 to A.9 presents the inversion results, using the SLM, UR-LM and LHS methods for the HICO-derived r_{rs} spectra at pixel positions B (row 1083, col 212), C (row 1031, col 210) and D (row 1200, col 445). Figure A.10 illustrates how the uncertainties of the retrieved parameters (P , G , X , H , B_{sand} , $B_{seagrass}$) change when using the LHS method, as the number of noise-perturbed r_{rs} spectra increase for seven selected HICO pixels. Figure A.10 shows that the uncertainty of each model parameter plateaus when the number of noise-perturbed spectra exceeds 100. However, this may be too large a number for operational satellite/airborne imagery, especially because the difference in uncertainty from 50 to 100 noise-perturbed spectra is quite small. We therefore suggest setting the number of noise-perturbed spectra to 50. Using the MPFIT LM algorithm in C language, processing 50 noise-perturbed spectra per pixel takes an average of 0.12 seconds using a standard PC (quad-core, 8 GB RAM, without parallel processing).

Figures for HICO pixel B:

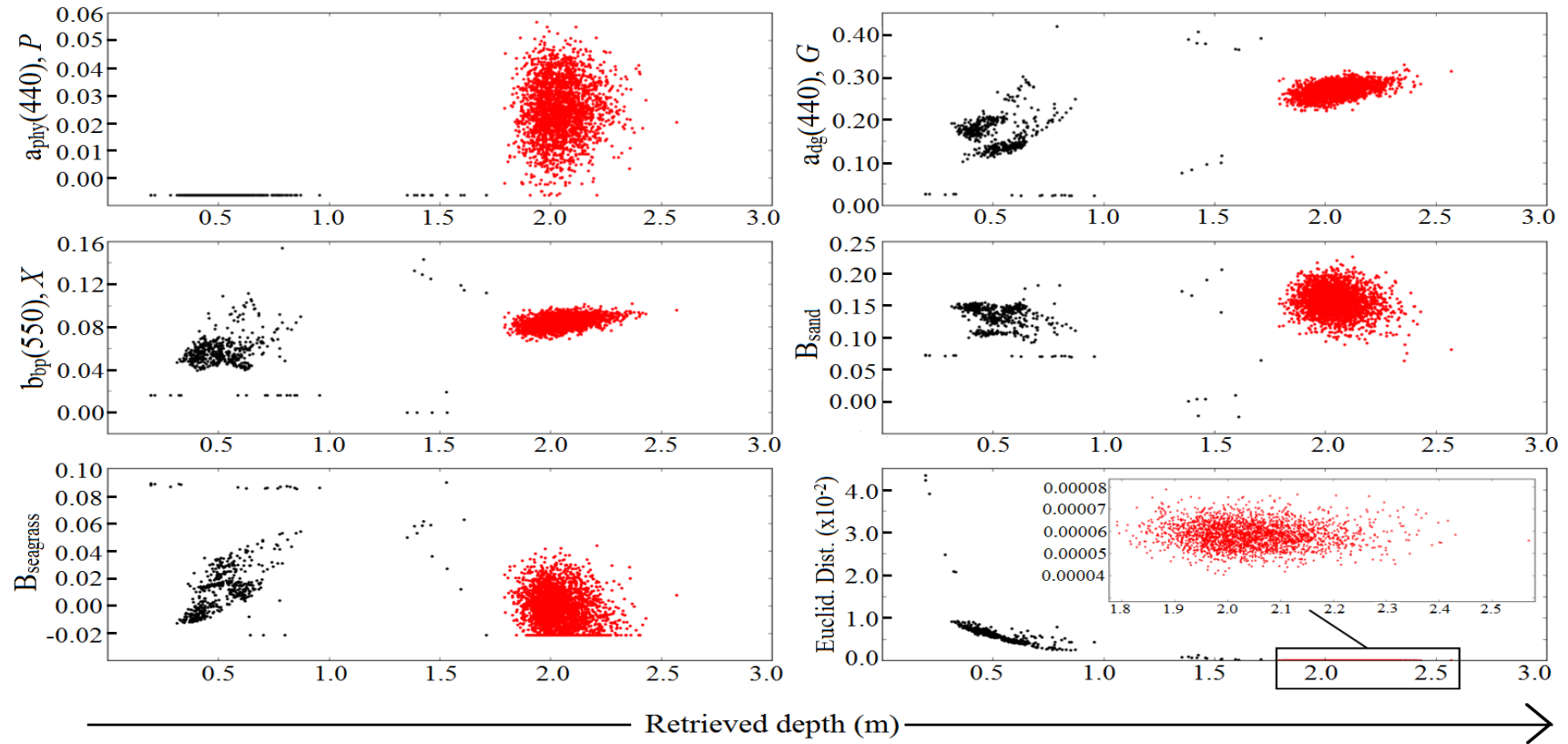


Figure A.1: Retrieved BRUCE model parameters vs. retrieved depth for the 3000 noise perturbed r_{rs} spectra of HICO pixel B (row 1083, col 212) using SLM optimization. The fixed guess model parameters were arbitrarily set. The red dot points are the retrieved values that converged onto the group with the lowest Euclidean distance.

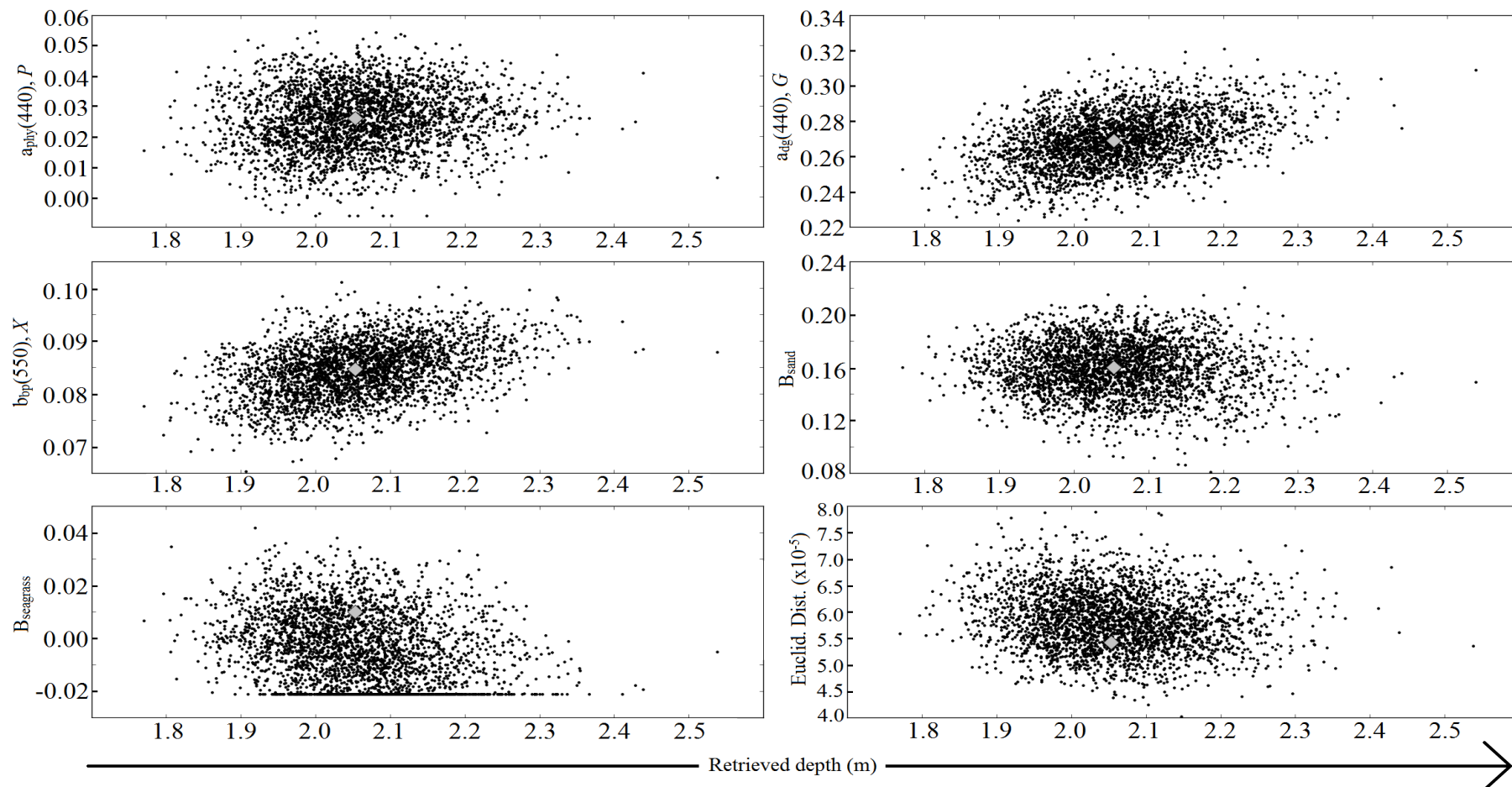


Figure A.2: Retrieved BRUCE model parameters vs. retrieved depth, for the 3000 noise perturbed r_{rs} spectra of the HICO pixel B (row 1083, col 212). The optimized guess values were dynamically chosen using the UR-LM method and are shown as grey diamonds.

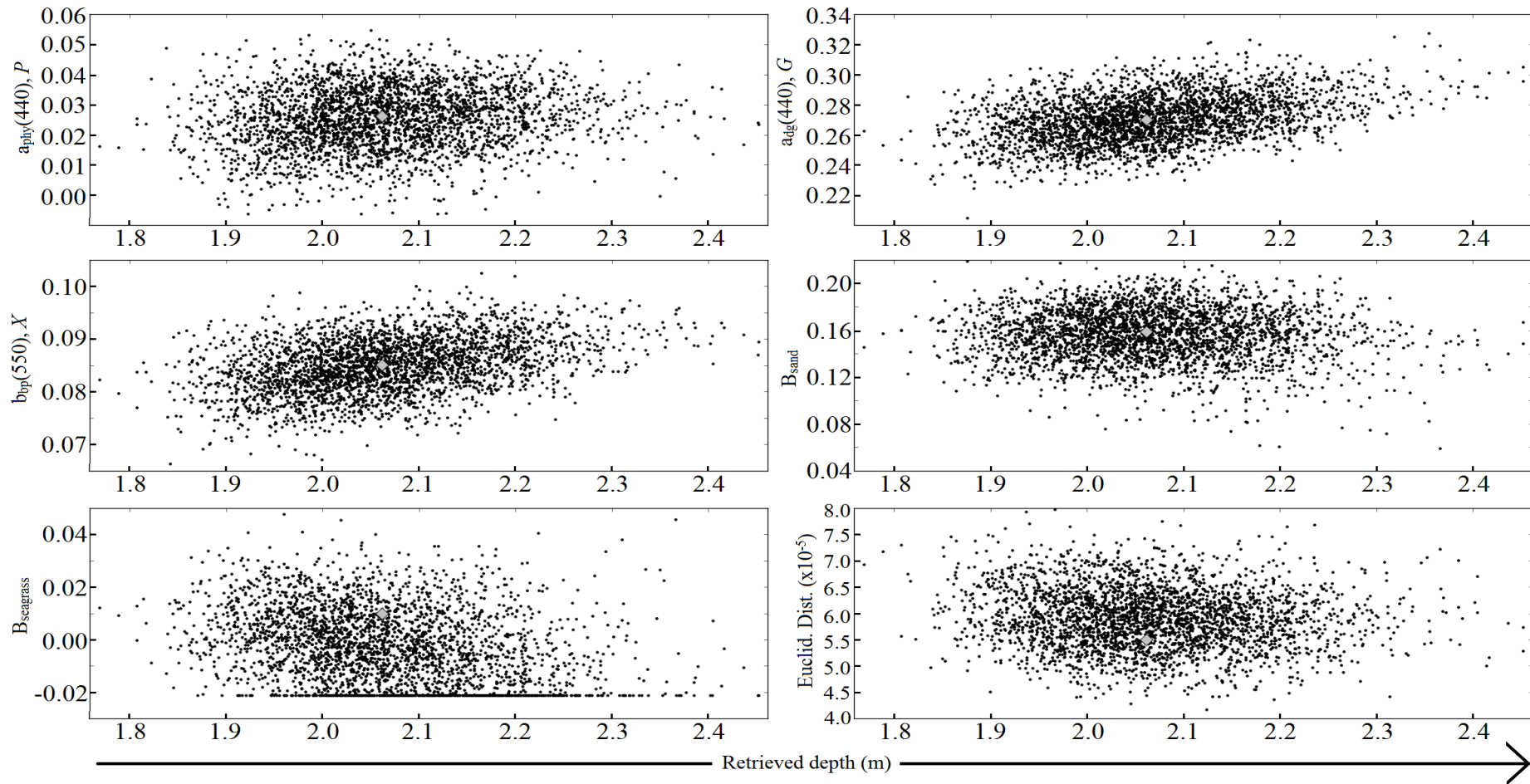


Figure A.3: Retrieved BRUCE model parameters vs. retrieved depth, for the 3000 noise perturbed r_{rs} spectra of the HICO pixel B (row 1083, col 212). The optimized guess values were dynamically chosen using the LHS method and are shown as grey diamonds.

Figures for HICO pixel C:

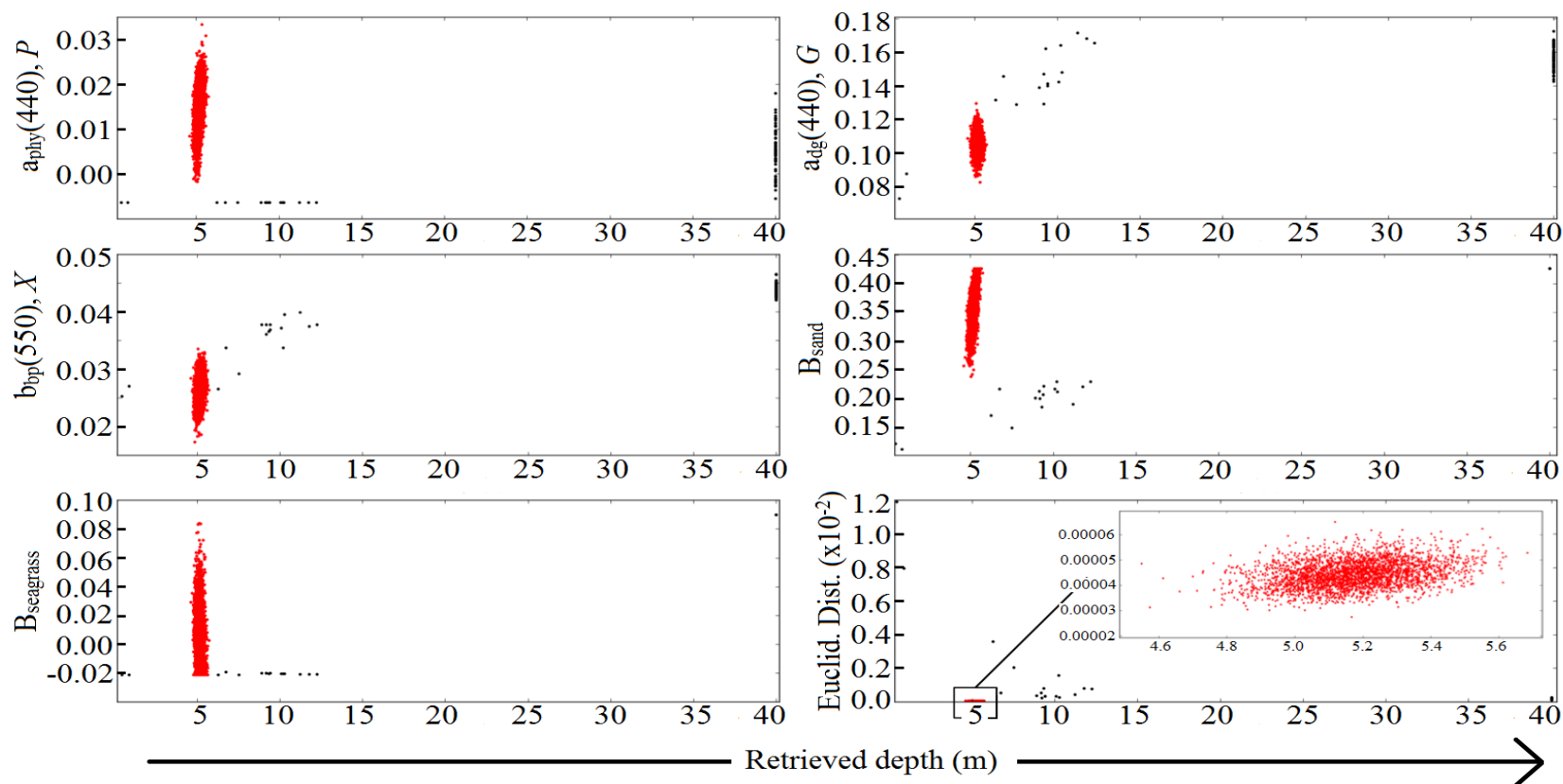


Figure A.4: Retrieved BRUCE model parameters vs. retrieved depth for the 3000 noise perturbed r_{rs} spectra of HICO pixel C (row 1031, col 210) using SLM optimization. The fixed guess model parameters were arbitrarily set. The red dot points are the retrieved values that converged onto the group with the lowest Euclidean distance.

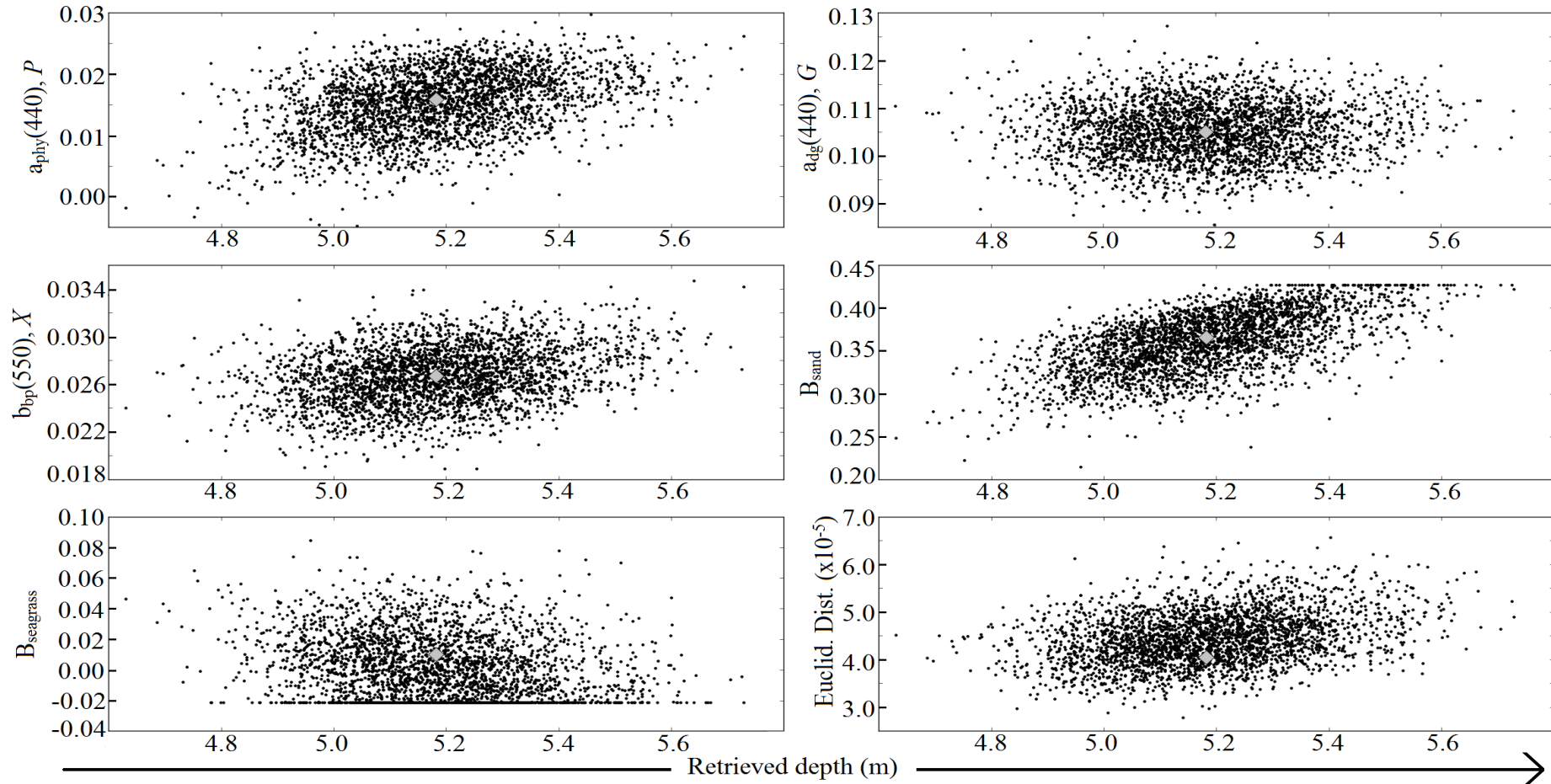


Figure A.5: Retrieved BRUCE model parameters vs. retrieved depth, for the 3000 noise perturbed r_{rs} spectra of the HICO pixel C (row 1031, col 210). The optimized guess values were dynamically chosen using the UR-LM method and are shown as grey diamonds.

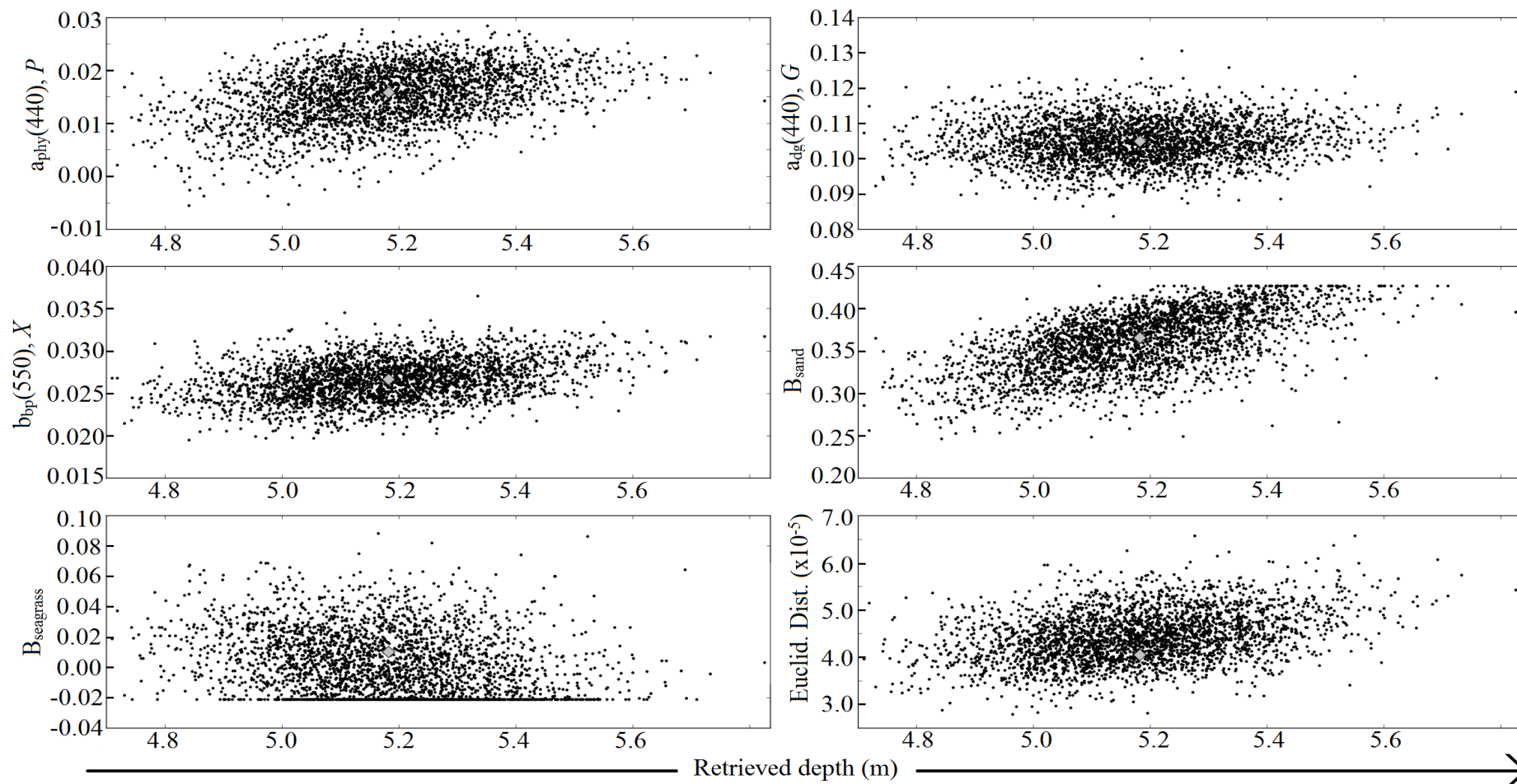


Figure A.6: Retrieved BRUCE model parameters vs. retrieved depth, for the 3000 noise perturbed r_{rs} spectra of the HICO pixel C (row 1031, col 210). The optimized guess values were dynamically chosen using the LHS method and are shown as grey diamonds.

Figures for HICO pixel D:

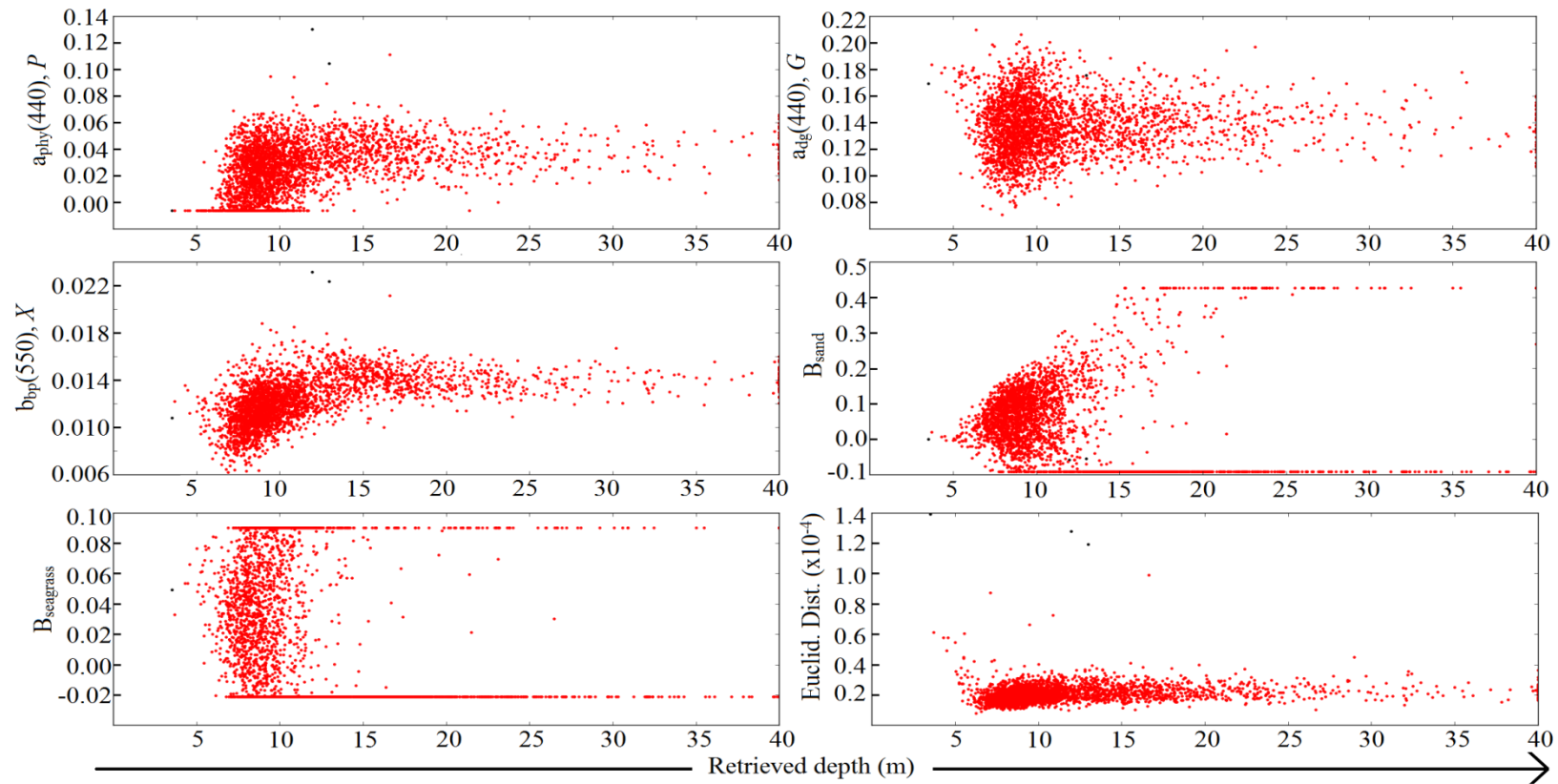


Figure A.7: Retrieved BRUCE model parameters vs. retrieved depth for the 3000 noise perturbed r_{rs} spectra of HICO pixel D (row 1200, col 445) using SLM optimization. The fixed guess model parameters were arbitrarily set. The red dot points are the retrieved values that converged onto the group with the lowest Euclidean distance.

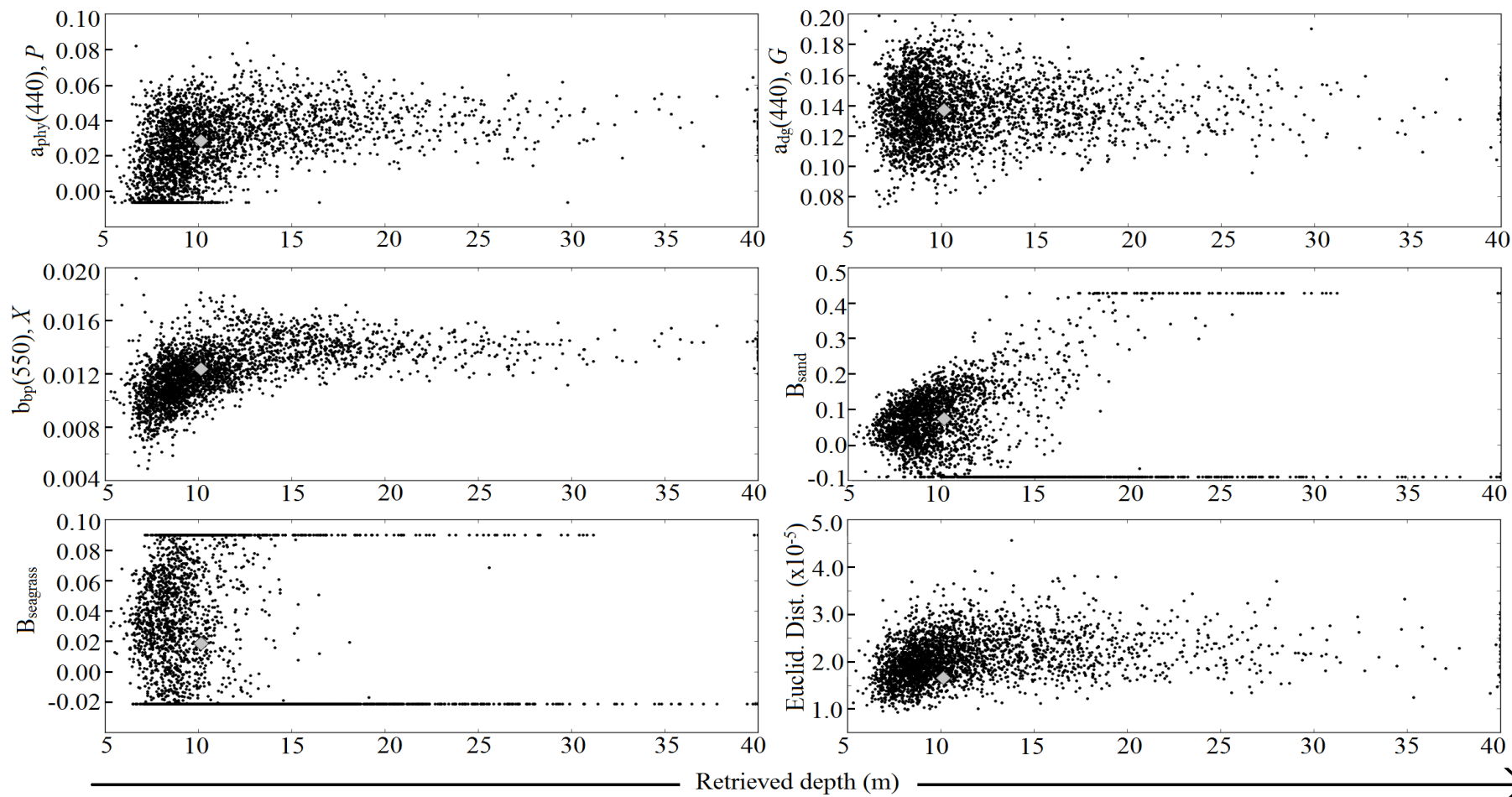


Figure A.8: Retrieved BRUCE model parameters vs. retrieved depth, for the 3000 noise perturbed r_{rs} spectra of the HICO pixel D (row 1200, col 445). The optimized guess values were dynamically chosen using the UR-LM method and are shown as grey diamonds.

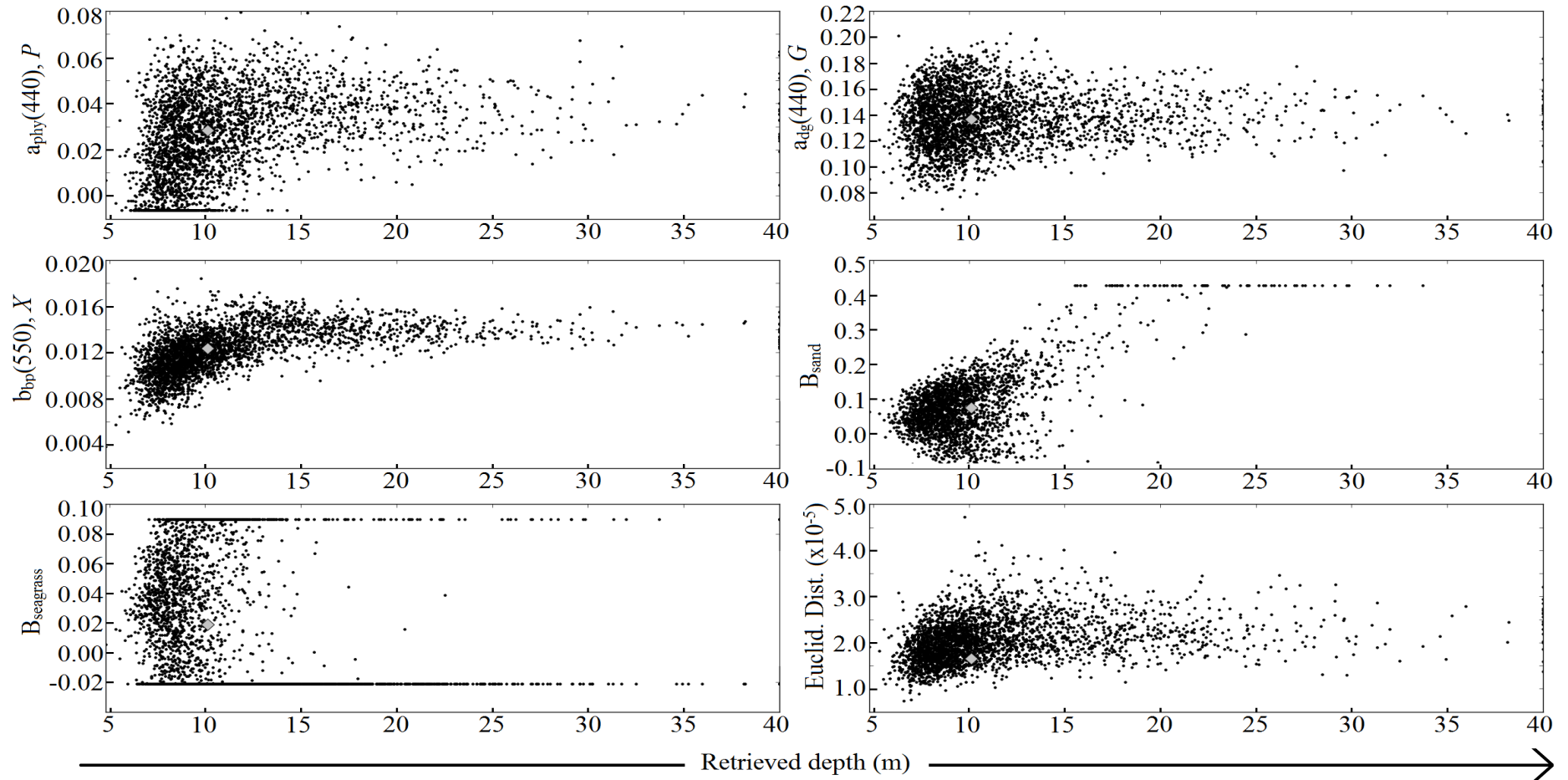


Figure A.9: Retrieved BRUCE model parameters vs. retrieved depth, for the 3000 noise perturbed r_{rs} spectra of the HICO pixel D (row 1200, col 445). The optimized guess values were dynamically chosen using the LHS method and are shown as grey diamonds.

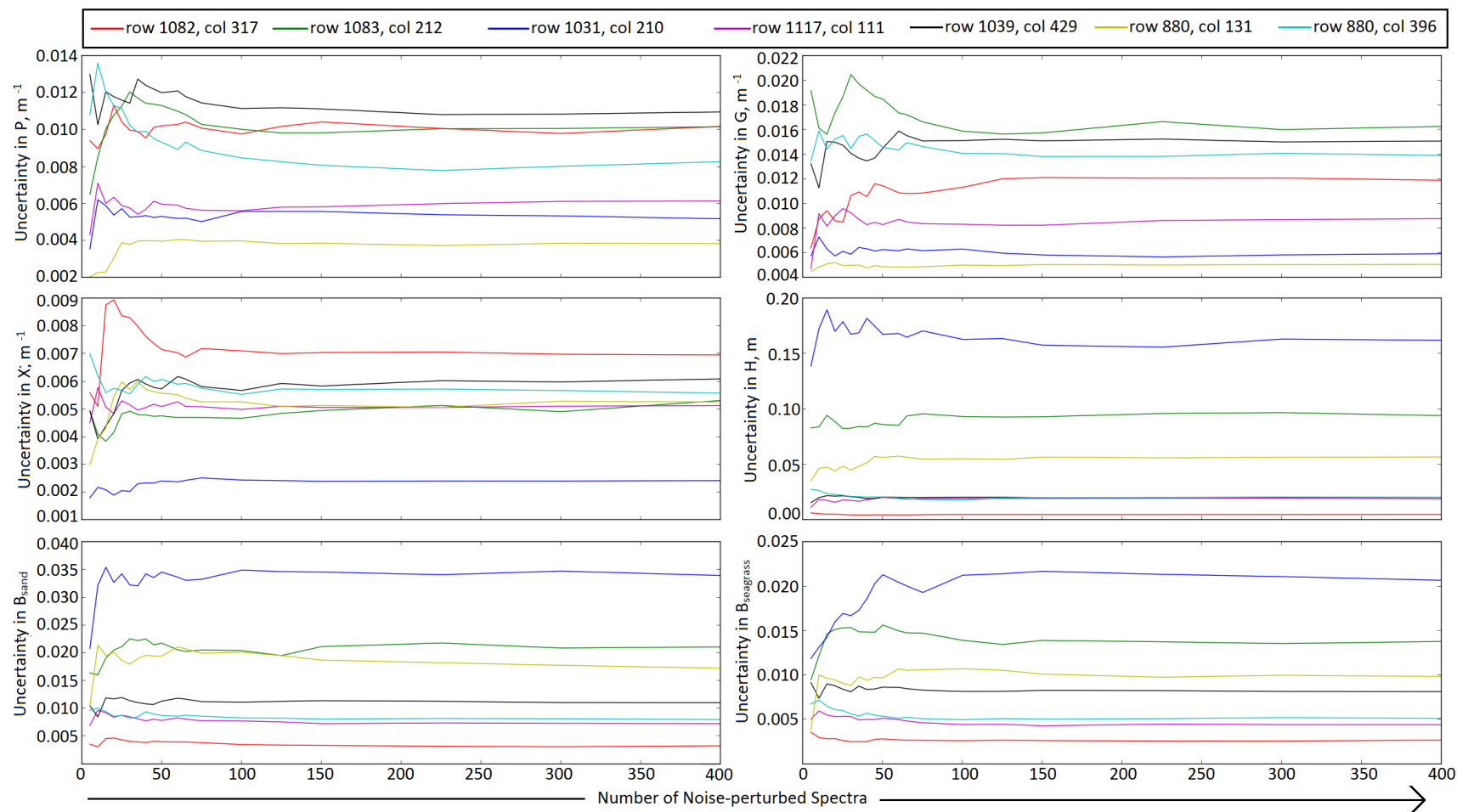


Figure A.10: The uncertainties of the BRUCE model parameters vs. number of noise-perturbed r_{rs} spectra for seven pixels selected from the HICO image of Shark Bay, 14 December 2011. Here the LHS implementation of the BRUCE model was used

APPENDIX B

Table B.1 and Figures B.1 to B.3 compare the inversions of the simulated r_{rs} dataset using the SLM, UR-LM and LHS implementation of the BRUCE model with the model constraints set as $0.0 < P < 2.0 \text{ m}^{-1}$, $0.0 < G < 2.0 \text{ m}^{-1}$, $0.0 < X < 2 \text{ m}^{-1}$, $0.0 < H < 40 \text{ m}$, $0.0 < B_{\text{sand}}, B_{\text{seagrass}}, B_{\text{algae}} < 1.4 \times \rho_i(550 \text{ nm})$.

Although the SLM approach is comparable to the UR-LM and LHS methods, it is less efficient, having performed 55,525,786 (approximately 4 times more) iterations compared to 14,261,286 and 13,905,756 for the UR-LM and LHS methods respectively. In the presence of noise, setting the lower bounds to zero can underestimate the uncertainty of a model parameter if its value is near zero (or the boundary). This is illustrated in Figure B.4, which shows the different model parameters, including the Euclidean distance, plotted against the retrieved depth for the inversions of a simulated r_{rs} spectrum. Here, the simulated r_{rs} spectrum was obtained by forward modelling of the BRUCE model using two benthic end-members of sand and *Possidonia sp.*, where the model parameters were set to $P = 0.10 \text{ m}^{-1}$, $G = 0.005 \text{ m}^{-1}$, $X = 0.05 \text{ m}^{-1}$, $H = 4.0 \text{ m}$, $B_{\text{sand}} = 0.1589$, $B_{\text{possidonia}} = 0.0159$. The latter two model parameters represent a pixel that has 70% sand and 30% seagrass. Spectral noise extracted from the HICO image of Shark Bay on 14 December 2014, was added to the simulated r_{rs} , in the same way as described in forward modelling section, to generate 3000 noise-perturbed r_{rs} spectra. Inversions that had a retrieved value equal to the lower bound were not included in the calculation of the average retrieved value and standard error, as the global or local minima of these inversions exist beyond the imposed constraints and are therefore not physically possible. However these inversions are shown in Figures B.4 and B.5.

The only notable difference between the two sets of inversions in Table B.2 is the retrieved value of $B_{\text{possidonia}}$, and its relative uncertainty. When the lower bounds are set to zero the uncertainty is 24% lower than when the lower bounds are set to negative values. This reduced uncertainty is the result of the existence of minima located beyond the imposed boundary, which causes the optimized value to have the value of this boundary – as shown in Figure B.4. In contrast, when the lower bound is set to a negative value, the optimization is able to find these minima and hence produce a more correct representation of the scatter of retrievals and hence a better

representation of the uncertainty (Figure B.5). Additionally, when the lower bounds are set to negative values the average retrieved value for B_{seagrass} is 0.0154, compared to 0.0213 when the lower bounds are set to zero – noting that the input was 0.0159. This effect of over-estimating the retrieved value whilst over-estimating the uncertainty is heightened as the input value approaches zero.

Table B.1: An inter-comparison of the RMSE (scatter), percent accuracy and average relative uncertainty for each BRUCE model parameter between the three optimization approaches. Here, the lower bounds of each model parameter were set to zero.

Actual values	Average retrieved value (centroid)			Average uncertainty			RMSE			Accuracy (%)		
	SLM	UR-LM	LHS	SLM	UR-LM	LHS	SLM	UR-LM	LHS	SLM	UR-LM	LHS
<i>P</i> (m ⁻¹)												
0.01	0.018	0.018	0.018	0.021	0.021	0.021	0.019	0.019	0.019	2.86	3.09	3.09
0.03	0.035	0.035	0.035	0.027	0.027	0.027	0.018	0.018	0.018	5.83	6.06	6.06
0.05	0.053	0.053	0.053	0.032	0.032	0.032	0.016	0.017	0.017	8.23	8.11	8.11
0.07	0.072	0.072	0.072	0.037	0.037	0.037	0.016	0.016	0.016	9.94	10.97	10.97
0.1	0.100	0.101	0.101	0.043	0.043	0.043	0.017	0.016	0.016	12.80	13.94	13.94
<i>G</i> (m ⁻¹)												
0.01	0.010	0.010	0.010	0.004	0.004	0.004	0.002	0.002	0.002	15.09	15.77	15.77
0.10	0.100	0.099	0.099	0.015	0.015	0.015	0.005	0.005	0.005	39.43	39.09	39.09
0.25	0.244	0.244	0.244	0.035	0.036	0.036	0.012	0.013	0.013	48.00	47.31	47.31
0.35	0.335	0.335	0.335	0.052	0.053	0.053	0.026	0.026	0.026	38.40	38.97	38.97
0.50	0.467	0.468	0.468	0.082	0.084	0.084	0.053	0.050	0.050	24.69	25.49	25.49
<i>X</i> (m ⁻¹)												
0.006	0.008	0.005	0.005	0.010	0.003	0.003	0.005	0.001	0.001	4.57	4.46	4.46
0.010	0.009	0.009	0.009	0.004	0.004	0.004	0.001	0.001	0.001	6.97	6.74	6.74
0.030	0.029	0.029	0.029	0.004	0.003	0.003	0.005	0.001	0.001	26.29	27.20	27.20
0.070	0.069	0.069	0.069	0.003	0.003	0.003	0.001	0.001	0.001	62.74	63.31	63.31
0.100	0.100	0.100	0.100	0.003	0.003	0.003	0.001	0.001	0.001	79.43	80.00	80.00
<i>H</i> (m)												

Limitations & potential of remotely sensed shallow water bathymetry & benthic classification

1	1.00	1.00	1.00	0.04	0.04	0.04	0.018	0.011	0.011	72.91	72.91	72.91
3	2.95	2.95	2.95	0.28	0.28	0.28	0.103	0.103	0.103	37.26	37.37	37.37
6	5.55	5.62	5.62	1.24	1.44	1.44	0.592	0.559	0.559	9.83	9.94	9.94
11	8.67	9.51	9.51	4.57	5.86	5.86	3.622	3.405	3.406	1.83	1.94	1.94
20	10.23	11.48	11.48	6.01	7.50	7.50	11.156	10.314	10.314	0.46	0.69	0.69
<i>B_{sand}</i>												
0	0.049	0.048	0.048	0.052	0.053	0.053	0.077	0.075	0.075	0.00	0.00	0.00
0.0757	0.086	0.085	0.085	0.061	0.061	0.061	0.044	0.043	0.043	11.36	11.52	11.52
0.1135	0.107	0.106	0.106	0.062	0.063	0.063	0.040	0.039	0.039	13.68	13.76	13.76
0.2270	0.174	0.174	0.174	0.064	0.065	0.065	0.077	0.077	0.077	12.16	12.48	12.48
<i>B_{posidonia}</i>												
0	0.017	0.016	0.016	0.017	0.018	0.018	0.023	0.023	0.023	0.00	0.00	0.00
0.0177	0.023	0.023	0.023	0.020	0.020	0.020	0.013	0.012	0.012	7.20	6.88	6.88
0.0265	0.027	0.027	0.027	0.020	0.020	0.020	0.011	0.010	0.010	4.08	4.40	4.40
0.0530	0.038	0.038	0.038	0.019	0.020	0.020	0.020	0.020	0.020	5.92	6.24	6.24
<i>B_{sargassum}</i>												
0	0.009	0.009	0.009	0.011	0.011	0.011	0.012	0.011	0.011	0.00	0.00	0.00
0.011	0.013	0.013	0.013	0.013	0.013	0.013	0.006	0.006	0.006	5.76	5.76	5.76
0.0165	0.014	0.014	0.014	0.012	0.012	0.012	0.007	0.006	0.006	2.16	2.16	2.16
0.0330	0.019	0.019	0.019	0.012	0.012	0.012	0.017	0.016	0.016	0.00	0.00	0.00
				Number of L-M iterations								
SLM				55,525,786								
UR-LM				14,261,286								
LHS				13,905,756								

Table B.2: Comparison between the inversions (using the UR-LM optimization) that had the lower bounds set to zero and negative values. Here, inversions that had a retrieved value equal to the lower bound were not included in the calculation of the average retrieved value and standard error (uncertainty).

Model parameters	Actual parameter value	Retrieved parameter value (Lower bounds set to zero)	Retrieved parameter value (Lower bounds set to negative values)
P [m ⁻¹]	0.1	0.0981 ± 0.0047	0.0992 ± 0.0049
G [m ⁻¹]	0.005	0.0046 ± 0.0025	0.0047 ± 0.0025
X [m ⁻¹]	0.05	0.0492 ± 0.003	0.0496 ± 0.003
H [m]	4.0	3.91 ± 0.27	3.95 ± 0.27
B_{sand} [unitless]	0.1589	0.1551 ± 0.0258	0.1603 ± 0.028
$B_{possidonia}$ [unitless]	0.0159	0.0213 ± 0.0126	0.0154 ± 0.017

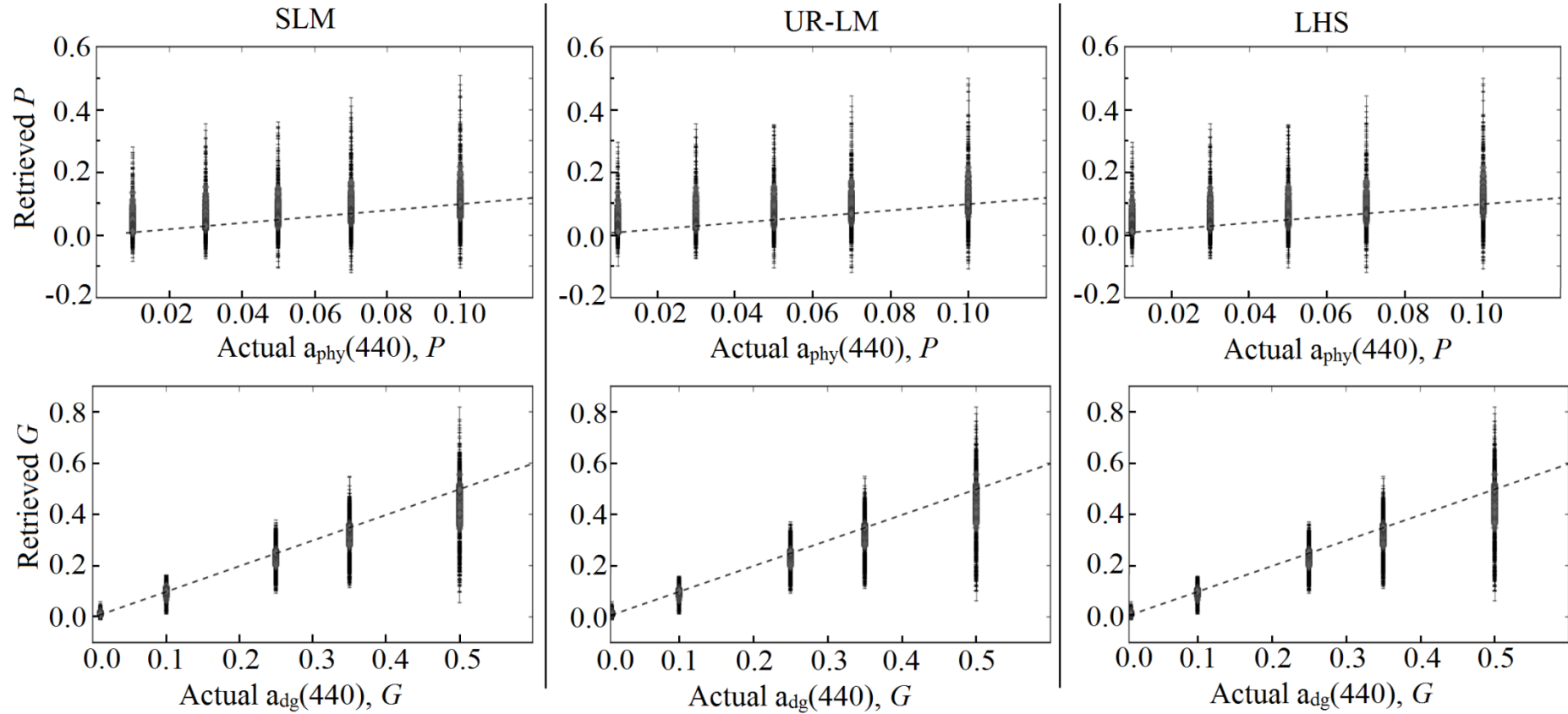


Figure B.1: Inter-comparison between the SLM (left-hand panels), UR-LM (central panels) and LHS (right-hand panels) optimization of the noise-added, simulated r_{rs} spectra using the BRUCE forward model. These graphs show the retrieved vs. actual model parameters for P and G . Here the lower bounds for the constrained LM optimization were set to zero.

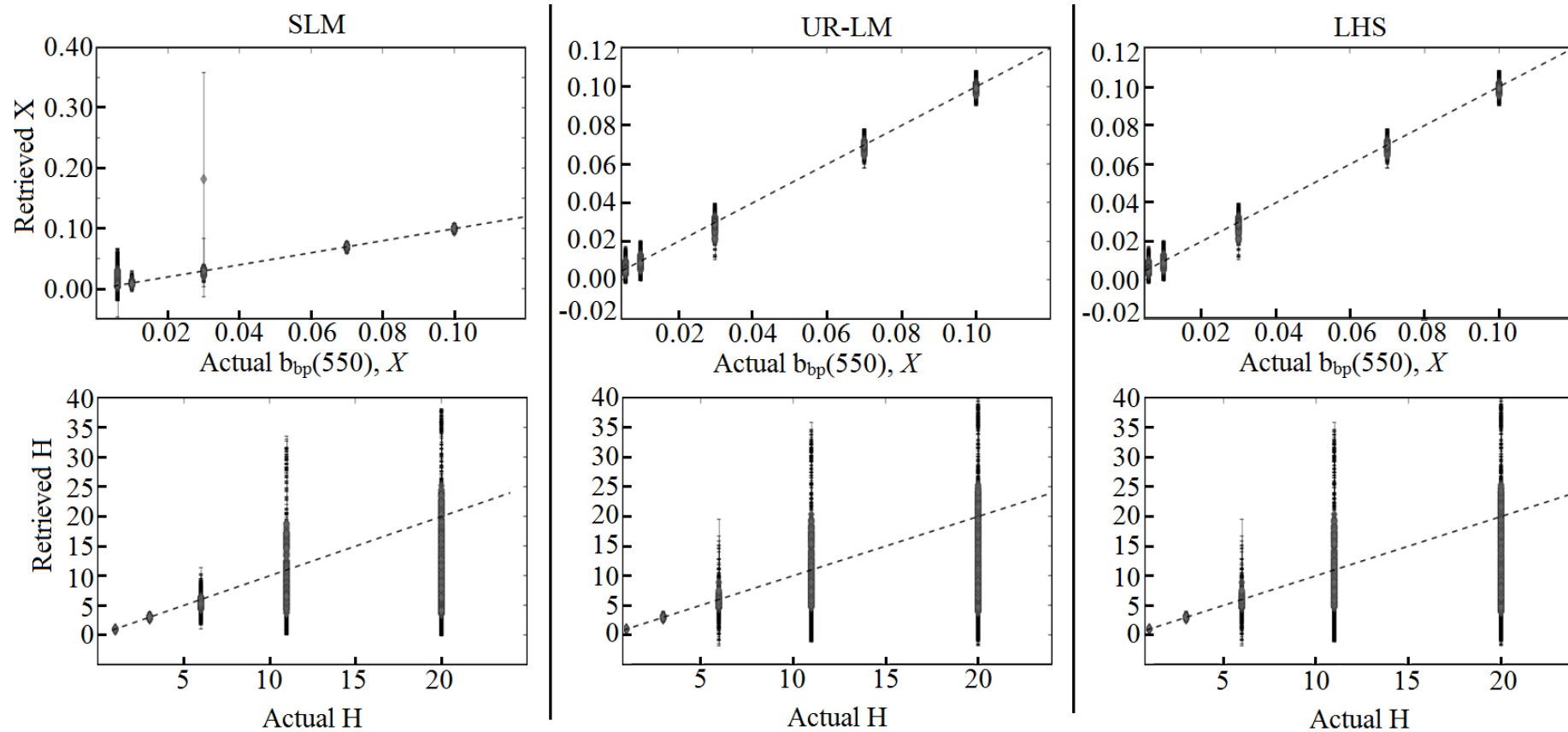


Figure B.2: Inter-comparison between the SLM, UR-LM and LHS optimization of the noise-added, simulated r_{rs} spectra using the BRUCE forward model. These graphs show the retrieved vs. actual model parameters for X and H . Here the lower bounds for the constrained LM optimization were set to zero.

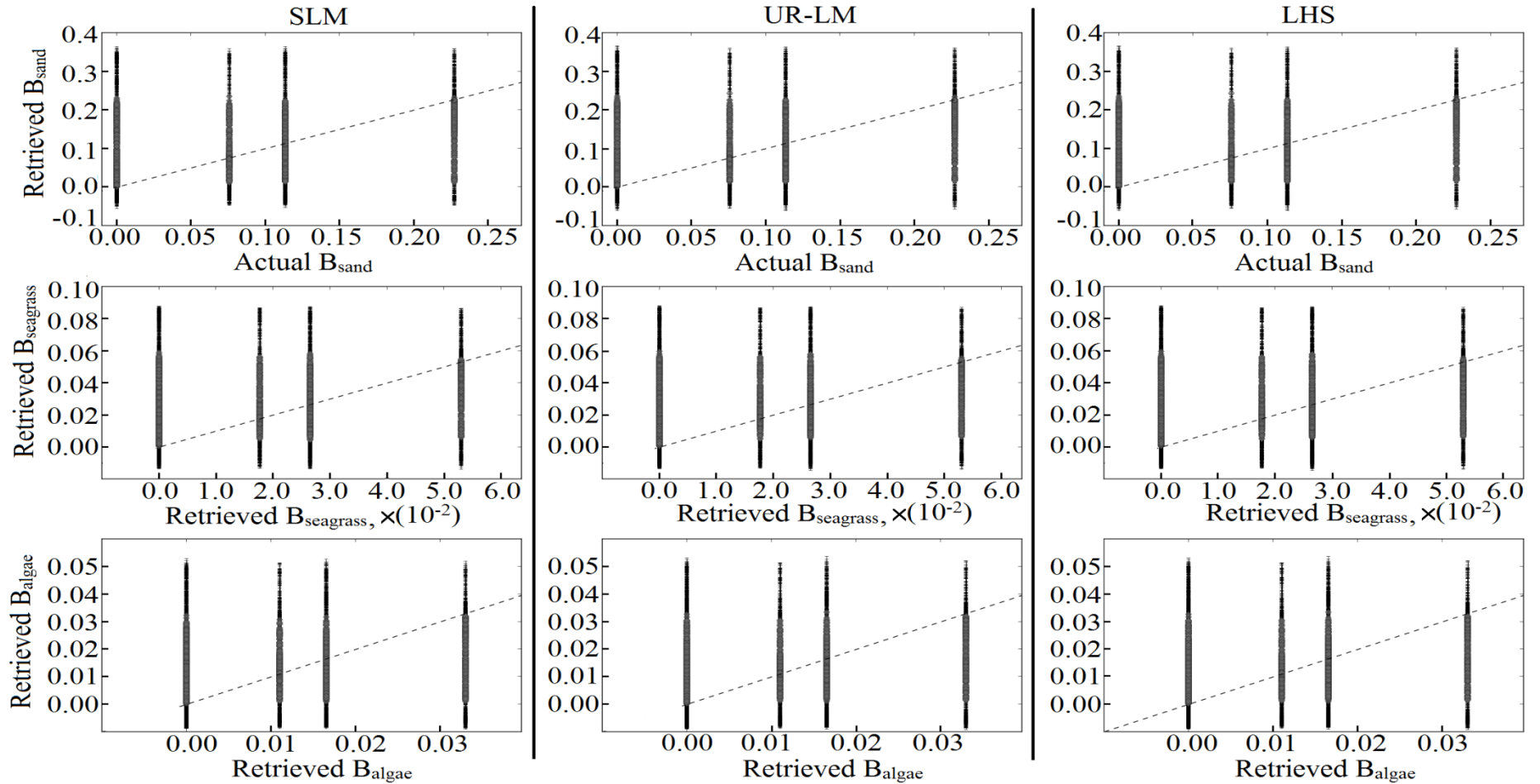


Figure B.3: Inter-comparison between the SLM, UR-LM and LHS optimization of the noise-added, simulated r_{rs} spectra using the BRUCE forward model. These graphs show the retrieved vs. actual model parameters for B_{sand} , $B_{seagrass}$, and B_{algae} . Here the lower bounds for the constrained LM optimization were set to zero.

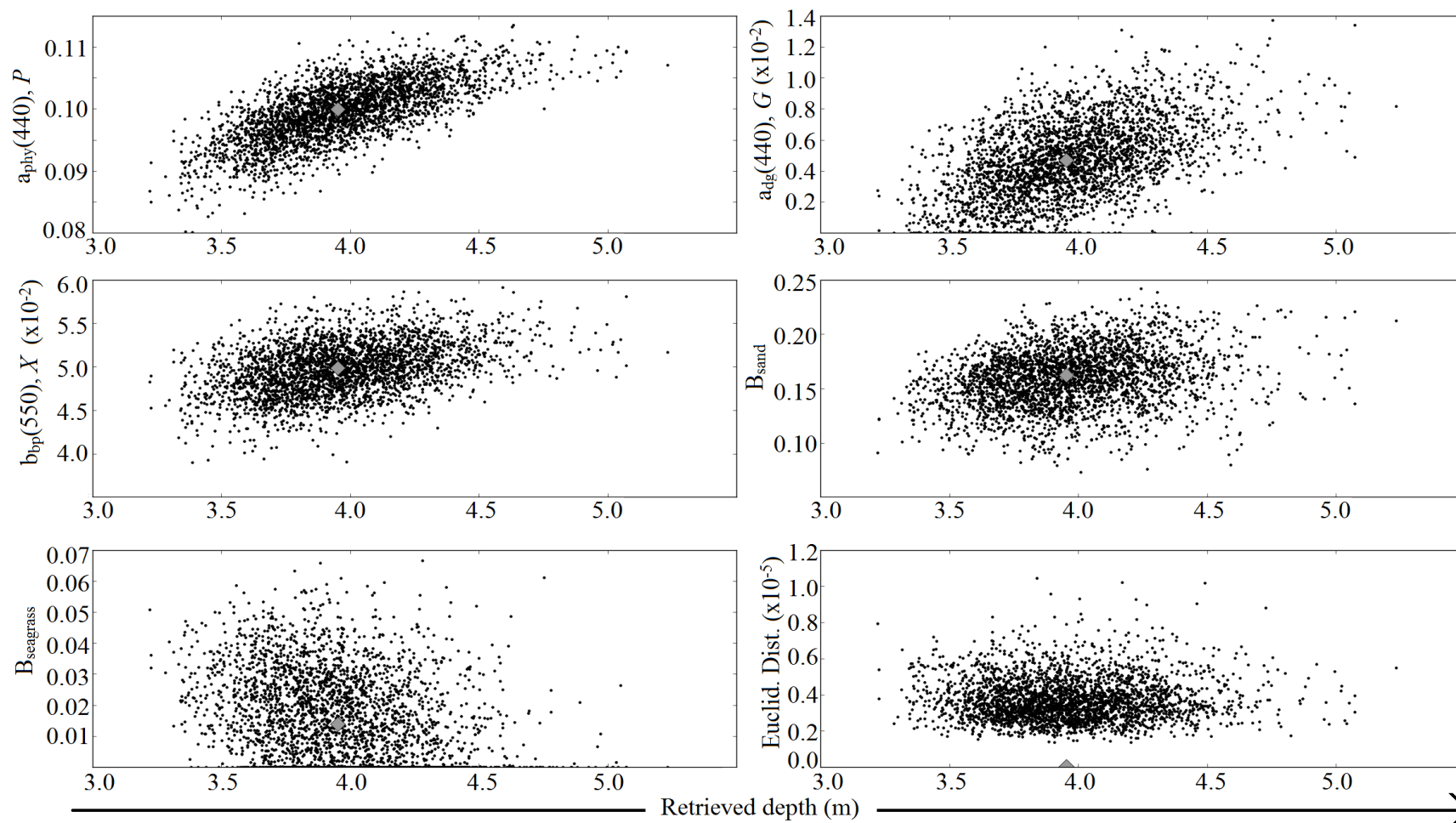


Figure B.4: Retrieved BRUCE model parameters vs. retrieved depth, for the 3000 noise perturbed r_{rs} spectra. Here the UR-LM method was used and the lower bounds for each model parameter were set to zero.

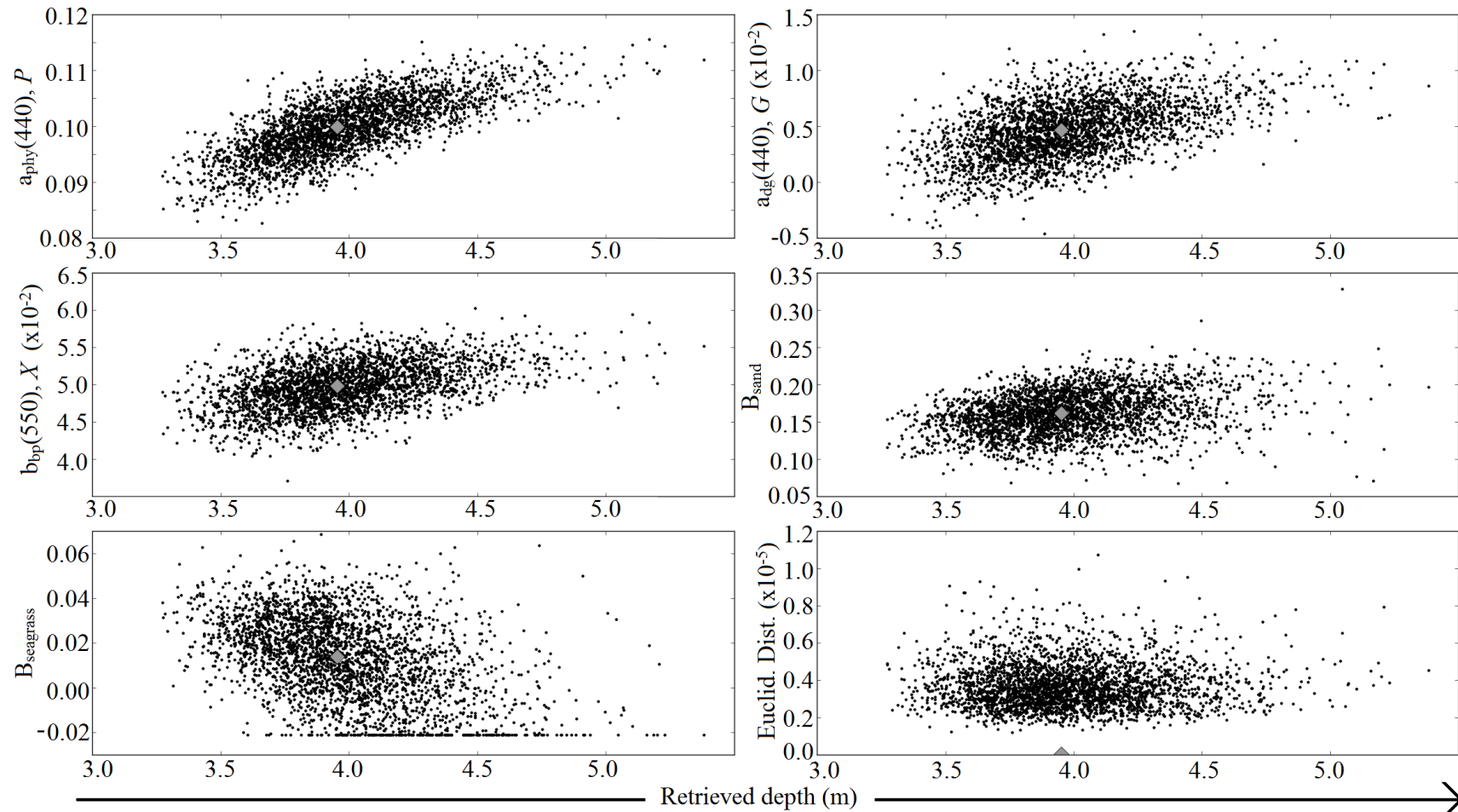


Figure B.5: Retrieved BRUCE model parameters vs retrieved depth, for the 3000 noise perturbed r_{rs} spectra. Here the UR-LM method was used and the lower bounds set to negative values.

APPENDIX C

This appendix describes in detail the mathematical steps employed in the HDC algorithm given in section 5.3.2.2; provides additional figures for the case of the HyMap spectral bands, and; describes the limitations and possible improvements to the HDC algorithm. Figure C.1a shows the measured 29 ρ_b spectra of *Possidonia sp.* that were convolved from the ASD spectrometer to HyMap spectral bands. Each spectrum were perturbed by $NE\Delta r_{rs}$ to generate 69 noise perturbed, $\rho_b \pm \delta\rho_{SE}$ spectra. This produced a total of 2001 noise perturbed spectra from which 2000 were randomly selected (Figure C.1b). Figures C.1a and C.1b also illustrates the non-normality of the reflectance values at a given waveband (LDA variable).

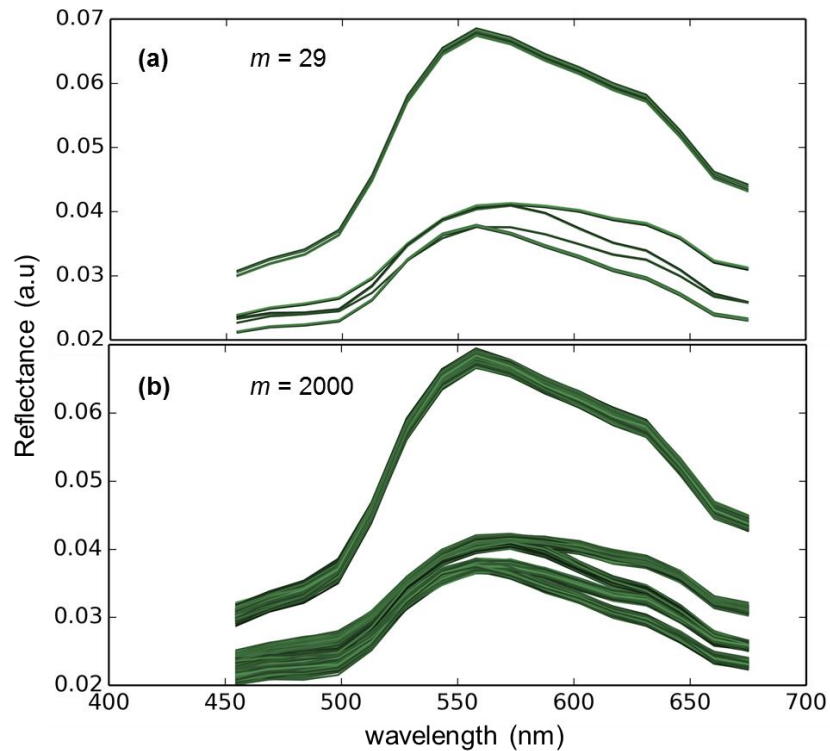


Figure C.1: (a) The measured benthic irradiance reflectance spectrum of *Possidonia sp.* convolved to HyMap wavelengths; (b) After the addition of sensor and environmental noise to each spectrum in (a).

The inclusion of $NE\Delta r_{rs}$ resulted in a spectral library of 44,000 ρ_b spectra over 22 benthic classes. These spectra were then transformed to their corresponding LD coordinates following the LDA procedure given by Rencher and Christensen (2012, p. 288-290). LDA seeks to find a set of linear functions of the variables (the wavebands)

that maximise the distance between class means while minimising the within-class scatter. The coefficients for these linear functions are the eigenvectors that are computed from the between-class (**H**) and within-class (**E**) scatter matrices. The **H** matrix was computed using the *i*th class mean ρ_b spectrum, $\overline{\rho_{b,i}}$, and the population average ρ_b , $\overline{\rho_{b,pop}}$ (Rencher & Christensen, 2012, p. 173),

$$\rho m c_i = \overline{\rho_{b,i}} - \overline{\rho_{b,pop}} \quad (C.1a)$$

$$\mathbf{H} = \sum_{i=1}^k m_i (\rho m c_i \cdot \rho m c_i^T) \quad (C.1b)$$

$\rho m c_i$ is the mean centred ρ_b spectrum for class *i*, and m_i and k are the number of spectra (=2000) and number of classes (=22) respectively. The $n \times n$ **E** matrix was computed using the spectral covariance matrices from each benthic class, **Cb_i**,

$$\mathbf{E} = \sum_{i=1}^k (m_i - 1) \mathbf{C}b_i \quad (C.2)$$

where, **Cb_i** was calculated from the 2000 $\rho_b \pm \delta\rho_{SE}$ spectra of each class, and contains the total system's spectral variability. The $n \times n$ eigenvector matrix, **a**, were then determined from $\mathbf{E}^{-1}\mathbf{H}$ (see Rencher & Christensen 2012, p. 289-290). Finally, the transformation from *n* band spectral space to LD coordinates was calculated by,

$$\mathbf{z}_i = \mathbf{R}_i \cdot \mathbf{a} \quad (C.3)$$

Here \mathbf{z}_i and **R_i** are the 2000×*n* LD coordinates and noise-perturbed ρ_b spectra matrices respectively. Figure C.2 shows a plot of the LD points using the first two eigenvectors, z_1 and z_2 , which give the greatest separation of the means in a multi-class situation. Although some classes appear to overlap additional separability is afforded with additional dimensions.

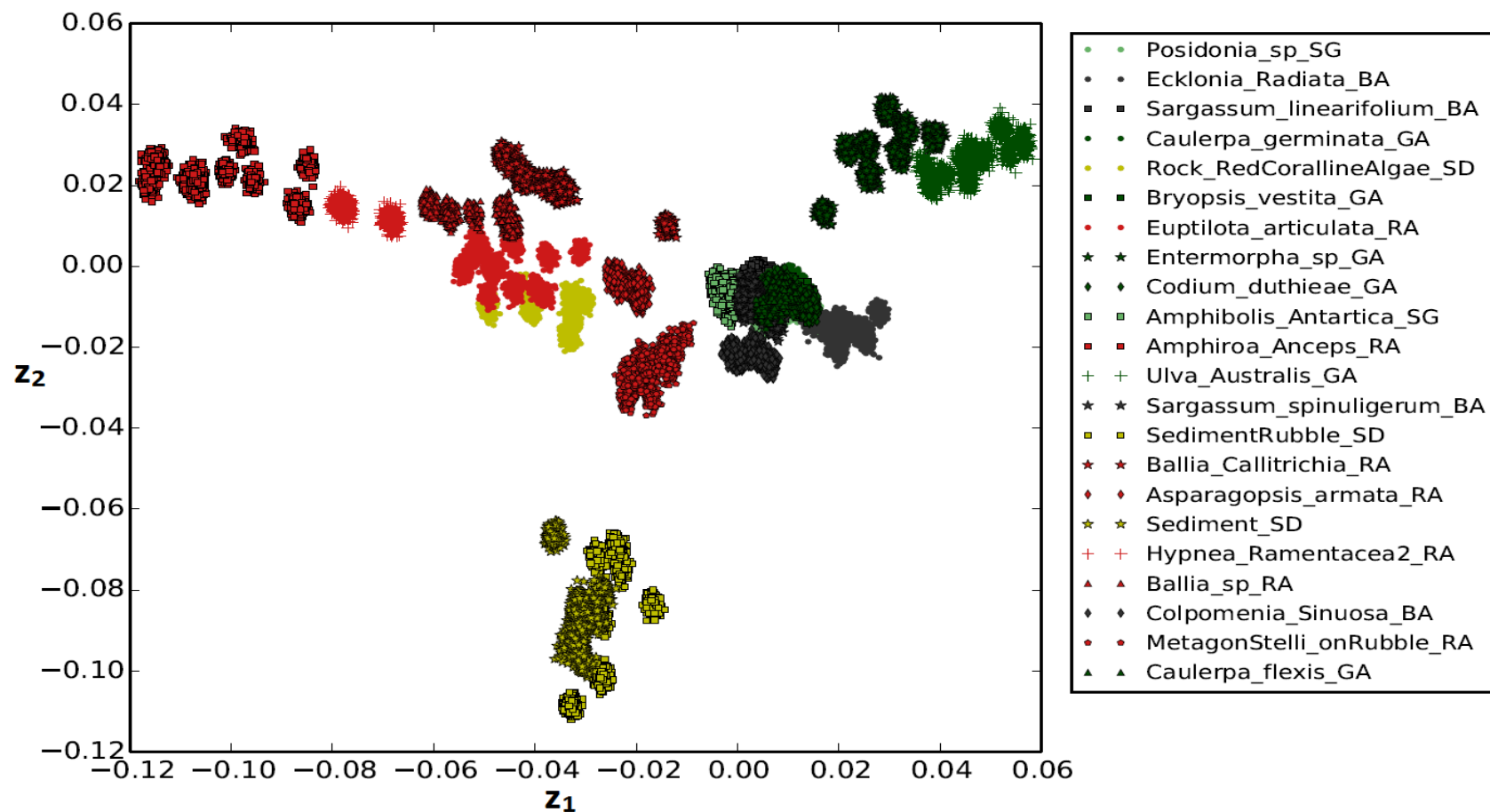


Figure C.2: An example of a LD plot generated from the HyMap ρ_b spectral library. Here each point represents an individual spectrum, where each class (a total of 22) has 2000 points. The colours of the LD points represent their genera, such that yellow, red, grey, light green and dark green represent sediment, red algae, brown algae, seagrass and green algae respectively.

The eigenvalues of the matrix \mathbf{a} give the proportional contribution of each eigenvector to the optimal separation of the class means. Preliminary results have shown that using all n eigenvectors from the matrix \mathbf{a} does not necessarily maximise the number of classes remaining from the hierarchical clustering (step 3 – see section 5.3.2.2). As such we first exclude those eigenvectors whose eigenvalues contribute less than 1% to the separation. From the remaining eigenvectors, an iterative approach was implemented where the number of eigenvectors, s , were successively increased to maximise the number of separable classes, k , generated from step (3), (Figure C.3). If k remained constant with increasing s for more than three successive increments of s then the iteration was ceased and the s that produced the last improvement in k was selected. To reduce the amount of computer processing we set the initial s as that which constituted 80% of the separation. The iterative eigenvector approach to dimensionality reduction effectively crops each \mathbf{z}_i matrix from a $2000 \times n$ to a $2000 \times s$ matrix where $s < n$.

The importance of the subsequent iterative eigenvector selection step is presented in Figure C.3. This figure plots the number of separable benthic classes derived from the HDC against the cumulative proportional contribution of successive eigenvectors at different depths of a modelled water column. Computing the number of separable benthic classes from a given water column at depth is describe in section 5.3.2.3. The blue at-surface curve (Figure C.3) has no modelled water column and was derived using ρ_b spectra. The highlighted circles on the at-surface, 0.5-, 1.5-, and 3.0-m curves are the location (i.e. number of eigenvectors) selected by the iterative eigenvector procedure. For the HyMap at-surface ρ_b spectral library the iterative eigenvector selection step selected the first seven eigenvalues, thus the dimensionality of the spectra were reduced from $n = 16$ to $s = 7$.

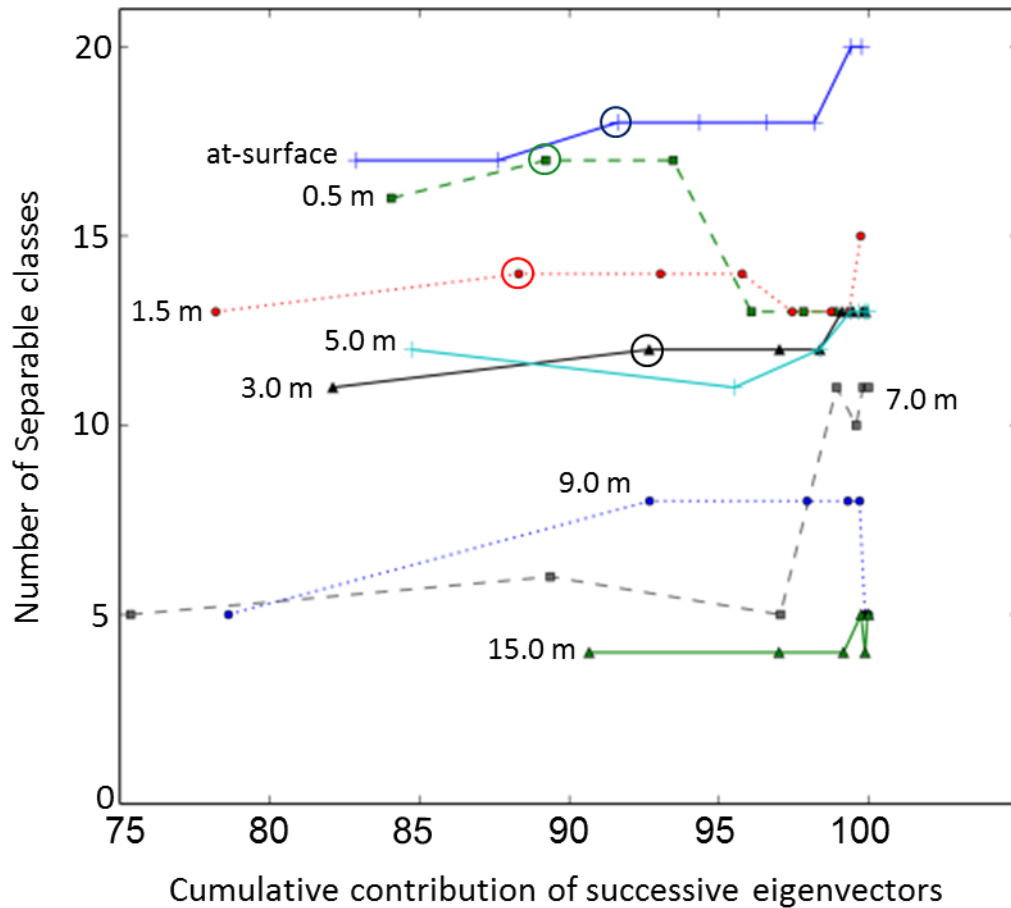


Figure C.3: The number of classes output from the LDHC vs. the cumulative proportional contribution of successive eigenvectors for different depths for a modelled water column. Here the IOPs were set to $P = 0.01 \text{ m}^{-1}$, $G = 0.01 \text{ m}^{-1}$ and $X = 0.001 \text{ m}^{-1}$.

Step 3 of the HDC procedure consists of an iterative centroid-based hierarchical clustering to merge benthic classes whose variance overlap exceed a user-defined misclassification proportion threshold, τ_m . Here τ_m was set to 5%. The iterative clustering begins with the computation of the RMSE between all possible pairs of class means, and τ_m between those pairs. The pair of classes that had the lowest RMSE and whose $\tau_m > 5\%$ were merged to form a single class. In this step the LD coordinates of the two merging classes remain unchanged only that they are labelled as one. The ρ_b spectra, however, of these two classes were computed using the appropriate weighted average,

$$\rho_c = \frac{N_i \rho_i + N_j \rho_j}{N_i + N_j} \quad (\text{C.4a})$$

$$N_c = N_i + N_j \quad (\text{C.4b})$$

where ρ_c is the irradiance reflectance spectrum of the newly merged class formed from the preceding classes i and j . N_i and N_j are the number of spectra measured to create the averaged ρ_i and ρ_j for benthic classes i and j , respectively. This iteration continues until the remaining classes all have a $\tau_m \leq 5\%$; in other words the clustering ceases when there is a 95% clustering accuracy that all classes are optically separable above the sensor and environmental noise and the benthos' natural spectral variability. This clustering accuracy can be reduced (with a corresponding increase in number of 'separable' classes) according to the desire of the user or application. The output of this entire procedure is a spectral library that contains the optimum set of endmembers for classifying the set of substrates of interest

The ability to separate between classes is given by the misclassification proportion, τ_m , calculated from the number of LD points in a given class that are closer or equal in distance to the mean of another class via the RMSE. To illustrate, consider a hypothetical point A_1 from class A with a LD coordinate of $A_1 = \langle z_{1A1}, z_{2A1}, \dots, z_{sA1} \rangle$. The LD coordinates of the class means \bar{A} and \bar{B} are then used to compute the RMSE between (i) A_1 and \bar{A} and; (ii) A_1 and \bar{B} ,

$$\begin{aligned}
 & RMSE(A_1, \bar{A}) \\
 &= \sqrt{(z_{1A1} - \bar{z}_{1A})^2 + (z_{2A1} - \bar{z}_{2A})^2 + \dots + (z_{sA1} - \bar{z}_{sA})^2} \\
 & RMSE(A_1, \bar{B}) \\
 &= \sqrt{(z_{1A1} - \bar{z}_{1B})^2 + (z_{2A1} - \bar{z}_{2B})^2 + \dots + (z_{sA1} - \bar{z}_{sB})^2}
 \end{aligned} \tag{C.5}$$

if $RMSE(A_1, \bar{A}) \geq RMSE(A_1, \bar{B})$ then the point A_1 would be labelled as misclassified. This is exemplified in Figure C.4, which displays the merging of two optically indistinguishable green algae classes *Caulerpa germinata* and *Caulerpa flexis*. This figure highlights a misclassified *C. germinata* point that is closer to mean of *C. flexis* (via RMSE) than to its own mean. The dendrogram for the HDC using ρ_b spectra at HyMap's spectral bands is presented in Figure C.5.

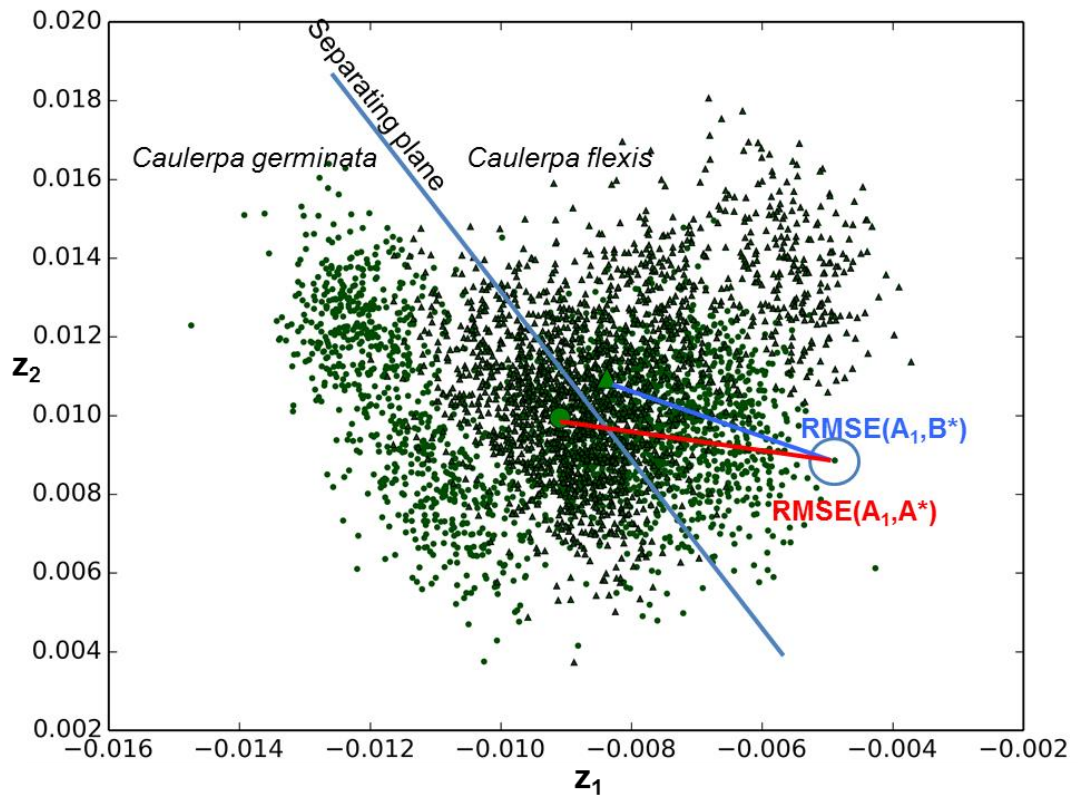


Figure C.4: An example of two optically indistinguishable green algae classes, *C. germinata* (green dots) and *C. flexis* (green triangles) using LD coordinates. Here, the blue circle highlights the misclassified *C. germinata* point, and the larger green circle and triangle represent the position of the two class means.

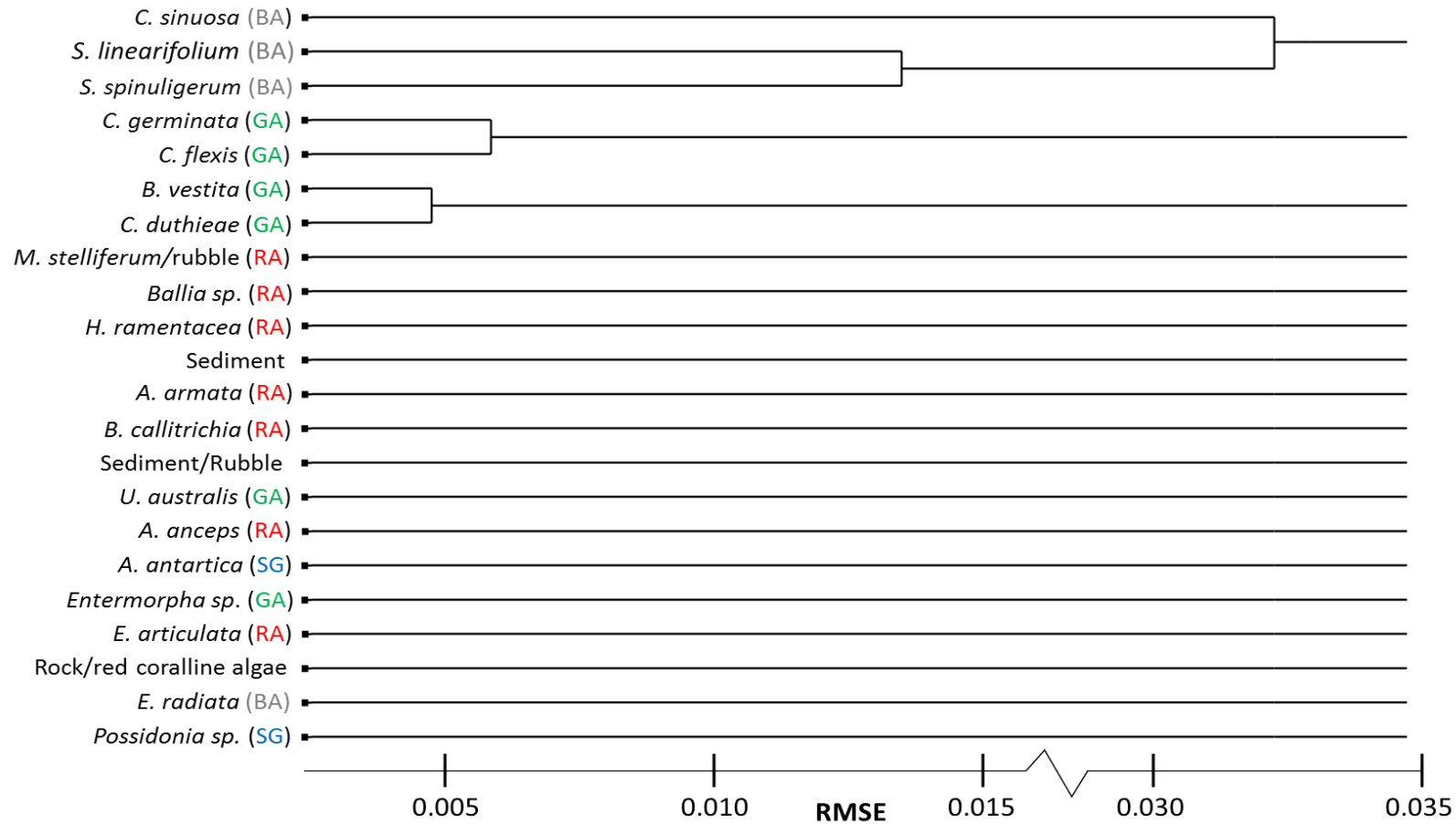


Figure C.5: HDC Dendrogram of the ρ_b spectra using HyMap's spectral bands. The iterative selection of eigenvectors chose the first seven, and consequently produced 18 classes

Limitations and improvements

The HDC procedure relies on linear discriminant functions (LDFs) that elicit optimal separability when all classes have equal variance-covariance and normally distributed within-class scatter. Though these conditions affect accuracies of subsequent classification they need not be met when a projection to lower dimensional space is sought that maximise the between-group distance (the \mathbf{H} matrix, equation C.1b) while reducing within-class scatter (the \mathbf{E} matrix, equation C.2). There are fundamental differences between classification and clustering. The former would aim at labelling a newly measured ρ_b spectrum into one of the 22 initial benthic classes based on the LDFs, whereas clustering aims at merging groups into clusters based on similarity measures (Hastie et al., 2009). Thus the lower dimensional space that best separates the groups is an appropriate platform for hierarchical (or any type of) clustering.

Unequal variance-covariance between groups is perhaps the greatest factor that influences the computation of the misclassification proportion, τ_m , between group pairs. In the HDC a misclassified point is one where its RMSE is closer to the mean of another group than to its own. This is equivalent to having a separating plane at equal distance between two group means and counting the number of points on their incorrect side. Thus if two groups do not have equal variance-covariance then the location of the separating plane will not be optimal and τ_m will be overestimated. Figure C.6a illustrates that although two groups do not overlap, the unequal variance-covariance causes an unjustified $\tau_m > 5\%$ and hence their amalgamation. Figure C.6b shows that when a water column is modelled the distributions become normal with either increasing depth or water turbidity. Indeed the distributions of *A. anceps* and *H. ramentacea* are multimodal at 0 m depth (Figure C.6a) but then become normal at 3 m (Figure C.6b) and as a consequence τ_m decreases. Note as the water column's depth/turbidity increase, the distance between groups decreases relative to the within-class scatter. The reason for this is that $NE\Delta r_{rs}$ has remained constant, however the attenuating properties of a water column reduce the bottom reflected signal such that its influence on r_{rs} diminishes exponentially with increasing water depth and turbidity. As such the difference in r_{rs} between classes eventually becomes less than the uncertainty and thus the LDA becomes less effective. This suboptimal projection is demonstrated in Figure C.6b where the distributions are normal and separate yet with

$\tau_m > 5\%$. Thus the lack of separation is not necessarily a consequence of the LDA method rather due to the attenuating properties of a water column.

Equations (C.1a) and (C.1b) states that the between class scatter is effectively calculated via the RMSE between the class means and population mean, and therefore influenced by the magnitude (brightness) and shape of the ρ_b spectra. For this reason we have found that bright sediment substrates that are already distinct from the other benthic vegetation classes in spectral space (see Figure 5.1) are also distinct in LD space. This can be detrimental as Loog, Duin, and Haeb-Umbach (2001) demonstrated that the presence of an outlying class (or classes) reduces the separability of the remaining classes in LD space. This has been attributed to the LDA seeking a projection that maximises the distances between groups; in this case one that maximally separates the outlier class from the others (Loog et al., 2001). As such the LDA maintains the distances of existing distinct classes at the cost of higher overlap between the remaining classes. To overcome this Loog et al. (2001) incorporated a weighting scheme to the LDA model that dampened the effect of outlying classes and resulted in a decrease in the overall misclassification rate. In the context of this research, applying such a weighting scheme will likely increase (though slightly) the number of benthic vegetation species able to be discriminated at a given depth and turbidity and thus forms a potential improvement to the HDC algorithm.

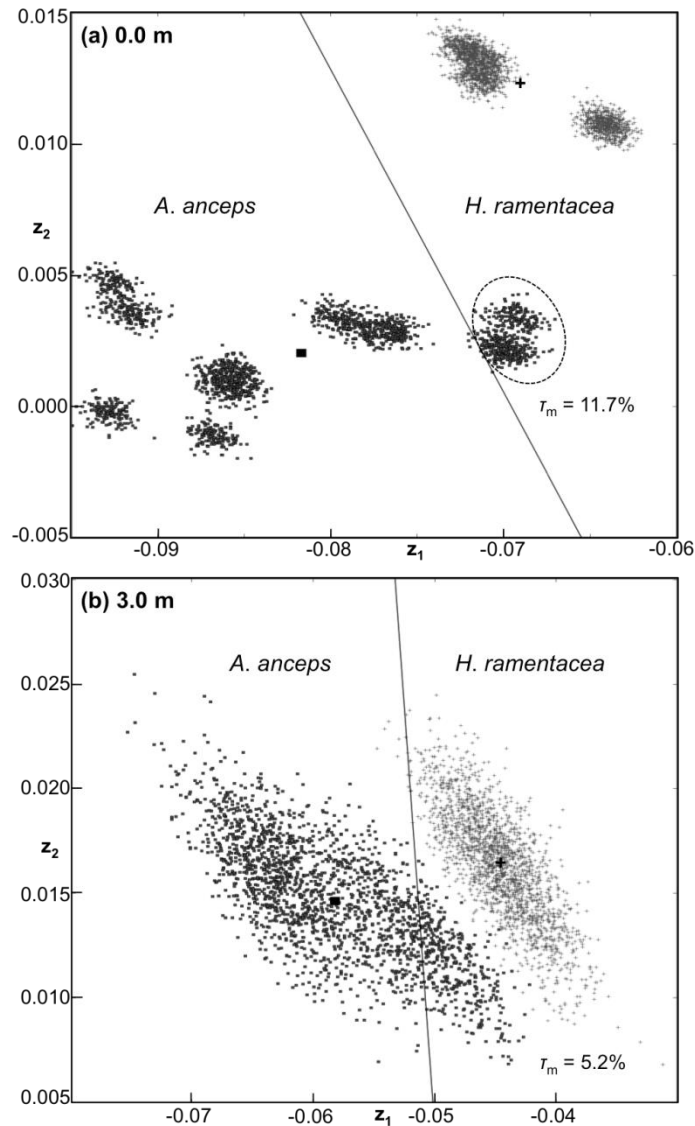


Figure C.6: Effect of non-normality and unequal variance-covariance on the merging of red alga *A. anceps* (squares) and *H. ramentacea* (+) in LD space with WV2 bands. The group means are shown in bold along with the separating plane. (a) ρ_b spectra with no modelled water column, $\tau_m = 11.7\%$; (b) ρ_b with a modelled water column at 3 m depth and IOP type 1 ($P=0.01$, $G=0.01$, $X=0.001$), $\tau_m = 5.2\%$. The circle in (a) highlights the misclassified *A. anceps* spectra.

Quadratic discriminant analysis (QDA) allows the assumption of unequal variances, however this approach was not taken because we are interested in hierarchical clustering rather than improved supervised classification and that QDA performs poorly in the presence of non-normality compared to LDA (Lachenbruch et al., 1973). Furthermore in assigning a group a particular classification the QDA uses the covariance matrix of the individual group. Issues will arise when merging two groups (via averaging) during the hierarchical clustering and then estimating the covariance matrix of this newly formed group. Analysis (results not shown here) have

demonstrated that computing the covariance matrix from the combined ρ_b spectra of two classes dramatically increases the variance of the merged class and subsequent merging eventually leads to all groups clustering together.

APPENDIX D

Statement of Contribution of Others for Chapter 3: “Detecting trend and seasonal changes in bathymetry derived from HICO imagery: A case study of Shark Bay, Western Australia”.

25 June 2015

To Whom It May Concern

I, *Dr. Fearn*s, provided atmospherically corrected HICO imagery and contributed by project supervision and manuscript editing to the paper/publication entitled:

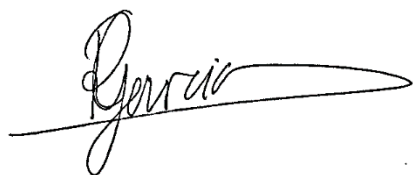
Garcia, R. A., Fearns, P. R. C. S, and McKinna, L. I. W. (2014). Detecting trend and seasonal changes in bathymetry derived from HICO imagery: A case study of Shark Bay, Western Australia. *Remote Sensing of Environment*, 147, 186-205. DOI: <http://dx.doi.org/10.1016/j.rse.2014.03.010>

Undertaken with Rodrigo Garcia



(Signature of Co-Author)

Peter Fearns



(Signature of First Author)

Rodrigo Garcia

Statement of Contribution of Others for Chapter 3:“Detecting trend and seasonal changes in bathymetry derived from HICO imagery: A case study of Shark Bay, Western Australia”.

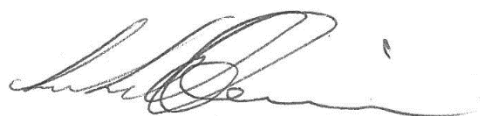
25 June 2015

To Whom It May Concern

I, ***Dr Lachlan Ian William McKinna***, provided atmospherically corrected HICO imagery and contributed by project supervision and manuscript editing to the paper/publication entitled:


Garcia, R. A., Fearn, P. R. C. S, and McKinna, L. I. W. (2014). Detecting trend and seasonal changes in bathymetry derived from HICO imagery: A case study of Shark Bay, Western Australia. *Remote Sensing of Environment*, 147, 186-205. DOI: <http://dx.doi.org/10.1016/j.rse.2014.03.010>

Undertaken with Rodrigo Garcia



(Signature of Co-Author)

Lachlan Ian William McKinna, PhD



(Signature of First Author)

Rodrigo Garcia

ELSEVIER LICENSE TERMS AND CONDITIONS

Jan 19, 2016

This is a License Agreement between Rodrigo A Garcia ("You") and Elsevier ("Elsevier") provided by Copyright Clearance Center ("CCC"). The license consists of your order details, the terms and conditions provided by Elsevier, and the payment terms and conditions.

All payments must be made in full to CCC. For payment instructions, please see information listed at the bottom of this form.

Supplier	Elsevier Limited The Boulevard, Langford Lane Kidlington, Oxford, OX5 1GB, UK
Registered Company Number	1982084
Customer name	Rodrigo A Garcia
Customer address	
License number	3792391021344
License date	Jan 19, 2016
Licensed content publisher	Elsevier
Licensed content publication	Remote Sensing of Environment
Licensed content title	Detecting trend and seasonal changes in bathymetry derived from HICO imagery: A case study of Shark Bay, Western Australia
Licensed content author	Rodrigo A. Garcia, Peter R.C.S. Fearn, Lachlan I.W. McKinna
Licensed content date	5 May 2014
Licensed content volume number	147
Licensed content issue number	n/a
Number of pages	20
Start Page	186
End Page	205
Type of Use	reuse in a thesis/dissertation
Portion	full article
Format	both print and electronic
Are you the author of this Elsevier article?	Yes
Will you be translating?	No
Title of your thesis/dissertation	Uncertainty in Hyperspectral Remote Sensing: Analysis of the Potential and Limitation of Shallow Water Bathymetry and Benthic Classification
Expected completion date	Jan 2016

Estimated size (number of pages)	287
Elsevier VAT number	GB 494 6272 12
Permissions price	0.00 AUD
VAT/Local Sales Tax	0.00 AUD / 0.00 GBP
Total	0.00 AUD
Terms and Conditions	

INTRODUCTION

1. The publisher for this copyrighted material is Elsevier. By clicking "accept" in connection with completing this licensing transaction, you agree that the following terms and conditions apply to this transaction (along with the Billing and Payment terms and conditions established by Copyright Clearance Center, Inc. ("CCC"), at the time that you opened your Rightslink account and that are available at any time at <http://myaccount.copyright.com>).

GENERAL TERMS

2. Elsevier hereby grants you permission to reproduce the aforementioned material subject to the terms and conditions indicated.

3. Acknowledgement: If any part of the material to be used (for example, figures) has appeared in our publication with credit or acknowledgement to another source, permission must also be sought from that source. If such permission is not obtained then that material may not be included in your publication/copies. Suitable acknowledgement to the source must be made, either as a footnote or in a reference list at the end of your publication, as follows:

"Reprinted from Publication title, Vol /edition number, Author(s), Title of article / title of chapter, Pages No., Copyright (Year), with permission from Elsevier [OR APPLICABLE SOCIETY COPYRIGHT OWNER]." Also Lancet special credit - "Reprinted from The Lancet, Vol. number, Author(s), Title of article, Pages No., Copyright (Year), with permission from Elsevier."

4. Reproduction of this material is confined to the purpose and/or media for which permission is hereby given.

5. Altering/Modifying Material: Not Permitted. However figures and illustrations may be altered/adapted minimally to serve your work. Any other abbreviations, additions, deletions and/or any other alterations shall be made only with prior written authorization of Elsevier Ltd. (Please contact Elsevier at permissions@elsevier.com)

6. If the permission fee for the requested use of our material is waived in this instance, please be advised that your future requests for Elsevier materials may attract a fee.

7. Reservation of Rights: Publisher reserves all rights not specifically granted in the combination of (i) the license details provided by you and accepted in the course of this licensing transaction, (ii) these terms and conditions and (iii) CCC's Billing and Payment terms and conditions.

8. License Contingent Upon Payment: While you may exercise the rights licensed immediately upon issuance of the license at the end of the licensing process for the transaction, provided that you have disclosed complete and accurate details of your proposed use, no license is finally effective unless and until full payment is received from you (either by publisher or by CCC) as provided in CCC's Billing and Payment terms and conditions. If full payment is not received on a timely basis, then any license preliminarily granted shall be deemed automatically

revoked and shall be void as if never granted. Further, in the event that you breach any of these terms and conditions or any of CCC's Billing and Payment terms and conditions, the license is automatically revoked and shall be void as if never granted. Use of materials as described in a revoked license, as well as any use of the materials beyond the scope of an unrevoked license, may constitute copyright infringement and publisher reserves the right to take any and all action to protect its copyright in the materials.

9. **Warranties:** Publisher makes no representations or warranties with respect to the licensed material.

10. **Indemnity:** You hereby indemnify and agree to hold harmless publisher and CCC, and their respective officers, directors, employees and agents, from and against any and all claims arising out of your use of the licensed material other than as specifically authorized pursuant to this license.

11. **No Transfer of License:** This license is personal to you and may not be sublicensed, assigned, or transferred by you to any other person without publisher's written permission.

12. **No Amendment Except in Writing:** This license may not be amended except in a writing signed by both parties (or, in the case of publisher, by CCC on publisher's behalf).

13. **Objection to Contrary Terms:** Publisher hereby objects to any terms contained in any purchase order, acknowledgment, check endorsement or other writing prepared by you, which terms are inconsistent with these terms and conditions or CCC's Billing and Payment terms and conditions. These terms and conditions, together with CCC's Billing and Payment terms and conditions (which are incorporated herein), comprise the entire agreement between you and publisher (and CCC) concerning this licensing transaction. In the event of any conflict between your obligations established by these terms and conditions and those established by CCC's Billing and Payment terms and conditions, these terms and conditions shall control.

14. **Revocation:** Elsevier or Copyright Clearance Center may deny the permissions described in this License at their sole discretion, for any reason or no reason, with a full refund payable to you. Notice of such denial will be made using the contact information provided by you. Failure to receive such notice will not alter or invalidate the denial. In no event will Elsevier or Copyright Clearance Center be responsible or liable for any costs, expenses or damage incurred by you as a result of a denial of your permission request, other than a refund of the amount(s) paid by you to Elsevier and/or Copyright Clearance Center for denied permissions.

LIMITED LICENSE

The following terms and conditions apply only to specific license types:

15. **Translation:** This permission is granted for non-exclusive world **English** rights only unless your license was granted for translation rights. If you licensed translation rights you may only translate this content into the languages you requested. A professional translator must perform all translations and reproduce the content word for word preserving the integrity of the article.

16. **Posting licensed content on any Website:** The following terms and conditions apply as follows: Licensing material from an Elsevier journal: All content posted to the web site must maintain the copyright information line on the bottom of each image; A hyper-text must be included to the Homepage of the journal from which you are licensing at <http://www.sciencedirect.com/science/journal/xxxxx> or the

Elsevier homepage for books at <http://www.elsevier.com>; Central Storage: This license does not include permission for a scanned version of the material to be stored in a central repository such as that provided by Heron/XanEdu.

Licensing material from an Elsevier book: A hyper-text link must be included to the Elsevier homepage at <http://www.elsevier.com>. All content posted to the web site must maintain the copyright information line on the bottom of each image.

Posting licensed content on Electronic reserve: In addition to the above the following clauses are applicable: The web site must be password-protected and made available only to bona fide students registered on a relevant course. This permission is granted for 1 year only. You may obtain a new license for future website posting.

17. For journal authors: the following clauses are applicable in addition to the above:

Preprints:

A preprint is an author's own write-up of research results and analysis, it has not been peer-reviewed, nor has it had any other value added to it by a publisher (such as formatting, copyright, technical enhancement etc.).

Authors can share their preprints anywhere at any time. Preprints should not be added to or enhanced in any way in order to appear more like, or to substitute for, the final versions of articles however authors can update their preprints on arXiv or RePEc with their Accepted Author Manuscript (see below).

If accepted for publication, we encourage authors to link from the preprint to their formal publication via its DOI. Millions of researchers have access to the formal publications on ScienceDirect, and so links will help users to find, access, cite and use the best available version. Please note that Cell Press, The Lancet and some society-owned have different preprint policies. Information on these policies is available on the journal homepage.

Accepted Author Manuscripts: An accepted author manuscript is the manuscript of an article that has been accepted for publication and which typically includes author-incorporated changes suggested during submission, peer review and editor-author communications.

Authors can share their accepted author manuscript:

- immediately
 - via their non-commercial person homepage or blog
 - by updating a preprint in arXiv or RePEc with the accepted manuscript
 - via their research institute or institutional repository for internal institutional uses or as part of an invitation-only research collaboration work-group
 - directly by providing copies to their students or to research collaborators for their personal use

- for private scholarly sharing as part of an invitation-only work group on commercial sites with which Elsevier has an agreement
- after the embargo period
 - via non-commercial hosting platforms such as their institutional repository
 - via commercial sites with which Elsevier has an agreement

In all cases accepted manuscripts should:

- – link to the formal publication via its DOI
- – bear a CC-BY-NC-ND license - this is easy to do
- – if aggregated with other manuscripts, for example in a repository or other site, be shared in alignment with our hosting policy not be added to or enhanced in any way to appear more like, or to substitute for, the published journal article.

Published journal article (JPA): A published journal article (PJA) is the definitive final record of published research that appears or will appear in the journal and embodies all value-adding publishing activities including peer review co-ordination, copy-editing, formatting, (if relevant) pagination and online enrichment.

Policies for sharing publishing journal articles differ for subscription and gold open access articles:

Subscription Articles: If you are an author, please share a link to your article rather than the full-text. Millions of researchers have access to the formal publications on ScienceDirect, and so links will help your users to find, access, cite, and use the best available version.

Theses and dissertations which contain embedded PJAs as part of the formal submission can be posted publicly by the awarding institution with DOI links back to the formal publications on ScienceDirect.

If you are affiliated with a library that subscribes to ScienceDirect you have additional private sharing rights for others' research accessed under that agreement. This includes use for classroom teaching and internal training at the institution (including use in course packs and courseware programs), and inclusion of the article for grant funding purposes.

Gold Open Access Articles: May be shared according to the author-selected end-user license and should contain a [CrossMark logo](#), the end user license, and a DOI link to the formal publication on ScienceDirect.

Please refer to Elsevier's [posting policy](#) for further information.

18. **For book authors** the following clauses are applicable in addition to the above: Authors are permitted to place a brief summary of their work online only. You are not allowed to download and post the published electronic version of your chapter, nor may you scan the printed edition to create an electronic

version. **Posting to a repository:** Authors are permitted to post a summary of their chapter only in their institution's repository.

19. **Thesis/Dissertation:** If your license is for use in a thesis/dissertation your thesis may be submitted to your institution in either print or electronic form. Should your thesis be published commercially, please reapply for permission. These requirements include permission for the Library and Archives of Canada to supply single copies, on demand, of the complete thesis and include permission for Proquest/UMI to supply single copies, on demand, of the complete thesis. Should your thesis be published commercially, please reapply for permission. Theses and dissertations which contain embedded PJAs as part of the formal submission can be posted publicly by the awarding institution with DOI links back to the formal publications on ScienceDirect.

Elsevier Open Access Terms and Conditions

You can publish open access with Elsevier in hundreds of open access journals or in nearly 2000 established subscription journals that support open access publishing. Permitted third party re-use of these open access articles is defined by the author's choice of Creative Commons user license. See our [open access license policy](#) for more information.

Terms & Conditions applicable to all Open Access articles published with Elsevier:

Any reuse of the article must not represent the author as endorsing the adaptation of the article nor should the article be modified in such a way as to damage the author's honour or reputation. If any changes have been made, such changes must be clearly indicated.

The author(s) must be appropriately credited and we ask that you include the end user license and a DOI link to the formal publication on ScienceDirect.

If any part of the material to be used (for example, figures) has appeared in our publication with credit or acknowledgement to another source it is the responsibility of the user to ensure their reuse complies with the terms and conditions determined by the rights holder.

Additional Terms & Conditions applicable to each Creative Commons user license:

CC BY: The CC-BY license allows users to copy, to create extracts, abstracts and new works from the Article, to alter and revise the Article and to make commercial use of the Article (including reuse and/or resale of the Article by commercial entities), provided the user gives appropriate credit (with a link to the formal publication through the relevant DOI), provides a link to the license, indicates if changes were made and the licensor is not represented as endorsing the use made of the work. The full details of the license are available at <http://creativecommons.org/licenses/by/4.0>.

CC BY NC SA: The CC BY-NC-SA license allows users to copy, to create extracts, abstracts and new works from the Article, to alter and revise the Article, provided this is not done for commercial purposes, and that the user gives appropriate credit (with a link to the formal publication through the relevant DOI), provides a link to the license, indicates if changes were made and the licensor is not represented as endorsing the use made of the work. Further, any new works

must be made available on the same conditions. The full details of the license are available at <http://creativecommons.org/licenses/by-nc-sa/4.0>.

CC BY NC ND: The CC BY-NC-ND license allows users to copy and distribute the Article, provided this is not done for commercial purposes and further does not permit distribution of the Article if it is changed or edited in any way, and provided the user gives appropriate credit (with a link to the formal publication through the relevant DOI), provides a link to the license, and that the licensor is not represented as endorsing the use made of the work. The full details of the license are available at <http://creativecommons.org/licenses/by-nc-nd/4.0>. Any commercial reuse of Open Access articles published with a CC BY NC SA or CC BY NC ND license requires permission from Elsevier and will be subject to a fee.

Commercial reuse includes:

- – Associating advertising with the full text of the Article
- – Charging fees for document delivery or access
- – Article aggregation
- – Systematic distribution via e-mail lists or share buttons

Posting or linking by commercial companies for use by customers of those companies.

20. Other Conditions:

v1.8

Questions? customer@copyright.com or +1-855-239-3415 (toll free in the US) or +1-978-646-2777.

APPENDIX E

Statement of Contribution of Others for Chapter 4: “Improving the optimization solution for a semi-analytical shallow water inversion model in the presence of spectrally correlated noise”.

25 June 2015

To Whom It May Concern

I, *Dr Lachlan Ian William McKinna*, contributed by project supervision and manuscript editing to the paper/publication entitled:

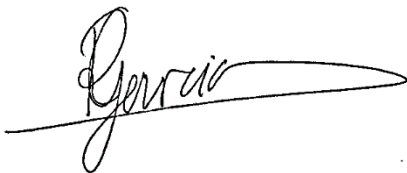
Garcia, R. A., L. I. W. McKinna, Hedley, J. D, and Fearn, P.R.C.S. (2014). Improving the optimization solution for a semi-analytical shallow water inversion model in the presence of spectrally correlated noise. *Limnology and Oceanography: Methods*, 12, 651-669. DOI: 10.4319/lom.2014.12.651

Undertaken with Rodrigo Garcia



(Signature of Co-Author)

Lachlan Ian William McKinna, PhD



(Signature of First Author)

Rodrigo Garcia

Statement of Contribution of Others for Chapter 4: “Improving the optimization solution for a semi-analytical shallow water inversion model in the presence of spectrally correlated noise”.

25 June 2015

To Whom It May Concern

I, Dr. Hedley contributed by project supervision and manuscript editing to the paper/publication entitled:

Garcia, R. A., L. I. W. McKinna, Hedley, J. D, and Fearn, P.R.C.S. (2014). Improving the optimization solution for a semi-analytical shallow water inversion model in the presence of spectrally correlated noise. *Limnology and Oceanography: Methods*, 12, 651-669. DOI: 10.4319/lom.2014.12.651

Undertaken with Rodrigo Garcia



(Signature of Co-Author)

John Hedley



(Signature of First Author)

Rodrigo Garcia

Statement of Contribution of Others for Chapter 4: “Improving the optimization solution for a semi-analytical shallow water inversion model in the presence of spectrally correlated noise”.

25 June 2015

To Whom It May Concern

I, **Dr. Peter Fearn**s, contributed by project supervision and manuscript editing to the paper/publication entitled:


Garcia, R. A., L. I. W. McKinna, Hedley, J. D, and Fearn, P.R.C.S. (2014).
Improving the optimization solution for a semi-analytical shallow water inversion model in the presence of spectrally correlated noise. *Limnology and Oceanography: Methods*, 12, 651-669. DOI: 10.4319/lom.2014.12.651

Undertaken with Rodrigo Garcia



(Signature of Co-Author)

Dr. Peter Fearns



(Signature of First Author)

Rodrigo Garcia

**JOHN WILEY AND SONS LICENSE
TERMS AND CONDITIONS**

Jan 19, 2016

This Agreement between Rodrigo A Garcia ("You") and John Wiley and Sons ("John Wiley and Sons") consists of your license details and the terms and conditions provided by John Wiley and Sons and Copyright Clearance Center.

License Number	3792800512946
License date	Jan 19, 2016
Licensed Content Publisher	John Wiley and Sons
Licensed Content Publication	Limnology and Oceanography: Methods
Licensed Content Title	Improving the optimization solution for a semi-analytical shallow water inversion model in the presence of spectrally correlated noise
Licensed Content Author	Rodrigo A. Garcia, Lachlan I.W. McKinna, John D. Hedley, Peter R.C.S. Fearn
Licensed Content Date	Oct 17, 2014
Pages	19
Type of use	Dissertation/Thesis
Requestor type	Author of this Wiley article
Format	Print and electronic
Portion	Full article
Will you be translating?	No
Title of your thesis / dissertation	Uncertainty in Hyperspectral Remote Sensing: Analysis of the Potential and Limitation of Shallow Water Bathymetry and Benthic Classification
Expected completion date	Jan 2016
Expected size (number of pages)	287
Requestor Location	Rodrigo A Garcia
Billing Type	Attn: Rodrigo A Garcia Invoice
Billing Address	Rodrigo A Garcia
Total	Attn: Rodrigo A Garcia 0.00 AUD
Terms and Conditions	

TERMS AND CONDITIONS

This copyrighted material is owned by or exclusively licensed to John Wiley & Sons, Inc. or one of its group companies (each a "Wiley Company") or handled on behalf of a society with which a Wiley Company has exclusive publishing rights in relation to a particular work (collectively "WILEY"). By clicking "accept" in connection with completing this licensing transaction, you agree that the following terms and conditions apply to this transaction (along with the billing and payment terms and conditions established by the Copyright Clearance Center Inc., ("CCC's Billing and Payment terms and conditions"), at the time that you opened your RightsLink account (these are available at any time at <http://myaccount.copyright.com>).

Terms and Conditions

- The materials you have requested permission to reproduce or reuse (the "Wiley Materials") are protected by copyright.
- You are hereby granted a personal, non-exclusive, non-sub licensable (on a stand-alone basis), non-transferable, worldwide, limited license to reproduce the Wiley Materials for the purpose specified in the licensing process. This license, **and any CONTENT (PDF or image file) purchased as part of your order**, is for a one-time use only and limited to any maximum distribution number specified in the license. The first instance of republication or reuse granted by this license must be completed within two years of the date of the grant of this license (although copies prepared before the end date may be distributed thereafter). The Wiley Materials shall not be used in any other manner or for any other purpose, beyond what is granted in the license. Permission is granted subject to an appropriate acknowledgement given to the author, title of the material/book/journal and the publisher. You shall also duplicate the copyright notice that appears in the Wiley publication in your use of the Wiley Material. Permission is also granted on the understanding that nowhere in the text is a previously published source acknowledged for all or part of this Wiley Material. Any third party content is expressly excluded from this permission.
- With respect to the Wiley Materials, all rights are reserved. Except as expressly granted by the terms of the license, no part of the Wiley Materials may be copied, modified, adapted (except for minor reformatting required by the new Publication), translated, reproduced, transferred or distributed, in any form or by any means, and no derivative works may be made based on the Wiley Materials without the prior permission of the respective copyright owner. **For STM Signatory Publishers clearing permission under the terms of the STM Permissions Guidelines only, the terms of the license are extended to include subsequent editions and for editions in other languages, provided such editions are for the work as a whole in situ and does not involve the separate exploitation of the permitted figures or extracts**, You may not alter, remove or suppress in any manner any copyright, trademark or other notices displayed by the Wiley Materials. You may not license, rent, sell, loan, lease, pledge, offer as security, transfer

or assign the Wiley Materials on a stand-alone basis, or any of the rights granted to you hereunder to any other person.

- The Wiley Materials and all of the intellectual property rights therein shall at all times remain the exclusive property of John Wiley & Sons Inc, the Wiley Companies, or their respective licensors, and your interest therein is only that of having possession of and the right to reproduce the Wiley Materials pursuant to Section 2 herein during the continuance of this Agreement. You agree that you own no right, title or interest in or to the Wiley Materials or any of the intellectual property rights therein. You shall have no rights hereunder other than the license as provided for above in Section 2. No right, license or interest to any trademark, trade name, service mark or other branding ("Marks") of WILEY or its licensors is granted hereunder, and you agree that you shall not assert any such right, license or interest with respect thereto
- NEITHER WILEY NOR ITS LICENSORS MAKES ANY WARRANTY OR REPRESENTATION OF ANY KIND TO YOU OR ANY THIRD PARTY, EXPRESS, IMPLIED OR STATUTORY, WITH RESPECT TO THE MATERIALS OR THE ACCURACY OF ANY INFORMATION CONTAINED IN THE MATERIALS, INCLUDING, WITHOUT LIMITATION, ANY IMPLIED WARRANTY OF MERCHANTABILITY, ACCURACY, SATISFACTORY QUALITY, FITNESS FOR A PARTICULAR PURPOSE, USABILITY, INTEGRATION OR NON-INFRINGEMENT AND ALL SUCH WARRANTIES ARE HEREBY EXCLUDED BY WILEY AND ITS LICENSORS AND WAIVED BY YOU.
- WILEY shall have the right to terminate this Agreement immediately upon breach of this Agreement by you.
- You shall indemnify, defend and hold harmless WILEY, its Licensors and their respective directors, officers, agents and employees, from and against any actual or threatened claims, demands, causes of action or proceedings arising from any breach of this Agreement by you.
- IN NO EVENT SHALL WILEY OR ITS LICENSORS BE LIABLE TO YOU OR ANY OTHER PARTY OR ANY OTHER PERSON OR ENTITY FOR ANY SPECIAL, CONSEQUENTIAL, INCIDENTAL, INDIRECT, EXEMPLARY OR PUNITIVE DAMAGES, HOWEVER CAUSED, ARISING OUT OF OR IN CONNECTION WITH THE DOWNLOADING, PROVISIONING, VIEWING OR USE OF THE MATERIALS REGARDLESS OF THE FORM OF ACTION, WHETHER FOR BREACH OF CONTRACT, BREACH OF WARRANTY, TORT, NEGLIGENCE, INFRINGEMENT OR OTHERWISE (INCLUDING, WITHOUT LIMITATION, DAMAGES BASED ON LOSS OF PROFITS, DATA, FILES, USE, BUSINESS OPPORTUNITY OR CLAIMS OF THIRD PARTIES), AND WHETHER OR NOT THE PARTY HAS BEEN ADVISED OF THE POSSIBILITY OF SUCH DAMAGES. THIS LIMITATION SHALL APPLY NOTWITHSTANDING ANY FAILURE

OF ESSENTIAL PURPOSE OF ANY LIMITED REMEDY PROVIDED HEREIN.

- Should any provision of this Agreement be held by a court of competent jurisdiction to be illegal, invalid, or unenforceable, that provision shall be deemed amended to achieve as nearly as possible the same economic effect as the original provision, and the legality, validity and enforceability of the remaining provisions of this Agreement shall not be affected or impaired thereby.
- The failure of either party to enforce any term or condition of this Agreement shall not constitute a waiver of either party's right to enforce each and every term and condition of this Agreement. No breach under this agreement shall be deemed waived or excused by either party unless such waiver or consent is in writing signed by the party granting such waiver or consent. The waiver by or consent of a party to a breach of any provision of this Agreement shall not operate or be construed as a waiver of or consent to any other or subsequent breach by such other party.
- This Agreement may not be assigned (including by operation of law or otherwise) by you without WILEY's prior written consent.
- Any fee required for this permission shall be non-refundable after thirty (30) days from receipt by the CCC.
- These terms and conditions together with CCC's Billing and Payment terms and conditions (which are incorporated herein) form the entire agreement between you and WILEY concerning this licensing transaction and (in the absence of fraud) supersedes all prior agreements and representations of the parties, oral or written. This Agreement may not be amended except in writing signed by both parties. This Agreement shall be binding upon and inure to the benefit of the parties' successors, legal representatives, and authorized assigns.
- In the event of any conflict between your obligations established by these terms and conditions and those established by CCC's Billing and Payment terms and conditions, these terms and conditions shall prevail.
- WILEY expressly reserves all rights not specifically granted in the combination of (i) the license details provided by you and accepted in the course of this licensing transaction, (ii) these terms and conditions and (iii) CCC's Billing and Payment terms and conditions.
- This Agreement will be void if the Type of Use, Format, Circulation, or Requestor Type was misrepresented during the licensing process.
- This Agreement shall be governed by and construed in accordance with the laws of the State of New York, USA, without regards to such state's conflict of law rules. Any legal action, suit or proceeding arising out of or relating to these Terms and Conditions or the breach thereof shall be instituted in a court of competent jurisdiction in New York County in the State of New

York in the United States of America and each party hereby consents and submits to the personal jurisdiction of such court, waives any objection to venue in such court and consents to service of process by registered or certified mail, return receipt requested, at the last known address of such party.

WILEY OPEN ACCESS TERMS AND CONDITIONS

Wiley Publishes Open Access Articles in fully Open Access Journals and in Subscription journals offering Online Open. Although most of the fully Open Access journals publish open access articles under the terms of the Creative Commons Attribution (CC BY) License only, the subscription journals and a few of the Open Access Journals offer a choice of Creative Commons Licenses. The license type is clearly identified on the article.

The Creative Commons Attribution License

The Creative Commons Attribution License (CC-BY) allows users to copy, distribute and transmit an article, adapt the article and make commercial use of the article. The CC-BY license permits commercial and non-

Creative Commons Attribution Non-Commercial License

The Creative Commons Attribution Non-Commercial (CC-BY-NC) License permits use, distribution and reproduction in any medium, provided the original work is properly cited and is not used for commercial purposes.(see below)

Creative Commons Attribution-Non-Commercial-NoDerivs License

The Creative Commons Attribution Non-Commercial-NoDerivs License (CC-BY-NC-ND) permits use, distribution and reproduction in any medium, provided the original work is properly cited, is not used for commercial purposes and no modifications or adaptations are made. (see below)

Use by commercial "for-profit" organizations

Use of Wiley Open Access articles for commercial, promotional, or marketing purposes requires further explicit permission from Wiley and will be subject to a fee.

Further details can be found on Wiley Online Library <http://olabout.wiley.com/WileyCDA/Section/id-410895.html>

Other Terms and Conditions:

v1.10 Last updated September 2015

Questions? customercare@copyright.com or +1-855-239-3415 (toll free in the US) or +1-978-646-2777.

APPENDIX F

Statement of Contribution of Others for Chapter 5: “A method to analyze the potential of optical remote sensing for benthic habitat mapping”.

21 September 2015

To Whom It May Concern

I, Dr. Hedley, contributed by project supervision and manuscript editing to the paper/publication entitled:

Garcia, R. A., Hedley, J. D., Hoang, T. C., and Fearn, P. R. C. S. (2015). A method to analyze the potential of optical remote sensing for benthic habitat mapping. *Remote Sensing*, 7(10), 13157-13189. DOI: 10.3390/rs71013157.

Undertaken with Rodrigo Garcia

(Signature of Co-Author)

Dr. John Hedley

A handwritten signature in black ink, appearing to read 'J Hedley', with a long horizontal stroke extending to the right.

(Signature of First Author)

Rodrigo Garcia

A handwritten signature in black ink, appearing to read 'Rodrigo Garcia', with a long horizontal stroke extending to the right.

Statement of Contribution of Others for Chapter 5: “A method to analyze the potential of optical remote sensing for benthic habitat mapping”.

21 September 2015

To Whom It May Concern

I, Mr. Tin C. Hoang, contributed by project supervision and manuscript editing to the paper/publication entitled:

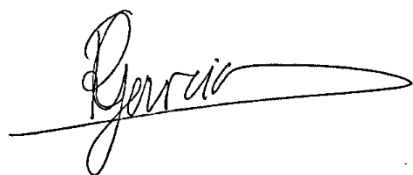
Garcia, R. A., Hedley, J. D., Hoang, T. C., and Fearn, P. R. C. S. (2015). A method to analyze the potential of optical remote sensing for benthic habitat mapping. *Remote Sensing*, 7(10), 13157-13189. DOI: 10.3390/rs71013157.

Undertaken with Rodrigo Garcia

(Signature of Co-Author)



Hoang Cong Tin



(Signature of First Author)

Rodrigo Garcia

Statement of Contribution of Others for Chapter 5: “A method to analyze the potential of optical remote sensing for benthic habitat mapping”.

21 September 2015

To Whom It May Concern

I, **Dr. Peter Fearn**s, contributed by project supervision and manuscript editing to the paper/publication entitled:

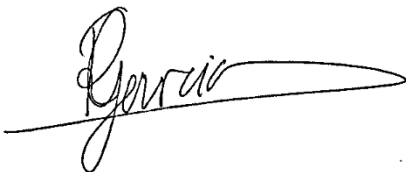
Garcia, R. A., Hedley, J. D., Hoang, T. C., and Fearns, P. R. C. S. (2015). A method to analyze the potential of optical remote sensing for benthic habitat mapping. *Remote Sensing*, 7(10), 13157-13189. DOI: 10.3390/rs71013157.

Undertaken with Rodrigo Garcia



(Signature of Co-Author)

Dr. Peter Fearns



(Signature of First Author)

Rodrigo Garcia

REFERENCES

- Ahmad, Z., Franz, B. A., McClain, C. R., Kwiatkowska, E. J., Werdell, J., Shettle, E. P., & Holben, B. N. (2010). New aerosol models for the retrieval of aerosol optical thickness and normalized water-leaving radiances from the SeaWiFS and MODIS sensors over coastal regions and Open Oceans. *Applied Optics*, 49(29), 5545-5560.
- Albert, A., & Mobley, C. D. (2003). An analytical model for subsurface irradiance and remote sensing reflectance in deep and shallow case-2 waters. *Optics Express*. 11(22): 2873-2890.
- Anderberg, M. R. (1973). *Cluster Analysis For Applications*. New York: Academic Press
- Anderson, G. P., Felde, G. W., Hoke, M. L., Ratkowski, A. J., Cooley, T. W., Chetwynd, J. H., ... Lewis, P. E. (2002). MODTRAN4-based atmospheric correction algorithm: FLAASH (fast line-of-sight atmospheric analysis of spectral hypercubes). *Proceedings of SPIE*, 4725, Algorithms and Technologies for Multispectral, Hyperspectral, and Ultraspectral Imagery VIII, 65 (August 1, 2002); doi:10.1117/12.478737.
- Andrefouet, S., Kramer, P., Torres-Pulliza, D., Joyce, K. E., Hochberg, E. J., Garcia-Perez, R., ... Muller-Karger, F. E. (2003). Multi-site evaluation of IKONOS data for classification of tropical coral reef environments. *Remote Sensing of Environment*, 88, 128-143.
- Antoine, D., d'Ortenzio, F., Hooker, S. B., Becu, G., Gentili, B., Tailliez, D., & Scott, A. J. (2008). Assessment of uncertainty in the ocean reflectance determined by three satellite ocean color sensors (MERIS, SeaWiFS and MODIS-A) at an offshore site in the Mediterranean Sea (BOUSSOLE project). *Journal of Geophysical Research*, 113, C07013

- Aronson, R. B., & Pretch, W. F. (2006). Conservation, precaution, and Caribbean reefs. *Coral Reefs*, 25, 441-450.
- Babin, M., Morel, A., Fournier-Sicre, V., Fell, F., & Stramski, D. (2003a). Light scattering properties of marine particles in coastal and open ocean waters as related to the particle mass concentration. *Limnology and Oceanography*, 48(2), 843-859.
- Babin, M., Stramski, D., Ferrari, G. M., Claustre, H., Bricaud, A., Obolensky, G., & Hoepffner, N. (2003b). Variations in the light absorption coefficients of phytoplankton, nonalgal particulates, and dissolved organic matter in coastal waters around Europe. *Journal of Geophysical Research*, 108(C7), 3211-3231.
- Bachmann, C. M., Ainsworth, T. L., Fusina, R. A., Montes, M. J., Bowles, J. H., Korwan, D. R., & Gillis, D. B. (2009). Bathymetric retrieval from hyperspectral imagery using manifold coordinate representations. *IEEE Transactions on Geoscience and Remote Sensing*, 47(3), 884-897.
- Bailey, S. W., Franz, B. A., & Werdell, P. J. (2010). Estimation of near-infrared water-leaving reflectance for satellite ocean color data processing. *Optics Express*, 18(7), 7521-7527.
- Barbera, C., Moranta, J., Ordines, F., Ramon, F., de Mesa, A., Diaz-Valdes, M., ... Massuti, E. (2012). Biodiversity and habitat mapping of Menorca Channel (western Mediterranean): implications for conservation. *Biodiversity and Conservation*, 21, 701-728.
- Basheer, I. A., & Hajmeer, M. (2000). Artificial neural networks: fundamentals, computing, design, and application. *Journal of Microbiology Methods*, 43, 3-31.

- Bax, N. J., & Williams, A. (2001). Seabed habitat on the south-eastern Australian continental shelf: context, vulnerability and monitoring. *Marine and Freshwater Research*, 52, 491-512.
- Benfield, S. L., Guzman, H. M., Mair, J. M., & Young, J. A. T. (2007). Mapping the distribution of coral reefs and associated sublittoral habitats in Pacific Panama: a comparison of optical satellite sensors and classification methodologies. *International Journal of Remote Sensing*, 28(22), 5047-5070, DOI: 10.1080/01431160701258062.
- Berk, A., Anderson, G. P., Acharya, P. K., Bernstein, L. S., Muratov, L., Lee, J., ... Shettle, E. P. (2006). MODTRAN5: 2006 Update, *Proceedings of SPIE*, 6233, Algorithms and Technologies for Multispectral, Hyperspectral, and Ultraspectral Imagery XII, 62331F (8 May 2006); doi:10.1117/12.665077.
- Bicheron, P., Amberg, V., Bourg, L., Petit, D., Huc, M., Miras, B., ... Arino, O. (2011). Geolocation assessment of MERIS GlobCover orthorectified products. *IEEE Transactions on Geoscience and Remote Sensing*, 49(8), 2972-2982.
- Botha, E. J., Brando, V. E., Anstee, J. M., Dekker, A. G., & Sagar, S. (2013). Increased spectral resolution enhances coral detection under varying water conditions. *Remote Sensing of Environment*, 131, 247-261.
- Bowers, D. G., Harker, G. E. L., & Stephan, B. (1996). Absorption spectra of inorganic particles in the Irish Sea and their relevance to remote sensing of chlorophyll. *International Journal of Remote Sensing*, 17(12), 2449-2460.
- Brando, V. E., & Dekker, A. G. (2003). Satellite hyperspectral remote sensing for estimating estuarine and coastal water quality. *IEEE Transactions on Geoscience and Remote Sensing*, 41(6), 1378-1387.
- Brando V. E., Anstee J. M., Wettle, M., Dekker, A. G., Phinn, S. R., & Roelfsema, C. (2009). A physics based retrieval and quality assessment of bathymetry

from suboptimal hyperspectral data. *Remote Sensing of Environment*, 113, 755-770.

Bricaud, A., M. Babin, A. Morel, & H. Claustre. (1995). Variability in the chlorophyll-specific absorption coefficients of natural phytoplankton: Analysis and parameterisation. *Journal of Geophysical Research*, 100(C7), 13321-13332.

Bricaud, A., Morel, A., & Prieur, L. (1981). Absorption by dissolved organic matter of the sea (yellow substance) in the UV and visible domains. *Limnology and Oceanography*, 26(1), 43-53.

Burling, M. C. (1998). Oceanographic aspects of Shark Bay Western Australia. M. S. thesis, Centre Water Research, University of Western Australia, Perth, Western Australia, Australia.

Burling, M. C., Pattriaratchi, C. B., & Ivey, G. N. (2003). The tidal regime of Shark Bay, Western Australia. *Estuarine, Coastal and Shelf Science*. 57, 725-735.

Burne, R. V., & Johnson, K. (2012). Sea-level variation and the zonation of microbialites in Hamelin Pool, Shark Bay, Western Australia. *Marine and Freshwater Research*, 64, 994-1004.

Call, K. A., Hardy, J. T., & Wallin, D.O. (2003). Coral reef habitat discrimination using multivariate spectral analysis and satellite remote sensing. *International Journal of Remote Sensing*, 24, 2627-2639.

Calvo, S., Ciraolo, G., La Loggia, G. (2003). Monitoring *Posidonia oceanica* meadows in a Mediterranean coastal lagoon (Stagnone, Italy) by means of neural network and ISODATA classification methods. *International Journal of Remote Sensing*, 24(13), 2703-2716.

Carder, K. L., Hawes, S. K., Baker, K. A., Smith, R. C., Steward, R. G., & Mitchell, B. G. (1991). Reflectance model for quantifying chlorophyll a in the presence

- of productivity degradation products. *Journal of Geophysical Research*, 96, 20599-20611.
- Carder, K. L., Steward, R. G., Harvey, G. R., & Ortner, P. B. (1989). Marine humic and fulvic acids: Their effects on remote sensing of ocean chlorophyll. *Limnology and Oceanography*, 34(1), 68-81.
- Cendrero, A. (1989). Mapping and evaluation of coastal areas for planning. *Ocean and Shoreline Management*, 12, 427-462.
- Ceyhun, O., & Yalcin, A. (2010). Remote Sensing of water depths in shallow waters via artificial neural networks. *Estuarine, Coastal and Shelf Science*, 89, 89-96.
- Chang, C-I. (2000). An information-theoretic approach to spectral variability, similarity, and discrimination for hyperspectral image analysis. *IEEE Transactions on Information Theory*, 46(5), 1927-1932.
- Clark, R. K., Fay, T. H., & Walker, C. L. (1987). Bathymetry calculations with Landsat 4 TM imagery under a generalised ratio assumption. *Applied Optics*, 26(19), 4036-4038.
- Clark, C. D., Mumby, P. J., Chisholm, J. R. M., Jaubert, J., & Andrefouet, S. (2000). Spectral discrimination of coral mortality states following a severe bleaching event. *International Journal of Remote Sensing*, 21, 2321-2327.
- Cogan, C. B., Todd, B. J., Lawton, P., & Noji, T. T. (2009). The role of marine habitat mapping in ecosystem-based management. *ICES Journal of Marine Science*, 66, 2033-2042.
- Conroy, M. J., & Noon, B. R. (1996). Mapping species richness for conservation of biological diversity: conceptual and methodological issues. *Ecological Applications*, 6(3), 763-773.

- Cooper, K., Boyd, S., Eggleton, J., Limpenny, D., Rees, H., & Vanstaen, K. (2007), Recovery of the seabed following marine aggregate dredging on the Hastings Shingle Bank off the southeast coast of England. *Estuarine, Coastal and Shelf Science*, 75, 547-558.
- Coppin, P., Jonckheere I., Nackaerts K., & Muys B. (2004). Digital change detection methods in ecosystem monitoring: a review. *International Journal of Remote Sensing*, 25(9), 1565-1595.
- Corucci, L., Masini, A., & Cococcioni, M. (2011). Approaching bathymetry estimation from high resolution multispectral satellite images using a neuro-fuzzy technique. *Journal of Applied Remote Sensing*, 5, 053515.
- Costanza, R., d'Arge, R., de Groot, R., Farber, S., Grasso, M, Hannon, B., ... van den Belt, M. (1997). The value of the world's ecosystem services and natural capital. *Nature*, 387, 253-260.
- Crebassol, P., Ferrier, P., Dedieu, G., Hagolle, O., Fournie, B., Tinto, F., ... Herscovitz, J. (2010). VEN μ S (Vegetation and Environment Monitoring on a New Micro Satellite). In R. Sandau, H. P. Roser and A. Valenzuela (Eds.), *Small Satellite Missions for Earth Observation: New Development and Trends* (pp. 47-65). Heidelberg, Germany: Springer
- Dai, X., & Khorram, S. (1998). The effects of image misregistration on the accuracy of remotely sensed change detection. *IEEE Transactions on Geoscience and Remote Sensing*. 36(5), 1566-1577.
- Dalleau, M., Andrefoeut, S., Wabnitz, C. C. C., Payri, C., Wantiez, L., Pichon, M., ... Benzoni, F. (2010). Use of habitats as surrogates of biodiversity for efficient coral reef conservation planning in Pacific Ocean islands. *Conservation Biology*, 24(2), 541-552.

- Defoin-Platel, M., & Chami, M. (2007). How ambiguous is the inverse problem of ocean color in coastal waters. *Journal of Geophysical Research*, 112(C3), C03004
- Dekker, A. G., Brando, V. E., & Anstee, J. M. (2005). Retrospective seagrass change detection in a shallow coastal tidal Australian lake. *Remote Sensing of Environment*, 97, 415-433.
- Dekker, A. G., Phinn, S. R., Anstee, J., Bissett, P., Brando, V. E., Casey, B., ... Roelfsema, C. (2011). Intercomparison of shallow water bathymetry, hydro-optics, and benthos mapping techniques in Australian and Caribbean coastal environments. *Limnology and Oceanography, methods*. 9, 396-425.
- Department of Environment and Conservation, n.d. *Birridas*.
<http://www.sharkbay.org/assets/documents/fact%20sheets/birridas%20v2.pdf>
(accessed February 4, 2013).
- Diaz, R. J., Solan, M., & Valente, R. M. (2004). A review of approaches for classifying benthic habitats and evaluating habitat quality. *Journal of Environmental Management*, 73, 165-181.
- Dierssen, H. M., Zimmerman, R. C., Leathers, R. A., Downes, T. V., & Davis, C. O. (2003). Ocean color remote sensing of seagrass and bathymetry in the Bahamas Banks by High-Resolution airborne imagery. *Limnology and Oceanography*. 48(1 part 2), 444-455.
- Doodson, A. T., & Warburg, H. D. (1941). *Admiralty Manual of Tides*. Admiralty, London: Hydrographic Department.
- Egbert, G. D., & Erofeeva, S. Y. (2002). Efficient inverse modeling of barotropic ocean tides. *Journal of Atmospheric and Oceanic Technology*, 19(2), 183-204.
- Ester, M., Kriegel, H-P., Sander, J., & Xu, X. (1996). A density-based algorithm for discovering clusters in large spatial datasets with noise. In *Proceedings of the*

Second International Conference on Knowledge Discovery and Data Mining (KDD-96), Portland, Oregon (pp. 226-231).

In Proceedings of the 10th Australasian Remote Sensing and Photogrammetry Conference, Adelaide, Australia, August 21-25 (pp. 296-311).

Everitt, B. S., Landau, S., Leese, M., & Stahl, D. (2011). *Cluster Analysis* (5th ed.). Wiley Series in Probability and Statistics, John Wiley & Sons, Ltd. ISBN: 9780470977811.

Fabbri, K. P. (1998). A methodology for supporting decision making in integrated coastal zone management. *Ocean and Coastal Management*, 39(1-2), 51-62.

Fabricius, K. E. (2005). Effects of terrestrial runoff on the ecology of corals and coral reefs: review and synthesis. *Marine Pollution Bulletin*, 50, 125-146.

Fairweather, P. G. (1991). Statistical Power and Design Requirements for Environmental Monitoring. *Australian Journal of Marine and Freshwater Research*, 42, 555-567.

Fearn, P. R. C., Klonowski, W., Babcock, R. C., England, P., & Phillips, J. (2011). Shallow water substrate mapping using hyperspectral remote sensing. *Estuarine, Coastal and Shelf Science*, 31:1249-1259.

Ferguson, R. L., & Korfmacher, K. (1997). Remote sensing and GIS analysis of seagrass meadows in North Carolina, USA. *Aquatic Botany*, 58, 241-258.

Fornes, A., Basterretxea, G., Orfila, A., Jordi, A., Alvarez, A., & Tintore, J. (2006). Mapping *Posidonia oceanica* from IKONOS. *ISPRS Journal of Photogrammetry and Remote Sensing*, 60, 315-322

Fyfe, S. K. (2003). Spatial and temporal variation in spectral reflectance: are seagrass species spectrally distinct? *Limnology and Oceanography*, 48(1 part 2), 464-479.

- Galparsoro, I., Borja, A., Legorburu, I., Hernandez, C., Chust, G., Liria, P., & Uriarte, A. (2010). Morphological characteristics of the Basque continental shelf (Bay of Biscay, northern Spain); their implications for Integrated Coastal Zone Management. *Geomorphology*, 118(3-4), 314:329.
- Gao, B., Montes, M. J., Ahmad, Z., & Davis, C. O. (2000). Atmospheric correction algorithm for hyperspectral remote sensing of ocean color from space. *Applied Optics*, 39(6), 887-896.
- Gao, B., Li, R., Lucke, R. L., Davis, C. O., Bevilacqua, R. M., Korwan, D. R., ... Corson M. R. (2012). Vicarious calibrations of HICO data acquired from the International Space Station. *Applied Optics*, 51(14), 2559 – 2567.
- Garcia, R. A., Fearn, P. R. C. S., & McKinna, L. I. W. (2014a). Detecting trend and seasonal changes in bathymetry derived from HICO imagery: A case study of Shark Bay, Western Australia. *Remote Sensing of Environment*, 147, 186-205.
- Garcia, R. A., McKinna, L. I. W., & Fearn, P. R. C. S. (2014b). Improving the optimization solution for a semi-analytical shallow water inversion model in the presence of spectrally correlated noise. *Limnology and Oceanography: Methods*, 12, 651-669.
- Garcia, R. A., Hedley, J. D., Hoang, T. C., & Fearn, P. R. C. S. (2015). A method to analyze the potential of optical remote sensing for benthic habitat mapping. *Remote Sensing*. 7(10), 13157-13189.
- Gholamalifard, M., Kutser, T., Esmaili-Sari, A., Abkar, A. A., & Naimi, B. (2013). Remotely sensed empirical modeling of Bathymetry in the Southeastern Caspian Sea. *Remote Sensing*, 5, 2746-2762.
- Goodman, J. A., Lee, Z., & Ustin, S. L. (2008). Influence of atmospheric and sea-surface corrections on retrieval of bottom depth and reflectance using a semi-

analytical model: a case study in Kaneohe Bay, Hawaii. *Applied Optics*, 47, F1-F11.

Goodman, J. A., Montes, M. J., & Ustin, S. L. (2003). Applying Tafkaa for atmospheric correction of AVIRIS over coral ecosystems in the Hawai'ian islands. *Proceedings of the 12th AVIRIS/HYPERION Earth Science Workshop* (pp. 91–96).

Goodman, J. A., & Ustin, S. L. (2007). Classification of benthic composition in a coral reef environment using spectral unmixing. *Journal of Applied Remote Sensing*, 1, 011501

Gordon, H. R. (1989). Can the Lambert-Beer law be applied to the diffuse attenuation coefficient of ocean water? *Limnology and Oceanography*, 34(8), 1389-1409.

Gordon, H. R., Smith, R. C., & Zaneveld, V. (1980). Introduction to Ocean Optics. *Proceedings of SPIE, vol. 208, Ocean Optics VI October 23-25, 1979* (pp. 14-55)

Gordon, H. R., & Wang, M. (1994). Retrieval of water-leaving radiance and aerosol optical thickness over the oceans with SeaWiFS: A preliminary algorithm. *Applied Optics*, 33, 443-452.

Gray, J. S. (1997). Marine biodiversity: patterns, threats and conservation needs. *Biodiversity and Conservation*, 6, 153-175.

Green, E. P., Mumby, P. J., Edwards, A. J., & Clark, C. D. (1996). A review of remote sensing for the assessment of tropical coastal resources. *Coastal Management*, 21(1), 1-40.

Guenther, G. C., Cunningham, A. G., LaRocque, P. E., & Reid, D. J. (2000). Meeting the accuracy challenge in airborne lidar bathymetry. *20th EARSeL*

Symposium Workshop on Lidar Remote Sensing of Land and Sea, European Association of Remote Sensing Laboratories, Dresden, Germany.

- Gullstrom, M., Lunden, B., Bodin, M., Kangwe, J., Ohman, M. C., Mtolera, M. S. P., & Bjork, M. (2006). Assessment of changes in the seagrass-dominated submerged vegetation of tropical Chwaka Bay (Zanzibar) using satellite remote sensing. *Estuarine, Coastal and Shelf Science*, 67, 399-408.
- Halpern, B. S., Walbridge, S., Selkoe, K. A., Kappel, C. V., Micheli, F., D'Agrosa, C., ... Watson, R. (2008). A global map of human impact on marine Ecosystems. *Science*, 319, 948-952.
- Hardie, R. C., & Boncelet. C. G. (1993). LUM filters: a class of rank-order-based filters for smoothing and sharpening. *IEEE Transactions on Signal Processing*, 41(3), 1061-1076.
- Harvey, M. J., Kobryn, H. T., Beckley, L. E., Heege, T., Hausknecht, P., & Pinnel, N. (2007). Mapping the shallow marine benthic habitats of Rottnest Island, Western Australia. *3rd EARSeL Workshop Remote Sensing of the Coastal Zone, Bolzano, Italy, 7-9 June 2007*. Retrieved from http://researchrepository.murdoch.edu.au/6141/1/mapping_the_shallow_marine_benthic_habitats.pdf
- Hastie, T., Tibshirani, R., & Friedman, J. (2009). *The elements of statistical learning: data mining, inference and prediction* (2nd ed.). New York, NY: Springer. Retrieved from http://web.stanford.edu/~hastie/local.ftp/Springer/OLD/ESLII_print4.pdf
- Hedley, J. (2008). A three-dimensional radiative transfer model for shallow water environments. *Optics Express*, 16(26), 21887-21902.
- Hedley, J. D. (2013). Hyperspectral Applications. In J. A. Goodman, S. J. Purkis and S. R. Phinn (Eds.), *Coral Reef Remote Sensing: a guide for mapping*,

monitoring and management (pp. 79-112). New York, NY: Springer. doi: 10.1007/978-90-481-9292-2

Hedley, J., & Enriquez, S. (2010). Optical properties of canopies of the tropical seagrass *Thalassia testudinum* estimated by a three-dimensional radiative transfer model. *Limnology and Oceanography*, 55(4), 1537-1550.

Hedley, J. D., Harborne, A. R., & Mumby, P. J. (2005). Simple and robust removal of sun glint for mapping shallow-water benthos. *International Journal of Remote Sensing*, 26(10), 2107-2112.

Hedley, J. D., & Mumby, P. J. (2003). A remote sensing method for resolving depth and subpixel composition of aquatic benthos. *Limnology and Oceanography*, 48(1 part 2), 480-488.

Hedley, J. D., Mumby, P. J., Joyce, K. E., & Phinn, S. R. (2004). Spectral unmixing of coral reef benthos under ideal conditions. *Coral Reefs*, 23, 60-73.

Hedley, J., Roelfsema C., & Phinn S. R. (2009). Efficient radiative transfer model inversion for remote sensing applications. *Remote Sensing of Environment*, 113, 2527-2532.

Hedley, J., Roelfsema, C., & Phinn, S. (2010). Propagating uncertainty through a shallow water mapping algorithm based on radiative transfer model inversion. *Proceedings of Ocean Optics XX, Anchorage, AK, USA*.

Hedley, J., Roelfsema, C., Koetz, B., & Phinn, S. (2012a). Capability of the Sentinel 2 mission for tropical coral reef mapping and coral bleaching detection. *Remote Sensing of Environment*, 120, 145-155.

Hedley, J., Roelfsema, C. M, Phinn, S. R., & Mumby, P. J. (2012b). Environmental and sensor limitations in optical remote sensing of coral reefs: implications for monitoring and sensor design. *Remote Sensing*, 4, 271-302.

- Helton, J. C., & Davis, F. J. (2003). Latin Hypercube sampling and the propagation of uncertainty in analysis of complex systems. *Reliability Engineering and System Safety*, 81(1), 23-69.
- Hester, D. B., Nelson, S. A. C., Cakir, H. I., Khorram, S., & Cheshire, H. (2010). High-resolution land cover change detection based on fuzzy uncertainty analysis and change reasoning. *International Journal of Remote Sensing*, 31(2), 455-475.
- Hochberg, E. J., & Atkinson, M. J. (2000). Spectral discrimination of coral reef benthic communities. *Coral Reefs*, 19, 164-171.
- Hochberg, E. J., & Atkinson, M. J. (2003). Capabilities of remote sensors to classify coral, algae, and sand as pure and mixed spectra. *Remote Sensing of Environment*, 85, 175-189.
- Hochberg, E. J., Atkinson, M. J., Apprill, A., & Andrefouet, S. (2004). Spectral reflectance of coral. *Coral Reefs*, 23, 84-95.
- Hochberg, E. J., Atkinson, M. J., & Andrefouet, S. (2003). Spectral reflectance of coral reef bottom-types worldwide and implications for coral reef remote sensing. *Remote Sensing of Environment*, 85, 159-173.
- Holden, H., & LeDrew, E. (1998). Spectral discrimination of healthy and non-healthy corals based on cluster analysis, principal component analysis, and derivative spectroscopy. *Remote Sensing of Environment*, 65, 217-224.
- Holmes, R. W. (1970). The Secchi disk in turbid coastal waters. *Limnology and Oceanography*, 15, 688-694.
- Hu, C., Feng, L., Lee, Z., Davis, C. O., Mannino, A., McClain, C. R., & Franz, B. A. (2012). Dynamic range and sensitivity requirements of satellite ocean color sensors: learning from the past. *Applied Optics*, 51(25), 6045-6062.

- Huang, S., Li, Y., Shang, S., & Shang, S. (2013). Impact of computational methods and spectral models on the retrieval of optical properties via spectral optimization. *Optics Express*, 21(5), 6257-6273.
- Huntington, D. E., & Lyrintzis, C. S. (1998). Improvements to and limitations of Latin hypercube sampling. *Probabilistic Engineering Mechanics*, 13(4), 245-253.
- IOCCG (2006). Remote sensing of inherent optical properties: Fundamentals, tests of algorithms, and applications. In Z. P. Lee (Ed.), *Reports of the International Ocean colour Coordinating Group, No. 5, IOCCG, Dartmouth, Canada*.
- Irish, J. L., & Lillycrop, W. J. (1999). Scanning laser mapping of the coastal zone: the SHOALS system. *ISPRS Journal of Photogrammetry and Remote Sensing*, 54, 123-129.
- Jacobsen, A., Heidebrecht, K. B., and Goetz, A. F. H. (2000). Assessing the quality of the radiometric calibration of CASI data and retrieval of surface reflectance factors. *Photogrammetric Engineering and Remote Sensing*, 66(9), 1083-1091.
- Jahne, B. (2005). *Digital Image Processing*, 6th edn, Springer-Verlag Berlin Heidelberg, New York.
- Jahnert, R., & Collins, L. B. (2011). Significance of subtidal microbial deposits in Shark Bay, Australia. *Marine Geology*, 286, 106-111.
- Karpouzli, E., Malthus, T. J., & Place, C. J. (2004). Hyperspectral discrimination of coral reef benthic communities in the western Caribbean. *Coral Reefs*, 23, 141-151.
- Kay S., Hedley, J. D., & Lavender S. (2009). Sun glint correction of high and low spatial resolution images of aquatic scenes: a review of methods for visible and near-infrared wavelengths. *Remote Sensing*, 1, 697-730.

- Kendrick, G. A., Aylward, M. J., Hegge, B. J., Cambridge, M. L., Hillman, K., Wyllie, A., Lord, D. A. (2002). Changes in seagrass coverage in Cockburn Sound, Western Australia between 1967 and 1999. *Aquatic Biology*, 73, 75-87.
- Khan, M. A., Fadlallah, Y. H., & Al-Hinai, K. G. (1992). Thematic mapping of subtidal coastal habitats in the western Arabian Gulf using Landsat TM data – Abu Ali Bay, Saudi Arabia. *International Journal of Remote Sensing*, 13, 605-614.
- Kirk, J. T. O. (1989). The upwelling light stream in natural waters. *Limnology and Oceanography*, 34(8), 1410-1425.
- Kirkpatrick, S., Gelatt, C. D., & Vecchi, M. P. (1983). Optimization by Simulated Annealing. *Science*. 220(4598), 671-680.
- Kirkman, H. (1996). Baseline and monitoring methods for seagrass meadows. *Journal of Environmental Management*. 47, 191-201.
- Klonowski, W. M., Fearn, P. R. C. S., & Lynch, M. J. (2007). Retrieving key benthic cover types and bathymetry from hyperspectral imagery. *Journal of Applied Remote Sensing*, 1, 011505
- Ko, S-J., & Lee, Y. H. (1991). Center weighted median filters and their applications to image enhancement. *IEEE Transactions on Circuits and Systems*, 38(9), 984-993.
- Kobryn, H. T. Wouters, K., Beckley, L. E., & Heege, T. (2013). Ningaloo Reef: Shallow marine habitats mapped using a hyperspectral sensor. *Plos One*, 8(7), e70105.
- Kruse, K. A., Broadman, J. W., Lefkoff, A. B., Young, J. M., & Kierein-Young, K. S. (2000). HyMap: An Australian hyperspectral sensor solving global problems – results from USA HyMap data acquisitions. In *Proceedings of the 10th*

Australasian Remote Sensing and Photogrammetry Conference, Adelaide, Australia, August 21-25 (pp. 296-311).

Kruse, F.A. Lefkoff, A. B., Boardman, J. W., Heidebrecht, K. B., Shapiro, A. T., Barloon, P. J., & Goetz, A. F. H. (1993). The spectral image processing system (SIPS) – interactive visualization and analysis of imaging spectrometer data. *Remote Sensing of Environment*, 44, 145-163.

Kutser, T., Dekker, A. G., & Skirving, W. (2003). Modeling spectral discrimination of Great Barrier Reef Benthic Communities by Remote Sensing Instruments. *Limnology and Oceanography*, 48(1 part 2), 497-510.

Kutser, T. I., & Jupp, D. L. B. (2002). Mapping coral reef benthic habitat with a hyperspectral space borne sensor. *Proceedings of Ocean Optics XVI, Santa Fe, NM, USA*.

Kutser, T. I., & Jupp, D. L. B. (2006). On the possibility of mapping living corals to the species level based on their optical signatures. *Estuarine, Coastal and Shelf Science*, 69, 607-614.

Kutser, T., Vahtmae, E., Martin, G. (2006). Assessing suitability of multispectral satellites for mapping benthic macroalgal cover in turbid coastal waters by means of model simulations. *Estuarine, Coastal and Shelf Science*, 67, 521-529.

Lachenbruch, P. A., Sneeringer, C., & Revo, L. T. (1973). Robustness of the linear and quadratic discriminant function to certain types of non-normality. *Communications in Statistics*, 1(1), 39-56.

Larkum, A. W. D., & West, R. J. (1990). Long-term changes in seagrass meadows in Botany Bay, Australia. *Aquatic Botany*, 37, 55-70.

- Lee, Z., Arnone, R., Hu, C., Werdell, J. P., & Lubac, B. (2010). Uncertainties of optical parameters and their propagations in an analytical ocean color inversion algorithm. *Applied Optics*, 49(3), 369-381.
- Lee, Z., Carder, K. L., Arnone, R. A. (2002). Deriving inherent optical properties from water color: a multiband quasi-analytical algorithm for optically deep waters. *Applied Optics*, 41(27), 5755-5772.
- Lee, Z. P., Carder, K. L., Chen, R. F., & Peacock, T. G. (2001). Properties of the water column and bottom derived from Airborne Visible Infrared Imaging Spectroradiometer (AVIRIS) data. *Journal of Geophysical Research*, 106(C6), 11639-11651.
- Lee, Z. P., Carder, K. L., Hawes, S. K., Steward, R. G., Peacock, T. G., & Davis, C. O. (1994). Model for the interpretation of hyperspectral remote-sensing reflectance. *Applied Optics*, 33(24), 5721-5732.
- Lee, Z. P., Carder, K. L., Mobley, C. D., Steward, R. G., & Patch, J. S. (1998). Hyperspectral remote sensing for shallow waters. 1. A semianalytical model. *Applied Optics*, 37(27), 6329-6338.
- Lee, Z. P., Carder, K. L., Mobley, C. D., Steward, R. G., & Patch, J. S. (1999). Hyperspectral remote sensing for shallow waters: 2. Deriving bottom depths and water properties by optimization. *Applied Optics*, 38(18), 3831-3843.
- Lee, Z. P., Casey, B., Arnone, R., Weidemann, A., Parsons, R., Montes, M. J., ... Dye, J. (2007). Water and bottom properties of a coastal environment derived from Hyperion data measured from the EO-1 spacecraft platform. *Journal of Applied Remote Sensing*, 1, 011502.
- Lesser, M. P., & Mobley, C. D. (2007). Bathymetry, water optical properties, and benthic classification of coral reefs using hyperspectral remote sensing imagery. *Coral Reefs*, 26, 819-829.

- Lee, Z. P., Weidemann, A., and Arnone, R. (2013). Combined effect of reduced band number and increased bandwidth on shallow water remote sensing: the case of WorldView 2. *IEEE Transactions on Geoscience and Remote Sensing*, 51(5), 2577-2586.
- Lewis, D., Gould Jr, R. W., Weidemann, A., Ladner, S., and Lee, Z. P. (2013). Bathymetry estimations using vicariously calibrated HICO data. In W. W. Hu and R. A. Arnone (Eds.), *Ocean Sensing and Monitoring V, Proceedings of SPIE*, Vol. 8724.
- Li, R. R., Lucke, R., Korwan, D., & Gao, B-C. (2012). A Technique For Removing Second-Order Light Effects From Hyperspectral Imaging Data. *IEEE Transactions on Geoscience and Remote Sensing*, 50(3), 824-830.
- Liceaga-Correa, M. A., & Euan-Avila, J. I. (2002). Assessment of coral reef bathymetric mapping using visible Landsat Thematic Mapper data. *International Journal of Remote Sensing*, 23(1), 3-14.
- Lim, A., Hedley, J. D., LeDrew, E., Mumby, P. J., Roelfsema, C. (2009). The effects of ecologically determined spatial complexity on the classification accuracy of simulated coral reef images. *Remote Sensing of Environment*, 113(5), 965-978.
- Liu, S., Gao, Y., Zheng, W., & Li, X. (2015). Performance of two neural network models in bathymetry. *Remote Sensing Letters*, 6(4), 321-330.
- Logan, B. W., & Cebulski, D. E. (1970). Sedimentary environments of Shark Bay, Western Australia. *Carbonate sedimentation and environments, Shark Bay, Western Australia* (pp. 1–37). Tulsa, Oklahoma: American Association of Petroleum Geologists.
- Loog, M., Duin, R. P. W., & Haeb-Umbach, R. (2001). Multiclass linear dimension reduction by weighted pairwise fisher criteria. *IEEE Transactions on Pattern Analysis and Machine Intelligence*, 23(7), 762-766.

- Lubin, D., Li, W., Dustan, P., Mazel, C. H., & Stammes, K. (2001). Spectral signatures of coral reefs: features from space. *Remote Sensing of Environment*, 75, 127-137.
- Lucke, R. L., Corson, M., McGlothin, N. R., Butcher, S. D., Wood, D. L., Korwan, D. R., ... Chen, D. T. (2011). Hyperspectral Imager for the coastal ocean: Instrument description and first images. *Applied Optics*, 50(11), 1501-1516.
- Luczkovich, J. J., Wagner, T. W., Michalek, J. L., & Stoffle, R. W. 1993. Discrimination of coral reefs, seagrass meadows, and sand bottom types from space: A Dominican Republic case study. *Photogrammetric Engineering and Remote Sensing*, 59(3), 385-389.
- Lyard, F., Lefevre, F., Letellier, T., & Francis, O. (2006). Modeling the global ocean tides: A modern insight from FES2004. *Ocean Dynamics*, 56, 394-415, doi: 10.1007/s10236-006-0086-x.
- Lyzenga, D. R. (1978). Passive remote sensing techniques for mapping water depth and bottom features. *Applied Optics*, 17(3), 379-383.
- Lyzenga, D. R. (1981). Remote sensing of bottom reflectance and water attenuation parameters in shallow water using aircraft and Landsat data. *International Journal of Remote Sensing*, 2, 71-82.
- Lyzenga, D. R. (1985). Shallow water bathymetry using combined lidar and passive multispectral scanner data. *International Journal of Remote Sensing*, 6(1), 115-125.
- Ma, S., Tao, Z., Yang, X., Yu, Y., Zhou, X., & Li, Z. (2014). Bathymetry retrieval from hyperspectral remote sensing data in optical-shallow water. *IEEE Transactions on Geoscience and Remote Sensing*, 52(2), 1205-1212.
- Maeder, J., Narumalani, S., Rundquist, D. C., Perk, R. L., Schalles, J., Hutchins, K., & Keck, J. (2002). Classifying and mapping general coral-reef structure using

IKONOS data. *Photogrammetric Engineering and Remote Sensing*, 68(12), 1297-1305.

Matthew, M. W., Alder-Golden, S. M., Berk, A., Felde, G., Anderson, G. P., Gorodetzky, D., Paswaters, S., & Shippert, M. (2003). Atmospheric correction of spectral imagery Evaluation of the FLAASH algorithm with AVIRIS data. *Proceedings of SPIE*, 5093, 474-482.

Maritorena, S., Morel, A., & Gentili, B. (1994). Diffuse reflectance of oceanic shallow waters: influence of water depth and bottom albedo. *Limnology and Oceanography*, 39(7), 1689-1703.

Maritorena, S. A., Siegel, D. A., & Peterson, A. R. (2002). Optimization of ocean color model for global scale applications. *Applied Optics*, 41(15), 2705-2714.

Marquardt, D. W. (1963). An algorithm for least-squares estimation of nonlinear parameters. *Journal of the Society for Industrial and Applied Mathematics*, 11(2), 431-441.

Markwardt, C. B. (2009). Non-Linear Least Squares Fitting in IDL with MPFIT. In D. Bohlender, P. Dowler & D. Durand (Eds.), *Astronomical Data Analysis Software and Systems XVIII, Quebec, Canada, ASP Conference Series, 2-5 November 2009* (pp. 251-254).

McKay, M. D., Conover, W. J., & Beckman, R. J. (1979). A comparison of three methods for selecting values of input variables in the analysis of output from computer code. *Technometrics*, 21, 239-245.

McClain, C., Hooker, S., Feldman, G., & Bontempi, P. (2006). Satellite data for ocean biology, biogeochemistry and climate research. *EOS, Transactions of American Geophysical Union*, 87(34), 337-

- Mied, R. P., Snow, C. M., Smith, G. B., Bachmann, C. M., Korwan, D. R., Fusina, R. A., ... Hagen, R. A. (2013). Tidal constituents from remote sensing image sequences. *Estuarine, Coastal and Shelf Science*, 117, 159-167.
- Minghelli-Roman, A., Chisholm, J. R. M., Marchioretto, M., Ripley, H., & Jaubert, J. M. (2002). Discrimination of coral reflectance spectra in the Red Sea. *Coral Reefs*, 21, 307-314.
- Mishra, D., Narumalani, S., Rundquist, D., & Lawson, M. (2005). High-resolution ocean color remote sensing of benthic habitats: a case study at the Roatan Island, Honduras. *IEEE Transactions on Geoscience and Remote Sensing*, 43(7), 1592-1604.
- Mishra, D., Narumalani, S., Rundquist, D., & Lawson, M. (2006). Benthic habitat mapping in tropical marine environments using QuickBird multispectral data. *Photogrammetric Engineering and Remote Sensing*, 72(9), 1037-1048.
- Mishra, D., Narumalani, S., Rundquist, D., Lawson, M., & Perk, R. (2007). Enhancing the detection and classification of coral reef and associated benthic habitats: A hyperspectral remote sensing approach. *Journal of Geophysical Research*, 112, C08014.
- Moberg, F., & Folke, C. (1999). Ecological goods and services of coral reef systems. *Ecological Economy*, 29, 215-233.
- Mobley, C. D. (1994). *Light and Water*, San Diego, CA: Academic Press
- Mobley, C. D., & Sundman, L. K. (2000). *Hydrolight 4.1 Users Guide* [Computer Software]. Seattle, WA: Sequoia Scientific, Inc.
- Mobley, C. D. (2012). Shallow-water remote sensing: Lecture 1: Overview. *IOCCG Course*, Villefranche-sur-Mer, France. Retrieved from www.ioccg.org/training/SLS-2012/Mobley_Lect1.pdf.

- Mobley, C. D., Sundman, L. K., Davis, C. O., Bowles, J. H., Downes, T. V., Leathers, R. A., ... Gleason A. (2005). Interpretation of hyperspectral remote-sensing imagery by spectrum matching and look-up tables. *Applied Optics*, 44(17), 3576-3592.
- Mobley, C. D., Zhang, H., & Voss, K. J. (2003). Effects of optically shallow bottoms on upwelling radiances: Bidirectional reflectance distribution function effects. *Limnology and Oceanography*, 48, 337-345.
- Montes, M. J., Gao, B-C., & Davis, C. O. (2004). *NRL atmospheric correction algorithms for oceans: Tafkaa User's Guide* [Computer Software]. Washington DC: Naval Research Laboratory.
- Morel, A. (1974). Optical properties of pure water and pure sea water, *Optical aspects of oceanography*, 1, 1-24.
- Morel, A. (1980). In-water and remote measurements of ocean color. *Boundary-Layer Meteorology*, 18, 177-201.
- Morel, A. (1988). Optical modelling of the upper ocean in relation to its biogenous matter content (case 1 waters). *Journal of Geophysical Research*, 93, 10749-10768.
- Morel, A., & Bricaud, A. (1981). Theoretical results concerning light absorption in a discrete medium, and application to specific absorption of phytoplankton. *Deep-Sea Research*, 28A(11), 1375-1393.
- Morel, A., & Maritorena, S. (2001). Bio-optical properties of oceanic waters: A reappraisal. *Journal of Geophysical Research*, 106(C4), 7163-7180.
- Morel, A., & Prieur, L. (1977). Analysis of variations in ocean color, *Limnology and Oceanography*, 22(4), 709-722.

- Morton, R. A. (2002). Factors controlling storm impacts on coastal barriers and beaches - a preliminary basis for near real-time forecasting. *Journal of Coastal Research*, 18(3), 486-501.
- Morton, R. A., & Sallenger, A. H. (2003). Morphological impacts of extreme storms on sandy beaches and barriers. *Journal of Coastal Research*, 19(3), 560-573.
- Moses, W. J., Bowles, J. H., Lucke, R. L., & Corson, M. R. (2012). Impact of signal-to-noise ratio in hyperspectral sensor on the accuracy of biophysical parameter estimation in case II waters. *Optics Express*, 20(4), 4309-4330.
- Moses, W. J., Bowles, J. H., and Corson, M. R. (2015). Expected improvements in the quantitative remote sensing of optically complex waters with the use of an optically fast hyperspectral spectrometer – a modeling study. *Sensors*, 15(3), 6152-6173.
- Moses, W. J., Gitelson, A. A., Berdnikov, S., Bowles, J. H., Povazhnyi, V., Saprygin, V., ... Patterson, K. W. (2014). HICO-Based NIR–Red Models for Estimating Chlorophyll-a Concentration in Productive Coastal Waters. *IEEE Geoscience and Remote Sensing Letters*, 11(6), 1111-1115, doi: 10.1109/LGRS.2013.2287458.
- Mueller, J. L. (2000). SeaWiFS algorithm for the diffuse attenuation coefficient, K(490), using water-leaving radiances at 490 and 555 nm. In S. B. Hooker and E. R. Firestone (Eds.), *NASA Technical Memorandum 2000-206892*, NASA Goddard Space Flight Centre (pp. 9 -23)
- Mumby, P. J., Clark, C. D., Green, E. P., & Edwards, A. J. (1998a). Benefits of water column correction and contextual editing for mapping coral reefs. *International Journal of Remote Sensing*, 19(1), 203-210.
- Mumby, P. J., & Edwards, A. J. (2002). Mapping marine environments with IKONOS imagery: enhanced spatial resolution can deliver greater thematic accuracy. *Remote Sensing of Environment*, 82, 248-257.

- Mumby, P. J., Green, E. P., Edwards, A. J., & Clark, C. D. (1997). Coral reef habitat mapping: how much detail can remote sensing provide. *Marine Biology*, 130, 193-202.
- Mumby, P. J., Green, E. P., Clark, C. D., & Edwards, A. J. (1998b). Digital analysis of multispectral airborne imagery of coral reefs. *Coral Reefs*, 17, 59-69.
- Mumby, P. J., & Harborne, A. R. (1999). Development of a systematic classification scheme of marine habitats to facilitate regional management and mapping of Caribbean coral reefs. *Biological Conservation*, 88, 155-163.
- Mumby, P. J., Hedley, J. D., Chisholm, J. R. M., Clark, C. D., Ripley, H., & Jaubert, J. (2004). The cover of living and dead corals from airborne remote sensing. *Coral Reefs*, 23, 171-183.
- Nelder, J. A., & Mead, R. (1965). A simplex method for function minimization. *The Computer Journal*. 7, 308-313.
- Nichols, J. D., & Williams, B. K. (2006). Monitoring for conservation. *Trends in Ecology and Conservation*, 21(12), 668-673.
- Obura, D., & Grimsditch, G. (2009). Coral Reefs, Climate change and resilience – An agenda for action from the IUCN World Conservation Congress. October 6-9 2008.
- O'Neill, J. D., & Costa, M. (2013). Mapping eelgrass (*Zostera marina*) in the Gulf Islands National Park Reserve of Canada using high spatial resolution satellite and airborne imagery. *Remote Sensing of Environment*, 133, 152-167.
- O'Reilly, J. E., Maritorena, S., Mitchell, B. G., Seigel, D. A., Carder, K. L., Garver, S. A., ... McClain, C. (1998). Ocean color chlorophyll algorithms for SeaWiFS. *Journal of Geophysical Research*, 103(C11), 24937-24953.

- O'Reilly, J. E., Maritorena, S., Siegel, D. A., O'Brien, M. C., Toole, D., Mitchell, B. G., ... Cluver, M. (2000). Ocean color chlorophyll a algorithms for seawifs, oc2, and oc4: version 4. In S. B. Hooker and E. R. Firestone (Eds.), *NASA Technical Memorandum 2000-206892*, NASA Goddard Space Flight Centre (pp. 9 -23)
- Paredes, J. M., & Spero, R. E. (1983). Water depth mapping from passive remote sensing data under a generalised ratio assumption. *Applied Optics*, 22(8), 1134-1135.
- Pasqualini, V., Pergent-Martini, C., Clabaut, P., & Pergent, G. (1998). Mapping of *Posidonia oceanica* using Aerial Photographs and Side Scan Sonar: Application off the Island of Corsica (France). *Estuarine, Coastal and Shelf Science*, 47, 359-367.
- Pasqualini, V., Pergent-Martini, C., Pergent, G., Agreil, M., Skoufas, G., Sourbes, L., & Tsirika, A. (2005). Use of SPOT 5 for mapping seagrasses: An application to *Posidonia oceanica*. *Remote Sensing of Environment*, 94, 39-45.
- Paterson, K. W., & Lamela, G. (2011, May 04). Influence of aerosol estimation on coastal water products retrieved from HICO images. *Proc. SPIE 8030, Ocean Sensing and Monitoring III* (pp. 803005). <http://dx.doi.org/10.1117/12.883263>.
- Philpot, W. D. (1987). Radiative transfer in stratified waters: a single-scattering approximation for irradiance. *Applied Optics*, 26(19), 4123-4132.
- Philpot, W. D. (1989). Bathymetric mapping with passive multispectral imagery. *Applied Optics*, 28(8), 1569-1578.
- Philpot, W., Davis, C. O., Bissett, W. P., Mobley, C. D., Kohler, D. D. R., Lee, Z., ... Arnone, R.A. (2003). Bottom characterisation from Hyperspectral image data. *Oceanography*, 17(2), 76-85.

- Polcyn, F. C., Brown, W. L., & Sattinger, I. J. (1970). The measurement of water depth by remote sensing techniques. *Report 8973-26-F, Willow Run Laboratories, U. Michigan Ann Arbor.*
- Preisendorfer, R. W. (1976). *Hydrologic Optics Volume 1: Introduction*. Honolulu: U.S. Department of Commerce, National Oceanic and Atmospheric Administration, Environmental Research Laboratories, Pacific Marine Environmental Laboratory. Retrieved from <https://archive.org/details/hydrologicopt00prei>.
- Press, W. H., Teukolsky, S. A., Vetterling, W. T., & Flannery, B. P. (2007). *Numerical recipes: the art of scientific computing* (3rd ed.). Cambridge, U.K.: Cambridge University Press.
- Prieur, L., & Sathyendranath, S. (1981). An optical classification of coastal and oceanic waters based on the specific spectral absorption curves of phytoplankton pigments, dissolved organic matter, and other particulate materials. *Limnology and Oceanography*, 26(4), 671-689.
- Pu, R., Bell, S., Meyer, C., Baggett, L., & Zhao, Y. (2012). Mapping and assessing seagrass along the western coast of Florida using Landsat TM and EO-1 ALI/Hyperion imagery. *Estuarine, Coastal and Shelf Science*, 115, 234-245.
- Purkis, S. J. (2005). A 'reef-up' approach to classifying coral habitats from IKONOS imagery. *IEEE Transactions on Geoscience and Remote Sensing*, 43(6), 1375-1390.
- Purkis, S., Kenter, J. A. M., Oikonomou, E. K., & Robinson, I. S. (2002). High-resolution ground verification, cluster analysis and optical model of reef substrate coverage on Landsat TM imagery (Red Sea, Egypt). *International Journal of Remote Sensing*, 23(8), 1677-1698.

- Purkis, S. J., & Pasterkamp, R. (2004). Integrating in situ reef-top reflectance spectra with Landsat TM imagery to aid shallow-tropical benthic habitat mapping. *Coral Reefs*, 23, 5-20.
- Rand, W. M. (1971). Objective criteria for the evaluation of clustering methods. *Journal of the American Statistical Association*, 66(336), 846-850.
- Remillard, M. M., & Welch, R. A. (1992). GIS technology for aquatic macrophyte studies: I. Database development and changes in the aquatic environment. *Landscape Ecology*, 7(3), 151-162.
- Rencher, A. C., & Christensen, W. F. (2012). *Methods of Multivariate Analysis* (3rd ed.), John Wiley & Sons, Inc. ISBN:0-470-17896-5.
- Richards, J. A., & Jia, X. (2006). *Remote sensing digital analysis: An introduction*. Berlin, Germany: Springer-Verlag Berlin Heidelberg.
- Richter, R. (1990). A fast atmospheric correction algorithm applied to Landsat TM images. *International Journal of Remote Sensing*, 11(1), 159-166.
- Roelfsema, C., Kovacs, E. M., Saunders, M. I., Phinn, S., Lyons, M., & Maxwell, P. (2013). Challenges of remote sensing for quantifying changes in large complex seagrass environments. *Estuarine, Coastal and Shelf Science*, 133, 161-171.
- Roelfsema, C. M., Lyons, M., Kovacs, E. M., Maxwell, P., Saunders, M. I., Samper-Villarreal, J., & Phinn, S. R. (2014). Multi-temporal mapping of seagrass cover, species, and biomass: A semi-automated object based image analysis approach. *Remote Sensing of Environment*, 150, 172-187.
- Roesler, C. S., & Perry, M. J. (1995). In situ phytoplankton absorption, fluorescence emission, and particulate backscattering spectra determined from reflectance. *Journal of Geophysical Research*, 100(C7), 13279-13294.

- Roesler, C. S., Perry, M. J., & Carder, K. L. (1989). Modeling in situ phytoplankton absorption from total absorption spectra in productive inland marine waters. *Limnology and Oceanography*, 34(8), 1510-1523.
- Roff, J. C., & Taylor, M. E. (2000). National framework for marine conservation – a hierarchical geophysical approach. *Aquatic Conservation: Marine and Freshwater Ecosystems*, 10, 209-233.
- Roff, J. C., Taylor, M. E., & Laughren, J. (2003). Geophysical approaches to the classification, delineation and monitoring of marine habitats and their communities. *Aquatic Conservation: Marine and Freshwater Ecosystems*, 13, 77-90.
- Salama, S. M., & Stein, A. (2009). Error decomposition and estimation of inherent optical properties. *Applied Optics*, 48(26), 4947-4962.
- Salinas, S. V., Chang, C. W., & Liew, S. C. (2007). Multiparameter retrieval of water optical properties from above-water remote-sensing reflectance using the simulated annealing algorithm. *Applied Optics*, 46(16), 2727-2742.
- Salvador, S., & Chan, P. (2004). Determining the number of clusters/segments in hierarchical clustering/segmentation algorithms. In *Proceedings of 16th IEEE International Conference on Tools with Artificial Intelligence (ICTAI 2004)*, Boca Raton, USA, November 15-17 (pp. 576-584).
- Sathyendranath, S., Bukata, R. P., Arnone, R., Dowell, M. D., Davis, C. O., Babin, M., ... Campbell, J. W. (2000). Colour of Case 2 Waters. In S. Sathyendranath (Eds.), *IOCCG Report Number 3, Remote Sensing in Coastal, and Other Optically Complex, Waters* (pp. 23-46).
- Sathyendranath, S., Prieur, L., & Morel, A. (1989). A three component model of ocean colour and its application to remote sensing of phytoplankton pigments in coastal waters. *International Journal of Remote Sensing*, 10(8), 1373-1394.

- Sandidge, J. C., & Holyer, R. J. (1998). Coastal bathymetry from hyperspectral observations of water radiance. *Remote Sensing of Environment*, 65, 341-352.
- Santer, R., & Schmechtig, C. (2000). Adjacency effects on water surface: primary scattering approximation and sensitivity study. *Applied Optics*, 39, 361-375.
- Slade, W. H., Ransom, H. W., Musavi, M. T., & Miller, R. L. (2004). Inversion of ocean color observations using particle swarm optimization. *IEEE Transactions on Geoscience and Remote Sensing*, 42(9), 1915-1923.
- Shi, W. Z., & Ehlers, M. (1996). Determining uncertainties and their propagation in dynamic change detection based on classified remotely-sensed imagery. *International Journal of Remote Sensing*, 17(14), 2729-2741.
- Siegel, D. A., Maritorena, S., Nelson, N. B., Behrenfeld, M. J., & McClain, C. R. (2005). Colored dissolved organic matter and its influence on the satellite-based characterization of the ocean biosphere. *Geophysical Research Letters*, 32, L20605, doi: 10.1029/2005GL024310.
- Smith, R. C., & Baker, K. S. (1981). Optical properties of the clearest natural waters (200-800 nm). *Applied Optics*, 20(2), 177-184.
- Sohn, Y., & Rebello, N. S. (2002). Supervised and Unsupervised Spectral Angle Classifiers. *Photogrammetric Engineering and Remote Sensing*, 68(12), 1271-1280.
- Sokal, R. R., & Rohlf, F. J. (1962). The comparison of dendrograms by objective methods. *Taxon*, 11(2), 33-40.
- Sothoran, I. S., Foster-Smith, R. L., & Davis, J. (1997). Mapping of Marine Benthic Habitats Using Image Processing Techniques Within a Raster-based Geographic Information System. *Estuarine, Coastal and Shelf Science*, 44, 25-31.

- Stambler, N., & Shashar, N. (2007). Variation in spectral reflectance of hermatypic corals, *Stylophora pistillata* and *Pocillopora damicornis*. *Journal of Experimental Marine Biology and Ecology*, 351, 143-149.
- Sterckx, S., Knaeps, E., & Ruddick, K. (2011). Detection and correction of adjacency effects in hyperspectral airborne data of coastal and inland waters: the use of the near infrared similarity spectrum. *International Journal of Remote Sensing*, 32(21), 6479-6505.
- Stumpf, R.P., Holderied, K., & Sinclair, M. (2003). Determination of water depth with high-resolution satellite imagery over variable bottom types. *Limnology and oceanography*, 48(1, part 2), 547-556.
- Tassan, S. (1996). Modified Lyzenga's method for macroalgae detection in water with non-uniform composition. *International Journal of Remote Sensing*, 17, 1601-1607.
- Torrecilla, E., Stramski, D., Reynolds, R. A., Millan-Nunez, E., & Piera, J. (2011). Cluster analysis of hyperspectral optical data for discriminating phytoplankton pigment assemblages in the open ocean. *Remote Sensing of Environment*, 115, 2578-2593.
- Townshend, J. R. G., Justice, C. O., Gurney, C., & McManus, J. (1992). The impact of misregistration on change detection. *IEEE Transactions on Geoscience and Remote Sensing*, 30, 1054-1060.
- Twardowski, M. S., Boss, E., Macdonald, J. B., Pegau, W. S., Barnard, A. H., & Zaneveld, J. R. V. (2001). A model for estimating bulk refractive index from the optical backscattering ratio and the implications for understanding particle composition in case I and case II waters. *Journal of Geophysical Research*, 106(C7), 14129-14142.
- Ungar, S. G. (2003). Overview of the Earth Observing One (EO-1) Mission. *IEEE Transactions on Geoscience and Remote Sensing*, 41(6), 1149-1159.

- Vahtmae, E., & Kutser, T. (2007). Mapping bottom type and water depth in shallow coastal waters with satellite remote sensing. *Journal of Coastal Research*, SI 50, 185-189.
- Vahtmae, E., & Kutser, T. (2013). Classifying the Baltic Sea shallow water habitats using image-based and spectral library methods. *Remote Sensing*, 5, 2451-2474.
- Vahtmae, E., Kutser, T., Kotta, J., & Parnoja, M. (2011). Detecting patterns and changes in a complex benthic environment of the Baltic Sea. *Journal of Applied Remote Sensing*, 5, 053559.
- Vahtmae, E., T. Kutser, G. Martin, & J. Kotta. (2006). Feasibility of hyperspectral remote sensing for mapping benthic macroalgal cover in turbid coastal waters – a Baltic Sea case study. *Remote Sensing of Environment*, 101, 342-351.
- Vermote, E. F., Tanre, D., Deuze, J. L., Herman, M., & Morcette, J. J. (1997). Second Simulation of the Satellite Signal in the Solar Spectrum, 6S: An overview. *IEEE Transactions on Geoscience and Remote Sensing*, 35(3), 675-686.
- Volpe, V., Silvestri, S., & Marani, M. (2010). Remote sensing retrieval of suspended sediment concentration in shallow waters. *Remote Sensing of Environment*, 115, 44-54.
- Voss, K.J., 1992, A spectral model of the beam attenuation coefficient in the ocean and coastal areas. *Limnology and Oceanography*, 37(3): 501-509.
- Walker, D. I., Kendrick, G. A., & McComb, A. J. (1988). The distribution of seagrass species in Shark Bay, Western Australia, with notes on their ecology. *Aquatic Botany*, 30: 305-317.

- Wang, P., Boss, E. S., & Roesler, C. (2005). Uncertainties of inherent optical properties obtained from semianalytical inversions of ocean color. *Applied Optics*, 44(9), 4074-4085.
- Ward, T. J., Vanderkleft, M. A., Nicholls, A. O., & Kenchington, R. A. (1999). Selecting marine reserves using habitats and species assemblages as surrogates for biological diversity. *Ecological Applications*, 9(2), 691-698.
- Werdell, P. J., Franz, B. A., Bailey, S. W., Feldman, G. C., Boss, E., Brando, V. E., ... Mangin, A. (2013). Generalized ocean color inversion model for retrieving marine inherent optical properties. *Applied Optics*, 52(10), 2019-2037.
- Wettle, M., & Brando, V. E. (2006). SAMBUCA: semi-analytical model for bathymetry, un-mixing and concentration assessment. *Report 22/06*, CSIRO Land and Water. Retrieved from www.clw.csiro.au/publications/science/2006/sr22-06.pdf
- Wolfe, R. E., Nishihama, M., Fleig, A. J., Kuyper, J. A., Roy, D. P., Storey, J. C., & Patt, F. S. (2002). Achieving sub-pixel geolocation accuracy in support of MODIS land science. *Remote Sensing of Environment*, 83, 31-49.
- Wyss, G. D., & Jorgensen, K. H. (1998). A user's guide to LHS: Sandia's Latin Hypercube Sampling Software. *Report SAND98-210, Risk Assessment and Systems Monitoring Department, Sandia Laboratories*. Retrieved from <http://prod.sandia.gov/techlib/access-control.cgi/1998/980210.pdf>
- Zainal, A. J. M., Dalby, D. H., & Robinson, I. S. (1993). Monitoring marine ecological changes on the east coast of Bahrain with Landsat TM. *Photogrammetric Engineering and Remote Sensing*, 59(3), 415-421.
- Zapata-Ramirez, P. A., Blanchon, P., Oliosio, A., Hernandez-Nunez, H., & Sobrino, J. A. (2013). Accuracy of IKONOS for mapping benthic coral-reef habitats: a case study from Puerto Morelos Reef National Park, Mexico. *International Journal of Remote Sensing*, 34(9-10), 3671-3687.

Zaneveld, J. R. V. (1989). An asymptotic closure theory for irradiance in the sea and its inversion to obtain the inherent optical properties. *Limnology and Oceanography*, 34(8), 1442-1452.

Zhan, H., Lee, Z., Shi, P., Chen, C., & Carder, K. L. (2003). Retrieval of water optical properties for optically deep waters using genetic algorithms. *IEEE Transactions on Geoscience and Remote Sensing*, 41(5), 1123-1128.

Zhang, C., Selch, D., Xie, Z., Roberts, C., Cooper, H., & Chen, G. (2013). Object-based benthic habitat mapping in the Florida Keys from hyperspectral imagery. *Estuarine, Coastal and Shelf Science*, 134, 88-97.

Every reasonable effort has been made to acknowledge the owners of copyright material. I would be pleased to hear from any copyright owner who has been omitted or incorrectly acknowledged.